Wave Loads and Motions of the Exowave Wave Energy Converter

Master thesis

Structural and Civil Engineering

Asger Odderskov, Frederik Thomsen and Johan Eskesen

Aalborg University

6th June 2024

AALBORG UNIVERSITY

3rd and 4th semester, M.Sc. programme in Structural and Civil Engineering
Thomas Manns Vej 23
9220 Aalborg Øst

Title:

Wave Loads and Motions of the Exowave Wave Energy Converter

Project:

Master thesis

Project period:

September 2023 - June 2024

Project group:

Master - Group 1

Group members:

Asger Frankert Odderskov
Frederik Thomsen
Johan Eskesen

Supervisor:

Thomas Lykke Andersen
Peter Frigaard
Sarah Krogh Iversen

Asger Frankert Odderskov
aodder19@student.aau.dk
20194157

Frederik Thomsen
fthoms19@student.aau.dk
20194708

Johan Eskesen
jeskes18@student.aau.dk
20183568

Main report page count: 89
Appendix page count: 318
Submitted: 6th June 2024
ECTS: 45

Abstract

The purpose of this master thesis is to investigate the accuracy of different approaches for modelling the wave-structure interaction of the floater of the Exowave WEC. The Exowave WEC is a fixed oscillating wave surge converter. The wave-structure interaction is investigated for four different floater geometries. The wave-structure interaction is investigated by examining the wave excitation forces on the floaters in a fixed position. Afterwards, the motions of the floaters due to wave excitation forces are examined. Two experiments are conducted to determine a benchmark for the forces and motions. To describe the wave excitation forces on the floaters, two calculation methods are considered: A method based on the Morison equation and a BEM-based method using NEMOH. The calculation methods are compared to the measured data, showing that both methods can be used to estimate the wave forces adequately.

Several numerical models based on the equation of motion are investigated using the calculation methods. A numerical model based on the calculation method using the Morison equation shows a significant deviation for the motions of the floaters compared to the measured motion from the experiment. A BEM-based numerical model with a drag contribution calculated with a relative velocity formulation of the Morison equation shows promising results. It is attempted to improve the BEM-based numerical model by implementing experimentally determined damping coefficients.

It is determined that the wave-structure interaction of the floater of the Exowave WEC can be described with an acceptable degree of accuracy using BEM-based numerical models utilising both experimental and BEM-based damping.

Foreword

This report has been written by Asger Odderskov, Frederik Thomsen, and Johan Eskesen in the 3rd and 4th semester of the Master's programme in Structural and Civil Engineering at Aalborg University.

The group would like to thank the supervisors Peter Frigaard, Sarah Krogh Iversen, and Thomas Lykke Andersen for their guidance and feedback.

Furthermore, the group would like to thank the technical staff in the AAU BUILD department in the wave laboratory Nikolaj Holk and Jesper Ryan for their help with the experimental work.

The gravitational acceleration used in this report is 9.82 $\frac{\mathrm{m}}{\mathrm{s}^2}$.

Reading guide

This thesis uses the Harvard referencing method for citations. Sources are referenced in the text as [author's last name, year of publication]. If the year of publication is not available it is given as "n.d.".

Citations placed before a full stop refer to the sentence in which it is placed.

Citations placed after a full stop refer to the entire previous paragraph.

The sources are compiled in an alphabetically arranged bibliography at the end of the report.

Tables and figures are named according to the chapter and order they occur in e.g. the first Figure in chapter one is called "Figure 1.1".

Equations are named in the same way, but marked by parentheses. e.g. the first equation in chapter one is called "Equation (1.1)".

All abbreviations are compiled in a list of abbreviations following the foreword. All symbols are compiled in a list of symbols following the list of abbreviations. Symbols and abbreviations are sorted alphabetically.

The appendices are presented after the bibliography and are sorted after the appearance with the exception of the appendices which shows the result.

The project is recommended to print in colour and double-sided to give the best reader experience.

List of abbreviations

In this chapter, the abbreviations used in this report are listed. The abbreviation is mentioned in alphabetical order.

BEM	Boundary element method
CAD	Computer-aided design
CFD	Computational fluid dynamics
CI	Confidence interval
CM	Center of mass
DoF	Degree of freedom
FVU	Fraction of variance unexplained
LCoE	Levelised cost of energy
LPF	Linear potential flow
NM	Numerical model
PTO	Power take off
QTM	Qualisys Track Manager
SFT	Stream function theory
SWL	Still water level
WEC	Wave energy converter
WG	Wave gauge

List of symbols

In this chapter, the symbols used in the report are explained. The symbol is mentioned in alphabetical order.

A	Cross-sectional area [m^2]
a	Wave amplitude [m]
c	Phase velocity [m/s]
c_h	Hydrodynamic damping coefficient [Nm/(rad/s)]
$Contrib$	Wave energy contribution [%]
C_A	Added mass coefficient [-]
C_D	Drag coefficient [-]
D	Diameter or cross-sectional dimension [m]
E	Error [−]
f_n	Normal force [N/m]
F_n	Normal force [N]
$F_{ex_{11}}$	Wave excitation force in surge direction [N]
$F_{ex_{33}}$	Wave excitation force in heave direction [N]
$F_{ex_{55}}$	Wave excitation force in pitch direction [N]
f_t	Transverse force [N/m]
F_t	Transverse force [N]
F_x	Horizontal force along of the wave direction [N]
F_y	Horizontal force transverse of the wave direction[N]
F_z	Vertical force [N]
H	Wave height [m]
h	Water depth [m]
H_{m0}	Significant wave height based on frequency domain analysis [m]
H_s	Significant wave height [m]
I	Mass moment of inertia [$kg \cdot m^2$]
KC	Keulegan-Carpenter [−]
k	Wave number [−]
L	Wave length [m]
l_c	Characteristic length [m]
M	Moment around hinge [Nm]
M_b	Buoyancy moment [Nm]
M_{ex}	Wave excitation moment [Nm]
$M_{ex,norm}$	Normalised wave excitation moment [Nm/m]
M_g	Gravitational moment [Nm]
M_{hs}	Hydrostatic moment [Nm]
M_{rad}	Radiation moment [Nm]
m	Mass of floater model [kg]
m_h	Hydrodynamic added mass moment of inertia [$kg \cdot m^2$]
n	Normal vector [-]
P	Possibility of occurrence [%]
P_{wave}	Wave power [kW/m]
p_d	Dynamic pressure [Pa]
p_{total}	Total hydrostatic pressure [Pa]

Re	Reynolds number [-]
r	Distance from hinge to area [m]
r_b	Distance from hinge to centre of buoyancy [m]
r_g	Distance from hinge to centre of gravity [m]
r_{bottom}	Distance from hinge to bottom of floater [m]
r_{top}	Distance from hinge to top of floater or η [m]
s	Wave steepness [−]
T	Wave period [s]
t	Time [s]
T_p	Peak period [s]
T_x	Measured torque around the x-axis [Nm]
T_y	Measured torque around the y-axis [Nm]
T_z	Measured torque around the z-axis [Nm]
u	Fluid particle velocity in x-direction [m/s]
u_b	Velocity of body in still water [m/s]
u_{max}	Maximum particle velocity in x-direction [m/s]
u_{rel}	Relative velocity [m/s]
V_n	Normal velocity [m/s]
w	Fluid particle velocity in z-direction [m/s]
x	Position in the x-direction [m]
$\mathbf{x}$	Position vector $\mathbf{x} = (x, y, z)$ [m]
z	Position in the z-direction [m]
η	Water surface elevation from SWL (positive upwards) [m]
θ, $\dot{\theta}$, $\ddot{\theta}$	Angular position, velocity and acceleration [rad, rad/s, rad/s^2]
θ_0	Initial angular position [rad]
μ	Dynamic viscosity [Pa/s]
ν	Kinematic viscosity [m^2/s]
ρ	Density of fluid [kg/m^3]
φ	Velocity potential [m^2/s]
Φ	Velocity potential [m^2/s]
ϕ	Phase [°]
ϕ_{11}	Phase in the surge direction [°]
ϕ_{33}	Phase in the heave direction [°]
ϕ_{55}	Phase in the pitch direction [°]
ω	Wave frequency [rad/s]

Contents

Introduction 1

The consequences of climate change are widespread and the effects are rapidly increasing. Climate change causes more extreme weather and climate events leading to the loss of homes and human life along with irreversible damage to nature [IPCC, 2023]. One of the main causes of climate change is that the world's energy production is dominated by the use of fossil fuels. It is estimated that fossil fuels contribute to almost 90% of all CO_2 emissions which makes it the leading cause of climate change according to Freund et al. [2005]. Furthermore, fossil fuels are a finite resource and will therefore at some point be depleted with the rate it is being used at the moment. Besides, a considerable amount of the world's fossil fuel deposits are located in some politically unstable countries which enhances the interest in becoming independent of the fossil fuel supply [IEA, 2024]. Therefore, there is a great interest in being able to meet the energy requirement locally and sustainably. This means that there is a need for alternative energy sources. [IPCC, 2023]

Renewable energy sources must be a part of the solution to alternative energy sources. Renewable energy sources are defined as energy sources that are unlimited and environmentally beneficial compared to fossil fuels. A key factor in the transition from fossil fuels to renewable energy sources is the levelised cost of energy (LCoE). The LCoE describes the cost of energy production throughout the lifetime of a specific energy source. To motivate the transition from fossil fuels to renewable energy sources, the LCoE of a renewable energy source should be close to the same as for fossil fuels. Comparing the LCoE in 2010 and 2020 a decrease in the LCoE can be seen for several types of renewable energy sources. The LCoE of solar energy and wind power technologies has significantly dropped in the period. The LCoE of these renewable energy sources is the same or even less than the LCoE of fossil fuels in the same period. [IRENA, 2021]

Another essential part of converting to renewable energy is the ability to create a stable energy production from renewable energy. This is accomplished by having a variety of energy sources that can fulfil the need for energy at all times. Furthermore, a vast portfolio of technologies within renewable energy is necessary to ensure sufficient solutions to fit the local demand. [Pecher and Kofoed, 2017]

Wave energy is a renewable energy source that is largely unutilised in comparison with other renewable energy sources. Wave energy has the potential to supply a significant part of the world's energy demand. Wave energy has the advantage that it produces a more stable energy output compared to other renewable energy sources such as wind and solar energy. [CorPower Ocean, 2022]

Wave energy is less developed than other renewable energy sources such as wind turbines but to reduce the cost and increase wave energy utilisation further research and development is needed. In order to utilise ocean wave energy, a wave energy converter (WEC) is required. A WEC consists of four subsystems, which are the hydrodynamic, reaction, power take-off, and control subsystems. The hydrodynamic subsystem is a mechanical energy conveyer that converts a hydrodynamic motion to a mechanical motion.

The reaction subsystem consists of the foundation and support structure. The power take-off subsystem (PTO) is required to turn the mechanical motion into applicable energy. The control subsystem is used to optimise the PTO by controlling it in order to extract as much energy as possible. [Pecher and Kofoed, 2017]

The design of a WEC has a significant influence on the ability to extract wave energy. The six degrees of freedom (DoF) for the motions of a WEC are shown in Figure 1.1. There are many possible designs for a WEC, however there are some types that are more prevalent than others. Among the more common designs are point absorber buoys, surface attenuators, oscillating water columns, and overtopping devices [The Liquid Grid, n.d]. The point absorber buoy is fixed to the seabed and utilises the wave energy in a single point by a heave motion. It is one of the most developed methods to utilise ocean wave energy. The surface attenuators are often constructed as a modular design with flexing joints in between which are oriented in the wave direction. The contribution of motion for energy production is primarily from surge, sway, and heave. The oscillating water columns are fixed constructions that are designed to trap air which is compressed by the wave-induced pressure. The compressed air can then pass by a turbine and produce energy. Lastly, the overtopping devices also run a turbine by letting water pass through it. The overtopping device lets the waves overtop where the water is trapped on top of the device. The water is forced down by gravity and runs a turbine. Several full-scale tests have been conducted on the different concepts of WEC but they are still in the research and development phase. A sketch of the WECs is shown in Figure 1.2. [Pecher and Kofoed, 2017]

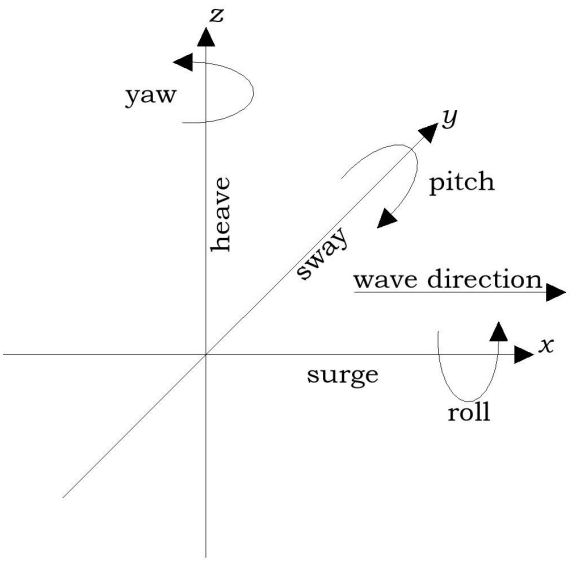

Figure 1.1. Illustration showing the six DoF of a body.

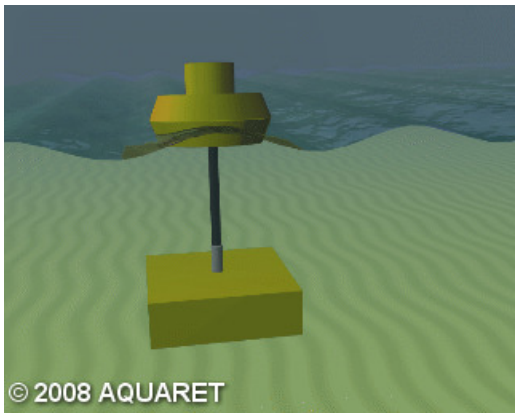

(a) Point absorber

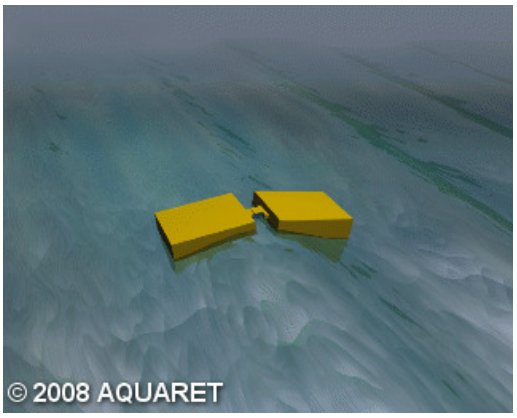

(b) Surface attenuator

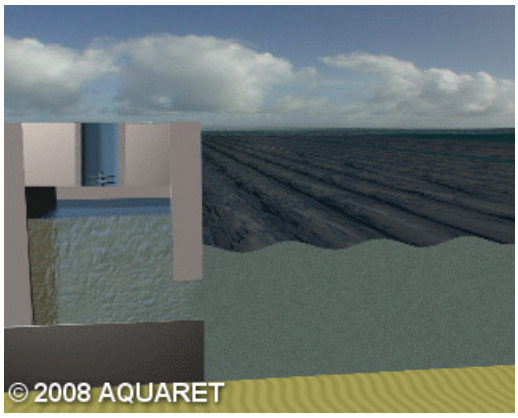

(c) Osciliating water column

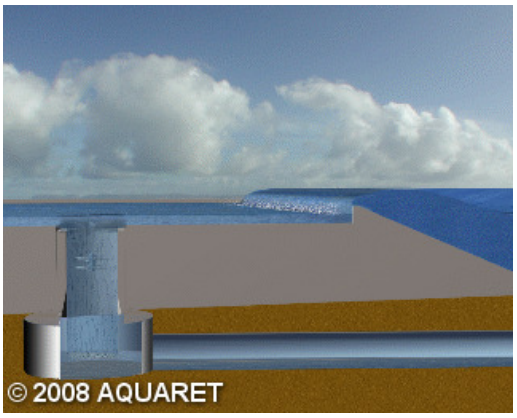

(d) Overtopping

Figure 1.2. Common wave design for a WEC. [Aqua-RET, 2008]

This thesis investigates the Exowave WEC which is a new suggestion for a WEC. The Exowave WEC is a fixed oscillating wave surge converter. It consists of a structure that is fixed to the seabed, on top of which a bottom-hinged floater is placed. The hydrodynamic subsystem in the Exowave WEC is a floater which is activated by the motions of the waves. The floater moves by rotating around the hinge which engages a PTO system. The principle is illustrated in Figure 1.3. The hinge is able to swivel so that the rotation of the floater is in the wave direction in order to maximise energy extraction. Therefore, the movement of the floater is effectively restricted to one DoF which is the pitch motion around the hinge. Additionally, having a structure that is fixed to the seabed ensures that most of the wave energy goes into the movement of the floater. [Exowave, 2024]

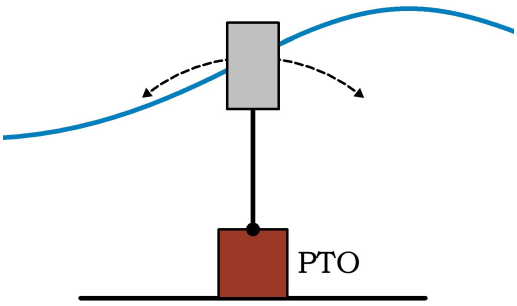

Figure 1.3. Sketch of the Exowave WEC activated in rotation by waves.

One of the problems with wave energy utilisation lies in creating a technology capable of extracting energy from waves while withstanding extreme wave forces. The wave energy that a body absorbs depends on the forces on the body and the motions of the body. Therefore, it is of great interest to be able to predict the forces and the movement of the body in order to optimise the PTO subsystem. In order to predict the forces and motions of the floater, it is necessary to develop numerical models that are able to describe the wave-structure interaction with sufficient accuracy.

The aim of this thesis is to investigate the accuracy of different approaches for modelling the wave-structure interaction of the floater of the Exowave WEC.

The geometry of the Exowave floater will affect both the forces and the motions of the floater. To examine the influence of the floater geometry, four different geometries are investigated. These floaters are shown in Figure 1.4 and are named according to the figure.

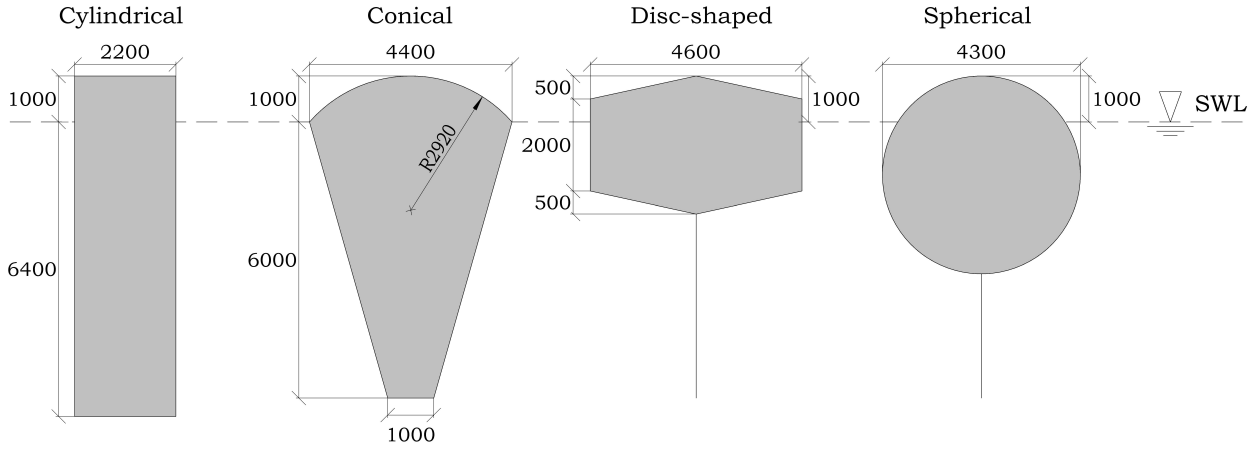

Figure 1.4. Floaters with intended still water level (SWL). All measurements are in mm.

There are plans for an open sea experiment of the Exowave WEC at the Danish Wave Energy Centre (DanWEC) test site off the coast of Hanstholm, Denmark. The DanWEC is founded to establish a research and science environment in order to conduct full-scale tests of offshore structures in harsh sea conditions. The Exowave WEC will be placed at a depth of 14.0 m at the DanWEC test site. The placement of the DanWEC test site is shown in Figure 1.5 along with a wave buoy deployed at 14.5 m water depth. The wave buoy has made wave measurements at its position. [DanWEC, 2022]

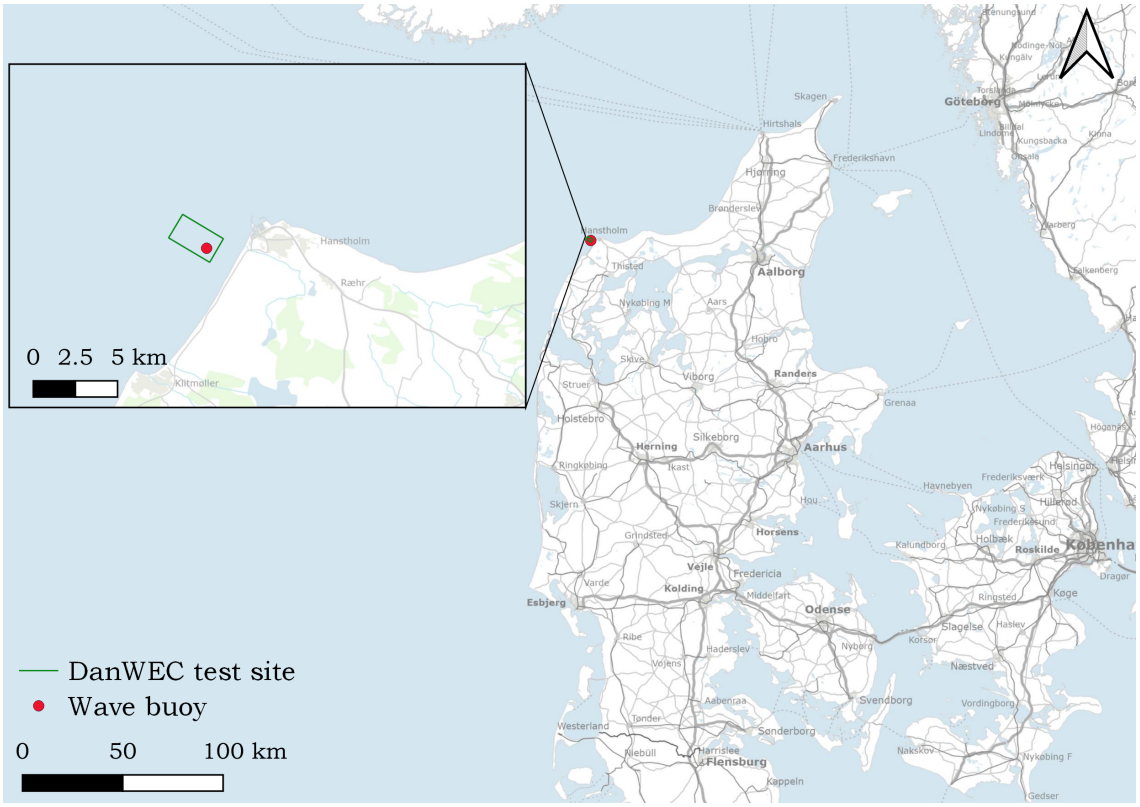

Figure 1.5. The location of the DanWEC test site off the coast of Hanstholm.

1.1 Report structure

In this section, the structure of the report is explained. In order to investigate the wave-structure interaction of the Exowave WEC the report is divided into the determination of wave forces on fixed floaters and motions of the floaters. Initially, different modelling approaches are examined for the cylindrical floater since this geometry is common in offshore structures and is therefore well described in the existing literature. The report structure is illustrated in Figure 1.6. In the report structure it is shown which of the floater models are used in the different chapters.

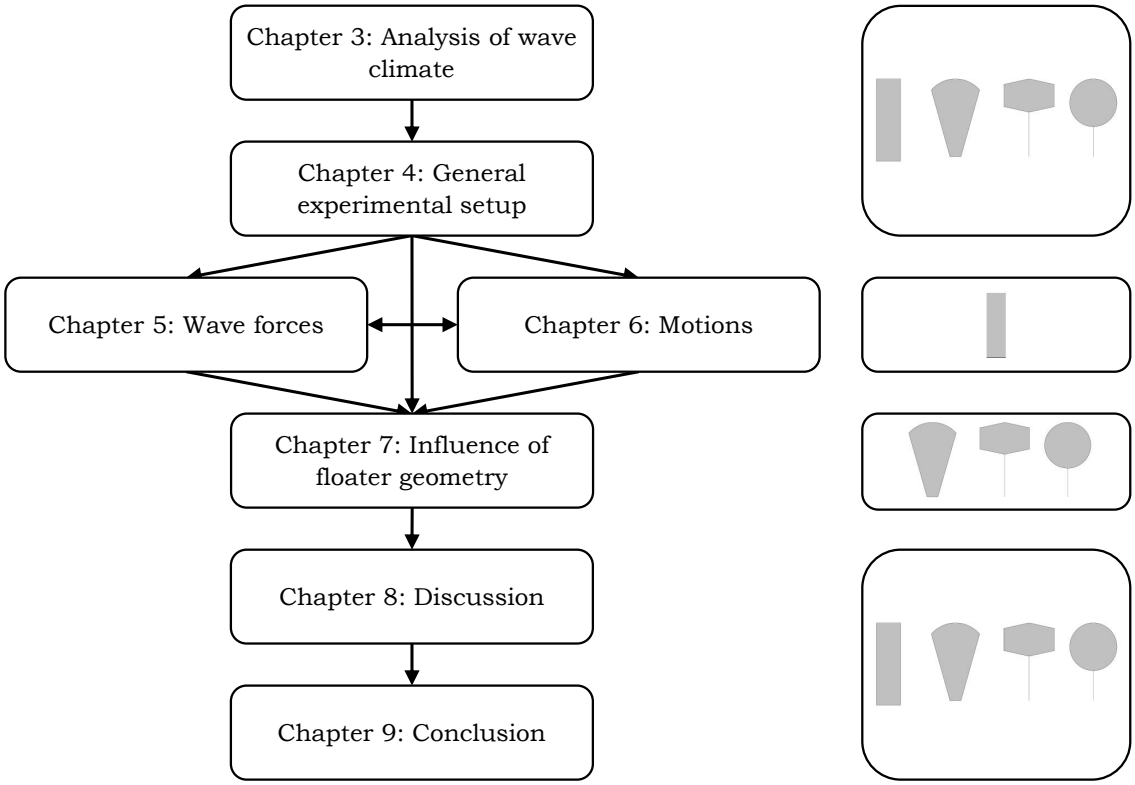

Figure 1.6. Report structure.

As can be seen, all four floaters are included until Chapter 5, which is then focused only on the cylindrical floater. In Chapter 7 the other three floaters are examined.

The present thesis is delimited to examinations of the wave-structure interaction in regular waves. Furthermore, the energy production of the Exowave WEC is disregarded in this thesis. This limitation implies that the PTO subsystem and control subsystem are not examined. The settings of the control subsystem can affect the motion of the floaters. The limitation is assumed to be acceptable because the setting of the control subsystem is an extension of the investigated problem.

The sea states are based on data from a wave buoy at DanWEC test site. In this thesis, the examined water depth is assumed to be constant at all times even though it will in reality change due to tides.

State-of-the-art 2

In this chapter, an introduction to different approaches used for modelling wave-structure interaction is given in order to grant an overview of the prevalent numerical modelling approaches and the recent stage of development within this research area.

Definitions and symbols used to describe waves are shown in Figure 2.1 along with a coordinate system. The origin of the coordinate system is set to zero at the still water level (SWL).

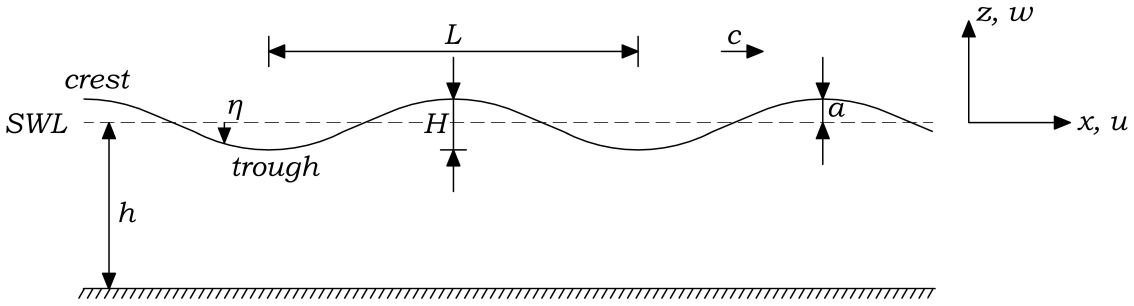

Figure 2.1. Definitions of relevant wave symbols.

Where:

η	Water surface elevation from SWL [m]
H	Wave height [m]
a	Wave amplitude [m]
L	Wave length [m]
h	Water depth [m]
c	Phase velocity of wave [m/s]
u	Fluid particle velocity in x-direction [m/s]
w	Fluid particle velocity in z-direction [m/s]

When numerical models are used to describe the complex reality of wave-structure interaction they inevitably do so by introducing simplifications and assumptions which impact the results. One of the first places where assumptions and simplifications are introduced is in the description of wave kinematics.

2.1 Wave kinematics

To determine the water surface elevation and the particle velocities, boundary conditions are applied. The boundary conditions imply no flow through the seabed and that the waves are periodic. Furthermore, there is a kinematic and a dynamic boundary condition at the free surface. The kinematic boundary condition, which is shown in Equation (2.1), states that a particle at the surface will remain at the surface.

$$\frac{\partial \varphi}{\partial z} = \frac{\partial \eta}{\partial t} + \frac{\partial \varphi}{\partial x} \cdot \frac{\partial \eta}{\partial x} \tag{2.1}$$

Where:

φ	Velocity potential [m^2/s]
t	Time [s]

The dynamic boundary condition states that the pressure at the free surface is equal to the atmospheric pressure, under the assumption that the influence from wind pressure is disregarded. The dynamic boundary condition can be seen in Equation (2.2).

$$g \cdot \eta + \frac{1}{2} \cdot \left(\left(\frac{\partial \varphi}{\partial x} \right)^2 + \left(\frac{\partial \varphi}{\partial z} \right)^2 \right) + \frac{\partial \varphi}{\partial t} = 0 \quad \text{at} \quad z = \eta \tag{2.2}$$

Both of the boundary conditions at the free surface are non-linear which makes it impossible to find an analytical solution for the water surface elevation and the particle velocities. Therefore, the problem needs to be simplified before the wave kinematics can be described. The degree of simplification depends on the used wave theory. [Andersen et al., 2014]

In the linear wave theory the assumptions of a deep water wave ($H/h << 1$) and small wave steepness ($H/L << 1$) make it possible to linearise the free surface boundary conditions. After the linearisation, it is possible to solve the mathematical problem and achieve solutions for the water surface elevation and the wave kinematics. However, the linearisation means that the linear wave theory can only accurately describe waves with a linear behaviour which follows a cosine wave. Measurements have shown that real waves have a short and steeper crest and a longer and less steep trough compared to the cosine wave from linear wave theory. [Brorsen, 2007]

To achieve a better description of real waves it is necessary to avoid the gross assumptions made in linear wave theory. One possible way to avoid this is by the use of Stokes' wave theories where the non-linear problem is solved by using a perturbation method [Stokes, 1847]. The Stokes waves have been developed in five different orders where each order discards less of the boundary conditions. This also increases the calculation time as more variables are included in the calculation. The fifth order Stokes wave theory is able to accurately describe waves with large steepness. However, a general problem for the Stokes wave theories is that they struggle to describe waves in shallow water. [Brorsen, 2007]

Instead, the stream function theory (SFT) can be used to describe waves at all water depths and all wave steepnesses [Dean, 1965]. Stream function theory uses the stream function instead of the velocity potential and is based on an approximate numerical solution to the governing partial differential equations and the boundary conditions are fulfilled at $z = \eta$. [Brorsen, 2007]

The areas of applicability of the different wave theories are illustrated in Le Mehaute's diagram which can be seen in Figure 2.2.

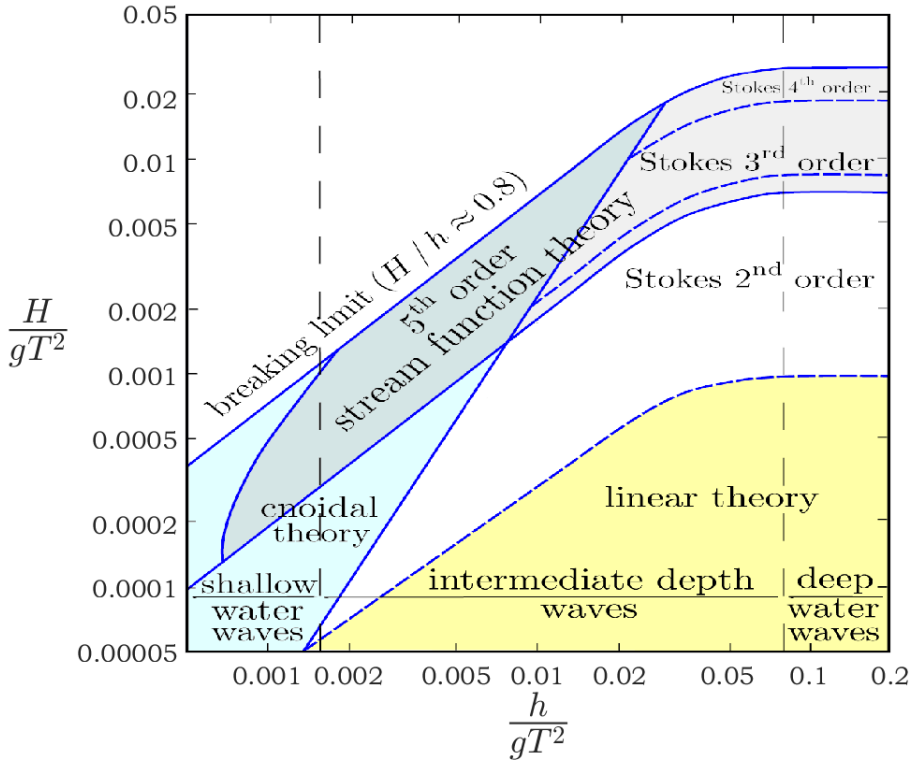

Figure 2.2. Le Mehaute's diagram. [Le Mehaute, 1976]

The choice of wave theory and governing equations plays a big part in the numerical modelling of the wave-structure interaction and is often a compromise between time-efficiency and accuracy. In the following section, different approaches for modelling wave-structure interaction are described.

2.2 Numerical modelling of wave-structure interaction

The description of wave-structure interaction, where a wave interacts with a solid body, is traditionally divided into wave forces on small bodies and large bodies. The size of a body depends on the relative physical size of the body compared to the size of the wave. For a large body, the wave is altered when it interacts with the body which leads to the wave being reflected and diffracted. Reflection is when a wave becomes reflected by the structure. Diffraction is when a wave interferes with a structure and the wave bends around the structure. The two phenomena only occur when the characteristic dimension of the structure is of the same magnitude as the wavelength of the incident wave.

For a small body, it is assumed that the wave-structure interaction does not lead to any significant changes in the form of the wave, meaning that effects from reflection, refraction, and diffraction are negligible. Instead, the wave-structure interaction for small bodies is dominated by two different phenomena which are drag and inertia forces. The drag force is a force in the opposite direction of the wave velocity, which is caused by form drag and skin drag. The inertia force is caused by the acceleration of the wave and its direction is in the wave direction.

The drag force is a viscous force that can be neglected if separation does not occur. It is also necessary to consider whether separation occurs since this also affects the wave forces. The Keulegan-Carpenter number, KC, which is shown in Equation (2.3), can be used to indicate whether separation will occur. [Keulegan and Carpenter, 1958]

$$KC = \frac{u_{max} \cdot T}{D} \tag{2.3}$$

Where:

u_{max}	Maximum particle velocity in x-direction [m/s]
T	Wave period [s]
D	Characteristic dimension [m]

If the KC number is small, it is assumed that separation does not occur and potential theory can be used. For large KC numbers separation does occur and drag forces need to be considered. For a large body effects from flow separation are not as important and drag forces are negligible meaning that it is reasonable to assume that the flow is inviscid and irrotational. Therefore, potential theory can be used.

The numerical modelling of the wave-structure interaction for a WEC ranges from the computationally expensive computational fluid dynamics (CFD) to solutions using linear potential flow (LPF) such as the boundary element method, which has a low computational cost. The development of computational capacity has made it possible to achieve high-fidelity hydrodynamic modelling of WECs. However, despite the increase in computational capacity, these high-fidelity models come with a significant computational cost. Because of this lower fidelity solutions are often used for hydrodynamic modelling in the industry. Listed below are some commonly used approaches for the numerical modelling of wave-structure interaction.

- The Morison equation
- The boundary element method (BEM)
- Computational fluid dynamics (CFD)

These approaches are described in the following sections.

2.2.1 The Morison equation

In the case of a small body where both drag forces and inertia forces may be important, Morison et al. [1950] proposed calculating the total force on the body as the sum of these two forces. The Morison equation for the sectional wave-induced normal force on a fixed structure is shown in Equation (2.4).

$$f_n(z,t) = \underbrace{\overbrace{\rho \cdot A \cdot \frac{d}{dt}u}^{\text{FK}} + \overbrace{C_A \cdot \rho \cdot A \cdot \frac{d}{dt}u}^{\text{added mass}}}_{\text{inertia}} + \underbrace{\frac{1}{2} \cdot C_D \cdot \rho \cdot D \cdot u \cdot |u|}_{\text{drag}} \tag{2.4}$$

Where:

ρ	Density of fluid [kg/m^3]
A	Cross-sectional area [m^2]
D	Diameter or cross-sectional dimension [m]
C_A	Added mass coefficient [-]
C_D	Drag coefficient [-]

The Morison equation is a semi-empirical equation, which is expressed by the empirically determined Morison coefficients, C_A and C_D. The drag term which includes the drag coefficient, C_D, indicates the resistance of an object in a fluid. This is due to the drag force being opposite of the movement in a fluid. The inertia term which includes the added mass coefficient, C_A, is a summation of the Froude-Krylov force and the added mass contribution. The Froude-Krylov force is the force that acts on the body as if the body were transparent to the motion of the wave. The Froude-Krylov force can in some cases have a significant contribution to the total force on a body. The added mass contribution is due to the inertia a solid body has when it is accelerated through a fluid as it has to move its mass and the mass of some of the surrounding fluid.

The total normal force exerted on the floater is calculated by integrating over the height of the floater. The wave kinematics over the height of the floater must be established to determine the wave forces exerted on the floater. The wave kinematics are expressed as the particle velocity and the particle acceleration in the Morison equation.

Besides, the original Morison equation, several other formulations exist. One alternative formulation is for a body moving with the velocity u_b in still water. This formulation is shown in Equation (2.5).

$$f_n(z,t) = -\rho \cdot C_A \cdot A \cdot \frac{d}{dt} u_b - \frac{1}{2} \cdot C_D \cdot D \cdot \rho \cdot \cdot u_b \cdot |u_b| \tag{2.5}$$

By summing Equation (2.4) and (2.5) and introducing a relative velocity $u_{rel} = u - u_b$, it is possible to express the force on a moving structure in waves with a relative velocity formulation which is shown in Equation (2.6).

$$f_n(z,t) = \rho \cdot A \cdot \frac{d}{dt} u + \rho \cdot C_A \cdot A \cdot \frac{d}{dt} u_{rel} + \frac{1}{2} \cdot \rho \cdot C_D \cdot D \cdot u_{rel} \cdot |u_{rel}| \tag{2.6}$$

The Morison equation was originally proposed to calculate forces on cylindrical objects extending from the seabed to above the wave crest. As such the equation does not account for changes in velocity due to water flowing over or underneath the structure as in the case of the Exowave floater.

The Morison coefficients depend on several parameters which means that the Morison coefficients can not be characterised in any simple way. The Morison coefficients are determined as averaged values that depend on the shape and size of the body along with the inclination of the body. Furthermore, the coefficients depend on the Keulegan-Carpenter number, KC, the relative roughness, and the Reynolds number, Re, which is shown in Equation (2.7). [Sarpkaya et al., 1982]

$$Re = \frac{u_{max} \cdot D}{\nu} \tag{2.7}$$

Where:

ν	Kinematic viscosity [m^2/s]

The Morison coefficients are often determined based on literature such as DNV GL [2017]. When it is not possible to look up values for the coefficients in the existing literature, the coefficients can instead be determined from physical tests, where the time series of the surface elevation and the force are measured. It is then possible to determine the Morison coefficients by using e.g. the least squares method where an error, E, between the measured force, $F_{measured}$, and a force calculated with the Morison equation, $F_{Morison}$, is defined as in Equation (2.8).

$$E = F_{measured} - F_{Morison} \tag{2.8}$$

The coefficients are then determined by finding the minimum of E^2 by setting both of its derivatives equal to 0 as shown in Equation (2.9).

$$\frac{dE^2}{dC_A} = 0 \qquad \wedge \qquad \frac{dE^2}{dC_D} = 0 \tag{2.9}$$

In the case of the Exowave WEC, the floater is a truncated object that does not follow the original assumptions used in the Morison equation. Therefore, the floater is also exposed to a tangential force. The tangential force can be calculated by using the dynamic pressure caused by a change in surface elevation. The dynamic pressure is wave-induced and can be calculated using Equation (2.10). [Andersen et al., 2014]

$$p_d(z) = \rho \cdot g \cdot \eta \cdot \frac{\cosh(k \cdot (z + h))}{\cosh(k \cdot h)} \tag{2.10}$$

Where:

p_d	Dynamic pressure [Pa]
k	Wave number [1/m]

Equation (2.10) is only valid under the SWL therefore an approximation is needed when the surface elevation is positive. The approximation is instead to use the hydrostatic pressure distribution above the SWL as shown in Equation (2.11).

$$p_{total}(z) = \rho \cdot g \cdot (\eta - z) \tag{2.11}$$

Where:

p_{total}	Total hydrostatic pressure [Pa]

The tangential force is calculated using the dynamic pressure and the affected area of the floater.

Despite its shortcomings, the Morison equation is widely used since it can accurately predict the extreme wave force when calibrated coefficients are used. However, when designing a WEC it is necessary to predict not only the size of wave forces but also their variation with time. The Morison equation has the ability to implement a suitable wave kinematic to describe the waves, which can be advantageous. The Morison equation allows solving problems in a time domain which makes the equation straightforward and a popular approach.

2.2.2 The boundary element method

In the case of a large body that reflects and diffracts the incident wave, the Morison equation is no longer considered to be a viable option for estimating wave forces and therefore a different approach is needed.

A common approach for computing wave forces on larger structures is by the use of the boundary element method (BEM). The BEM is based on potential theory and estimates the correct wave-structure interaction. However, the BEM assumes linear wave theory and therefore simplified wave kinematics are used in some cases. Another assumption in the BEM is that the motions of the body are small and that the geometry of the body below the SWL does not change. In reality, the Exowave WEC will rotate around the hinge resulting in large motions and therefore violate this assumption. In the BEM, it is assumed that the fluid is incompressible and that the flow is inviscid and irrotational. Therefore, the velocity potential, Φ, needs to satisfy Laplace's equation, which is shown in Equation (2.12). [Faltinsen, 1990; Lee and Newman, 2005]

$$\nabla^2 \Phi = 0 \tag{2.12}$$

It is assumed that linear wave theory applies and that body motions are small. These assumptions make it possible to linearise the boundary conditions. The velocity potential can then be expressed as shown in Equation (2.13).

$$\Phi(\mathbf{x}, t) = \mathrm{Re}\{\phi(\mathbf{x}) e^{\mathrm{i}\omega t}\} \tag{2.13}$$

Where:

$\mathbf{x}$	Position vector $\mathbf{x} = (x, y, z)$ [m]
ω	Wave frequency [rad/s]

Because of the linearisation, the velocity potential can be expressed as the sum of the diffracted potential, ϕ_d, and the radiated potential, ϕ_r. The diffracted potential is the sum of the incident potential, ϕ_i, and the scattered potential, ϕ_s. This is shown in Equation (2.14).

$$\phi = \phi_d + \phi_r = \phi_i + \phi_s + \phi_r \tag{2.14}$$

When using the BEM to described the flow around a body, Laplace's equation and three boundary conditions are fulfilled. The first boundary condition is at the free surface, this is shown in Equation (2.15).

$$\frac{\partial \phi(\mathbf{x})}{\partial z} - \frac{\omega^2}{g}\phi(\mathbf{x}) = 0 \quad \text{for } z = 0 \tag{2.15}$$

The second boundary condition is at the seabed, this is shown in Equation (2.16).

$$\frac{\partial \phi(\mathbf{x})}{\partial z} = 0 \quad \text{for } z = -h \tag{2.16}$$

The third boundary condition is on the surface of the body, this is shown in Equation (2.17).

$$\frac{\partial \phi(\mathbf{x})}{\partial n} = V_n \quad \text{on the surface of the body} \tag{2.17}$$

Where V_n is the normal velocity for a point on the surface on the body and n is the normal vector. When using the BEM the three-dimensional flow problem around the body is transformed into a two-dimensional problem by approximating the body's geometry by several panels which makes it possible to solve the set of equations.

The assumptions used in the BEM make it a time-efficient method, but the gross assumptions used in linear wave theory make it necessary to validate the use of BEM in the modelling of WECs.

2.2.3 Computational fluid dynamics

Computational fluid dynamics involves finding approximate solutions to models of fluid behaviour such as the Navier-Stokes equations and the continuity equation, shown in Equation (2.18) and (2.19) respectively. The equations are shown for incompressible flow.

$$\rho\left(\frac{\partial V}{\partial t} + (V \cdot \nabla)V\right) = -\nabla p + \rho g + \mu \nabla^2 V \tag{2.18}$$

$$\nabla \cdot V = 0 \tag{2.19}$$

Where $V = [u\ v\ w]^{\mathrm{T}}$ and μ is the dynamic viscosity.

Solutions are found by replacing the partial differential equations with a set of approximate algebraic equations that are then solved numerically.

The algebraic equations are obtained from a discretisation of the Navier-Stokes equations by e.g. mesh-based methods. This makes it possible to describe the continuous flow field with discrete values at specified locations in the mesh. [Gerhart et al., 2016]

CFD is a method with high fidelity due to a limited number of simplifying assumptions in comparison with other methods. However, this also contributes to the significant

computational cost involved in using the method. The time-consuming nature of CFD modelling can render it impractical for industry-use where less computationally expensive solutions are sought, especially in the preliminary investigation. Using CFD for modelling fluid-structure interaction is out of the scope of this thesis.

In this thesis, the main focus is on the Morison equation and the boundary element method because of their time-efficiency and widespread use in the offshore industry. These reasons mean that it is of interest to examine whether reliable descriptions of the wave-structure interaction can be achieved with these approaches. The reduction of computational cost in these approaches is in large part caused by the introduction of assumptions and discretisation, however, this also has unknown effects on the results. Therefore, it is necessary to examine these effects by performing physical tests to gain a greater understanding of the validity of the assumptions used in these approaches.

2.3 Motions of the body

The floater model moves as a 1-DoF system, which is able to move in rotation around the hinge when activated by waves. The motions of the floater are calculated using the equation of motion, as shown in Equation (2.20).

$$I \cdot \ddot{\theta}(t) = M_{ex}(\theta) + M_{rad}(\dot{\theta}, \ddot{\theta}) + M_{hs}(\theta) \tag{2.20}$$

Where:

I	Mass moment of inertia [kg $\cdot$ m^2]
θ, $\dot{\theta}$, $\ddot{\theta}$	Angular position, velocity and acceleration of floater model [rad, rad/s, rad/s^2]
M_{ex}	Wave excitation moment [Nm]
M_{rad}	Radiation moment [Nm]
M_{hs}	Hydrostatic moment [Nm]

The restoring hydrostatic moment consists of a moment from buoyancy, M_b, and an opposing moment from gravity, M_g, as shown in Equation (2.21).

$$M_{hs} = M_b - M_g = \rho \cdot g \cdot V \cdot \sin(\theta) \cdot r_b(\theta) - m \cdot g \cdot \sin(\theta) \cdot r_g \tag{2.21}$$

Where:

r_b	Distance from hinge to centre of buoyancy [m]
m	Mass of floater model [kg]
r_g	Distance from hinge to centre of gravity [m]

It should be noted that the distance from the hinge to the centre of buoyancy, r_b, depends on the angular position of the floater since the centre of buoyancy changes as the floater becomes more submerged.

The radiation moment is calculated as shown in Equation (2.22).

$$M_{rad} = -m_h \cdot \ddot{\theta}(t) - c_h \cdot \dot{\theta}(t) \tag{2.22}$$

Where:

m_h	Hydrodynamic added mass moment of inertia [$\mathrm{kg} \cdot \mathrm{m}^2$]
c_h	Hydrodynamic damping coefficient [Nm/(rad/s)]

Based on the hydrodynamic modelling approaches described in this chapter it can be concluded that there is no single way to describe the wave-structure interaction of a WEC. Therefore, it is of interest to examine the validity of different approaches both for the determination of forces on the floaters and the motions of floaters. However, before this can be examined it is necessary to investigate the wave climate to which the Exowave WEC will be subjected.

Analysis of wave climate 3

In this chapter, the wave climate at the DanWEC test site is analysed and the wave force regimes are investigated with respect to the Exowave floaters.

3.1 MetOcean study

A MetOcean study is conducted to estimate the waves impacting the floater models. The MetOcean study is conducted with data from a bouy at the DanWEC test site. The buoy has measured the significant wave height, $H_{m0-buoy}$, for approximately 4.5 years from late 2016 to late 2022 with some downtime. The missing data in the downtime is excluded. The sea condition at the wave buoy is estimated to be comparable to the condition at the Exowave WEC because the water depths are nearly identical and the placements are close. The MetOcean study determines five representative sea states, with the focus on having a good representation of the probability of occurrence, P. The MetOcean study and the selection of the five sea states are described in Appendix A on page 91. The sea states are identified by a significant wave height, H_{m0}, and a peak period, T_p. The water depth, h, is 14.0 m at the Exowave WEC. In order to indicate which of the sea states have the largest contribution to possible energy production of the WEC, the wave energy contribution is determined.

The wave power, P_{wave}, for each sea state, is determined and multiplied by the possibility of occurrence, P, to provide the wave energy contribution. The sea state parameters are shown in Table 3.1. As shown in the table, the wave energy contribution is most considerable for sea state 4.

Sea state	H_{m0} [m]	T_p [s]	L [m]	*Contrib* [%]	P [%]	P_{wave} [kW/m]	$P \cdot P_{wave}$ [kW/m]
1	0.63	4.1	26.6	3.4	31.1	4.3	1.3
2	1.08	5.7	48.6	8.8	20.3	10.8	2.2
3	1.28	4.7	34.4	5.8	11.4	18.3	2.1
4	1.94	6.1	54.2	32.6	21.3	92.1	19.6
5	2.91	7.1	68.8	22.6	5.7	112.9	6.5
			Sum	73.2	89.8	-	31.6

Table 3.1. Sea state parameters determined by the MetOcean study at DanWEC test site.

The sea states are used to describe regular waves. The waves for each of the sea states can be classified as shallow water waves, intermediate depth waves, or deep water waves. The classification is determined as a ratio between the water depth, h, and the wavelength, L. The wavelength is determined by the dispersion relationship. The particle movement depends on the classification of the sea states. This is because the movement of the particle changes from being circular for a deep water wave to being elliptical for a shallow water wave. The sea states are classified using the relations shown in Equation (3.1).

$$\begin{aligned} &\frac{h}{L} < \frac{1}{20}, && \text{Shallow water wave} \\ &\frac{1}{20} \leq \frac{h}{L} \leq \frac{1}{2}, && \text{Intermediate water wave} \\ &\frac{h}{L} > \frac{1}{2}, && \text{Deep water wave} \end{aligned} \tag{3.1}$$

The classification of the sea states is shown in Table 3.2.

Sea state [-]	$\frac{h}{L}$ $[\frac{m}{m}]$	Classification
1	0.54	Deep
2	0.30	Intermediate
3	0.42	Intermediate
4	0.27	Intermediate
5	0.21	Intermediate

Table 3.2. Classification of sea states.

The sea states are classified as deep to intermediate depth waves. This means, that the particle movement is circular for sea state 1 and in between circular and elliptical for the other sea states.

3.1.1 Le Mehaute's diagram

In order to determine which wave theory is suitable for determining the wave kinematics of the sea states, Le Mehaute's diagram is implemented. Le Mehaute's diagram can be applied to the problem because the waves are regular. Le Mehaute's diagram also indicates if a wave is at risk of breaking due to the steepness of the wave becoming too high. The Le Mehaute's diagram is shown in Figure 3.1 including the sea states.

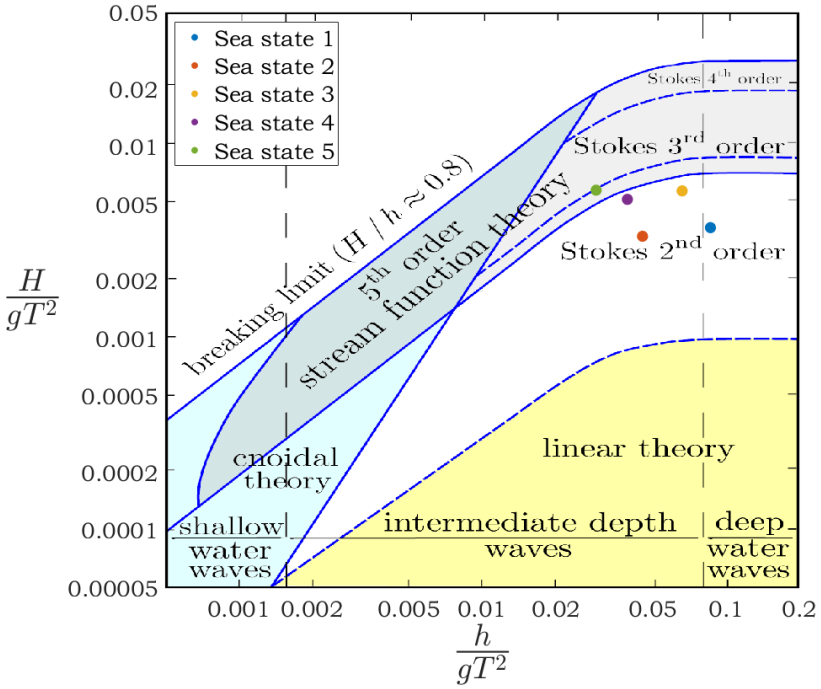

Figure 3.1. Le Mehaute's diagram. [Le Mehaute, 1976]

As can be seen in the Figure, Le Mehaute's diagram indicates that the sea states can be described with Stokes' second to third order theory and the sea states are intermediate to deep water waves. It can also be seen that linear wave theory can not fully describe the waves of the sea states.

3.1.2 Chakrabarti diagram

The relation between the sea states and the size of the body is also important since this can be used to indicate the nature of the forces on the body. To determine whether a body should be considered small or large in comparison to the waves, Chakrabarti's diagram of wave force regimes can be used. On the x-axis of the diagram is the diffraction parameter $\pi \cdot D/L$ and on the y-axis is H/D. In Figure 3.2 the results for Chakrabarti's wave force regimes are shown. [Chakrabarti, 2005]

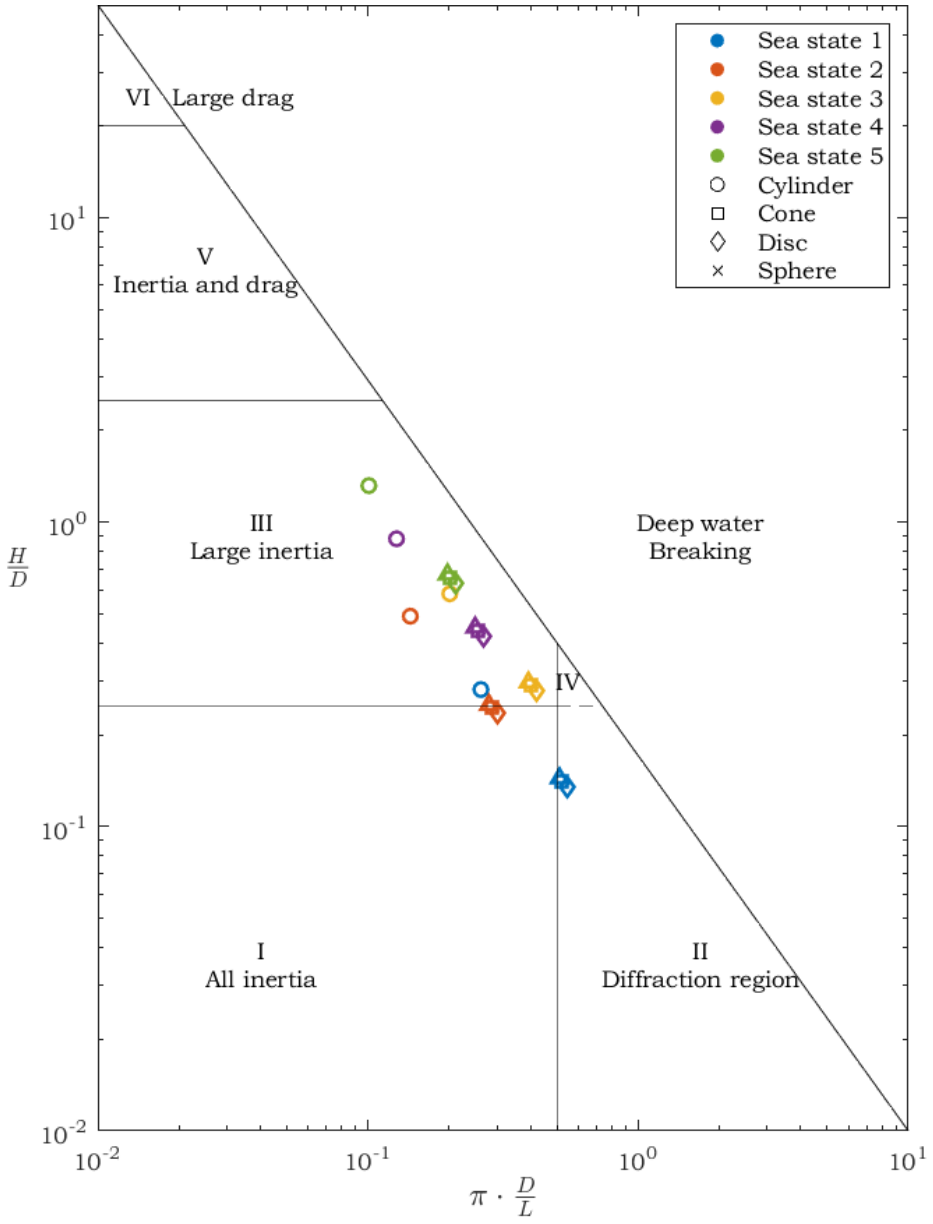

Figure 3.2. Diagram of wave force regimes with results for the floaters. [Chakrabarti, 2005]

As can be seen in the figure the results for the conical, disc-shaped, and spherical floaters are almost identical because of the similar characteristic dimensions. The wave forces on all of the floaters are expected to be inertia-dominated for most of the sea states. Furthermore, the diffraction parameter $\pi D/L < 0.5$, indicates that diffraction is small and that the floaters can be considered small in most cases. When a floater can be considered small it means that the structure will have a small influence on the wave field which fulfils the assumptions of the Morison equation. It can also be seen that the disc-shaped, conical, and spherical floaters are in the diffraction region for sea state 1. In the other sea states these floaters are not far from the diffraction region. This indicates that the BEM can also be used to investigate the wave-structure interaction.

To describe the influence of viscous forces the Keulegan-Carpenter number, KC, can be used. KC is shown for the sea states in Table 3.3. In the calculation of KC the maximum particle velocity is determined by stream function theory and the characteristic diameter is set to the maximum diameter of the floaters.

	KC [-]			
Sea state	Cylinder	Cone	Disc	Sphere
1	0.99	0.47	0.45	0.48
2	1.88	0.86	0.83	0.88
3	2.19	1.03	0.98	1.05
4	3.64	1.69	1.62	1.73
5	6.61	3.11	2.98	3.19

Table 3.3. KC for the floaters.

According, to Stansby [1992] separation of the flow occurs when $KC > 5$ for a circular cylinder in elliptical orbit flow. This means that drag force can influence the model when $KC > 5$. When $KC < 5$ separation does not occur and the drag force is negligible. A small $KC < 5$ also indicates that potential theory could be applied to the problem, due to the flow being inviscid and irrotational.

Based on the classification of the waves at the DanWEC test site, a suitable method to determine the forces can be selected. The Le Mehaute diagram indicates that the wave kinematics of the sea states will not be precisely determined by linear wave theory which a BEM uses. The wave forces regimes based on Chakrabarti specify that the forces are inertia dominated for the sea states which indicates that the Morison equation will be suitable. The KC number for the cylindrical floater indicates that there is a larger influence from drag forces in sea state 5, which supports the use of the Morison equation. The KC also indicates that BEM can be applied for the other sea states. Based on the Chakrabarti diagram and KC it is determined that both the Morison equation and the BEM can be applied to estimate the wave forces on the floaters.

In the following section, the use of the BEM and the Morison equation for the Exowave WEC will be evaluated.

3.2 Discussion

As described previously both the Morison equation and the BEM can be applied to calculate wave forces on the floaters. Even though two possible methods of estimating the wave forces on the floaters have been identified there are still uncertainties regarding both methods. As shown in the Le Mehaute diagram the waves from the sea states can not be described using linear wave theory. This makes it necessary to validate the use of the BEM for the calculation of the floater's wave-structure interaction.

The Morison equation can be applied when the floaters are considered to be small. DNV GL [2017] suggests using the Morison equation when the structure can be defined as a small body. If the relation shown in Equation (3.2) is fulfilled the body can be considered small.

$$L > 5 \cdot D \tag{3.2}$$

This is fulfilled for all the floaters. However, there are also uncertainties concerning the use of the Morison equation.

According to DNV GL [2017] the Morison equation can be applied to two-dimensional problems, which is an approximation of the true problem. It is assumed to be an acceptable approximation due to the placement of the WEC being close to the coast where the waves behave more in two dimensions than they do far from the coast due to refraction.

As stated the Morison equation uses the Morison coefficients which can be found in the literature. The values of the coefficients in the fixed upright position for cylinders are well established by tests performed on similar geometries. The cylindrical floater deviates from the literature due to the floater being truncated. The coefficients to the cylindrical floater in the existing literature are determined for a cylinder extending from the seabed to above the wave crests. Therefore, the possibility for the water to flow above or beneath the cylindrical floater is not taken into account. As the waves for the higher sea states go over the top of the floater, there is a possibility that the Morison coefficients change as the fluid behaves differently over the top of the cylindrical floater, than it does around the sides of the cylindrical floater.

The Morison coefficients regarding the spherical floater are established for it in a fully submerged state. The spherical floater is in this case not fully submerged and will deviate from the literature. However, the Morison coefficients for the conical and the disc-shaped floaters are not described in literature.

Furthermore, the Morison coefficients from the literature in DNV GL [2017] are normally used to estimate a design load scenario. This means that the estimated coefficients are conservative which is not desirable if the motion of a WEC is examined. [Sarpkaya, 2010]

The Morison equation normally determines the force in a fixed upright position however, as the floaters rotate around the hinge their angular position will change. Therefore, the geometry of the floaters, relative to the propagating wave, changes due to the tilting of the floaters. Because of this, it is expected that the Morison coefficients change for the floaters as the tilting occurs. Furthermore, the cross-sectional area and the volume which

are included in the Morison equation change as the angular position changes. An example of a floater in a tilted position is shown in Figure 3.3, which also shows the placement of the hinge and the wave direction.

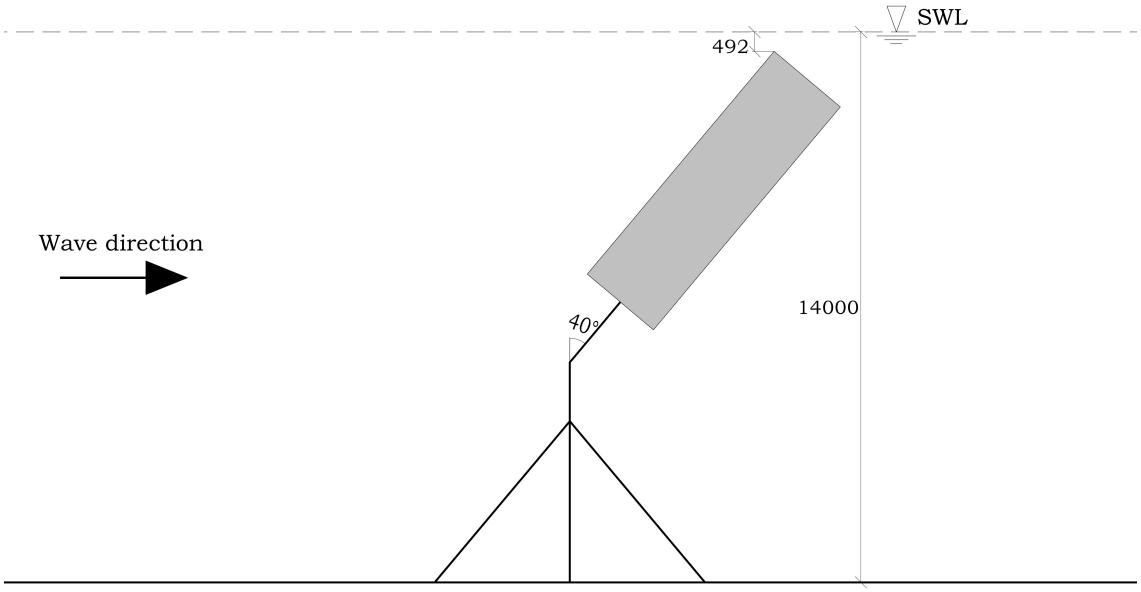

Figure 3.3. The cylindrical floater tilted at a 40°. All measurements are in mm.

To investigate the validity of using the Morison equation and the BEM on the floaters, an experiment is utilised. The aim of the experiment is to examine whether the BEM can be used to accurately describe the wave-structure interaction of the floater even though the waves can not be described by linear wave theory. Furthermore, it is examined whether the Morison equation can be used to describe the wave-structure interaction of varying floater geometries.

General experimental setup 4

In this chapter, the general experimental setup which is used throughout the different experiments is described. The experiments are performed on scaled floater models. The experimental setup in this chapter is used for the experiments where forces on fixed floaters are measured. The fixed floaters are placed in different angular positions. In Table 4.1 the angles in which the floaters are examined are shown.

	Angle [°]								
Floater model	-40	-30	-20	-10	0	10	20	30	40
Cylindrical	X		X	X	X	X	X		X
Disc-shaped	X	X	X		X		X	X	X
Conical		X	X		X		X	X	
Spherical					X				

Table 4.1. Angles and floater models that the force experiment was performed at.

Furthermore, the experimental setup is used in experiments where the motions of the floaters are examined in both decay and wave excitation tests.

4.1 Experimental setup

The wave flume in the Department of the Built Environment at Aalborg University is utilised for the experiments. The wave flume is used to investigate two-dimensional problems. As stated in Chapter 1 on page 1, the movements of the Exowave WEC can be described as a 1-DoF system, which means that the wave flume is a fitting tank to use for the experiments. The wave flume is 1.5 m wide and 22.5 m long, including an inlet, a wave generator, and passive absorption. The bathymetry of the wave flume is flat. The dimensions of the wave flume can be seen in Figure 4.1, where the first illustration is of the wave flume seen from above and the second is from the side at the cross-section A-A.

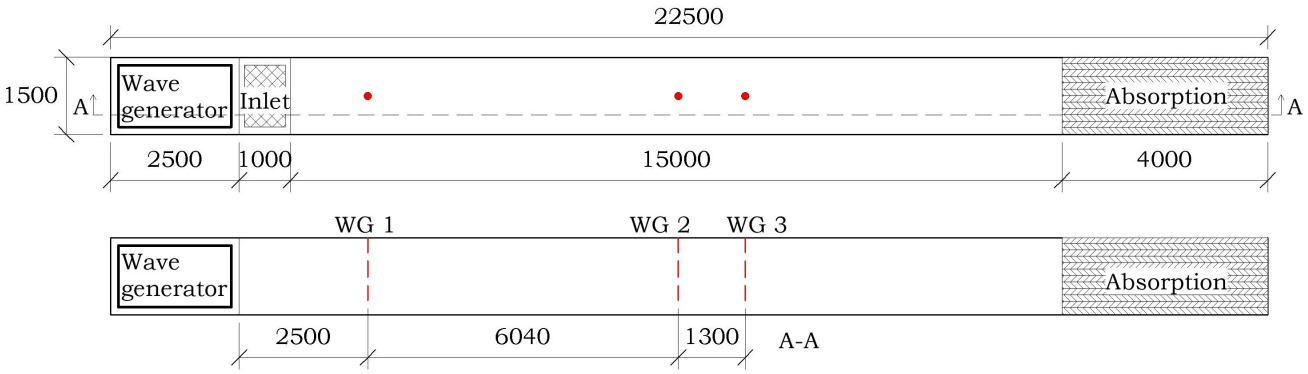

Figure 4.1. Wave flume including the wave gauges (WG). All measurements are in mm.

As can be seen, the wave flume contains three wave gauges (WG), which are used to measure the surface elevation at selected points in the wave flume. A WG measures the electrical resistance between two parallel rods when they are submerged in the water. The WGs are calibrated by measuring the resistance at two points with a change of 100 mm in the surface elevation. A linear calibration function is then fitted to determine the surface elevation. WG 1 is placed just in front of the wave generator and WG 2 is used to investigate possible interference from reflection as the waves propagate along the wave flume. WG 3 is located at the intended placement of the floater models. The purpose of WG 3 is to measure the surface elevation at the position of the model. The placement of WG 3 is then the point of interest in the wave flume. WG 2 and WG 3 in the wave flume can be seen in Figure 4.2.

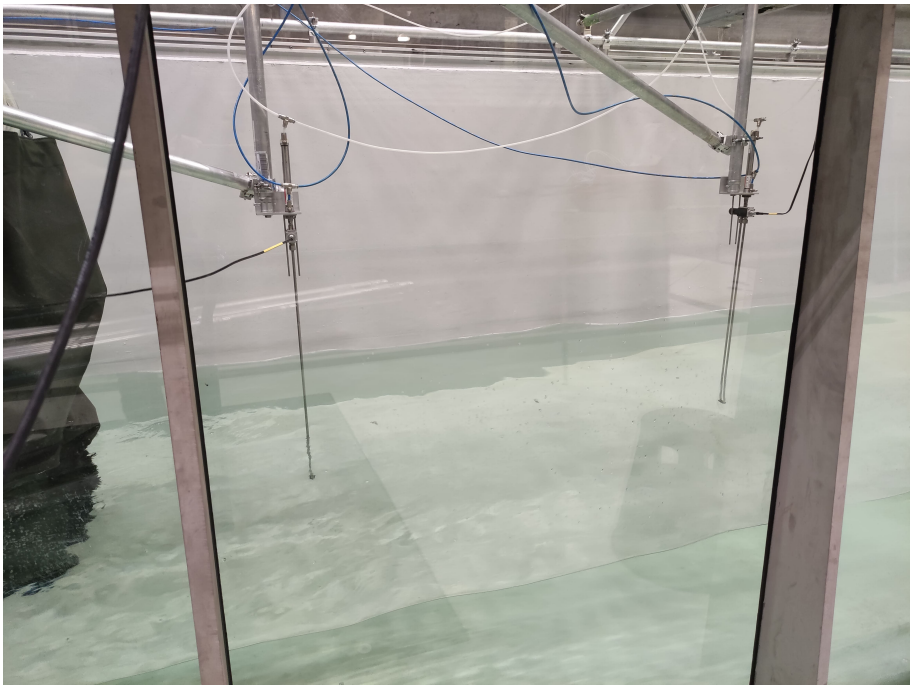

Figure 4.2. WG 2 and WG 3 in the wave flume.

4.1.1 Wave generator

A VTI piston wave generator generates the sea states in the wave flume. The wave generator moves a vertical paddle in the x-direction. The wave generator generates the waves by the program AwaSys version 7.0, which determines the movement of the paddle in order to match the predefined wave height, H, and the wave period, T. The software used in Awasys is based on Zhang and Schaffer [2005]. The waves are created to match a predefined wave theory, which in this case is selected to be tenth order stream function theory. Apart from settings of linear waves and active absorption are also set in the AwaSys software.

4.1.2 Wave absorption

A wave will reflect on a smooth surface normal to the wave direction. A reflected wave will interact with an incident wave and will disturb it. The wave flume is constructed with a passive wave absorption stationed at the end of the wave flume. The purpose of wave

passive absorption is to minimise the reflection in the wave flume. As the wave collides with the passive wave absorption some of the wave energy will dissipate. The part that is not absorbed will be reflected at the end of the wave flume and go through the passive wave absorption again. It is almost inevitable that some wave energy will be reflected into the wave flume and interfere with the incoming waves. Furthermore, the wave generator is adjusted to actively absorb the waves which means that the wave generator adjusts the waves that are being generated according to the incoming waves in the flume. In order to ensure that the influence of the reflected waves is negligible, the waves of interest are narrowed down to the first three fully developed waves. Additionally, the passive wave absorption ensures that the water in the wave flume settles down quickly. This means, that the wait time in between each test is shorter than in a similar flume without the passive wave absorption.

4.2 Scaling

In order to conduct the experiment in the flume, the floater models and the sea states must be down-scaled to match the flume's size. The geometrical scale ratio, λ, for the scaled floater models is 20. The scaled floater models are shown in Figure 4.3. The global coordinate system is shown as an example on the cylindrical floater model.

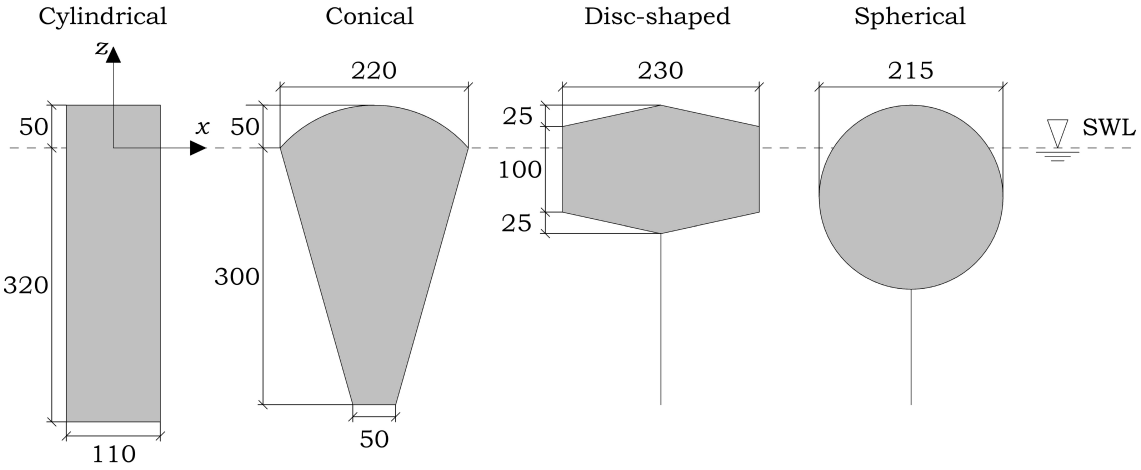

Figure 4.3. Floater models with intended SWL. All measurements are in mm.

The sea states are scaled according to the Froude model law which describes the ratio between the inertial forces and gravitational forces. The scaling depends on the geometrical scale ratio of the model. The scale ratios used to determine the scaled sea states are shown in Table B.1.

Physical parameter	Unit	Scale factor
Wave height and length	[m]	20
Wave period	[s]	$\sqrt{20}$

Table 4.2. Scale factor for the physical parameters. [Hughes, 1993]

The scaled sea states are shown in Table 4.3.

Sea state	H_{m0} [cm]	T_p [s]	h [cm]
1	3.13	0.92	72.0
2	5.38	1.27	72.0
3	6.41	1.05	72.0
4	9.71	1.36	72.0
5	14.54	1.58	72.0

Table 4.3. Sea states scaled accordingly to the scale ratio of 20.

Each sea state is used to describe a regular wave.

4.3 Test plan

In preparation for the experiments on the floater models, the sea states were examined in the wave flume. The sea states were examined for the time it took after a wave series for a sea state was finished until the water in the wave flume was still. A wave series for a sea state was run for 60 seconds and after the wave series, the water in the flume was still after three to four minutes depending on the sea state. The wait time between each wave series was set to five minutes to ensure that the water was still.

The surface elevation at the wave gauges is measured for the sea states and used later to align the waves from the different tests. The program WaveLab versions 3.87 and 3.888 are used for measuring. [Frigaard and Andersen, 2014]

The general experimental setup is used in experiments to measure both the forces and motions of the floater models. In Chapter 5 the forces on a fixed cylindrical floater model are examined. In Chapter 6 on page 49 the motions of the cylindrical floater model are examined. The cylindrical floater model is investigated at first because a cylinder is a common geometry for offshore structures and as such it is well described in existing literature. In Chapter 7 on page 63 the same examinations are performed for the three other floater models.

Wave forces on the fixed cylindrical floater model 5

This chapter will establish two calculation methods that are set up to estimate the wave forces on the fixed cylindrical floater model. The calculation methods used to determine the wave forces are based on the Morison equation and a BEM calculation using NEMOH. In order to validate the calculation methods, an experiment in the wave flume is conducted. The experiment measures the wave forces on the cylindrical floater model which can then be compared to the results from the calculation methods. The cylindrical floater model will be investigated at angles from -40° to 40° which is within the expected interval of rotation for the WEC.

5.1 Experimental investigation of wave forces

The purpose of the experiment is to measure the wave-induced forces that impact the cylindrical floater model when it is mounted in a fixed position. Furthermore, the effect of changing the angular position of the WEC is examined by performing experiments with the cylindrical floater model in a tilted position.

5.1.1 Setup and equipment

The primary experimental setup is described in Chapter 4 on page 23, but a variation to the general experimental setup is required to measure the forces on the cylindrical floater model. The cylindrical floater model is placed at the position of WG 3 as shown in Figure 5.1.

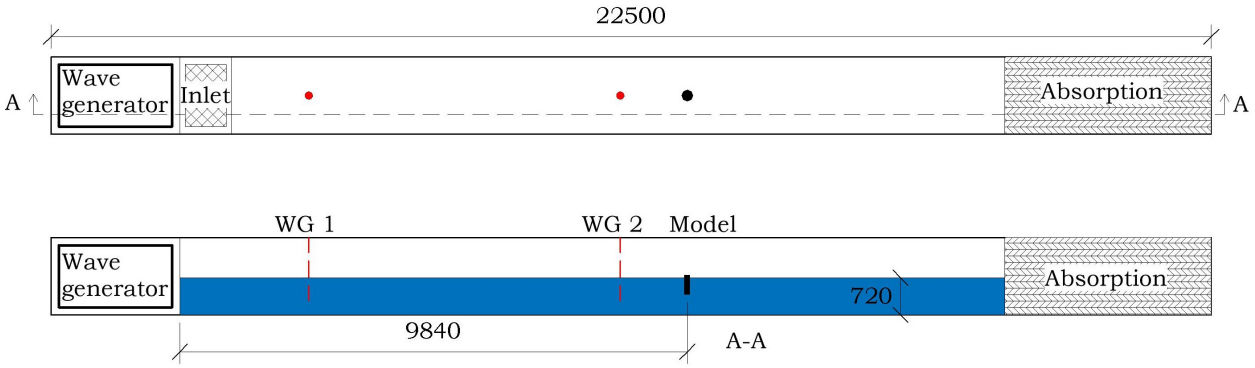

Figure 5.1. Flume including the cylindrical model. All measurements are in mm.

The cylindrical floater model is mounted to a 6-axis force transducer. The 6-axis force transducer is an ATI Industrial Automation Gamma IP68 force transducer which can measure forces and moments in three dimensions. The measurement range is 65 N for F_x, 200 N for F_z and 5 Nm for the moments. The accuracy of the 6-axis force transducer was compared to a bending beam force transducer. In the comparison, it was determined that the 6-axis force transducer gives reliable results for the forces. Furthermore, the use of the

6-axis force transducer results in an experimental setup with a higher stiffness meaning it is less susceptible to the influence of dynamic amplification. This comparison can be seen in Appendix B.4 on page 102.

The setup for mounting the 6-axis force transducer and the cylindrical floater model is shown in Figure 5.2. The cylindrical floater model is connected to the 6-axis force transducer by a joint which makes it possible to angle the model. The 6-axis force transducer is connected by clamps to a stiff construction which is reinforced with inclined struts. The eigenfrequency of the setup is also tested to determine if the model will go into resonance with the waves as resonance will affect the accuracy of the measurements. The test is done by subjecting the end of the cylindrical floater model to an impulse load. It is concluded that the eigenfrequencies are sufficiently high so that the measurements will not be influenced by dynamic amplification. The eigenfrequencies can be seen in Appendix B on page 95.

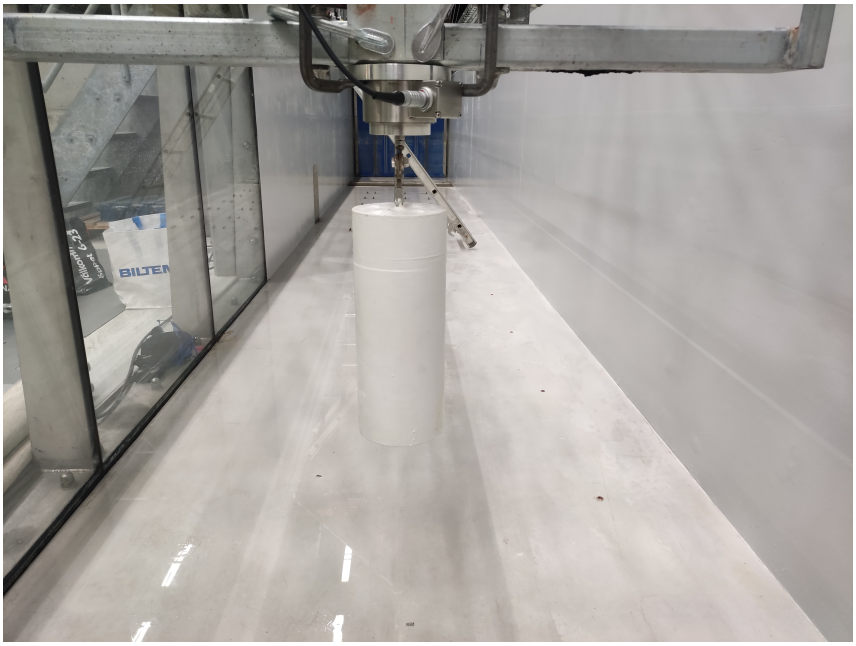

Figure 5.2. Setup for the 6-axis force transducer mounted with the cylindrical floater model.

The signals from the 6-axis force transducer and the wave gauges are obtained by using a data acquisition system. The signal from the wave gauges is passed through a wave gauge sensor before entering the data acquisition. To limit noise from the force measurements both a digital and analogue low-pass filter are used, which removes the higher frequencies of the measured signals. The 6-axis force signal is passed through the analogue 8 Hz low-pass filter before entering the data acquisition system. The setup with the data acquisition system is shown in Figure 5.3.

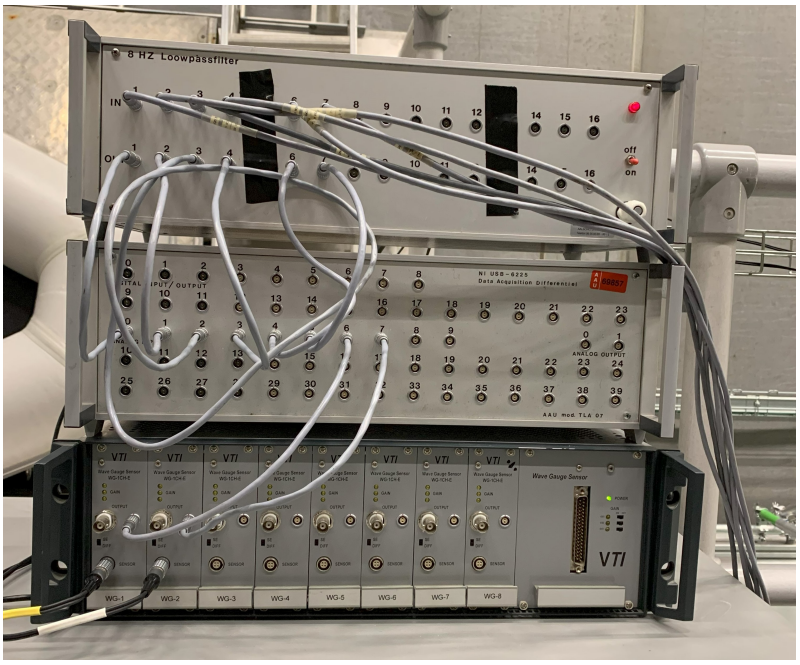

Figure 5.3. Setup with a low-pass filter at the top, data acquisition system in the middle, and the wave gauge sensor at the bottom.

5.1.2 Test plan

As mentioned, the cylindrical floater model is fixed at different angles to evaluate how the forces change with the angle of the model. The cylindrical floater model is investigated in the expected interval of rotation within ±40° to resemble the expected movement. The real rotation is around the hinge near the bottom of the wave flume. However, when the forces are measured the cylindrical floater model is fixed at the top of the model and is also rotated by a joint at the top of the model. The joint and the 6-axis force transducer can be seen in Figure 5.4. The angle of the cylindrical floater model is measured by a digital protractor to ensure it is within 0.1 ° of the desired angle.

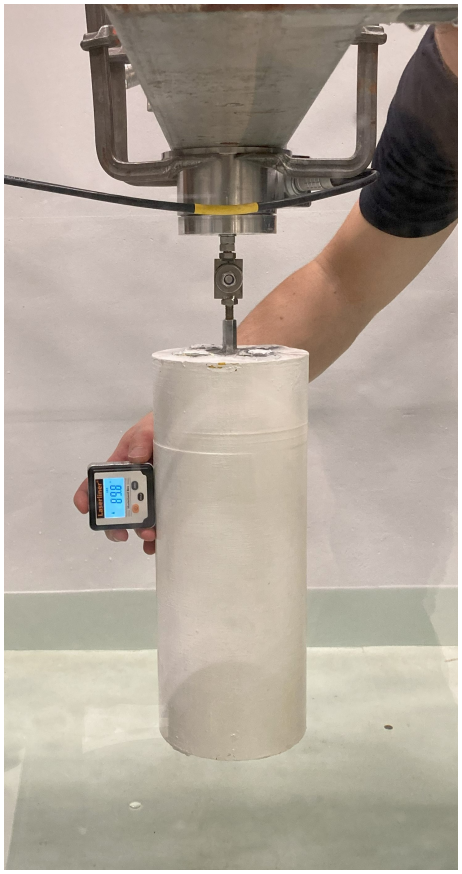

Figure 5.4. The force transducer with the cylindrical floater model at 0°.

As the WEC rotates it will become more submerged. To resemble the cylindrical floater model's position in the z-direction when rotating around the hinge as shown in Figure 5.5a. The height of the 6-axis force transducer is therefore adjusted in the experiment to match the new position of the cylindrical floater model as shown in Figure 5.5b

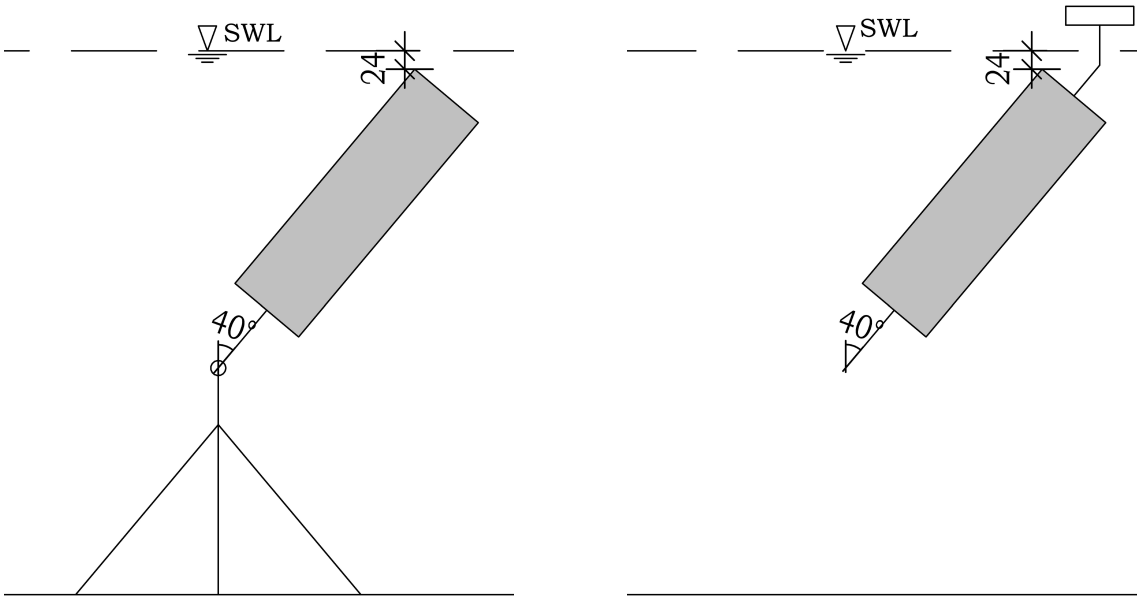

(a) Actual rotation. ***(b)*** Rotation during the experiment.

Figure 5.5. The cylindrical floater model at an angle of 40 °. All measurements are in mm.

The cylindrical floater model is tested in positive and negative angles. A rotation in the wave direction is positive. The cylindrical floater model is tested in the following angles: 0°, ±10°, ±20°, ±40°. For every angle, all five sea states are tested. Each sea state is repeated five times in order to have a representative dataset and exclude any small errors linked with a physical experiment.

5.1.3 Measured results

As stated earlier, the cylindrical floater model is exchanged with the WG 3 in this experiment. The forces on the model and the surface elevation at WG 3 are aligned using cross-correlation between the measurements of the surface elevation at WG 1. The measured forces are narrowed down to the first three fully developed waves to minimise the influence of wave reflection in the wave flume. The first three fully developed waves are shown in the marked area in Figure 5.6.

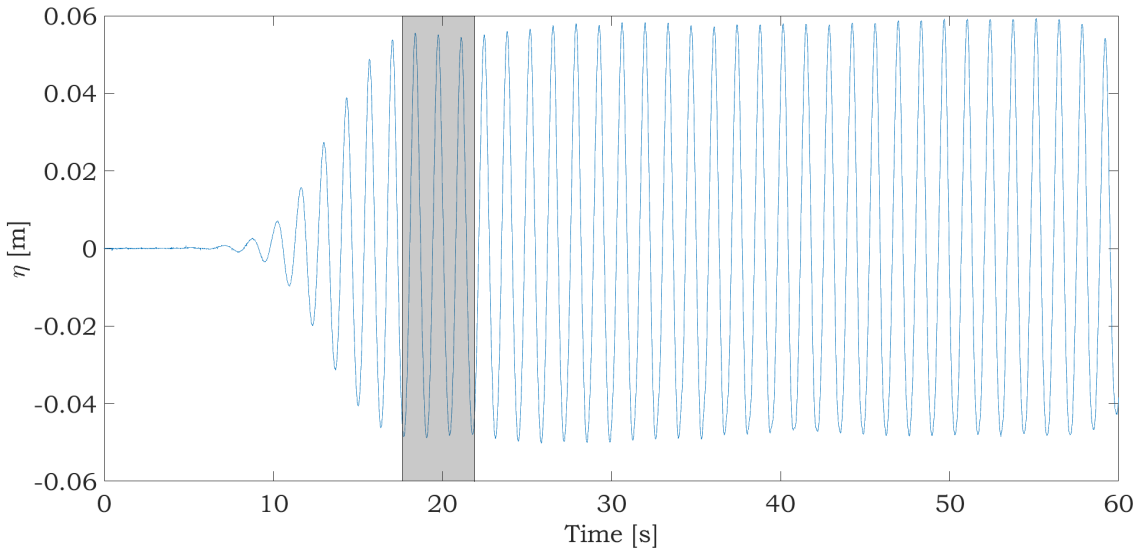

Figure 5.6. Surface elevation measured at WG 3 for sea state 4. The marked area is for the selected three fully developed waves.

The forces measured by the 6-axis force transducer are plotted with the surface elevation for WG 3 of the first three fully developed waves. This is shown for the cylindrical floater model for sea state 4 at 0° in Figure 5.7. The measured force, F_x, shows that the force peaks before the wave crest. This means that the force in the x-direction is partly or fully inertia dominated. The measured force, F_y, is approximately zero, which means that the transverse forces are negligible and support that the problem is investigated as a two dimensional problem. The measured force, F_z, varies with the surface elevation due to the buoyancy of the cylindrical floater model. The buoyancy does not contribute to a moment in this case due to it is placed at an angle of 0°. The torsional moment, T_x and T_z, are approximately zero due to F_y being approximately zero and the cylindrical floater model is symmetrical around its centroidal axis. The torsional moment, T_y, is shown with a calculated moment around the hinge, M, which is in phase. The rest of the measured forces are shown in Appendix D on page 151.

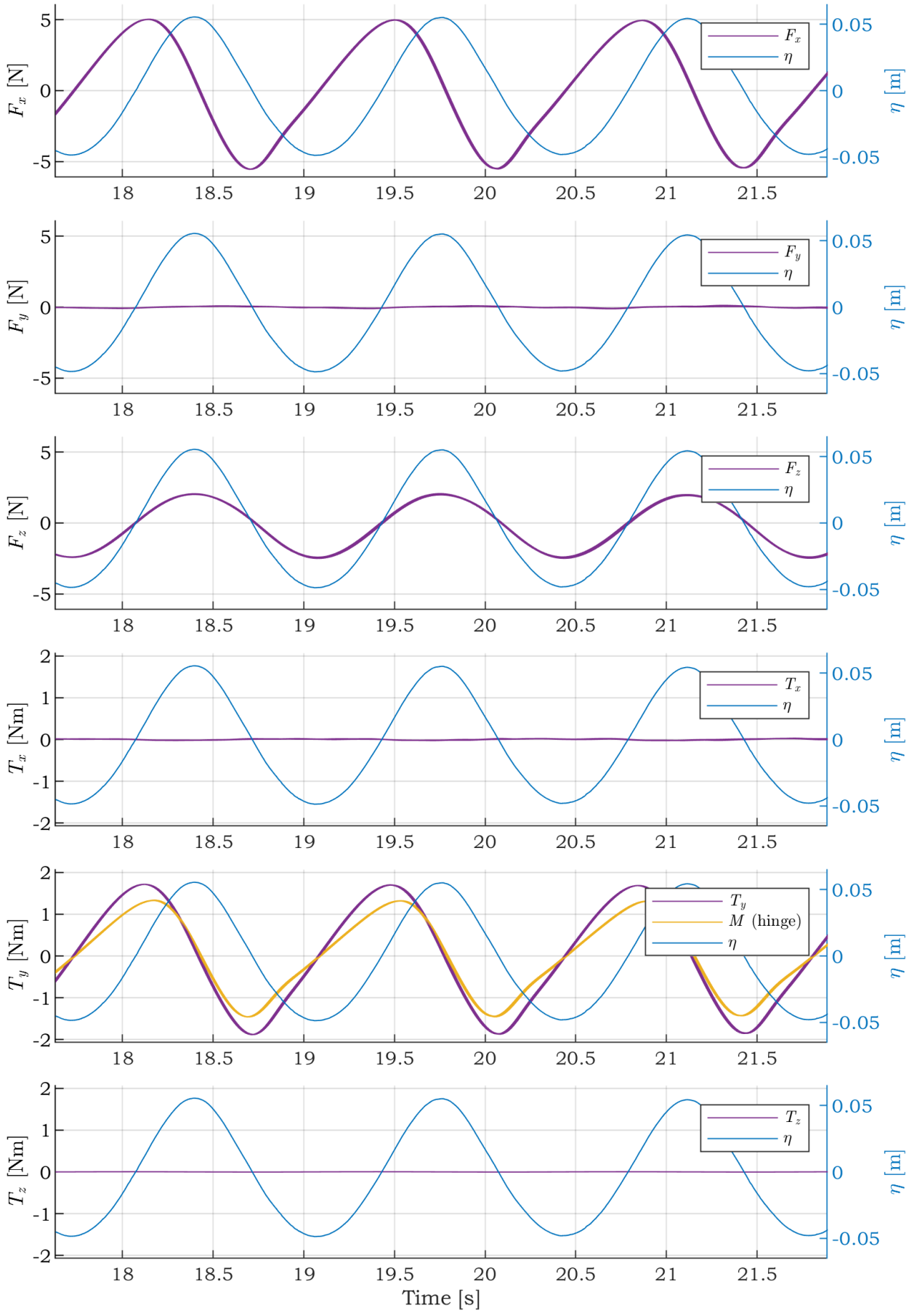

Figure 5.7. Output data for the cylindrical floater model at 0° for sea state 4.

In the following section two calculation methods are presented. The results from the calculation methods are compared to the measured wave forces from the experiment. Because of the controlled environment under which the experiment is conducted, the experimental data is used as a benchmark for validating the numerical results from the different calculation methods. However, Some errors have not been possible to avoid and could therefore have influenced the measured wave forces. These possible errors are listed in the following:

- The surface elevation which is used to align the data is measured without the model in the wave flume. The wave height could have slightly changed due to some reflection of the waves with the model. The data is narrowed down to the first three fully developed waves, which should ensure that the reflection has a small effect.
- The angle and the placement in the wave flume of the cylindrical floater model in the experiment were set up manually with care and precision but the actual angle and height in the wave flume could deviate from the theoretical values. The accuracy of the angle was within 0.1° according to a digital protractor. This could have a small influence on the measured wave forces but is estimated to be negligible.
- The water depth could deviate from the experiment where the surface elevation was measured at WG 3 and the experiment where the wave forces on the model were measured. This could have a small influence on the wave period. However the effects of this is considered to be negligible.

Even though there are some possible errors related to the experiment on the cylindrical floater model, the measured wave forces are still assumed to be the benchmark used to validate the calculation methods.

5.2 Method 1: Morison based calculation

Method 1 is based on the Morison equation. To determine the wave excitation force by the Morison equation it is necessary to establish the geometry of the model, the wave kinematics, and the Morison coefficients. The wave excitation forces on the cylindrical floater model are determined by dividing it into a normal force and a tangential force. Both forces have a significant influence when the model is rotated and are thus both of interest. The calculation is performed with a time step corresponding to the sampling frequency used in the experiment. The cylindrical floater model is imported into the calculation method as an STL model. An STL model describes the surface geometry of the floater model by using triangular panels.

The wave kinematics for each of the five sea states are determined using fifth order stream function theory. The wave kinematics are determined in sectional strips. The sectional strips are made by dividing the distance from the seabed to the wave crest into 3000 equal divisions. This means that each strip is approximately 0.3 mm. The sectional strips are used to determine the resulting Morison force on the cylindrical floater model.

5.2.1 Normal force

The normal force is determined by the Morison equation and is always calculated normal to the centroidal axis of the floater model.

The wave kinematics are found for each sectional strip and then projected normal onto the cylindrical floater model using simple trigonometry. At each sectional strip, the cross-sectional area and diameter used in the Morison equation are determined normal to the centroidal axis.

The sectional strips are shown as blue dashed lines in Figure 5.8. The wave kinematics are determined in the dots where the sectional strips intersect the centroidal axis of the floater model. Because the horizontal position of the dots changes with the angle of the cylindrical floater model the wave kinematics are shifted horizontally to account for the change in position.

In Figure 5.8 a sketch of the sectional strips along with the normal force, f_n, and the tangential force, f_t at a strip are shown.

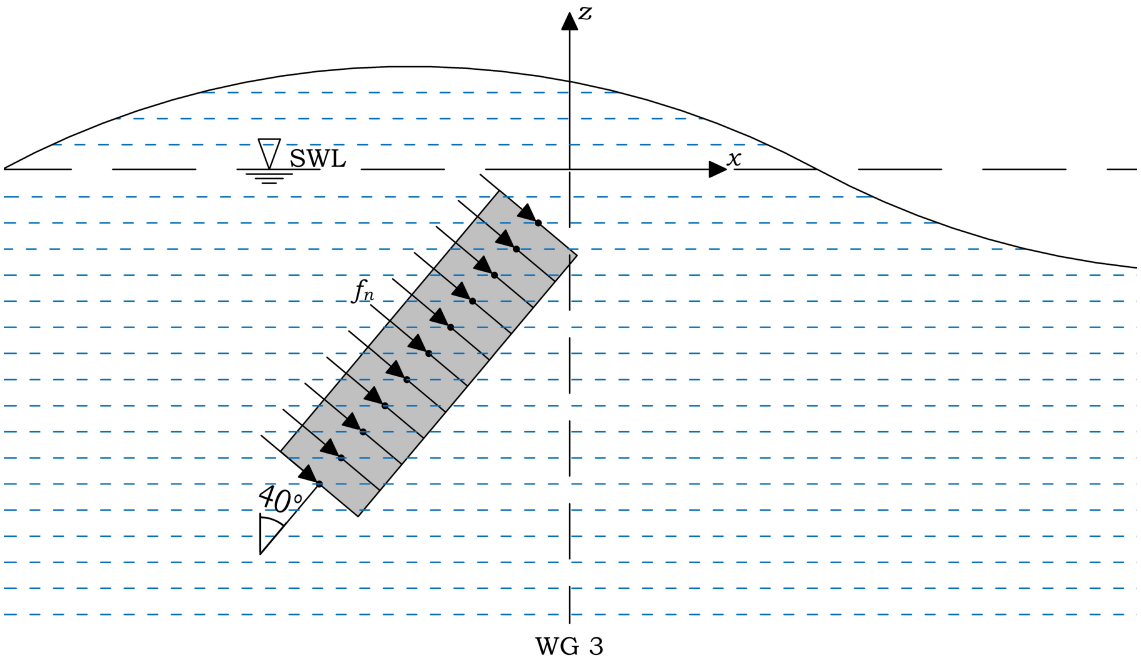

Figure 5.8. Cylindrical floater model at 40 ° including a sketch of the sectional strips. Dots show where the normal force, f_n, and tangential force, f_t are calculated.

The total normal force, F_n is determined by integrating the Morison force on each of the strips over the cylindrical floater's length. For the integration, Simpson's rule is used, which is a numerical integration method where the weight of each data point changes.

Determination of Morison coefficients

When fitting the Morison coefficients the drag coefficient is set to 0 as its influence is minimal. The added mass coefficient is fitted by combining the measured data in the x-direction and the z-direction to a normal force and comparing it to the normal force from the calculated with Method 1, F_n.

The fitting of the coefficients is conducted using the least squares method. The least squares method determines the minimum squared error between the measured force and the Morison force. The Morison coefficients are fitted to obtain the minimum squared

error. The fitting is performed with an accuracy of 0.01. The equation for the least squares method is shown in Equation (5.1).

$$E^2 = \sum (F_{n,Measured} - F_{n,Morison})^2 \tag{5.1}$$

5.2.2 Tangential force

The Morison equation is only used to calculate a force normal to the cylindrical floater model. Therefore a tangential force is calculated using the wave-induced pressure on the top and bottom area of the model. These areas are shown in Figure 5.9 along with the points where the tangential force is calculated.

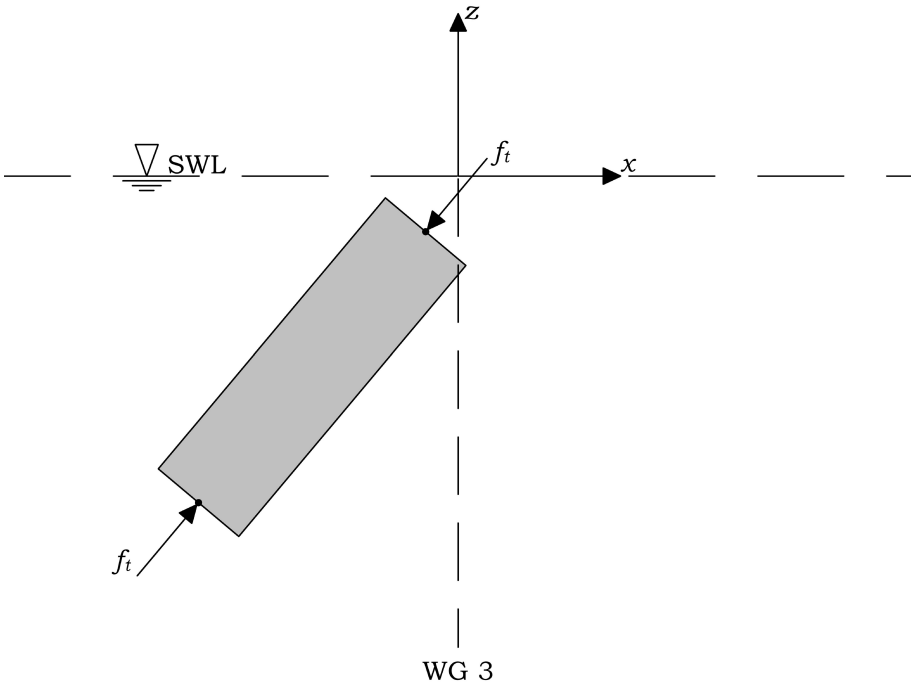

Figure 5.9. cylindrical floater model at 40 ° including a sketch of the areas and points used to determine f_t at.

Since the wave-induced pressure is zero at $\eta = 0$, the tangential force is zero. The wave-induced pressure acts normal on the top and bottom of the cylindrical floater model. The bottom of the cylindrical floater model is always submerged which means that the tangential force on the bottom varies with the surface elevation because the area is constant. The tangential force on the top of the cylindrical floater model is zero when no water is above the model. For the larger sea states and when the floater model is rotated at an angle, the surface elevation becomes larger than the freeboard of the cylindrical floater model. This means that the tangential force on the top of the floater model becomes negative.

5.2.3 Moment around hinge

The moment around the hinge is calculated by using the normal force on the cylindrical floater model at each sectional strip denoted by f_n. At each of the sectional strips, the arm

to the hinge is known. The total moment around the hinge is determined by summation by using Simpson's rule.

5.3 Method 2: BEM calculation

As an alternative to the Morison equation, a BEM model is used to examine the wave excitation forces on the floater model. The BEM calculations are performed using the open-source BEM solver NEMOH v.3.0.2 [Kurnia and Ducrozet, 2022]. NEMOH uses the governing equations and modelling principles described for the BEM in Section 2.2.2 on page 13.

To perform the BEM calculation in NEMOH, it is necessary first to describe the geometry of the floater. This is done by creating a mesh of the floater's geometry in the CAD program Autodesk Fusion version 2.0.18961. When creating the mesh for NEMOH the part of the floater above SWL is ignored and there is no lid on the mesh at the SWL. Therefore, there are only panels for $z \leq 0$. In Figure 5.10 an example of a mesh is shown. After creating the mesh as an STL file it is converted to a NEMOH-compatible mesh file using the open-source BEM mesh converter BEMRosetta.

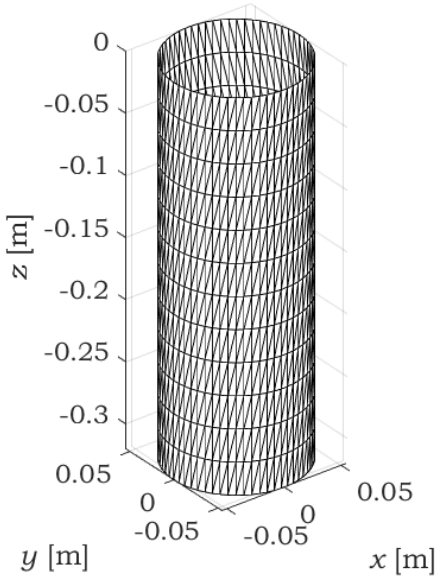

Figure 5.10. Mesh for the cylindrical floater model at an angular position of 0°.

Furthermore, an input file containing computational parameters such as the water depth, fluid density, etc., is made. This file also includes the reference point coordinates which are the coordinates of the hinge. In Table 5.1 the computational parameters for the cylindrical floater model at an angular position of 0° are shown as an example.

ρ [kg/m^3]	h [m]	No. of panels [-]	Ref. coordinates [m]
1000	0.72	743	(0, 0, -0.42)

Table 5.1. Overview of computational parameters for NEMOH.

A short convergence analysis is performed for the model at an angular position of 0° to examine the necessary number of panels in the numerical model. After determining a sufficient number of panels for the model at an angular position of 0° the same panel resolution is used when the floater model is rotated. The results from the convergence analysis are described in Appendix C.5.1 on page 126.

5.3.1 NEMOH results

The NEMOH calculation outputs hydrodynamic coefficients such as added mass and damping. Furthermore, wave excitation forces along with phases for these forces, ϕ, are given for the 6 degrees of freedom. The wave excitation forces consists of Froude-Krylov and diffraction forces. The output is given dependent on the wave frequency ω. The calculation is performed with a resolution of 0.1 for the wave frequencies. The force output is normalised with respect to the wave amplitude a. The excitation force and phase results for the cylindrical floater model at $\theta = 0\,°$ are shown in Figure 5.11, 5.12 and 5.13 for surge, heave and pitch respectively. The wave frequencies for the sea states are shown in the figures as dashed lines.

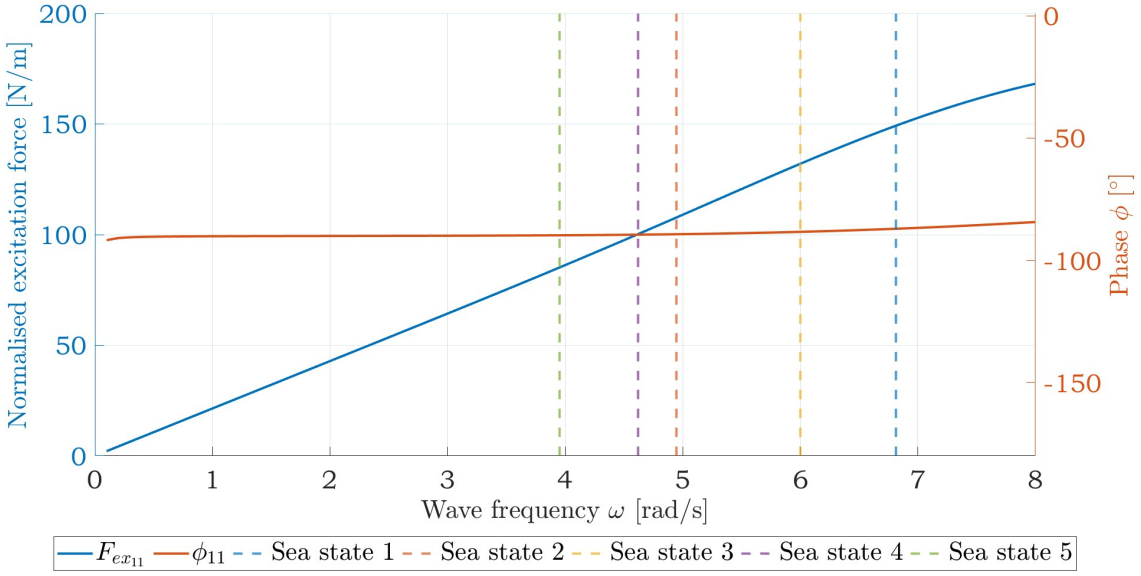

Figure 5.11. NEMOH normalised force and phase output for surge for the cylindrical floater model at $\theta = 0\,°$.

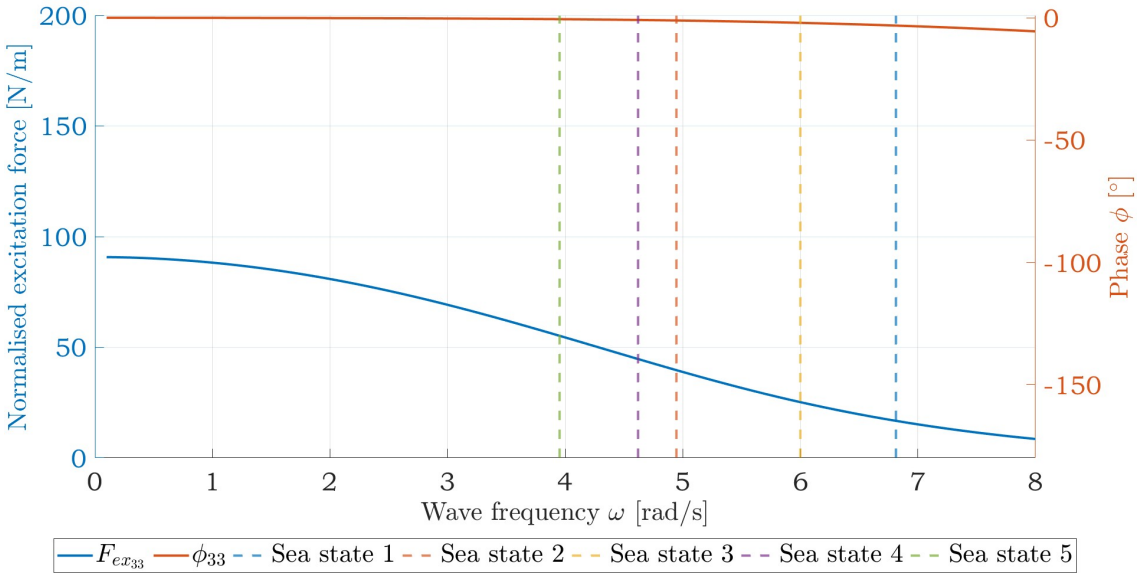

Figure 5.12. NEMOH normalised force and phase output for heave for the cylindrical floater model at $\theta = 0\,°$.

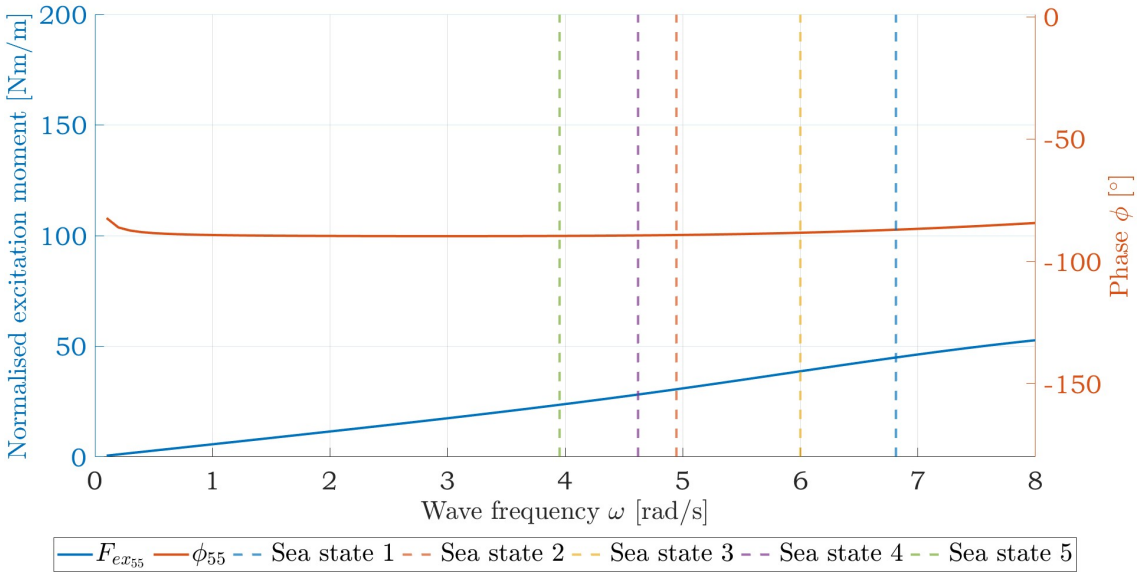

Figure 5.13. NEMOH normalised force and phase output for pitch the cylindrical floater model at $\theta = 0\,°$.

To determine the wave forces on the cylindrical floater model first, the normalised force for the given wave frequency is determined with linear interpolation. Then the forces on the cylindrical floater model are determined by multiplying the normalised forces with the water surface elevation and applying the phase shift to the force.

5.4 Validation of calculation methods

In this section the measured results from the experiment described in Section 5.1.3 on page 30 are compared to the calculated forces determined with Method 1, and Method 2. Only some of the results are shown in this section showing common tendencies for the results. Results not shown here are shown in Appendices E on page 253 and F on page 355.

Method 1 is only used in the same angles as the experiment since the added mass coefficient is fitted to the measured data. The Method 2 calculations are performed on the cylindrical model at angular positions from -40° to 40°. In the interval -20° to 20°, 5° increments are used, outside of this interval 10° increments are used.

As shown in the experiment the cylindrical floater model is rotated around a joint that is connected to the 6-axis force transducer. The STL model in Method 1 is placed in the same place as the floater model in the experiment. For Method 2, the cylindrical floater model is rotated around the hinge near the bottom. This means, that the cylindrical floater model ends up being placed at a different x-coordinate, but the z-coordinate is the same. To compare Method 2 to the measured force and Method 1, the cylindrical floater in Method 2 is shifted to match the other ones.

The results are shown in the global coordinate system. In Figures 5.14, 5.15 and 5.16, the calculation methods are compared to the measured force. Furthermore, a calculation using Morison coefficients suggested by DNV GL [2017] is included. This is denoted DNV on the plots. For the DNV calculation, the added mass coefficient is set to 1 and the drag

coefficient is set to 0.7. The DNV calculation is only included in 0° because it does not calculate the tangential force, which has an effect when the model is tilted. The confidence interval (CI) is also shown in the figure. It should be noted that the CI is narrow and therefore the measurements and the CI appear to be coinciding.

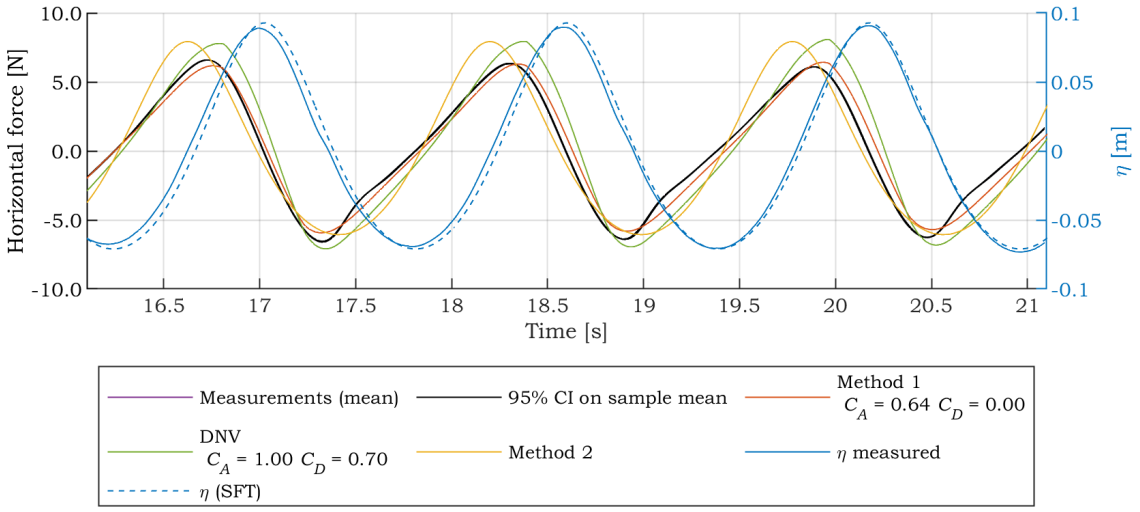

Figure 5.14. Horizontal force over time for the cylindrical floater model at 0 ° for sea state 5.

As can be seen in Figure 5.14, the measured surface elevation, η, and the surface elevation calculated by fifth order SFT, η (SFT), are shown. The measured surface elevation compared to the calculated surface elevation is close to being the same which supports the use of SFT.

The measured horizontal force shows that the force is inertia dominated since it peaks as the acceleration of the particle is largest. This supports the fact, that the drag coefficient, C_D, is set to zero for Method 1 when the floater model is fixed because its influence is minimal. Method 1 with the fitted $C_A = 0.64$ for the horizontal force follows the measured time variation best based on the figure. The calculation using DNV coefficients overestimates the horizontal force due to C_A being higher. Method 2 overestimates the horizontal force as well. Furthermore, the horizontal force in the BEM peaks at a different time than the measured horizontal force. This is due to the BEM using linear wave theory and the surface elevation can not be described by linear wave theory.

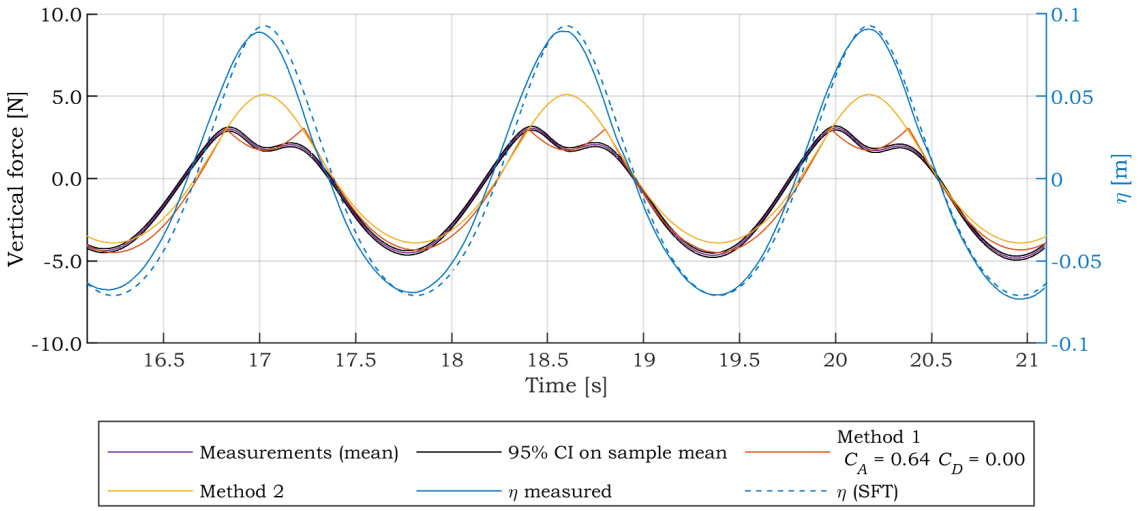

Figure 5.15. Vertical force over time for the cylindrical floater model at 0 ° for sea state 5.

As can be seen, in Figure 5.15 the measured vertical force drops as the wave becomes higher than the freeboard of the cylindrical floater model. This is due to the wave overtopping which results in a downward force on the top of the cylindrical floater model. Method 2 does not take into account the pressure on the cylindrical floater model due to potential theory which does not include hydrodynamic activity above SWL. Method 1 takes the overtopping into account with the tangential force calculated by the wave-induced pressure. As shown in the 5.15, the assumption used in Method 1 results in a good description of the time variation of the vertical force.

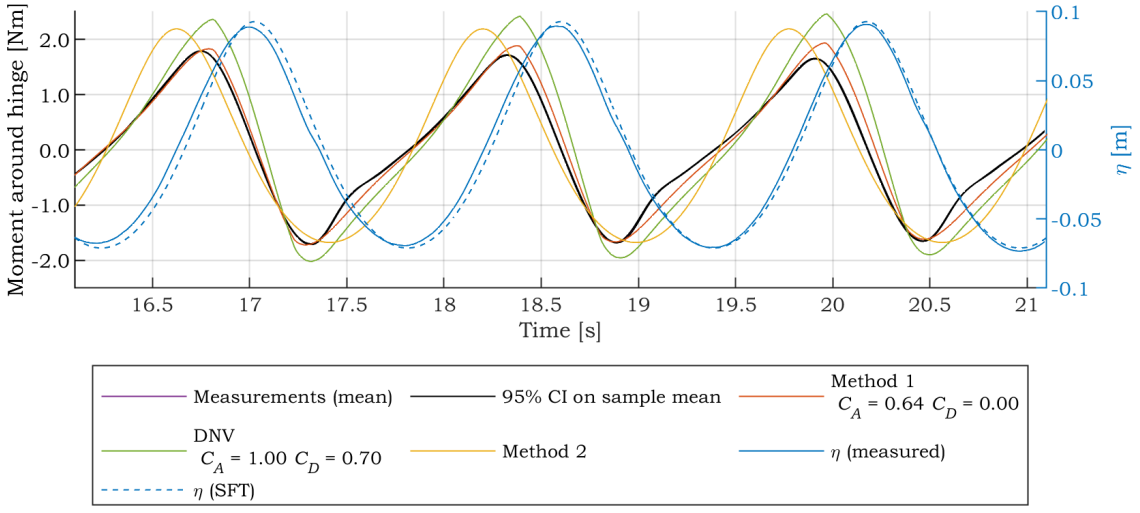

Figure 5.16. Moment around the hinge over time for the cylindrical floater model at 0 ° for sea state 5.

The moment around the hinge dictates the movement of the model which is important to predict the movements and energy production of the WEC. As can be seen in the 5.16 the time variation of the moment around the hinge is described well by Method 1. In comparison, the DNV-based calculation overestimates the moment, which again illustrates the importance of using fitted Morison coefficients. Method 2 results in an overestimation of the moment and a slight deviation with respect to the peak.

In Figures 5.17, 5.18 and 5.19 the calculation methods are compared to the measured force. The figure is shown for sea state 3 with the model at an angle of 20°.

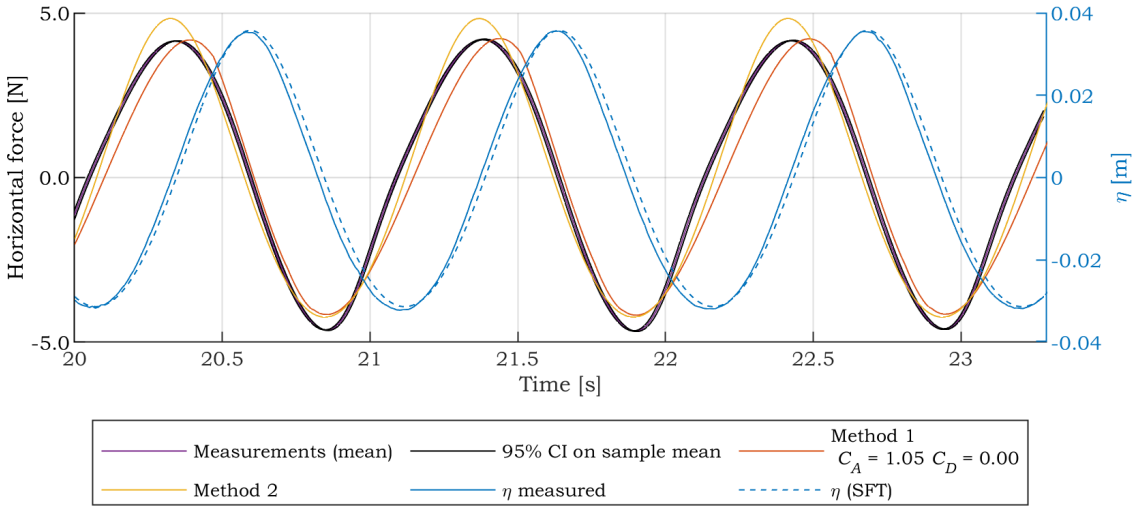

Figure 5.17. Horizontal force over time for the cylindrical floater model at 20 ° for sea state 3.

The horizontal force is shown in Figure 5.17 where both the calculation methods follow the measured horizontal force. Method 2 overestimates the maximum force in comparison with Method 1, which is close to the measured values but slightly offset at the peak.

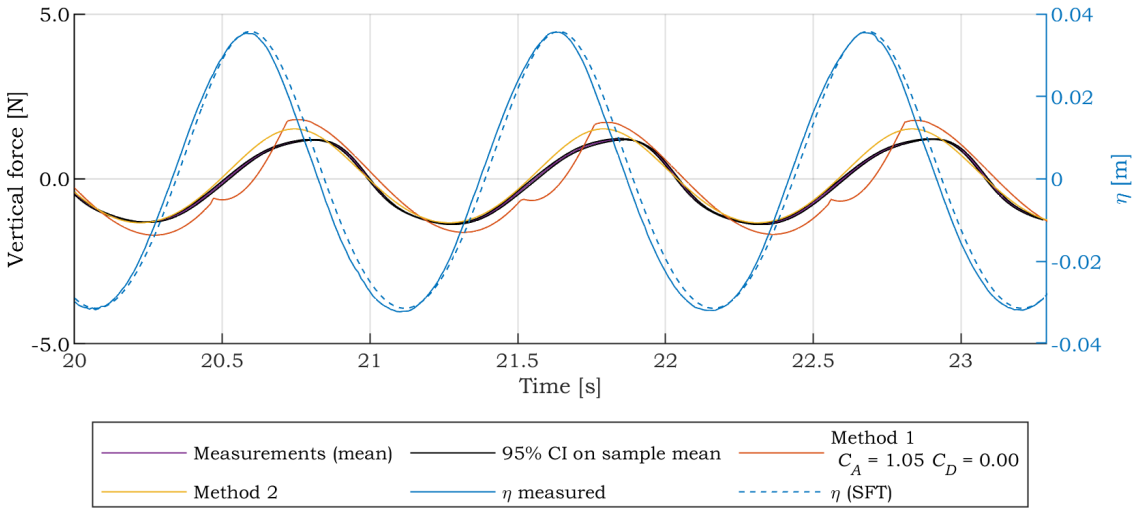

Figure 5.18. Vertical force over time for the cylindrical floater model at 20 ° for sea state 3.

In Figure 5.18 the vertical forces are shown. The calculated vertical force by Method 1 shows a sudden dip in the force. This is because the cylindrical floater model is submerged which results in a negative tangential force on top of the model. The vertical force then has a local minimum at the wave crest for Method 1 since the cylindrical floater model is submerged. Method 2 follows the progress of the measured vertical force but overestimates the maximum force. Method 1 does not follow the progress of the measured vertical force well.

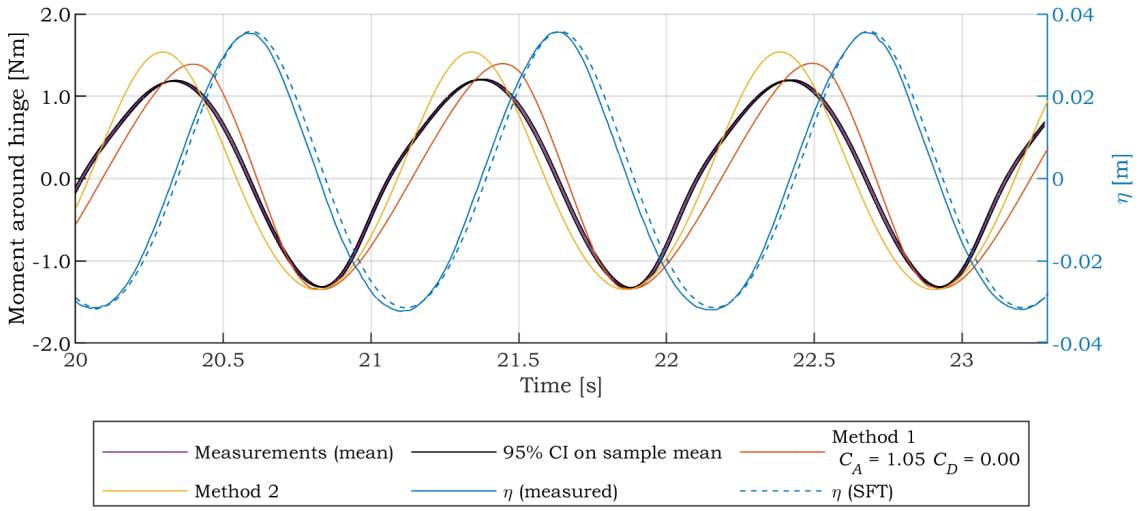

Figure 5.19. Moment around the hinge over time for the cylindrical floater model at 20 ° for sea state 3.

Figure 5.19 shows the moment around the hinge. Both calculation methods follow the time series of the measured moment, especially in the minimum values. The steepness of the measured moment is not symmetrical around its peaks. Method 2 estimates the moment as being symmetrical which deviates from the measured but the peak of the moment is at the same time. Method 1 is non-symmetrical and the moment does not peak at the same time as the measured moment.

In Figures 5.20, 5.21 and 5.22 the angle of the cylindrical floater model changes from 20° to −20° . This means that the top of the cylindrical floater model is pointed towards the wave direction.

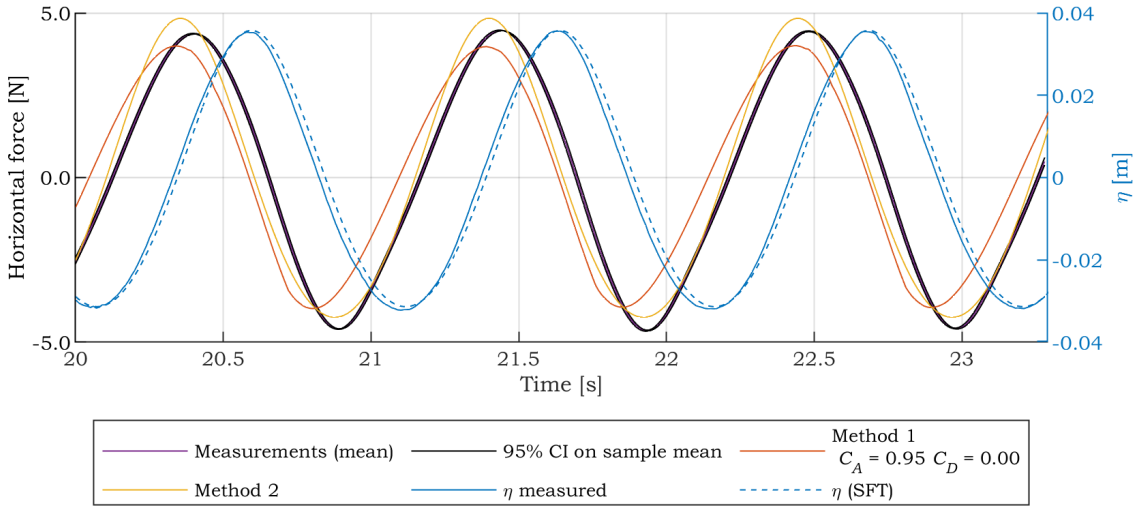

Figure 5.20. Horizontal force over time for the cylindrical floater model at −20 ° for sea state 3.

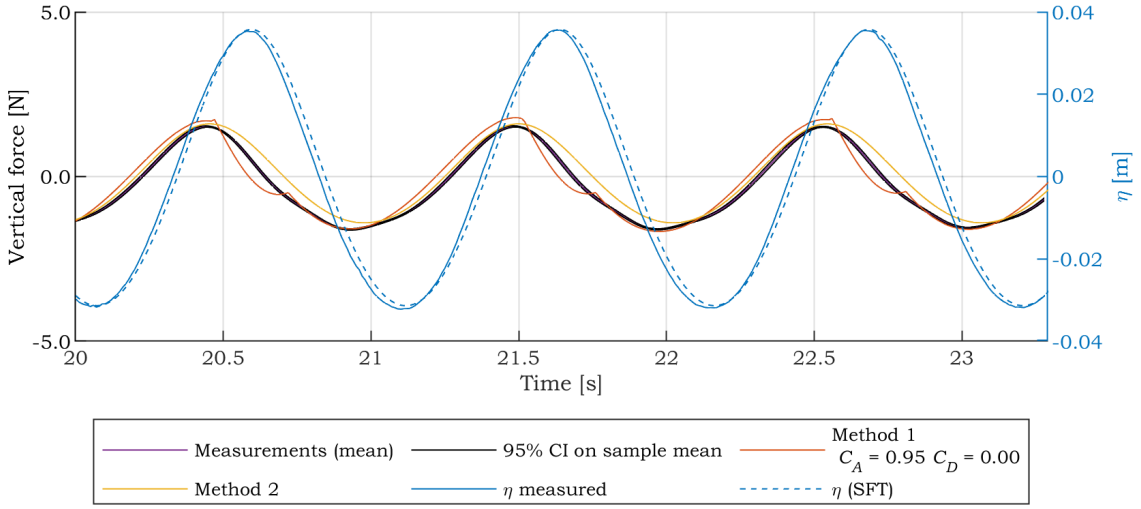

Figure 5.21. Vertical force over time for the cylindrical floater model at $-20\,^\circ$ for sea state 3.

The added mass coefficient in Method 1 is slighter smaller than in 20°. The overall tendencies of the forces are the same as for the cylindrical floater model in 20°.

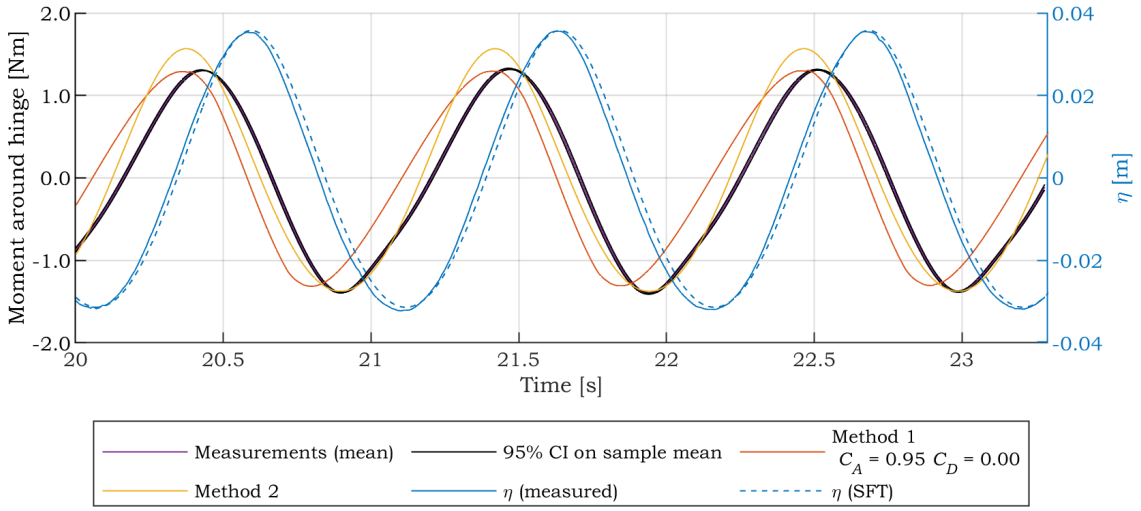

Figure 5.22. Moment around the hinge over time for the cylindrical floater model at $-20\,^\circ$ for sea state 3.

Method 2 in Figure 5.22 shows the moment around the hinge and estimates the moment's variation over time with good precision apart from at the peak. Method 1 estimates the time variation of the moment with good precision but is offset compared to the measured moment.

The relation between the wave force in the x-direction and z-direction is shown in Figures 5.23 and 5.24. The figures provide an insight into the time variation of the wave forces over the three wave periods shown in the previous figures. Method 1 is divided into the normal force and tangential force contribution in the figures.

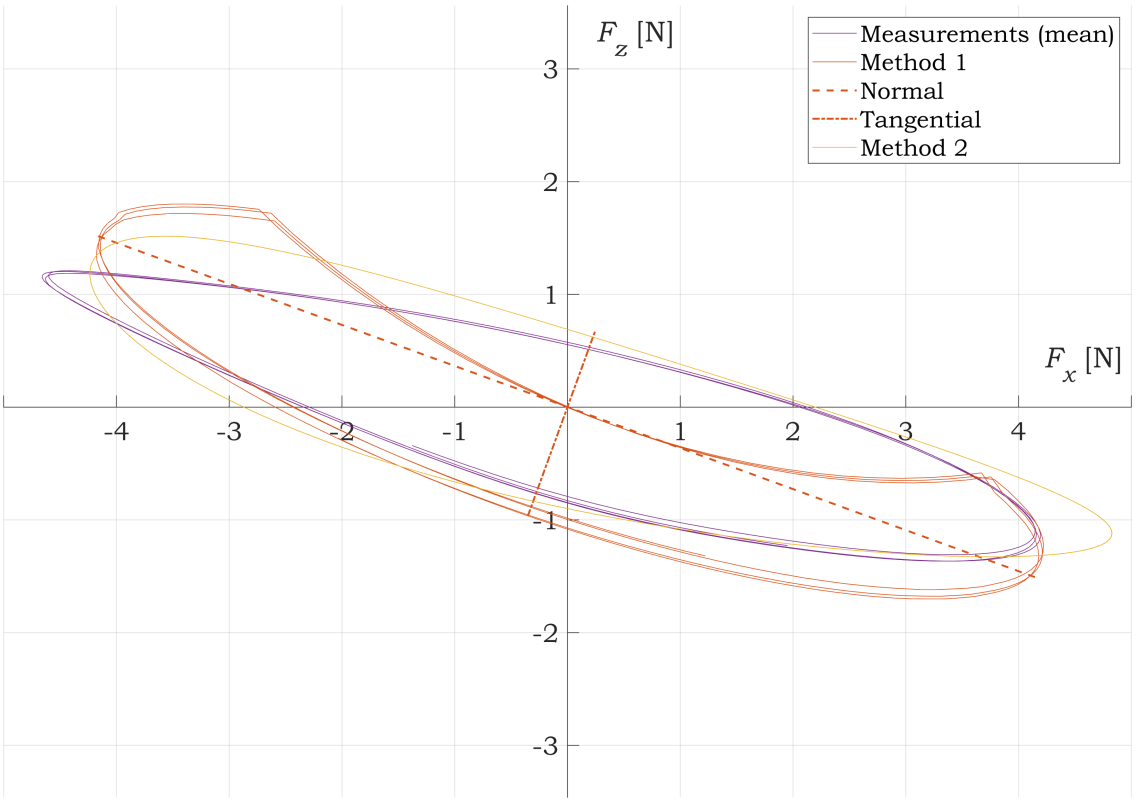

Figure 5.23. Horizontal force, F_x, compared to the vertical force, F_z, for the cylindrical floater model at 20 ° for sea state 3.

As can be seen in the figure, Method 1 drifts slightly. This is because the wave kinematics are determined by setting the discharge of the water to zero, which creates a small current that influences the wave kinematics. Method 2 estimates the wave forces better than Method 1 in 20°. Method 1 overestimates the negative tangential force on the cylindrical floater model in the first quadrant.

The relation between the wave force in the x-direction and z-direction in -20 ° is shown in Figure 5.24. Method 2 does not match the measured results as well at -20 ° as it did at 20 °. However, Method 1 still gives decent results.

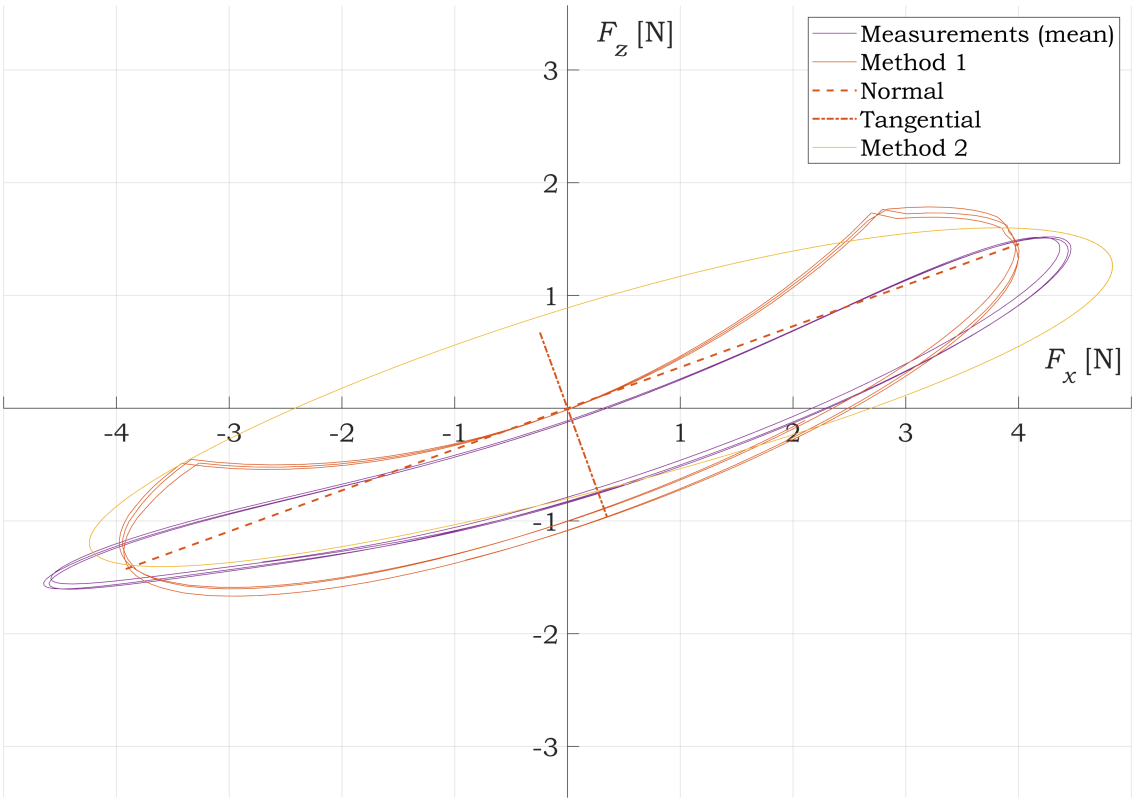

Figure 5.24. Horizontal force, F_x, compared to the vertical force, F_z, for the cylindrical floater model at $-20\,^\circ$ for sea state 3.

Method 2 does not match the measured results as well at $-20\,^\circ$ as it did at $20\,^\circ$. However, Method 1 still gives decent results.

Added mass coefficients

Method 1 based on the Morison equation determines the added mass coefficient by fitting it to the measured data. The added mass coefficients are shown in Table 5.2.

	Angle [°]						
Sea state	-40	-20	-10	0	10	20	40
1	1.40	0.96	0.88	0.98	1.06	1.13	1.44
2	1.42	0.91	0.91	0.89	0.90	0.88	1.47
3	1.45	0.95	0.94	0.96	1.00	1.05	1.50
4	1.39	0.94	0.91	0.91	0.91	0.90	1.39
5	1.17	0.75	0.70	0.64	0.60	0.54	0.88

Table 5.2. Added mass coefficients for the cylindrical floater model.

As stated earlier, DNV GL [2017] uses an added mass coefficient of 1.0 for a cylinder from the seabed to above the wave crest. Based on the fitted added mass coefficients in the table, it is observed that the coefficients are close to 1.0 for sea states 1 to 4 within the interval $-20\,^\circ$ to $20\,^\circ$. This emphasises that DNV GL [2017] is conservative but still close to the fitted coefficients. The added mass coefficients in the outermost angles deviate from the other coefficients. This is possible due to the wave-structure interaction behaving

considerably different at these angles. Furthermore, the added mass coefficient for sea state 5 is smaller than the others. This can be due to a larger drag contribution which is not included in the least squares fit.

5.5 Evaluation of calculation methods

In this section, the two calculation methods are evaluated based on the results presented in the previous section. The calculation methods are evaluated by calculating the fraction of variance unexplained (FVU). Which gives a fraction of how much the results from the calculation methods vary from the measured data. For an FVU-value of 0, there is no variation between the calculated and measured results. The FVU is calculated as shown in Equation (5.2).

$$\text{FVU} = \frac{\text{var}(F_{calc} - F_{meas})}{\text{var}(F_{meas})} \tag{5.2}$$

In the following, figures showing the FVU for each sea state at different angles are presented. If the FVU is larger than 0.6 the marker is shown at the top of the figure and the FVU value is written next to it. Figure 5.25 and 5.26 show how well the calculation methods follow the measured data for the horizontal force.

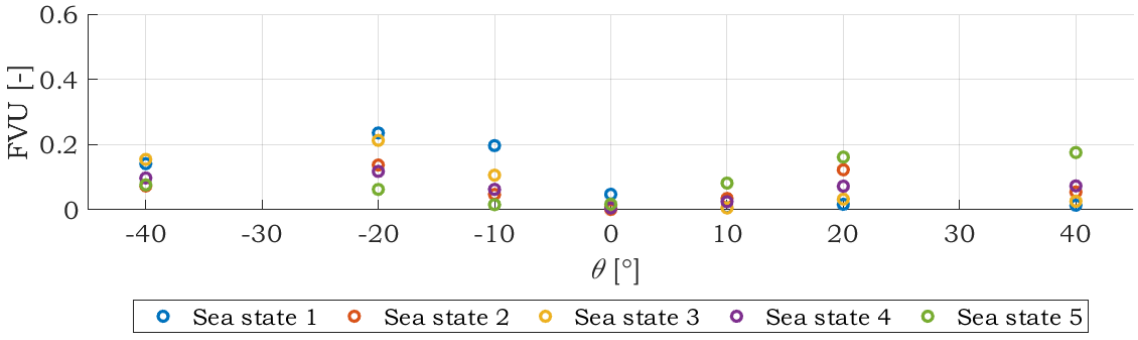

Figure 5.25. FVU for the horizontal force using Method 1.

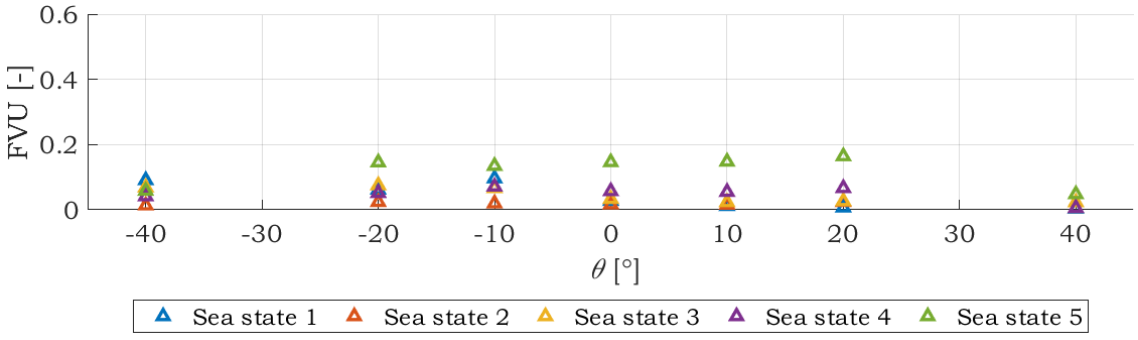

Figure 5.26. FVU for the horizontal force using Method 2.

Method 2 is fairly consistent with estimating the horizontal forces, and Method 1's accuracy varies more depending on the sea state and angle. Method 2 shows better accuracy in the

smaller sea states than the higher ones. This is due to the assumption of linear wave theory which can not be used to accurately describe the waves from the sea states. Sea states 1 to 3 are closer to following the assumptions used in linear wave theory. The accuracy of the calculation methods for the vertical forces is shown in Figure 5.27 and 5.28.

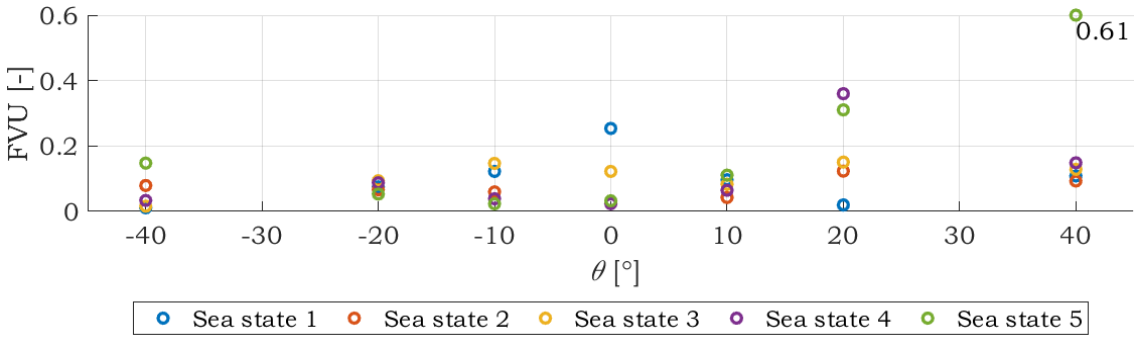

Figure 5.27. FVU for the vertical force using Method 1.

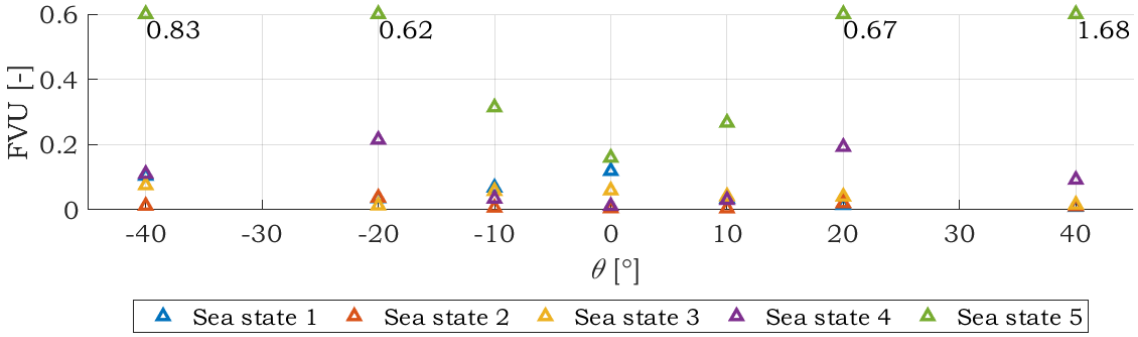

Figure 5.28. FVU for the vertical force using Method 2.

The accuracy of Method 1 varies as it also did for the horizontal forces. In general, the FVU is below 0.2 for the first four sea states. For sea state 5 larger deviations occur, particularly for large positive angles. The accuracy of Method 2 is again highly dependent on which sea state is being investigated. It is accurate for most of the sea states except for sea state 4 and sea state 5 where larger deviations occur.

The accuracy of the moment calculation based on the two different methods which are later used to determine the motions of the floater model are shown in Figure 5.29 and 5.30.

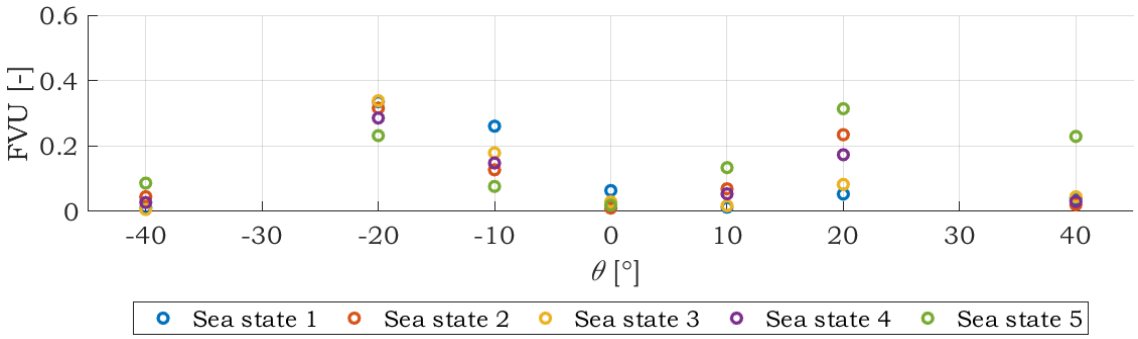

Figure 5.29. FVU for the moment using Method 1.

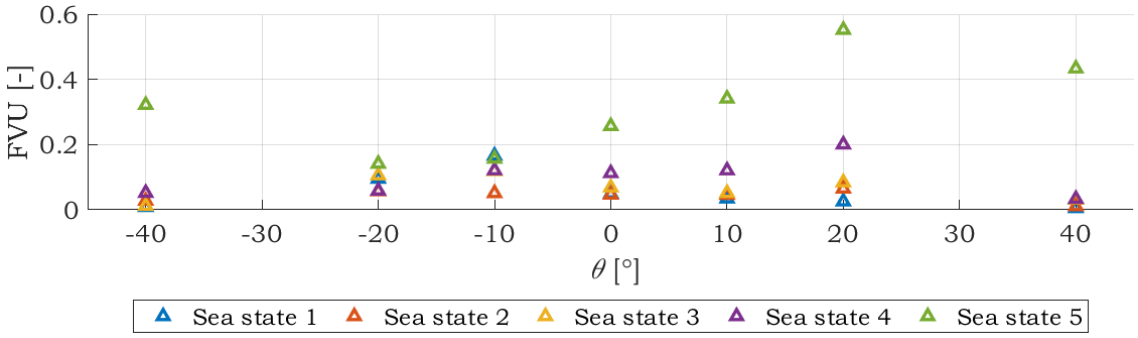

Figure 5.30. FVU for the moment using Method 2.

In 0° the horizontal force is the sole contribution to the normal force. This implies that the FVU of horizontal force has the largest contribution to the FVU of the moment around the hinge. The FVU using Method 1 becomes larger with the angle of the floater model except for the outermost angles. As shown sea state 5 has a smaller FVU in negative angles than in positive angles. In Figure 5.30 the FVU for the moment is shown using Method 2. The FVU shows an almost constant value for each sea state at different angles unless for sea state 5. Sea state 5 is the sea state with the steepest waves and linear wave theory is in this case a gross assumption to the problem. The lower sea states in the outermost angles have a small FVU value. This is because the cylindrical floater model is fully submerged which is closer to the assumptions used in BEM.

Method 1 describes the wave forces on the cylindrical floater model well at 0° for all sea states. Method 1 is imprecise when the cylindrical floater model is placed at an angle. This is due to Method 1 not estimating the wave-structure interaction with the same precision as the BEM even though the added mass coefficient is fitted to the measured data. Method 2, which is based on the BEM, is an adequate solution for particularly the sea states with smaller wave heights and lower wave steepness. This is because these waves are closer to the assumptions in linear wave theory which is used in BEM. Method 2 captures the wave-structure interaction as the cylindrical floater model is placed at an angle particularly when the cylindrical floater model is fully submerged at ±40°. This is because Method 2 does not account for the part of the model above the SWL. The drag contribution is assumed to be negligible therefore it is not included in the calculation methods on the fixed cylindrical floater model.

In Chapter 6, the calculation methods presented in this chapter will be used in numerical models to predict the motions of the cylindrical floater model.

Motions of the cylindrical floater model

6

This chapter will examine the validity of different numerical models used for determining the motions of the cylindrical floater model. This is done by comparing numerical results with experimental results obtained during both decay tests and tests where the floater model is excited by waves.

6.1 Experiments on moving cylindrical floater

The experiment is set up to measure the rotation of the cylindrical floater model around the hinge when it is subjected to waves. The experiment is performed without a PTO. The general experimental setup for the experiment is described in Chapter 4 on page 23. An illustration of the cylindrical floater model including the hinge is shown in Figure 6.1. In Figure 6.2 a picture of the hinge fastened to a structure of struts and a steel plate is shown. The hinge is constructed so its only movement is rotation in the wave direction. There is a little play in the hinge, which means that other degrees of freedom are activated. The motions in the other DoFs are examined in Appendix C.2 on page 118 and it is determined that the influence is minimal. After the cylindrical floater model is fastened to the steel plate, the weight of the steel plate secures it to the bottom.

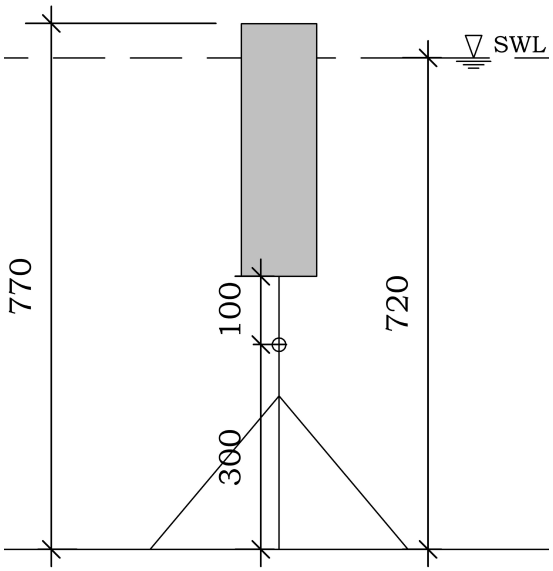

Figure 6.1. Illustration of the cylindrical floater model including the hinge and the struts.

Figure 6.2. Hinge secured to the steel plate placed in the wave flume.

In order to measure the rotation of the model, a motion capture system called Qualisys Track Manager (QTM) is used [Qualisys, 2020]. Four Qualisys Oqus cameras are used to capture the motion of the floater model. The motion capture system measures the motion in three dimensions. The cameras are placed along the wave flume and pointed toward the model. Three of the cameras are shown in Figure 6.3.

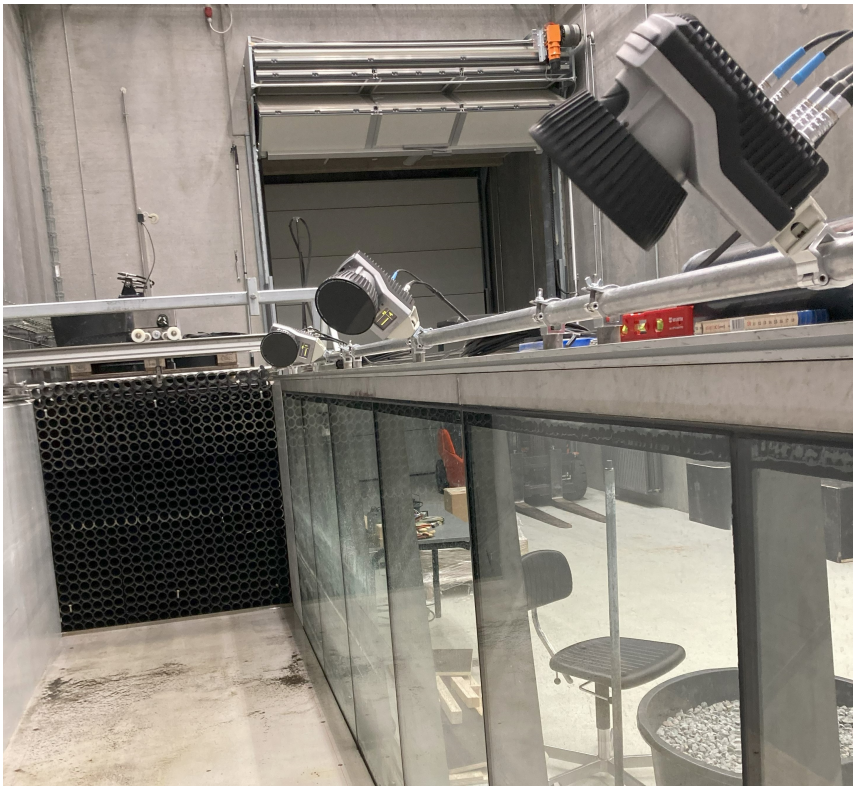

Figure 6.3. Three of the four Qualisys Oqus cameras.

The movement is measured by attaching a rigid structure with four reflective markers to the top of the cylindrical floater model. The four reflective markers form a rigid body which makes it possible for the cameras to track the motions of the floater model. Figure 6.4 shows the cylindrical floater model in the wave flume, including the reflective markers on top. Before the movement is measured the motion capture system is calibrated, this is described in Appendix C.1 on page 117. The system is set up so each reflective marker needs to be captured by a minimum of two cameras at all times to capture the motion.

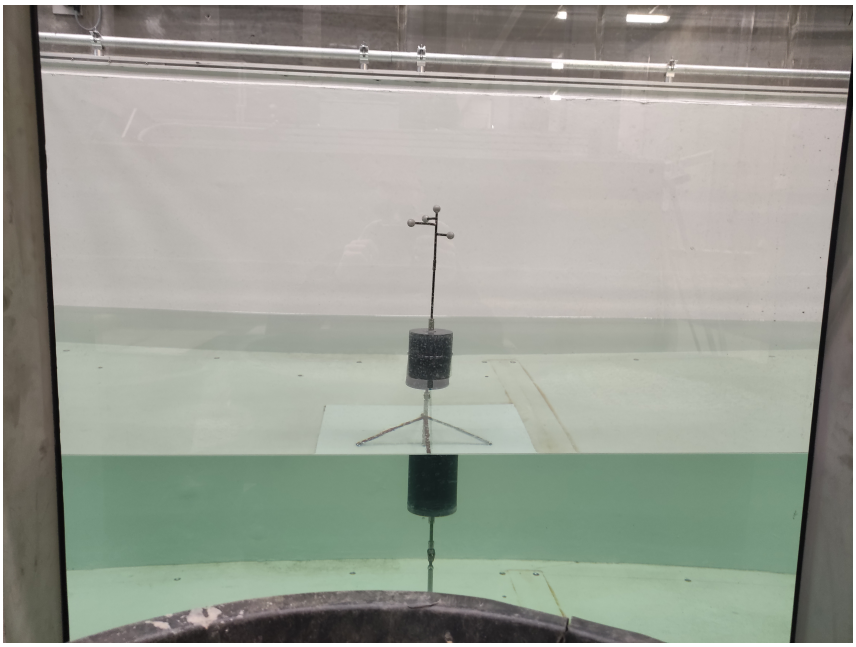

Figure 6.4. Cylindrical floater model in the wave flume with rigid body of reflective markers on top of the model.

6.1.1 Decay tests

A decay test is performed on the floater model to examine the natural frequencies of the cylindrical floater model. Furthermore, the decay test is used as an initial step in the validation of the numerical models. The decay test is conducted by positioning the cylindrical floater model at an angle and then releasing the model. The movement of the model is measured during the decay test to establish the decay of the movement. The water is still at the time of the release and the water depth is at SWL.

6.1.2 Wave excitation tests

The cylindrical floater model is subjected to waves from the five sea states causing a wave excitation force on the model. The wave excitation force causes the cylindrical floater model to rotate around the hinge as a 1-DoF system. The rotation of the model is measured in degrees by QTM.

6.2 Numerical models

In this section, the numerical models are presented. The numerical models are all based on the equation of motion shown in Equation 6.1.

$$I \cdot \ddot{\theta}(t) = M_{ex}(\theta) + M_{rad}(\dot{\theta}, \ddot{\theta}) + M_{hs}(\theta) \tag{6.1}$$

To solve the equation of motion it is rewritten as two ordinary differential equations which are used in a state-space representation of the system. This system is solved using a fourth order Runge-Kutta differential equation solver following the implementation by Cash and

Karp [1990] and Gavin [2020] as described in Iversen et al. [2023]. A time step of 10 ms is used in the calculation.

All of the numerical models use nonlinear hydrostatics where the buoyancy is dependent on the angular position of the floater since this alters the submerged volume and the distance from the hinge to the centre of buoyancy. The numerical models are based on the hydrostatic moment, M_{hs}, the radiation moment, M_{rad}, and the wave excitation moment, M_{ex}. By varying how the three different moments are determined, a number of numerical models are established.

The mass moment of inertia, I, for the cylindrical floater model is determined in a pendulum experiment, as described in Appendix C.3 on page 119. It is determined that $I = 0.41\,\mathrm{kg} \cdot \mathrm{m}^2$ for the cylindrical floater model.

In Table 6.1 parameters that are used in all of the numerical models are summarised.

ρ [kg/m^3]	g [m/s^2]	A [m^2]	D [m]	I [kg $\cdot$ m^2]	m [kg]	r_g [m]
1000	9.82	9.50^{-3}	0.11	0.41	1.94	0.29

Table 6.1. Overview of parameters used in the numerical models.

The aforementioned parameters and the calculation method for the hydrostatic moment are in common for the numerical models. However, the approaches used to determine the radiation moment and the wave excitation moment differ depending on the numerical model. The differences between the three numerical models are described in the following sections.

6.2.1 *NM1* Model

For the first numerical model, *NM1*, the radiation moment is calculated based on an added mass moment of inertia, m_h, and an experimentally determined hydrodynamic damping coefficient, c_h. This is shown in Equation (6.2).

$$M_{rad} = -m_h \cdot \ddot{\theta}(t) - c_h \cdot \dot{\theta}(t) \tag{6.2}$$

The added mass moment of inertia is calculated using the added mass coefficients, C_A, that are determined from a least squares fit to the experimental data as described for Method 1 in Section 5.2.1 on page 34. The added mass moment of inertia is then determined as shown in equation (6.3) following the method in Iversen et al. [2023].

$$m_h = \int_{r_{bottom}}^{r_{top}} C_A \cdot \rho \cdot A \cdot r^2 \tag{6.3}$$

Where:

r	Distance from hinge to area [m]
r_{bottom}	Distance from hinge to bottom of floater [m]
r_{top}	Distance from hinge to top of floater or η [m]

The damping coefficient, c_h, is determined experimentally using data from the decay tests performed on the cylindrical floater model. This is done using the method of extinction coefficients as described in Himeno [1981]. The method used to determine the damping coefficient is described in detail in Appendix C.4 on page 121.

The wave excitation moment is calculated with Method 1 based on the Morison equation as described in Section 5.2 on page 33. However, it should be noted that the velocity and acceleration are now relative since the floater model is moving. This means that a drag term is relevant to include due to the relative motion being larger. The drag coefficient used in the calculation is chosen as 0.7 based on DNV GL [2017] as stated in Section 5.4 on page 38. The added mass coefficients used in the calculation are the ones determined using Method 1 in Chapter 5. These are shown in Table 5.2 on page 45. The C_A value for the actual angular position is determined using linear interpolation.

6.2.2 *NM2* Model

The second numerical model, *NM2*, is primarily based on the outputs from the open-source BEM-code NEMOH. However, because of the assumption of potential theory in the boundary element method, the effects of viscosity are not taken into account in the outputs from NEMOH. To consider the viscous effects it was chosen to use a drag contribution calculated with the relative velocity formulation of the Morison equation. To illustrate the necessity of including the drag contribution, the results for a decay test calculated with and without a drag contribution are shown in Figure 6.5.

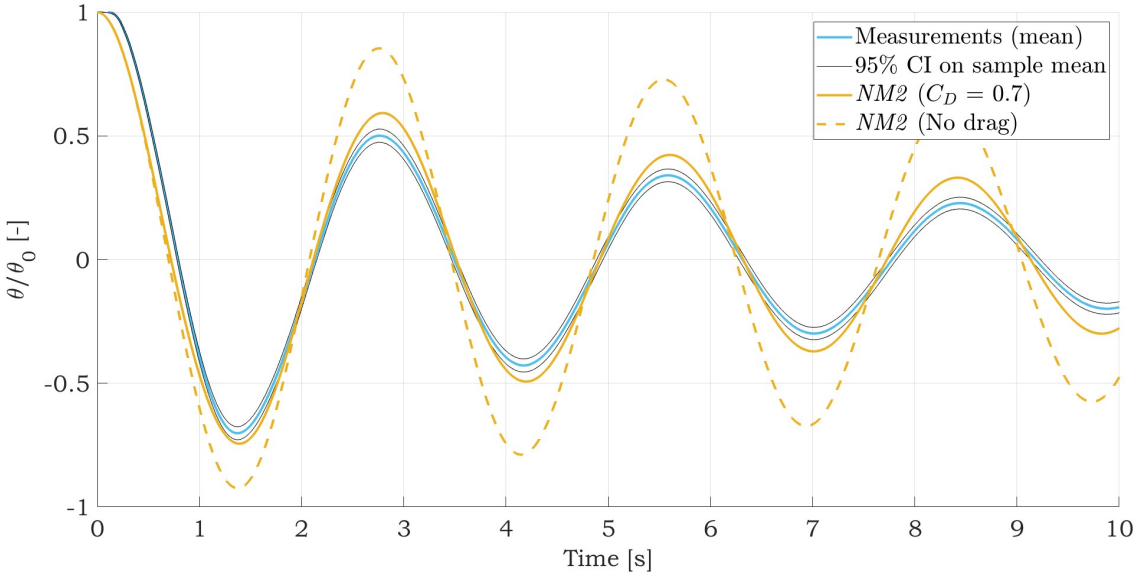

Figure 6.5. Comparison of normalised decay time series calculated with and without a drag contribution.

In the figure, it can clearly be seen that the inclusion of drag improves the accuracy of the calculated decay time series. This illustrates the necessity of including a drag contribution in a BEM-based numerical model, especially for longer waves where drag forces have a larger influence.

The NEMOH calculations are performed on the cylindrical model at angular positions from -40° to 40°. In the interval -20° to 20°, 5° increments are used, outside of this interval 10° increments are used. The NEMOH calculations give the added mass moment of inertia, m_h, and the damping coefficients c_h as outputs. In Figure 6.6, the added mass moment of inertia normalised with respect to the mass moment of inertia, I, is shown.

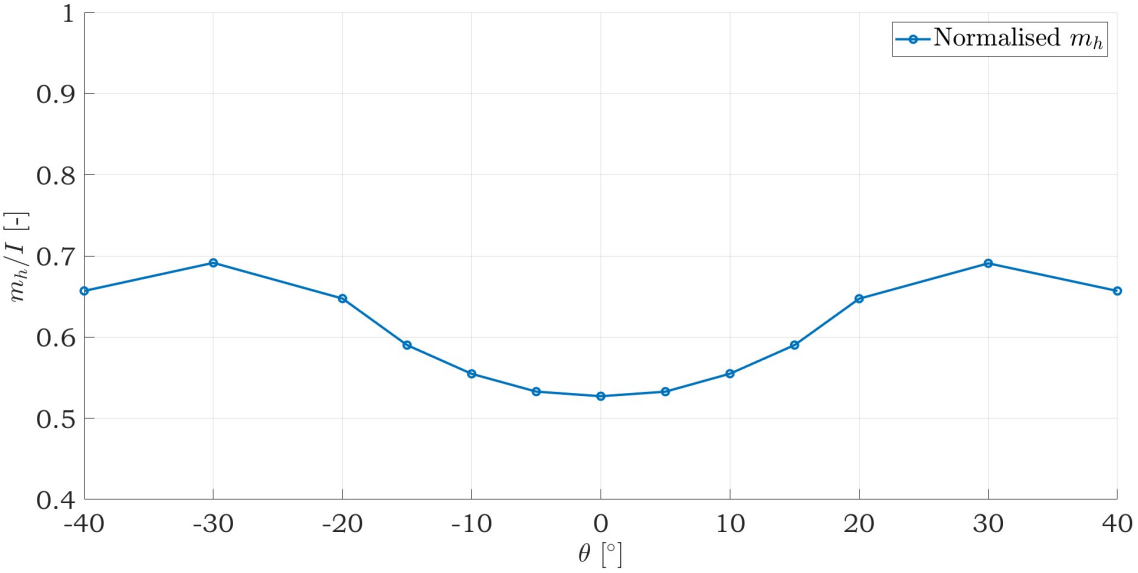

Figure 6.6. Normalised added mass at θ from -40° to 40°.

The damping coefficients are dependent on the wave frequency, which means that the damping changes depending on the sea state. In Figure 6.7 the damping dependent on the wave frequency for the cylindrical floater model at $\theta = 0°$ is plotted along with the values for the five sea states.

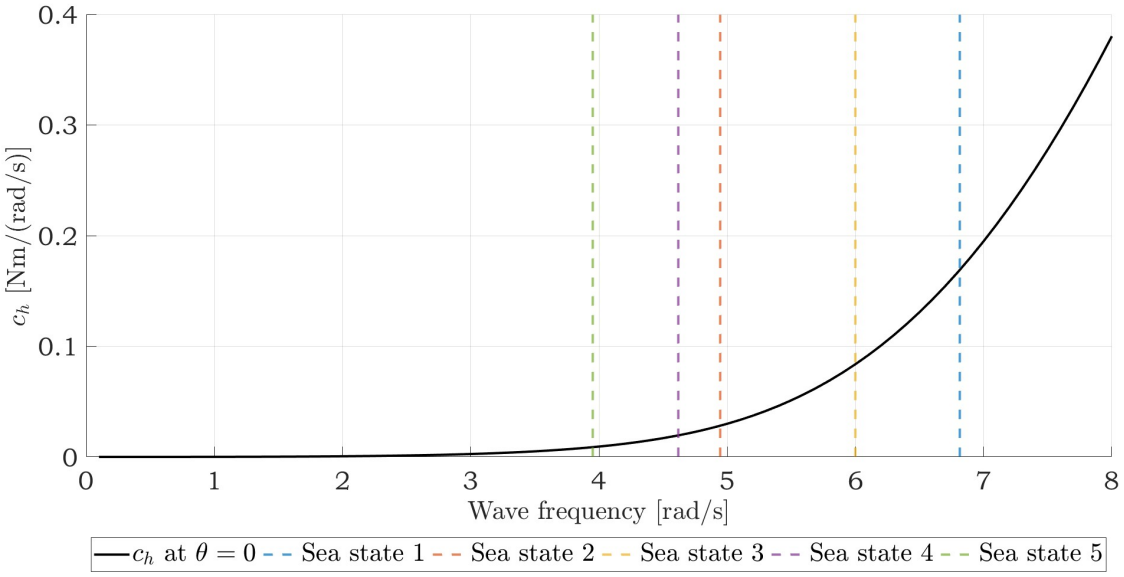

Figure 6.7. Damping coefficients for the cylindrical floater at $\theta = 0°$ with values for the sea states highlighted.

The damping coefficients for the other angular positions are found in the same way. This is shown in Figure 6.8 where it can be seen that the largest damping coefficient is for the smallest sea states.

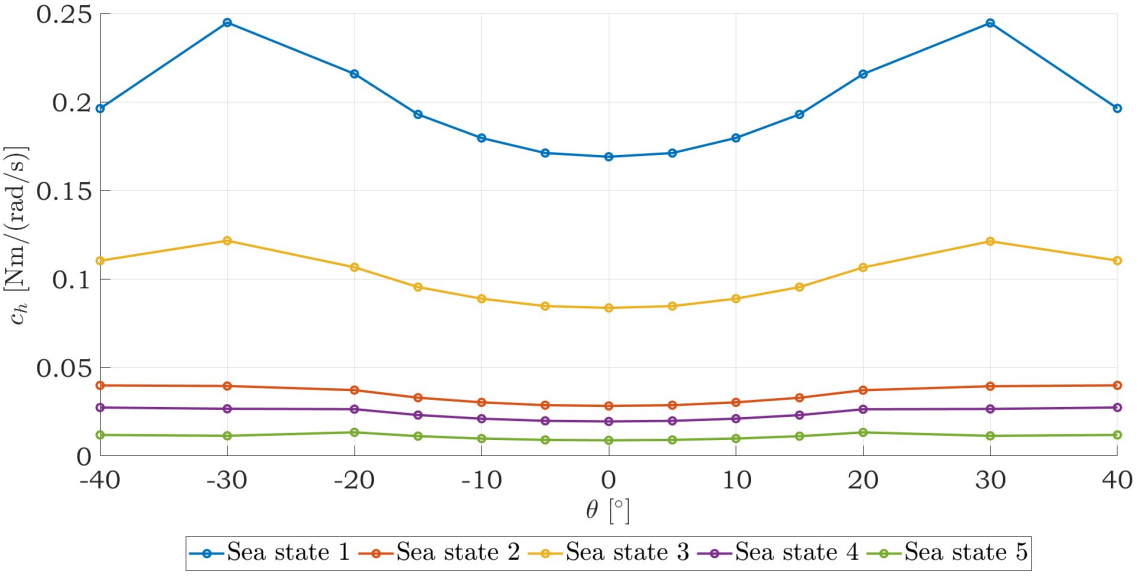

Figure 6.8. Damping coefficients at θ from -40° to 40°.

For both m_h and c_h linear interpolation is used to determine the values corresponding to the actual angular position of the cylindrical floater model.

The wave excitation moment is determined using the results from NEMOH as described for Method 2 in Section 5.3 on page 36. NEMOH outputs a normalised moment and a phase. Like the damping coefficient, the normalised wave excitation moment depends on the wave frequency. In Figure 6.9, this is shown for the cylindrical floater model at $\theta = 0°$ along with the values for the five sea states.

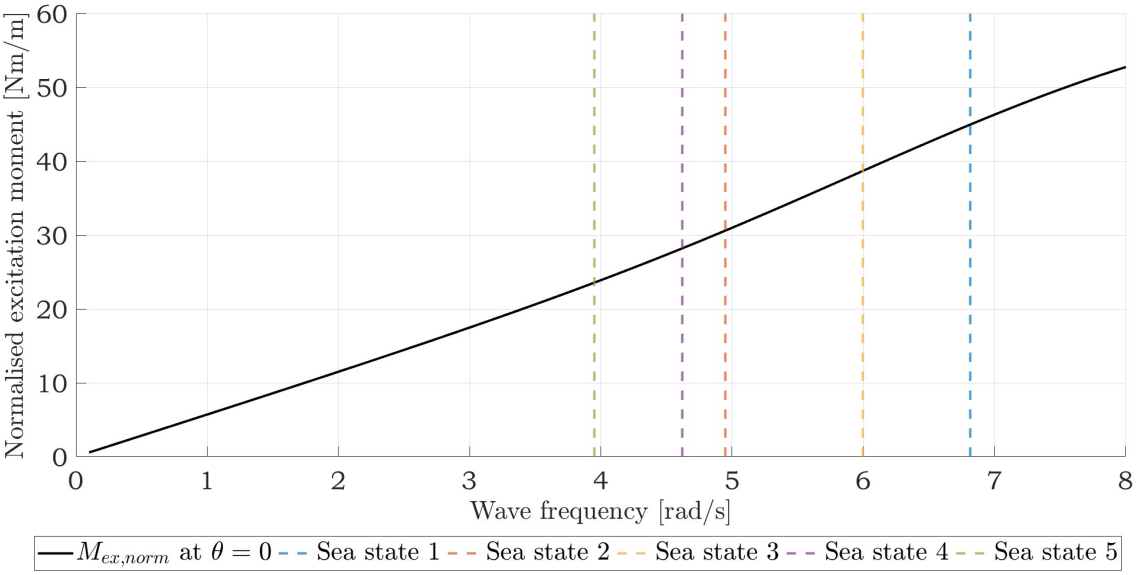

Figure 6.9. Normalised wave excitation moment at $\theta = 0°$ with values for the sea states highlighted.

In Figure 6.10 the normalised moment is shown for the different angular positions.

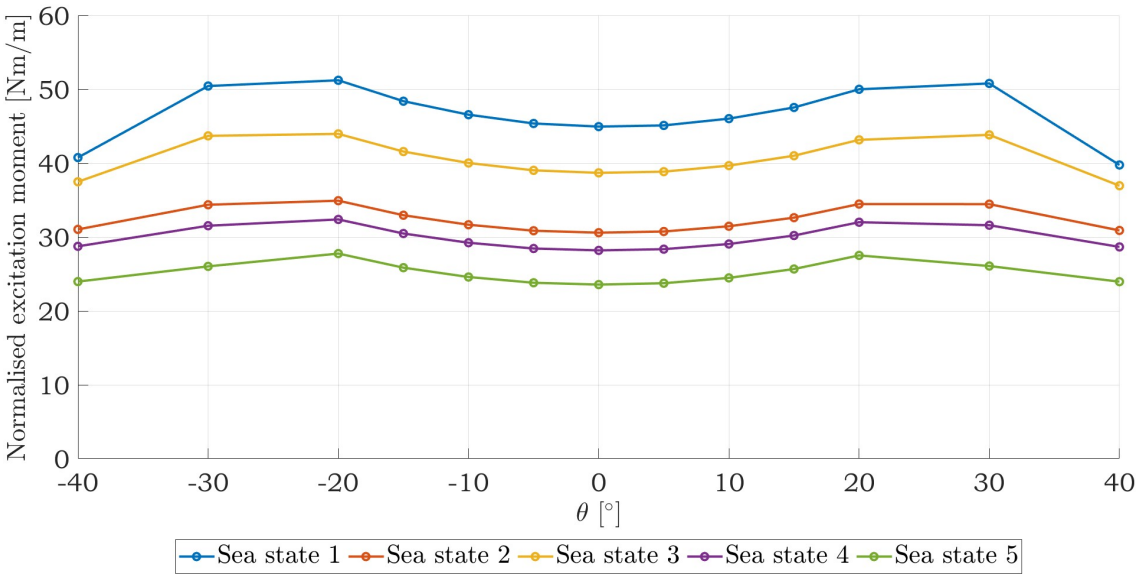

Figure 6.10. Normalised wave excitation moment at θ from -40° to 40°.

The value for the normalised moment corresponding to the angular position of the floater is determined with linear interpolation. The moment at a time step is then determined by multiplying the normalised moment with the water surface elevation and applying a phase shift. The water surface elevation is described using fifth order SFT, despite the assumption of linear wave theory in the BEM.

6.2.3 *NM3* Model

The third numerical model, *NM3*, is a hybrid between the two previously described models. It uses the added mass coefficient from NEMOH as in *NM2* and the same experimental approach from *NM1* to determine the damping coefficient. Like in *NM2* a drag contribution calculated with the Morison equation is used. Again the drag coefficient is set to 0.7.

The wave excitation moment is calculated from the normalised moment output from NEMOH in the same way as in *NM2*.

In Table 6.2 the inputs for the numerical models are summarised.

Model	Hydrostatic moment M_{hs}	Radiation moment M_{rad}	Wave excitation moment M_{ex}
NM1	Nonlinear hydrostatics with dependency on position.	Added mass from Method 1 Experimentally determined damping coefficient.	Moment using Method 1.
NM2	Nonlinear hydrostatics with dependency on position.	Added mass and damping coefficients from NEMOH.	Moment using Method 2 with drag contribution from the Morison equation.
NM3	Nonlinear hydrostatics with dependency on position.	Added mass from NEMOH. Experimentally determined damping coefficient.	Moment using Method 2 with drag contribution from the Morison equation.

Table 6.2. Summary of the inputs to the numerical models.

6.3 Validation of numerical models

To validate the numerical models the results obtained from the numerical models are compared with the results from the experimental investigation. Initially, the numerical models are compared to the decay tests performed on the floater model. Afterwards, it is attempted to validate the numerical models in the case where the cylindrical floater model is subjected to a wave excitation force.

6.3.1 Decay tests

As a first step in the validation of the numerical models, it is sought to describe the motion of the floater during a decay test. In the decay tests the equation of motion simplifies, as shown in Equation (6.4), since the wave excitation moment is zero.

$$I \cdot \ddot{\theta}(t) = M_{rad}(\dot{\theta}, \ddot{\theta}) + M_{hs}(\theta) \tag{6.4}$$

The simplified equation of motion means that a comparison of the results from the numerical models and the experimental decay tests can be used to indicate whether the hydrostatic moment and the radiation moment are accurate.

In Figure 6.11, the results from the numerical models are compared with the mean of the measurements from the decay experiment. The results are normalised with respect to the angular position at the start of the decay test, θ_{0°.

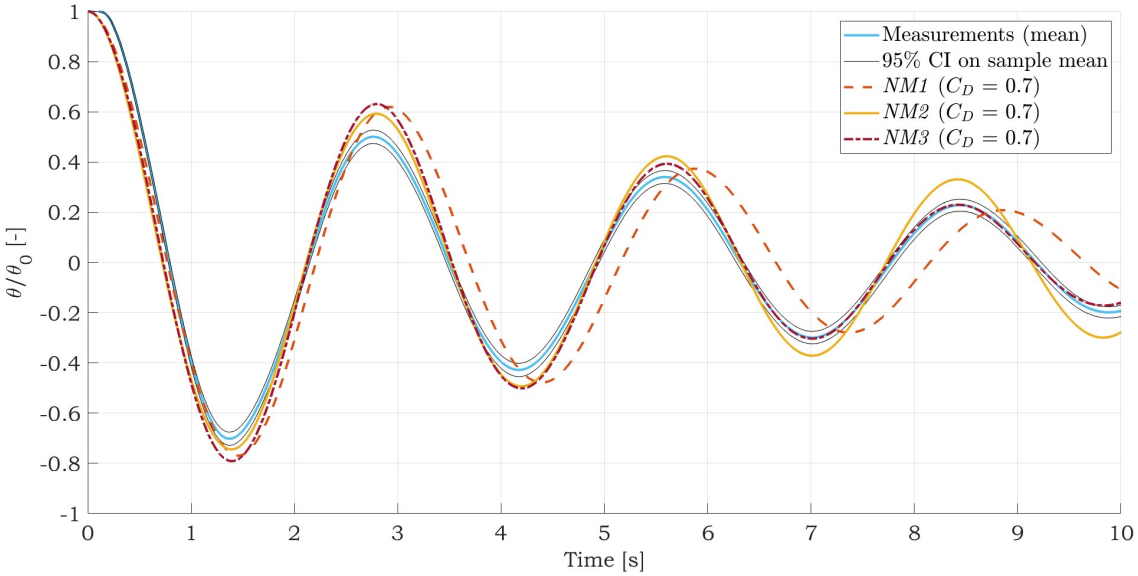

Figure 6.11. Comparison of normalised decay time series for the numerical models and the measured data.

In Figure 6.11, it can be seen that for the *NM1* model, the amplitudes of the oscillations are reasonably accurate however, the period of the oscillation deviates from the measurements. This is possibly caused by the added mass moment of inertia not being calculated with sufficient accuracy. Both *NM2* and *NM3* manage to capture the period of oscillation better than *NM1*. This indicates that the added mass moment of inertia calculated by NEMOH is reasonably accurate. The *NM2* model generally overestimates the motions during the decay test. For *NM3* the motion is overestimated at the first trough and peak. Afterwards, it captures the peaks and troughs with decent accuracy and is mostly within the 95% confidence interval (CI). Generally for all of the numerical models the damping of the oscillations is determined with decent accuracy indicating that both the experimentally determined c_h and the calculated c_h by NEMOH are reasonably accurate when used along with a drag contribution.

Natural frequencies

As part of the decay test on the cylindrical floater model, the natural frequency and period of the cylindrical floater model are examined. By investigating the time between consecutive peaks and consecutive troughs the natural period and frequency are determined. The natural frequency of the cylindrical floater model is 2.23 rad/s and the natural period is 2.82 s.

To examine whether there is a possibility that resonance will occur during the wave excitation tests the natural frequency is compared to the wave frequencies. The wave frequencies are shown in Table 6.3.

Sea state	Wave frequency [rad/s]
1	6.81
2	4.92
3	5.98
4	4.62
5	3.96

Table 6.3. The wave frequencies for the five sea states.

By comparing the wave frequencies and the natural period of the cylindrical floater it is determined that there is little chance of resonance in any of the sea states.

6.3.2 Wave excitation tests

When the floater model is moved because of wave excitation, an additional moment, M_{ex}, is added to the equation of motion as shown in Equation (6.5).

$$I \cdot \ddot{\theta}(t) = M_{ex}(\theta) + M_{rad}(\dot{\theta}, \ddot{\theta}) + M_{hs}(\theta) \tag{6.5}$$

In the following, the results from the numerical models are compared to the measured results from the experiment. Plots are only shown for some sea states. Plots for sea states not shown here can be found in Appendix C on page 117.

In Figure 6.12, the results from the numerical models for sea state 1 are compared to the measured results.

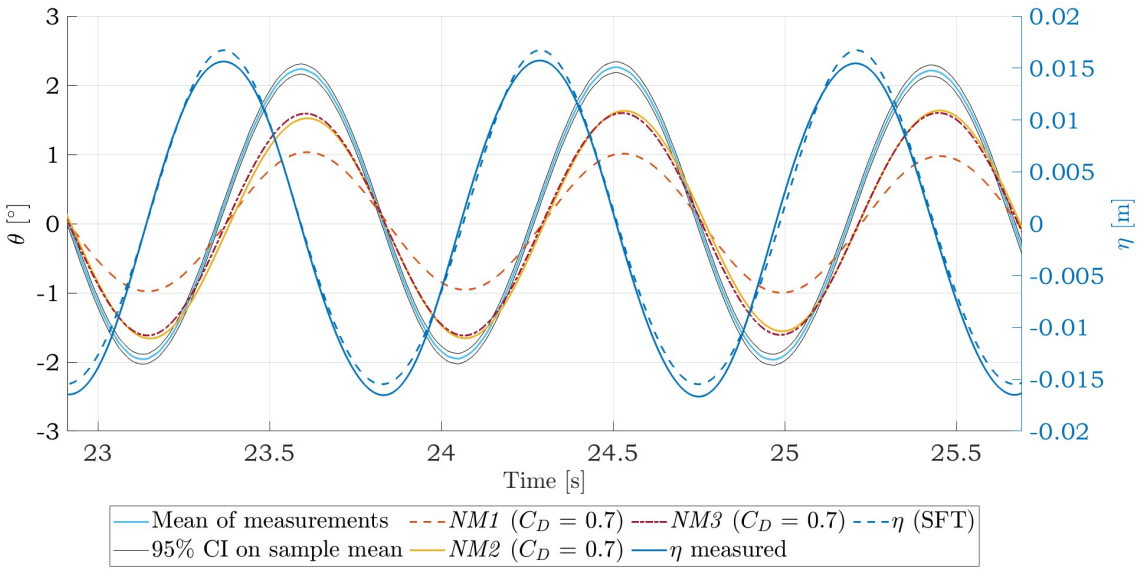

Figure 6.12. Comparison of results from numerical models and measured results for sea state 1.

In the figure, it can be seen that all of the numerical models produce results that are lower than the measured results. The Morison-based numerical model *NM1* in particular results in small rotations in comparison to the measured θ. The numerical models *NM2* and *NM3* give very similar results for θ with both giving results that are slightly underestimated. All

three numerical models result in deviations from the measured values, but it is clear that *NM1* results in the largest deviations by far. A part of this deviation is likely caused by the introduction of relative velocity and acceleration in the Morison equation, which results in a smaller moment around the hinge and thus smaller rotations. In Figure 6.13, the wave excitation moment around the hinge for the three numerical models are compared.

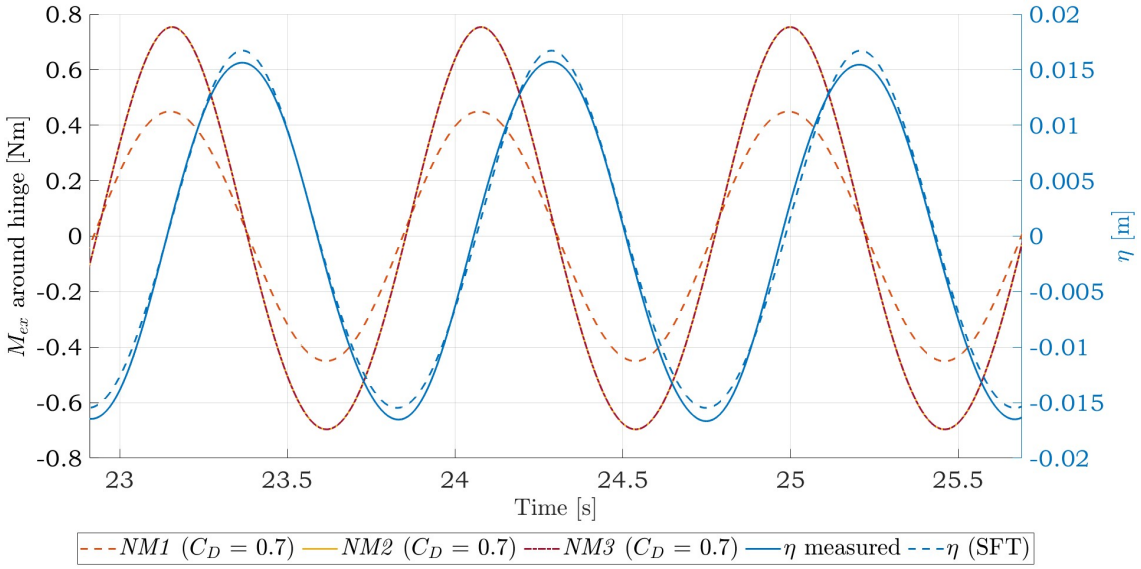

Figure 6.13. Comparison of M_{ex} around hinge for the numerical models for sea state 1. NB the results for *NM2* and *NM3* coincide.

Figure 6.13 clearly shows that *NM1* results in a lower moment around the hinge than the other numerical models. This explains that the θ values from *NM1* are smaller than for the other two numerical models.

In Figure 6.14, the results from the numerical models for sea state 3 are compared to the measured results.

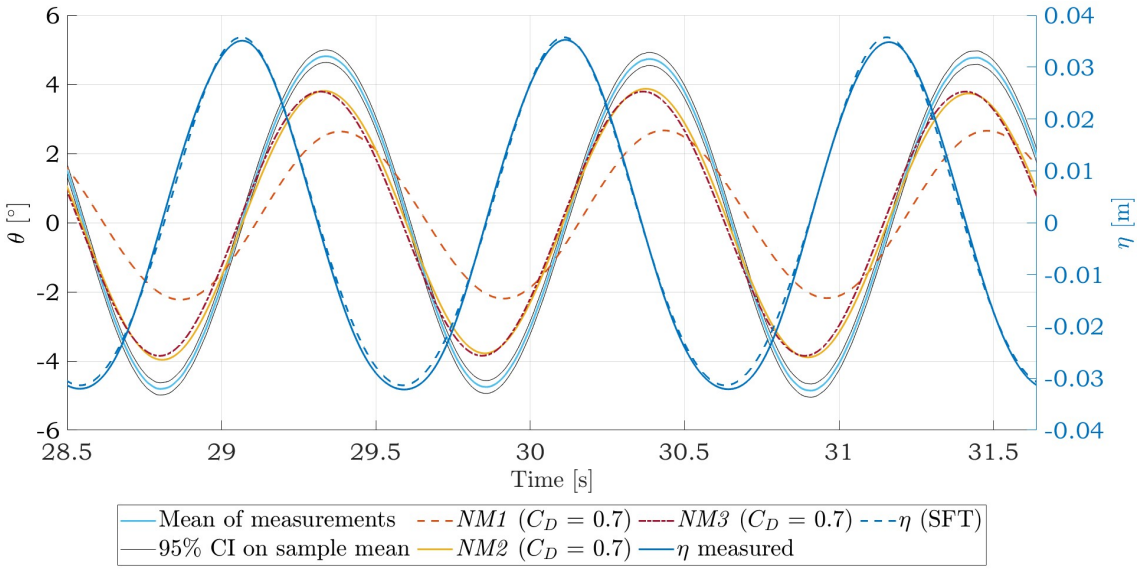

Figure 6.14. Comparison of results from numerical models and measured results for sea state 3.

The same tendencies are seen for sea state 3 with *NM1* resulting in larger deviations than the two other numerical models. For this sea state *NM1* also displays a deviation with regards to the time variation of θ. This deviation is not seen for *NM2* and *NM3* which describe the variation of θ well, although the amplitude is somewhat underestimated.

In Figure 6.15 results from the numerical models for sea state 5 are compared to the measured results.

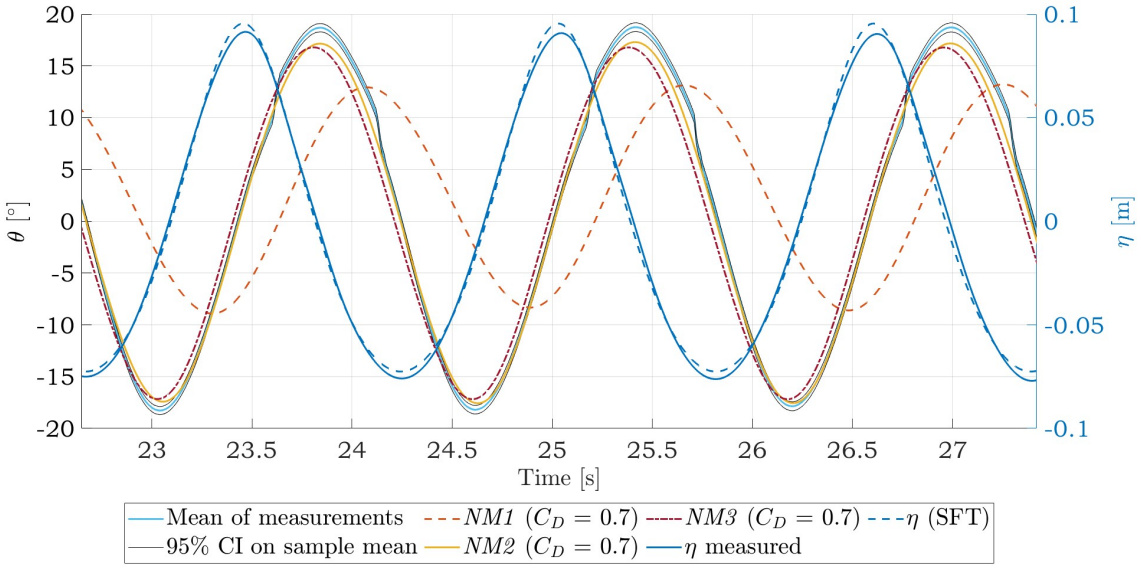

Figure 6.15. Comparison of results from numerical models and measured results for sea state 5.

Again the results show that *NM2* and *NM3* provide a good description of both the time variation of θ and the amplitude of the rotations. The numerical model *NM1* gives large deviations both with respect to the time variation and the amplitude of θ.

6.4 Evaluation of numerical models

In this section, the performances of the three numerical models are evaluated based on the results presented in the previous sections.

Decay test

From the numerical models' description of the decay test, it can be concluded that the added mass output from NEMOH, used in *NM2* and *NM3*, is calculated with sufficient accuracy to describe the period of oscillation of the cylindrical floater model. This indicates that NEMOH correctly describes the fluid-structure interaction. Contrarily, the method used to calculate the added mass in *NM1* does not provide the same accuracy, which results in a slight deviation from the measured results. Furthermore, it can be concluded that both the damping coefficients determined in NEMOH and those determined experimentally provide a good description of the hydrodynamic damping for the cylindrical floater model when used along with a drag contribution.

To compare the performance of the numerical models, the FVUs of θ for the decay test are determined. The FVU for the decay test is calculated for the interval shown in Figure

6.11. For *NM1* the FVU is 0.16 which is significantly higher than for both *NM2* and *NM3*, for which the FVU are 0.04 and 0.03 respectively. The larger FVU for *NM1* is mainly caused by the deviation for the period of oscillation.

Wave excitation tests

Based on the results of the wave excitation tests, it becomes clear that the relative velocity formulation of the Morison equation, used in *NM1*, results in an underestimated moment around the hinge. This leads to smaller rotations than both what is achieved with the other numerical models and what is measured in the experiment. Moreover, as the waves become larger *NM1* results for the rotations which peak later than the measured rotations, which leads to significant deviations for the time variation of θ.

In Figure 6.16, the FVU for θ from the three numerical models are compared.

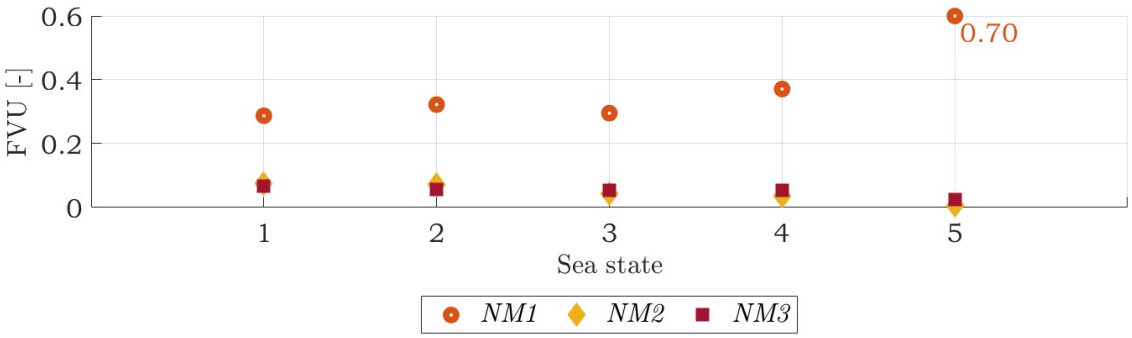

Figure 6.16. FVU for the results for θ from the numerical models.

By comparing the FVU values for the different numerical models it is clear that *NM2* and *NM3* perform the best for all sea states and result in significantly smaller deviations compared to *NM1*. This is true even as the sea states become increasingly steeper. Because of the assumption of linear wave theory in the boundary element method the NEMOH-based numerical models, *NM2* and *NM3*, should theoretically perform worse as the waves become steeper and less linear. However, the two BEM-based models with an included drag contribution manage to describe all of the sea states with reasonable accuracy.

Overall it can be concluded that the BEM-based numerical models with a drag contribution show promise in describing the oscillations of the cylindrical floater model in various sea states. It is now of interest to determine whether the same numerical modelling procedures can be used to describe the wave-structure interaction of a variation of different floater geometries.

Influence of floater geometry

7

Previously, the calculation methods for the force and numerical models for the motions were only investigated for the cylindrical floater model. This chapter examines the validity of using the calculation methods described in Chapter 5 on page 27 and the numerical models described in Chapter 6 on page 49 on the disc-shaped, conical, and spherical floater models. The floater models are downscaled according to the same factor for the cylindrical floater model which is 1:20. The floater models are shown in Figure 7.1.

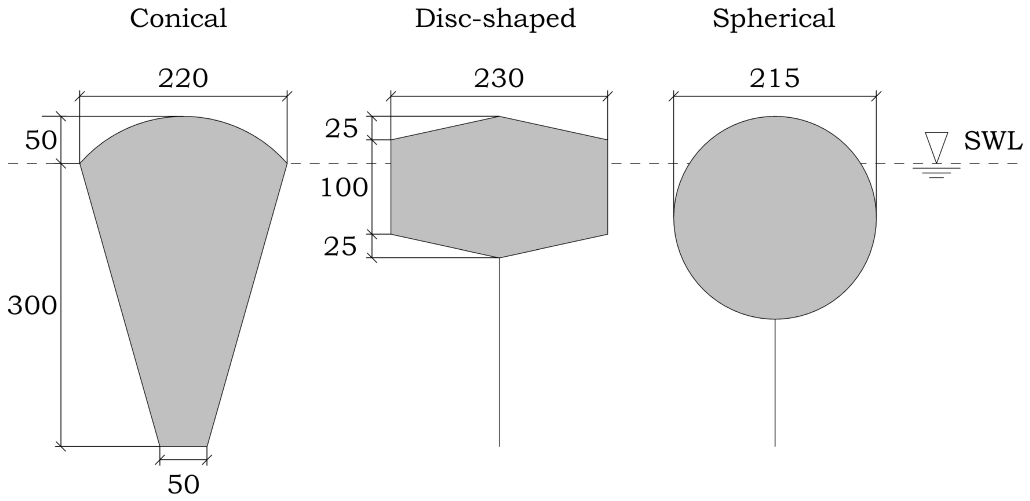

Figure 7.1. Floater models with intended SWL. All measurements are in mm.

The same experiments that are performed on the cylindrical floater model are performed on the three floater models shown in the figure. The forces on these floater models are examined following the procedure described in Section 5.1 on page 27. The floater models are examined in the angles shown in Table 7.1.

	Angle [°]								
Floater model	-40	-30	-20	-10	0	10	20	30	40
Cylindrical	X		X	X	X	X	X		X
Disc-shaped	X	X	X		X		X	X	X
Conical		X	X		X		X	X	
Spherical					X				

Table 7.1. Angles which the forces are measured in.

The spherical floater model is solely investigated in 0° due to the symmetry of the floater model which means that the sectional area does not change as the floater model is tilted. The spherical floater model would become more submerged as the angle becomes larger, but it is assumed to have a small effect. The conical floater model is not investigated in ±40° due to the buoyancy of the floater model. The maximum capacity of the 6-axis force

transducer is reached when the conical floater model is tilted in ±40°.

The motions of the floater models are investigated using the procedure described in 6.1 on page 49. Both decay tests and wave excitation tests are performed on the floater models.

In the following sections, the calculation methods and numerical models are applied to examine the forces and motions of the other floater models.

7.1 Forces on the other floater models

The same calculation methods are applied to the different floater geometries which are Method 1 based on the Morison equation and Method 2 based on the BEM. Method 1 calculates the normal force, F_n, on the floater models the same way as for the cylindrical floater model. This means, that the normal force is calculated normal to the centroidal axis of the floater models. The tangential force due to wave-induced pressure is included for the other floater models as well. The tangential force is calculated based on the same principle, by considering the tangential surface area. Due to the change in geometry for the other floater models, the tangential surface area is calculated along the height of the floater instead of as the top and bottom area as for the cylindrical floater model.

7.1.1 Validation of calculation methods on other floater models

The results from calculation methods and the measured data are plotted in the following figures. In Figures 7.2, 7.3, and 7.4, the measured and calculated forces are shown for the spherical floater model at an angle of 0 °.

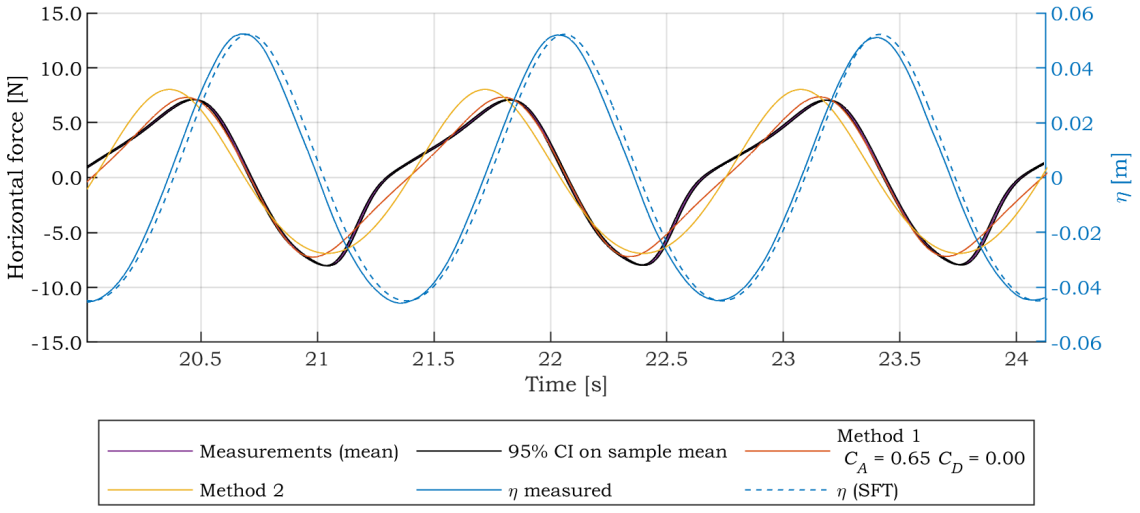

Figure 7.2. Horizontal force over time for the spherical floater model at 0 ° for sea state 4.

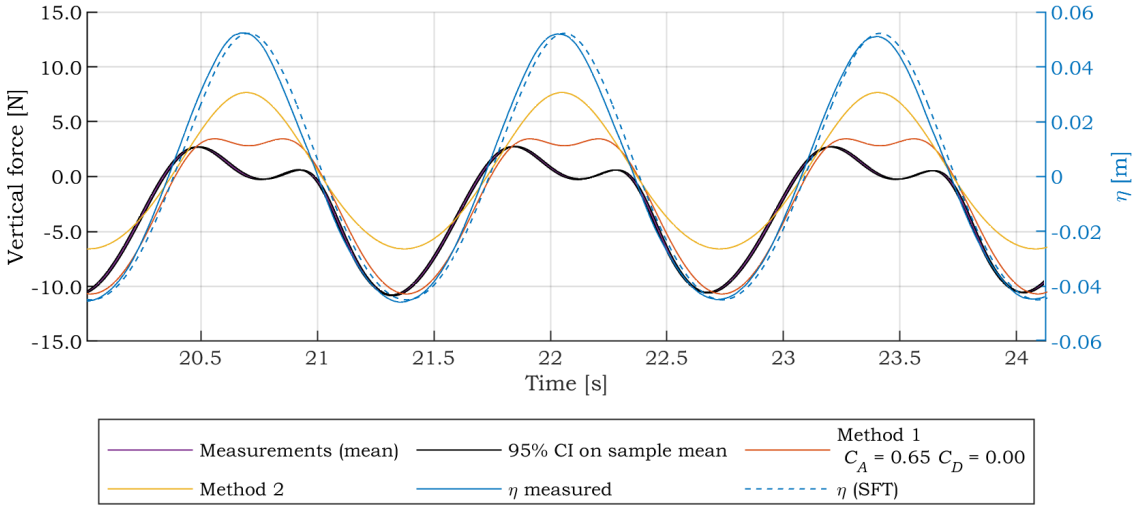

Figure 7.3. Vertical force over time for the spherical floater model at 0 ° for sea state 4.

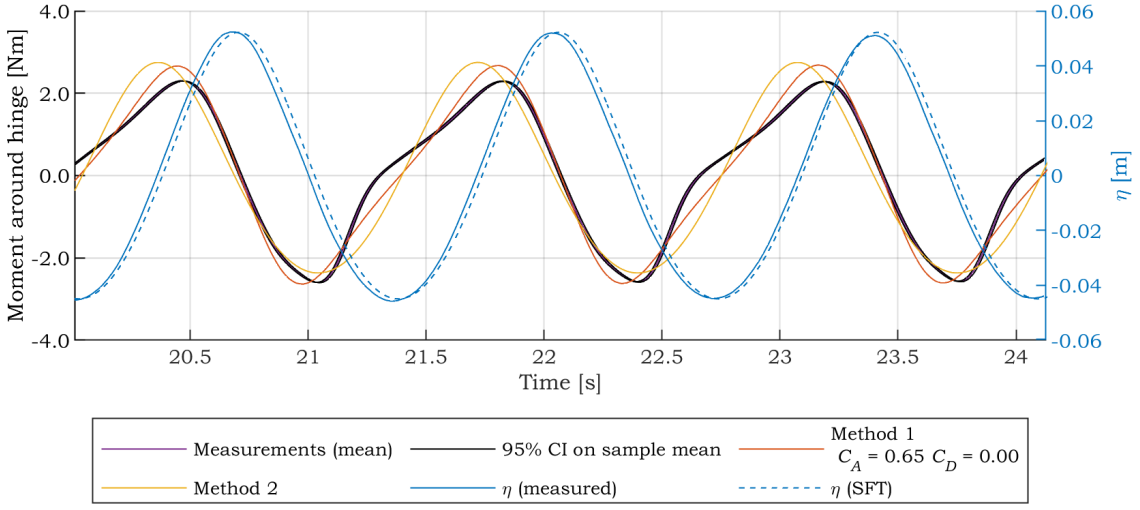

Figure 7.4. Moment around the hinge over time for the spherical floater model at 0 ° for sea state 4.

It shows that the sizes of the horizontal forces are estimated well for both calculation methods, but Method 2 peaks at a different time compared to Method 1 and the measured data. Method 1 is performs better when determining the vertical forces as it can account for overtopping and therefore follows the measured data better than Method 2. Both calculation methods overestimate the size of the moment compared to the measured moment.Method 1 predicts the peak and time variation of the moment better than Method 2. The same observations can be made for the other floater models in 0 °.

In Figures 7.5, 7.6, and 7.7, the calculated and measured forces are shown for the conical floater model at 20 °.

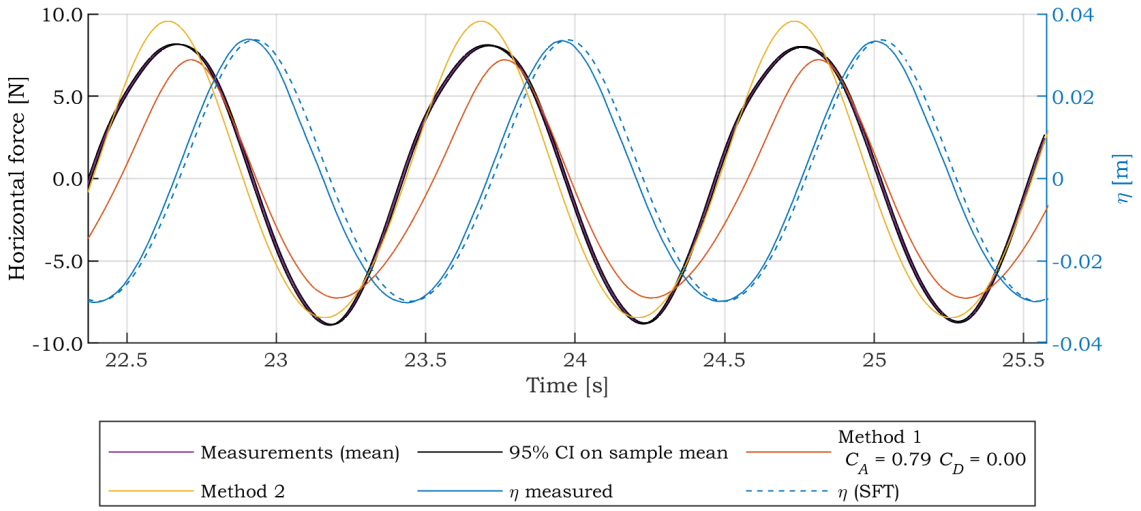

Figure 7.5. Horizontal force over time for the conical floater model at 0 ° for sea state 3.

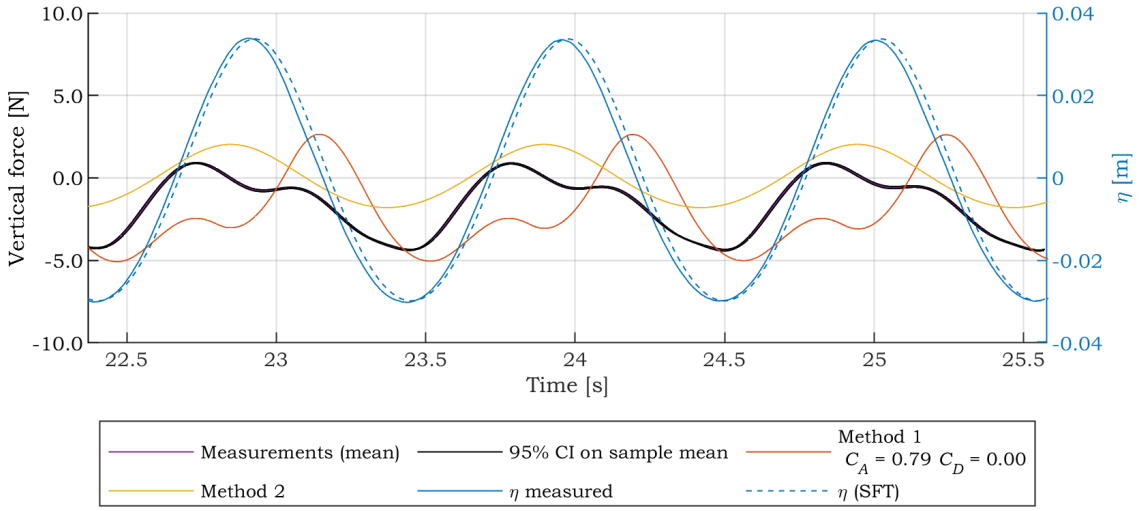

Figure 7.6. Vertical force over time for the conical floater model at 0 ° for sea state 3.

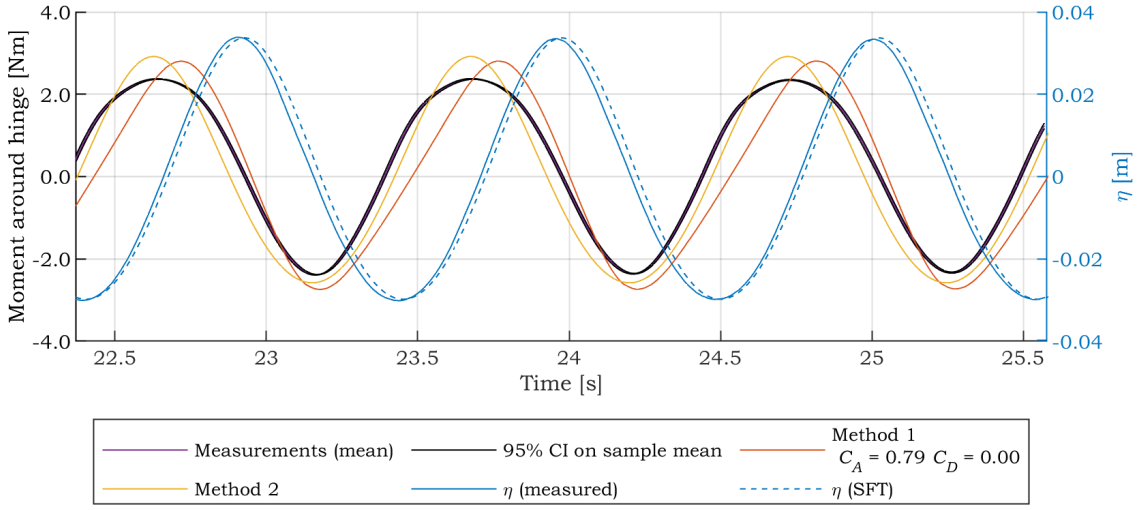

Figure 7.7. Moment around the hinge over time for the conical floater model at 0 ° for sea state 3.

Method 2 gives a better estimate of the horizontal forces, but a small overestimation is seen for the positive peak. Method 1 does not follow the time variation very well and the peaks are slightly underestimated. For the vertical forces, none of the calculation methods follow the data well. Method 2 does not follow it because of the inability to calculate a force on top of the model due to overtopping. Method 1 overestimates the vertical force and peaks at a different time. The moments calculated using the calculation methods show similar tendencies to the horizontal forces. This is because the horizontal force has the largest contribution to the moment around the hinge.

In Figures 7.8, 7.9, and 7.10, the calculated and measured forces for the disc-shaped floater model at an angle of $-20\,°$.

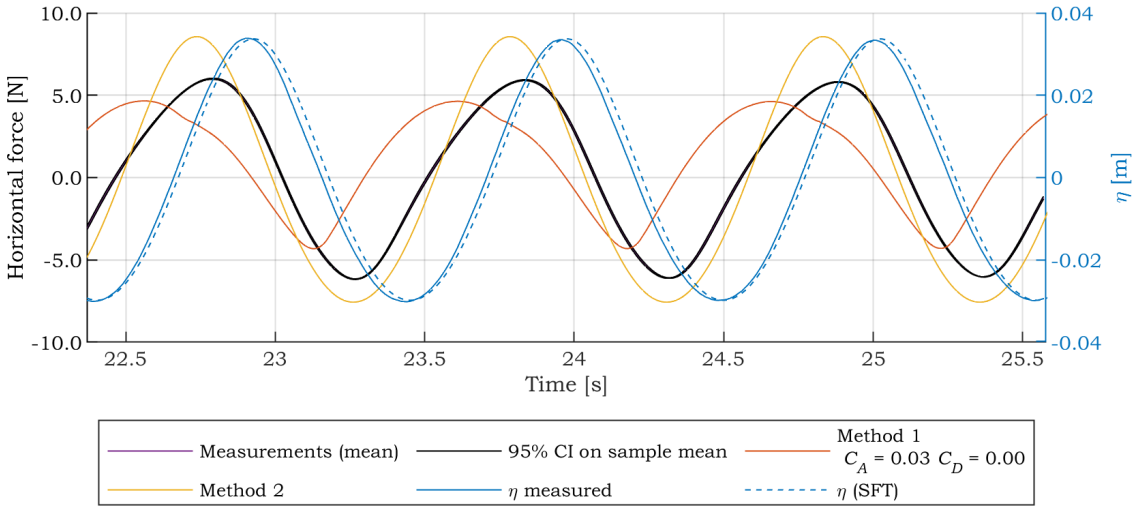

Figure 7.8. Horizontal force over time for the disc-shaped floater model at $-20\,°$ for sea state 3.

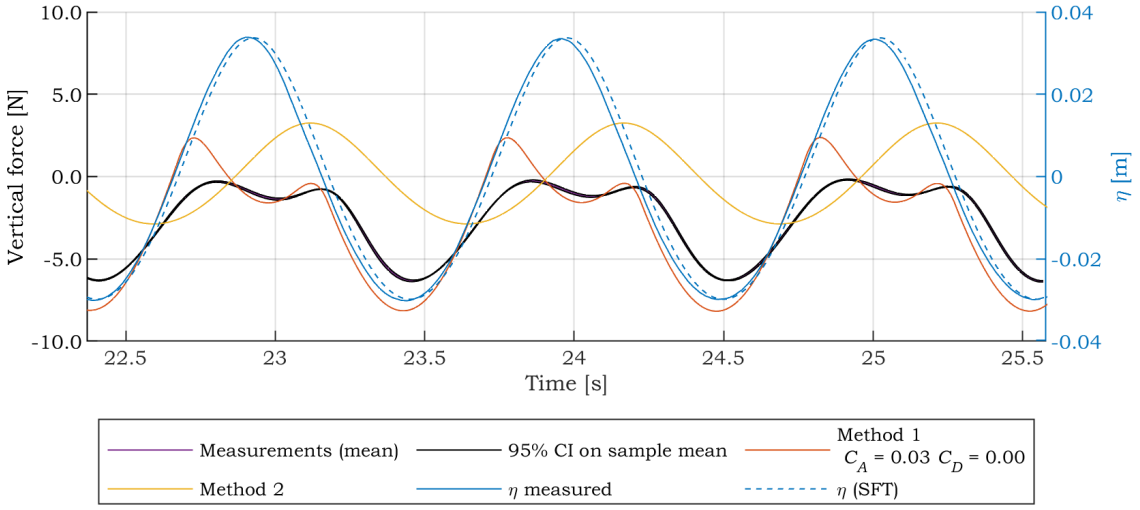

Figure 7.9. Vertical force over time for the disc-shaped floater model at $-20\,°$ for sea state 3.

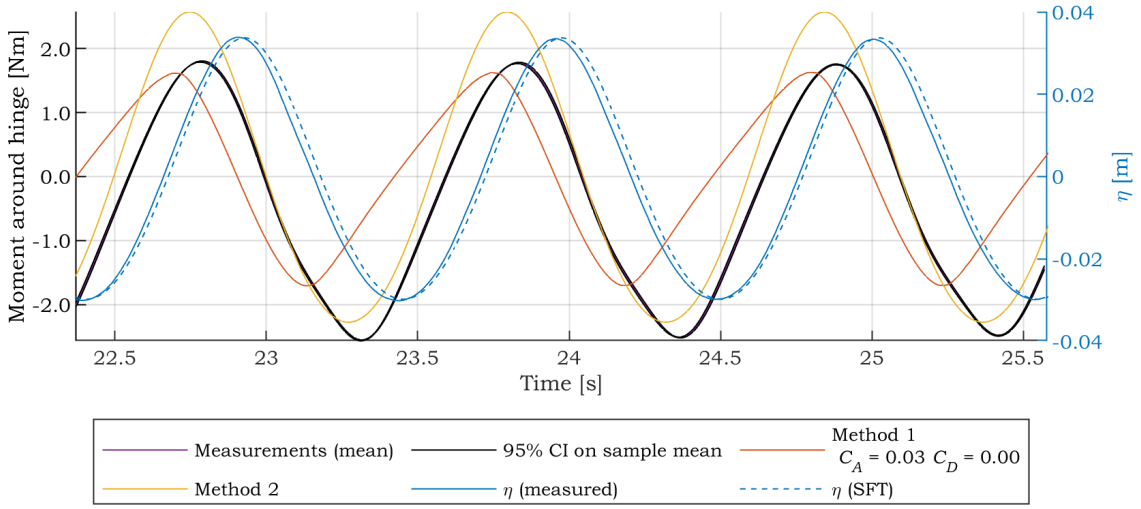

Figure 7.10. Moment around the hinge over time for the disc-shaped floater model at $-20\,^\circ$ for sea state 3.

Method 2 follows the time variation of the measured horizontal force but overestimates the force around the crest and trough. Method 1 does not fit the measured data time variation. This is most likely due to the geometry of the floater model, as the tangential force is only calculated using the change in pressure and does therefore not account for the impact of the waves. For the vertical force, Method 1 estimates the time variation well but overestimates the forces at the peaks. This is due to the structure not affecting the wave in the calculation method compared to the experiment in which the model affected the wave. Method 2 gives a better estimate of the moment around the hinge even though it overestimates the peak.

7.1.2 Evaluation of calculation methods on other floater models

The different calculation methods are compared to the measured data by calculating the FVU of the moment calculation for each sea state, model, and angle. They can be seen plotted in the following figures. Figures 7.11 and 7.12 show the FVU for the conical floater model.

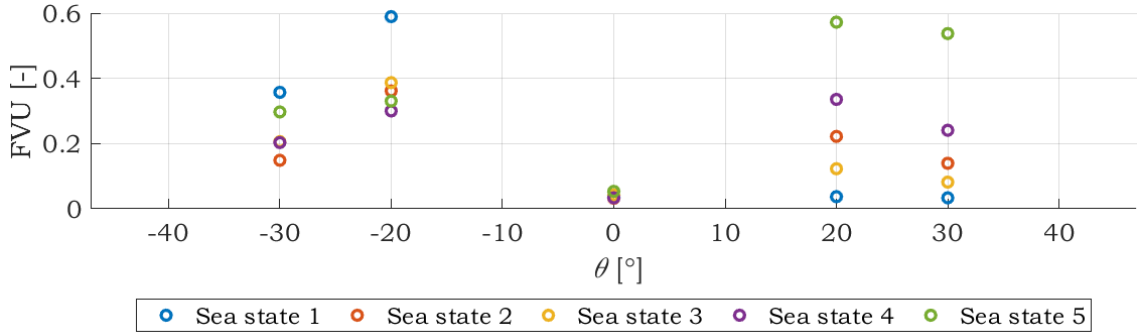

Figure 7.11. FVU for the moment using Method 1 for the conical floater model.

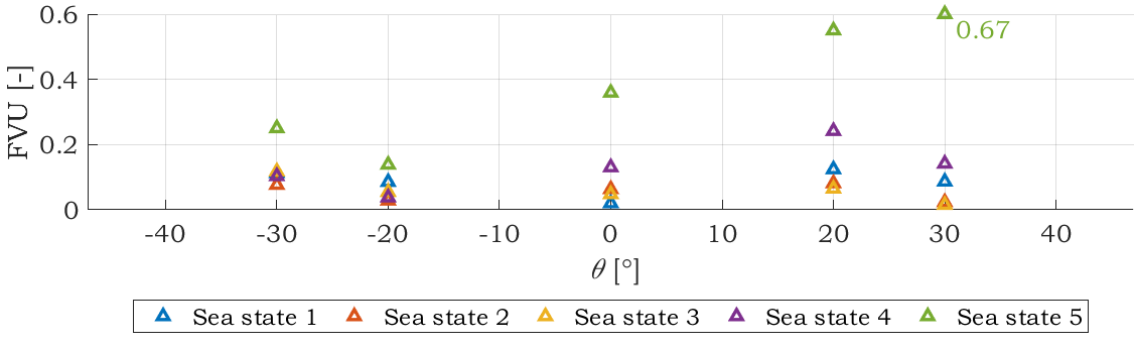

Figure 7.12. FVU for the moment using Method 2 for the conical floater model.

The FVU results for the conical floater model show similar tendencies to the FVU results for the cylindrical floater model. Method 1 at 0 ° is still very accurate for the conical floater model. Comparing the FVU results for the two floater models in 20 ° it can be seen that the accuracy of Method 1 becomes more inaccurate in most sea states when using the conical floater model compared to the cylindrical floater model. Method 2 maintains a similar level of accuracy for the conical floater model compared to the cylindrical floater model. It predicts the moments quite well except for sea state 5 which as with the cylindrical floater results in larger deviations.

Figures 7.13 and 7.14 show the FVU results for the disc-shaped floater model.

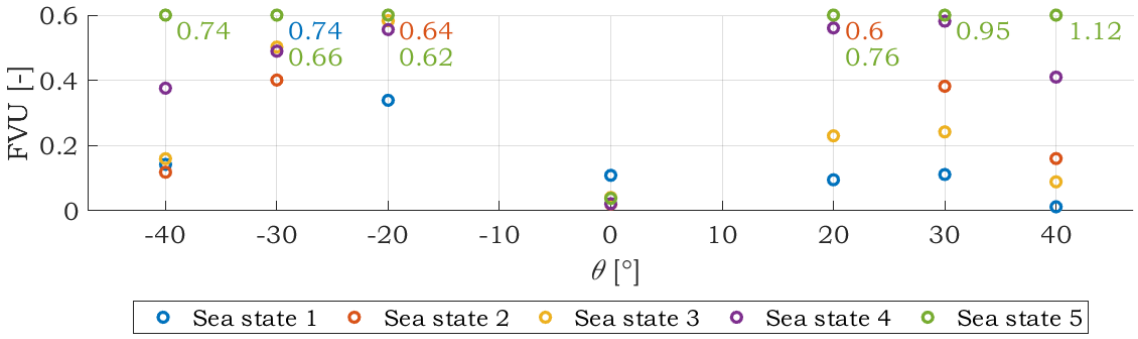

Figure 7.13. FVU for the moment using Method 1 for the disc-shaped floater model.

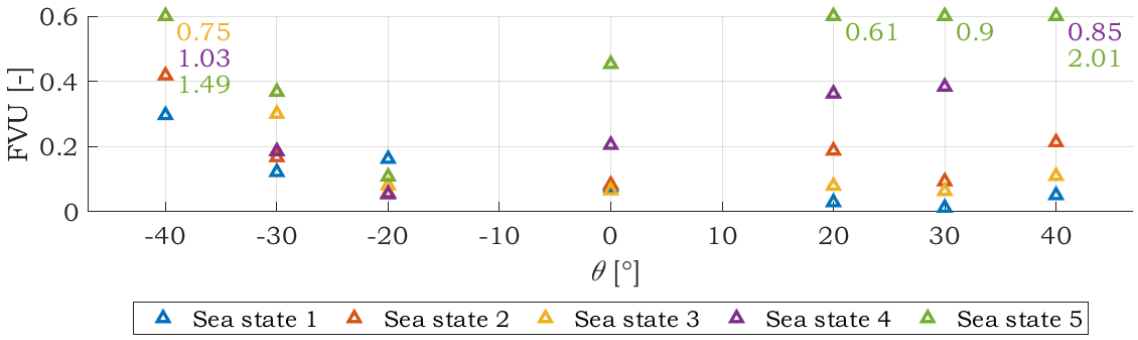

Figure 7.14. FVU for the moment using Method 2 for the disc-shaped floater model.

The results for the disc-shaped floater generally display larger deviations from the measured

results. When multiple markers are above the limit they are drawn at the limit and their value is written to the right in the colour of the sea state. The FVU shows that the accuracy when the floater model is at an angle of 0° is great for Method 1. Except for this using Method 1 on the disc-shaped instead of the cylindrical floater model gives more inaccurate results for most sea states and angles. The results are especially inaccurate for the negative angles which is possibly because Method 1 does not accurately calculate the tangential force on the model.

The tendencies for Method 2 are the same for the cylindrical and disc-shaped floater model in the interval between −20° and 20° for sea states 1, 2, and 3. For sea states 4 and 5, the results for the disc-shaped floater model show larger deviations from the measurements. This is especially evident in the large angles ±40 where Method 2 does not accurately describe the moment.

Figures 7.15 and 7.16 show the FVU results for the spherical floater model.

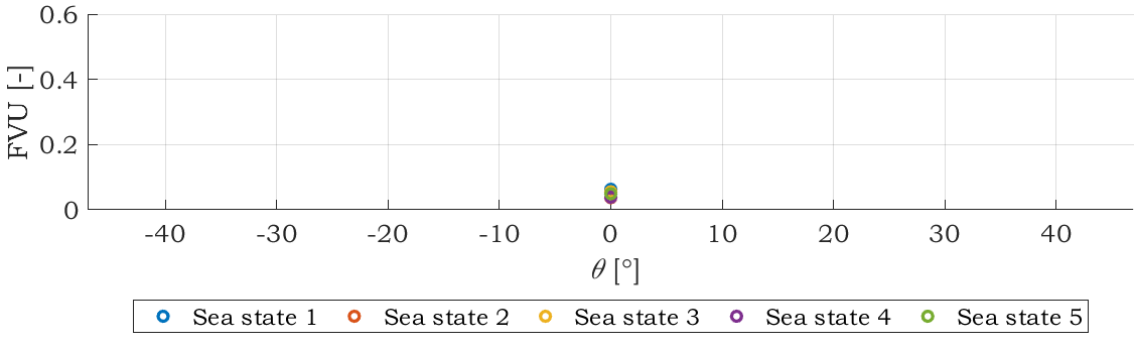

Figure 7.15. FVU for the moment using Method 1 for the spherical floater model.

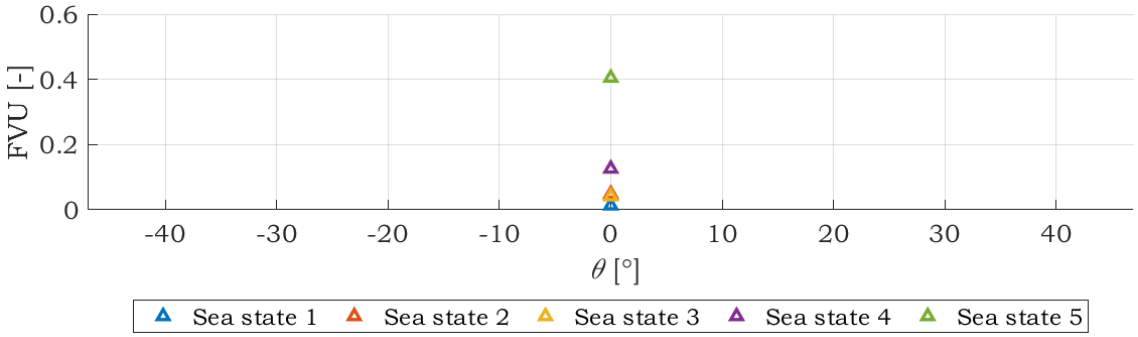

Figure 7.16. FVU for the moment using Method 2 for the spherical floater model.

The spherical floater model is only tested at an angle of 0°. The FVU results for Method 1 show that it can accurately predict the moment around the hinge for the spherical floater model. For the spherical floater model, Method 2 gives reasonably accurate results except for sea state 5, where a larger deviation is observed.

In general, the results for Method 1 show an accurate prediction of the forces at 0° for all of the floater models. As the floater models are placed at an angle the results show that Method 1 becomes less accurate. Method 1 uses the correct wave kinematics when determining the wave forces on the floater models. Nonetheless, the results for sea states

4 and 5 show larger deviations from the measured results. This is possibly caused by a larger drag contribution in sea states 4 and 5 which is not considered in the calculations for Method 1 on the fixed floater models. The results from Method 1 illustrate the complexity and difficulty of describing the wave-structure interaction using a Morison-based method when the geometry is changed from cylindrical to more irregular shapes. These difficulties become more evident as the floater models are angled.

The results for Method 2 show similar tendencies for the different floater models. The results are more accurate for sea states 1, 2, and 3 and less accurate for sea states 4 and 5. This is likely due to the assumption of linear wave theory used in the BEM. The results show that Method 2 is more consistent in determining the wave forces in an angled position. This is because Method 2 captures the wave-structure interaction correctly.

Comparing the two calculation methods shows that the accuracy of Method 2 is better when applied to the other floater models placed at an angle. Method 1 gives more accurate results for the floater models at an angle of $0\,^{\circ}$.

In the following section, the calculation methods applied in this section will be used in the numerical models to predict the motions of the other floater models.

7.2 Motions of the other floater models

To examine the motions of the other floater models, the same three numerical models that are described in Section 6.2 on page 51 are used. In the following, the inputs for the numerical models are described.

In order to calculate a drag contribution in the numerical models it is necessary to determine the drag coefficients for the floater models. The drag coefficient for a sphere is well established and can therefore be determined from literature with knowledge of the flow conditions. The Reynolds number for the sphere in the five sea states ranges from $Re \approx 2 \cdot 10^4$ to $9 \cdot 10^4$. Considering this the drag coefficient for the spherical floater model is determined as 0.5. [Schlichting and Gersten, 2017]

The drag coefficients for the conical and disc-shaped floater models are not well established in literature, which complicates the determination of the drag coefficients. However, in Iversen et al. [2023] numerical tests were performed using the CFD framework OpenFOAM in order to determine the drag coefficient of similarly shaped conical frustums with the results that a drag coefficient of 0.8 should be used. Therefore, a drag coefficient of 0.8 is used for the conical floater model.

For the disc-shaped floater model, the drag coefficient is determined using a rough estimate by simplifying the geometry of the floater. The shape of the disc is simplified into an ellipse, and considering the height and width of the ellipse it is determined that the drag coefficient is in the interval 0.6 - 1.0 [DNV GL, 2017]. Because the actual floater geometry has sharp edges, which the simplified elliptical geometry does not have, it is chosen to use a drag coefficient of 1.0 for the disc-shaped floater.

In Table 7.2 parameters that are used in the numerical models are summarised. The mass moment of inertia for the floater models are determined in Appendix C.2 on page 120.

Floater model	I [kg · m^2]	m [kg]	r_g [m]	C_D [-]
Conical	0.39	1.23	0.35	0.8
Disc-shaped	0.34	1.08	0.39	1.0
Spherical	0.33	1.12	0.35	0.5

Table 7.2. Overview of parameters used in the numerical models.

The inputs of the added mass, damping, and wave excitation moment are determined in the same way as described in Section 6.2 on page 51 for the cylindrical floater model. Therefore, it is not repeated here but can instead be found in Appendix C.5 on page 126. The NEMOH calculations for the disc-shaped, conical, and spherical floater models are performed with 10 ° increments in the interval from −40 ° to 40 °.

7.2.1 Decay tests on other floater geometries

As an initial step in the validation of the numerical models for the other floater models, it is attempted to describe the motions of the floater during a decay test. In Figure 7.17, the results from the numerical models are compared to the measured results for the decay test on the conical floater.

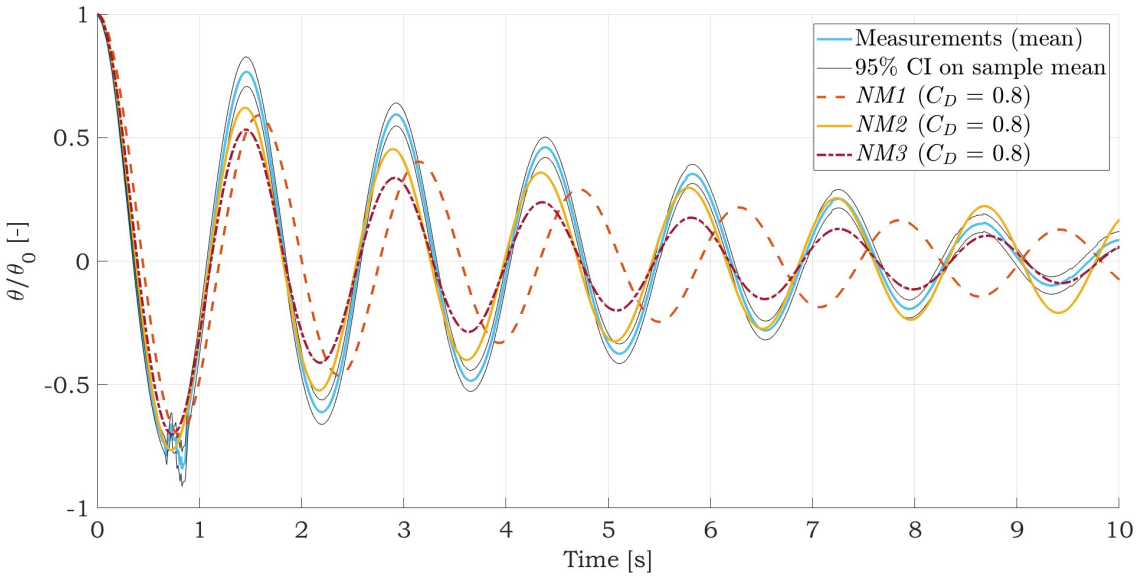

Figure 7.17. Comparison of normalised decay time series for the conical floater.

For the conical floater both *NM2* and *NM3* follow the period of oscillation with good accuracy, indicating that the added mass moment of inertia from NEMOH is accurate. The added mass moment of inertia, m_h, calculated from added mass coefficients, which is used in *NM1* does not accurately describe the period of oscillation. Both the damping from NEMOH and the experimentally determined damping are slightly overestimated, however the damping coefficients from NEMOH results in a better description of the decay time series.

In Figure 7.18, the results from the numerical models are compared to the measured results for the decay test on the disc-shaped floater.

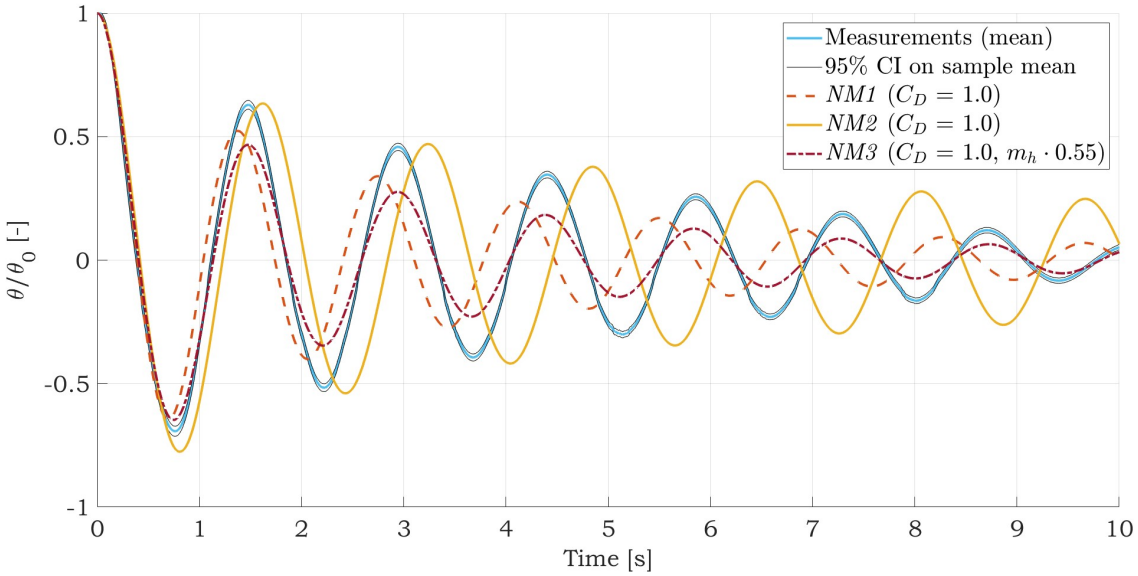

Figure 7.18. Comparison of normalised decay time series for the disc-shaped floater.

In the figure, it can be seen that the numerical models *NM1* and *NM2* do not accurately describe the period of the oscillations during the decay test. This indicates that the added mass moment of inertia used in these two numerical models is not correct. Because of this, it is chosen to alter the added mass coefficients from NEMOH in *NM3* to provide a better description of the period of oscillations. This is done iteratively and it is determined that a 45 % reduction of m_h results in a better description of the period of oscillation. The damping of the oscillations is determined with reasonable accuracy for *NM2*, especially at the beginning of the decay time series. For both *NM1* and *NM3* the damping is overestimated, which leads to an underestimation of the motions. This indicates that the experimentally determined damping is too high.

In Figure 7.19, the results for the decay test on the spherical floater are compared to the measured results.

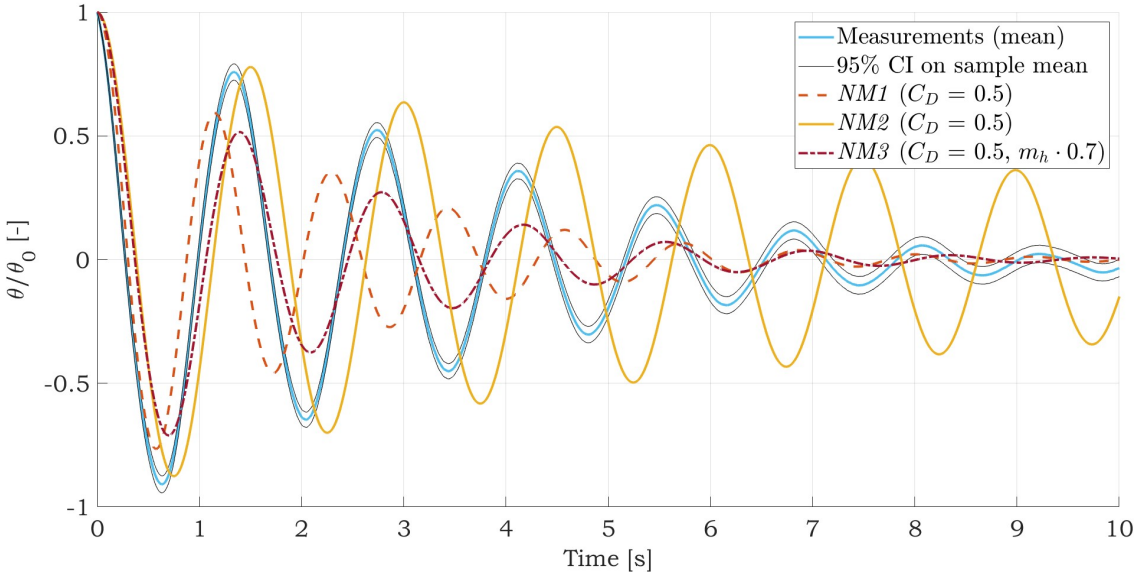

Figure 7.19. Comparison of normalised decay time series for the spherical floater model.

Similarly, the results for the disc-shaped floater *NM1* and *NM2* have trouble describing the period of oscillation for the spherical floater model. Again it is chosen to reduce m_h in the third numerical model *NM3*. This time a reduction of 30 % is used.

Neither the damping from NEMOH nor the experimentally determined damping results in a good description of the damping observed in the measured decay test. For *NM2* the damping is too low. This is especially evident towards the end of the interval shown in Figure 7.19 where the results from *NM2* keep oscillating when the measured oscillations have nearly stopped. For *NM1* and *NM3*, which use experimentally determined damping, the damping is instead too high and the oscillations stop before the measured oscillations.

Natural frequencies

As part of the decay tests on the floater models, the natural frequencies of the floater models are examined. The natural frequencies are determined from the time difference between consecutive peaks and consecutive troughs in the decay time series. In Figure 7.20 an example with highlighted peaks and troughs is shown.

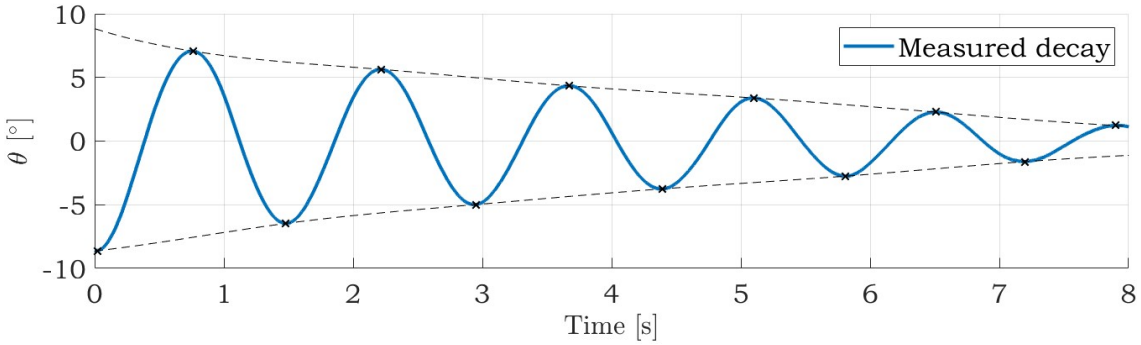

Figure 7.20. Decay time series for conical model.

The natural frequencies and periods for the floaters are then determined as a mean value for the five decay tests. The natural frequencies and periods for the floater models are shown in Table 7.3.

Floater model	Natural frequency [rad/s]	Natural period [s]
Conical	4.37	1.44
Disc-shaped	4.32	1.45
Spherical	4.56	1.38

Table 7.3. Natural frequencies for the floater models.

The natural frequency is especially relevant when compared to the frequency of the waves since resonance can occur if these frequencies are close to each other. In Figure 7.21 the natural frequencies of the floater models are compared with the frequencies of the waves in the five sea states.

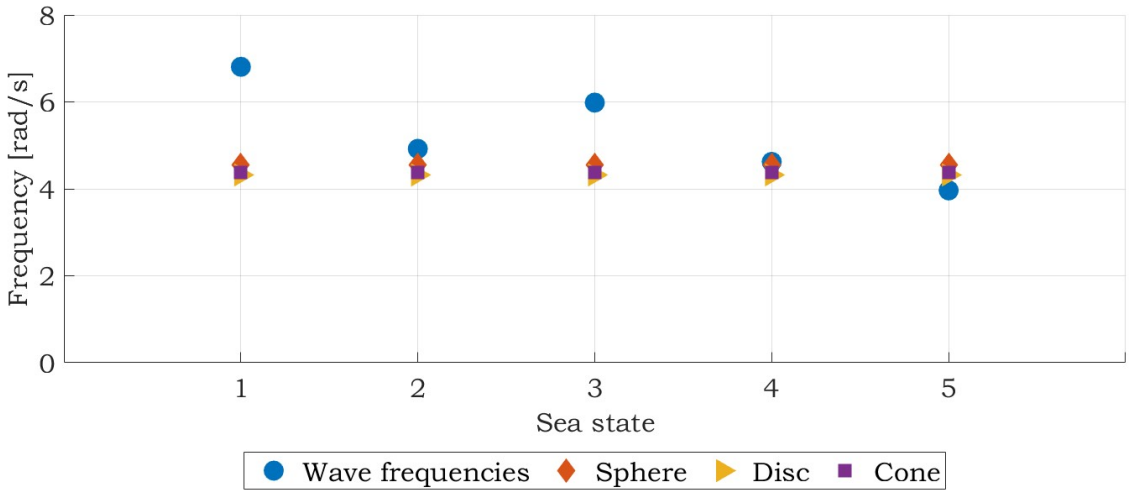

Figure 7.21. Comparison of wave frequencies and natural frequencies of floater models.

As can be seen in the figure, the natural frequencies of the floater models are close to the wave frequency in three of the sea states. In sea states 2 and 4 the natural frequency of the three floater models are especially close to the wave frequency. Because of this, there is a possibility that resonance will occur during the wave excitation tests, which will cause an increase in the motion of the floater.

7.2.2 Wave excitation tests on other floater geometries

In the following section, the results from the numerical models for the wave excitation tests on the spherical, conical, and disc-shaped floater models are presented and compared to the measured results. Only some of the results are shown in this section, however all of them can be found in Appendix C.6 on page 137.

In Figure 7.22, the results for the disc-shaped floater in sea state 1 are shown.

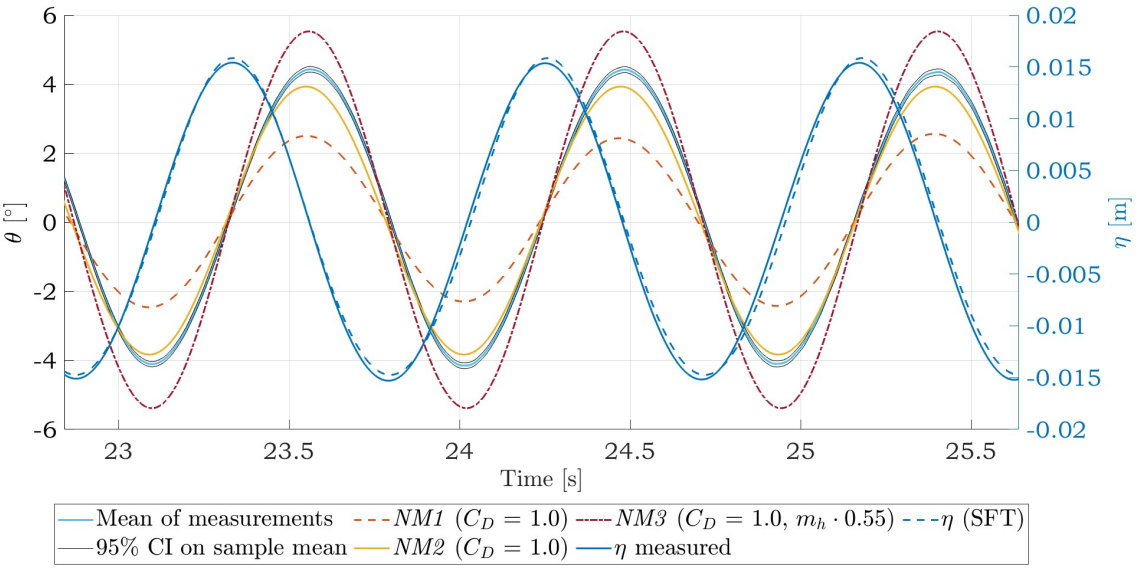

Figure 7.22. Comparison of results from numerical models and measured results for the disc-shaped floater in sea state 1.

In the figure, it can be seen that *NM1* underestimates the motions of the floater similarly to what was observed for the cylindrical floater in 6.3.2 on page 59. The same tendency is observed for the conical and spherical floaters in sea state 1. *NM2* provides a good description of the motions of the disc-shaped floater only slightly underestimating the maximum and minimum values of the rotations. For the conical and spherical floater in sea state 1, *NM2* also shows good agreement with the measured results. The third numerical model *NM3* overestimates the motions of both the disc-shaped and spherical floater. This is possibly caused by the reduction of the added mass to fit the period of oscillation in the decay tests for these two floaters.

In Figure 7.23, the results for the conical floater model in sea state 2 are shown.

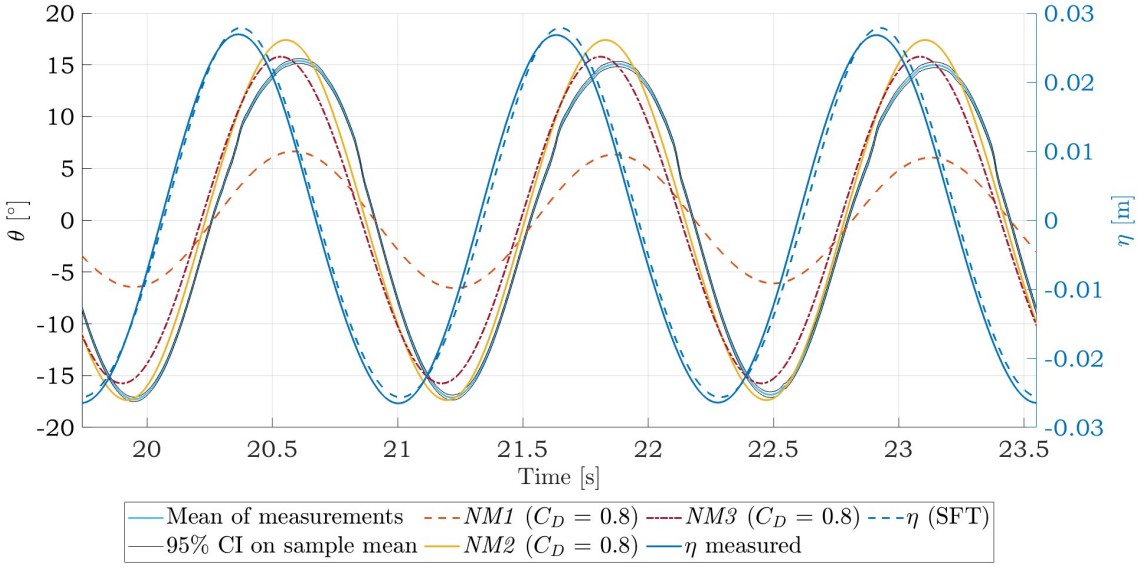

Figure 7.23. Comparison of results from numerical models and measured results for the conical floater in sea state 2.

For the conical floater in sea state 2, the first numerical model *NM1* again underestimates the movements. *NM1* also does not give usable results for the disc-shaped and spherical floater in sea state 2. *NM2* gives good results for the motions of the conical floater in sea state 2, although a slight overestimation of the peak rotation is seen. For the spherical floater model, the same tendency is seen with *NM2* giving a slight overestimation at the peak. For the disc-shaped floater in sea state 2 *NM2* underestimates the motions somewhat, but regardless of the floater geometry *NM2* gives useful results. *NM3* also gives good results for the conical floater, however for the disc-shaped and spherical floater these numerical models result in a small phase shift compared to the measured results.

It is observed that large motions are observed for this sea state especially considering the relatively low wave height. This is likely caused by resonance since the natural frequencies of all three floater models are close to the wave frequency for sea state 2.

In Figure 7.24, the results for sea state 3 for the spherical floater are shown.

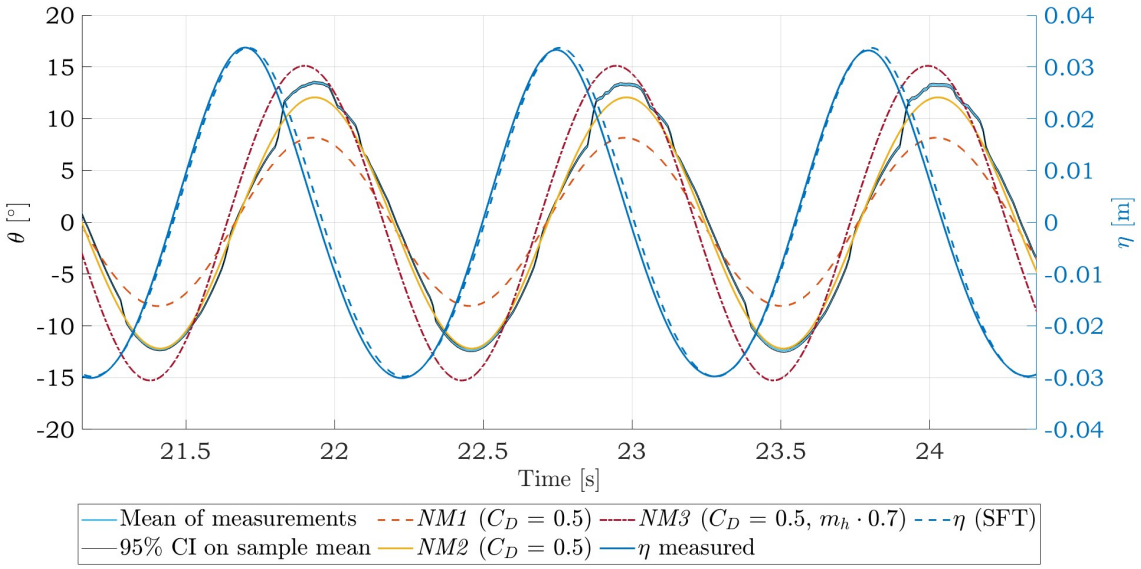

Figure 7.24. Comparison of results from numerical models and measured results for the spherical floater in sea state 3.

In sea state 3 similar results to sea state 1 and 2 are achieved. *NM1* underestimates the motions for all three floater geometries. *NM2* describes the motions of all three floaters well in sea state 3, although it slightly underestimates the motions for the disc-shaped floater. *NM3* also gives decent descriptions of the floaters' motions however slight overestimation is observed for both the disc-shaped and spherical floaters.

In Figure 7.25, the results for the conical floater in sea state 4 are shown.

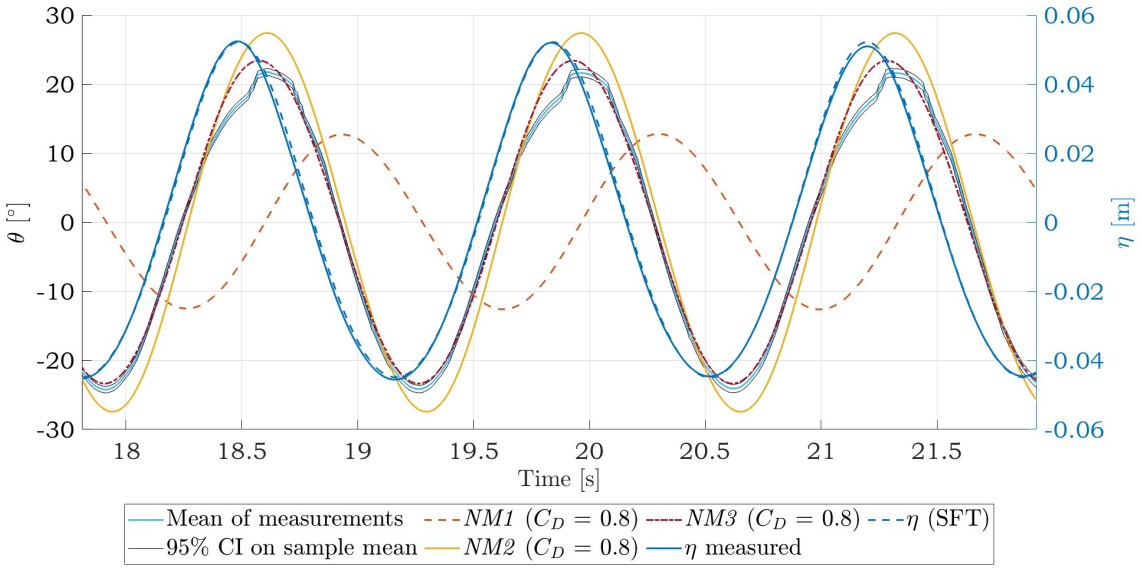

Figure 7.25. Comparison of results from numerical models and measured results for the conical floater in sea state 4.

For sea state 4 *NM2* still provides reasonable results for the conical and disc-shaped floater, even though the motions are somewhat overestimated. However, for the spherical floater, a large overestimation of the motions is seen along with a phase shift. This results in a large

deviation from the measured results for the spherical floater when using *NM2*. The third numerical model *NM3* provides similar results as *NM2* for the conical and disc-shaped floater and better results for the spherical floater.

In Figure 7.26, the results for the disc-shaped floater model in sea state 5 are shown.

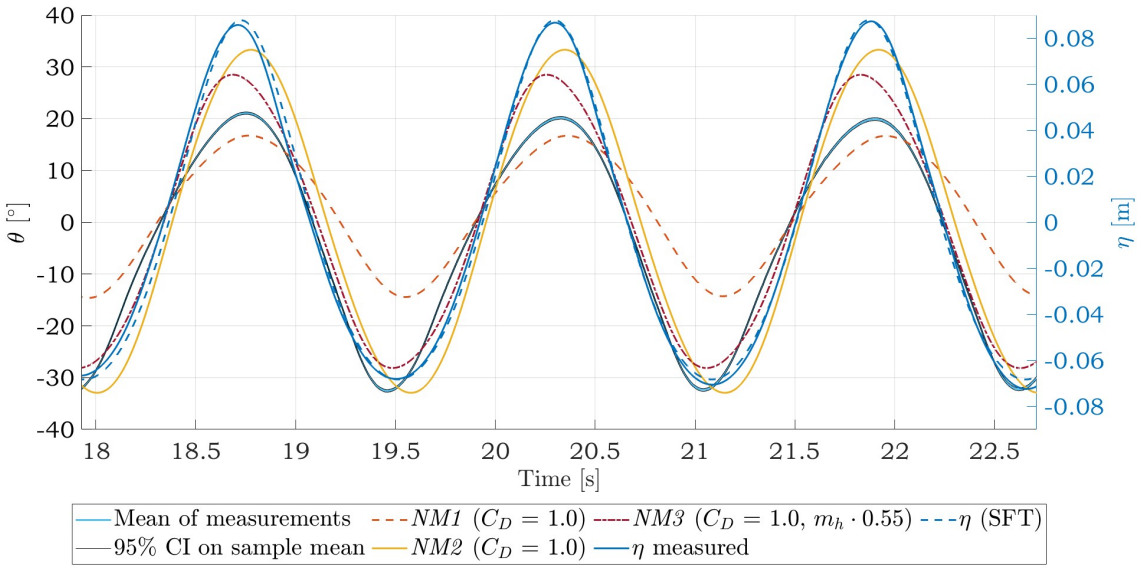

Figure 7.26. Comparison of results from numerical models and measured results for the disc-shaped floater in sea state 5.

For sea state 5 only *NM3* manages to describe the motions of the floaters with reasonable accuracy, and even then *NM3* still results in a large overestimation of the motions for all three floater geometries.

7.2.3 Evaluation of numerical models for other floater geometries

In this section, the numerical models are evaluated and discussed based on the results, which are presented in the previous sections.

Decay tests

For the decay tests, only the conical floater model was described with reasonable accuracy with the numerical models *NM2* and *NM3*.

For the disc-shaped and spherical floaters, the results from the numerical models do not match the period of oscillation of the measured results. In an attempt to rectify this, the added mass moment of inertia was reduced in the numerical model *NM3* for the disc-shaped and spherical floaters. This improved the description of the period of oscillation, however the decay tests are not accurately described by any of the numerical models.

The poor results for the decay tests for the disc-shaped and spherical floater highlight the sensitivity to the quality of the decay tests. During the decay tests for these two models, a large initial angle was used, which can possibly explain the deviations from the numerical models. Furthermore, the experimental damping is heavily influenced by the accuracy with which the decay tests are performed.

As witnessed for the cylindrical floater, *NM1* has difficulty predicting the period of the oscillations during the decay test. This is also observed for the three other floater models which is further indication that this method of estimating the added mass moment of inertia is not viable.

Wave excitation tests

To evaluate the accuracy of the numerical models they are compared to the measured results using the FVU. In Figures 7.27, 7.28, and 7.29, the FVU is shown for the disc-shaped, conical, and spherical floater respectively.

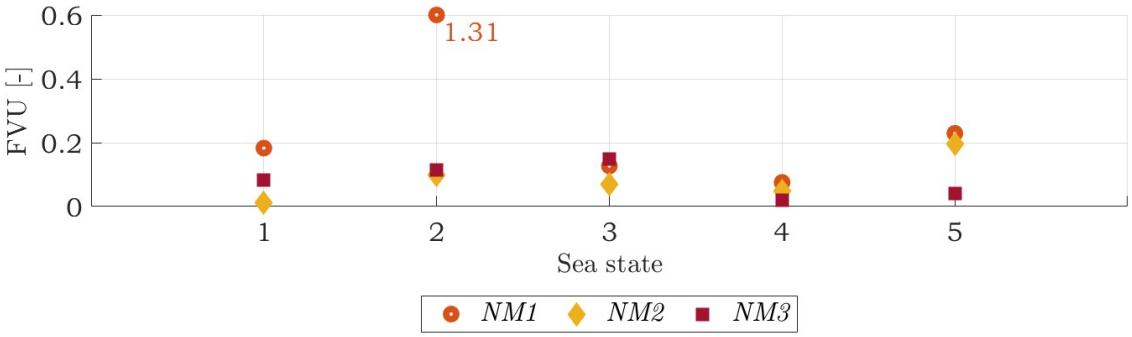

Figure 7.27. FVU for the results of the wave excitation tests on the disc-shaped floater.

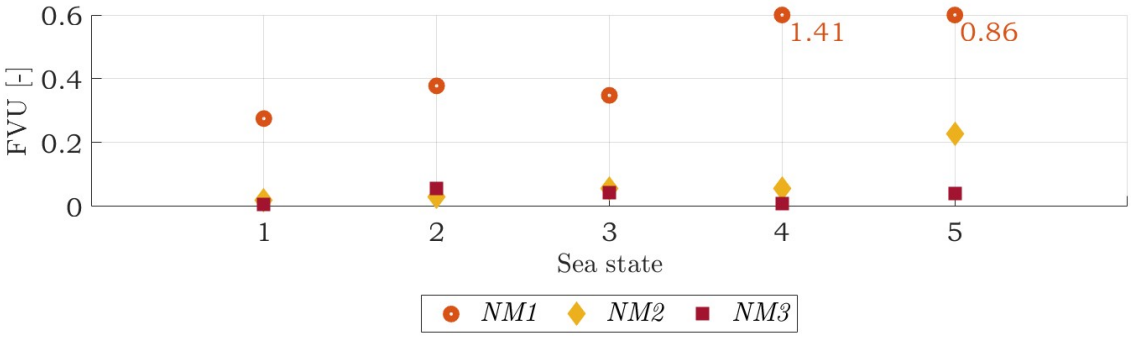

Figure 7.28. FVU for the results of the wave excitation tests on the conical floater.

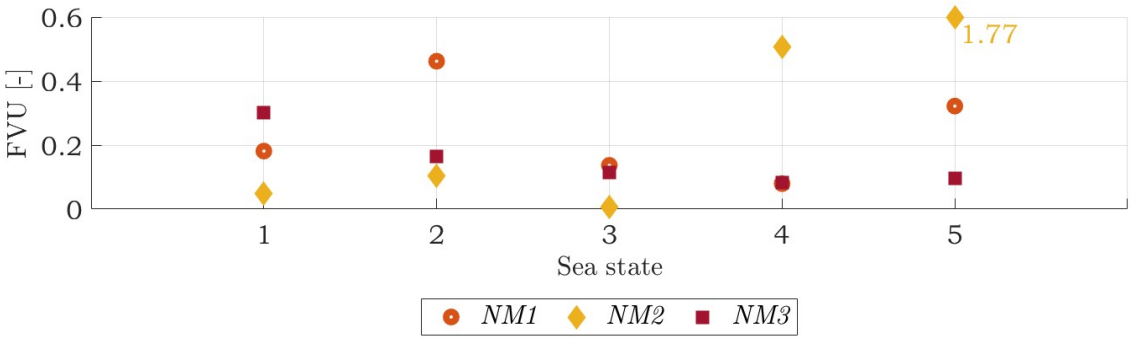

Figure 7.29. FVU for the results of the wave excitation tests on the spherical floater.

Similar to what was observed for the cylindrical floater model in Chapter 6 on page 49 it is

found that *NM1* generally results in the largest deviations from the measured results. It is concluded that *NM1* has trouble accurately describing the motions of any of the floaters.

The wave excitation moment in *NM1* is calculated with Method 1 which is based on the Morison equation. The Morison equation was originally proposed to determine wave forces on fixed structures. As shown earlier Method 1 is suitable to determine wave forces on floater models fixed at 0 °. Once the floater models are able to rotate around the hinge, Method 1 no longer gives reliable results for the wave forces on the floaters. Because of this, it is not considered a viable method of estimating the motions of a floater subjected to wave excitation.

The two BEM-based numerical models *NM2* and *NM3* provide good descriptions of the motions of all three floater models in sea states 1 to 3. In sea state 4 *NM2* and *NM3* still yield good results for the conical and disc-shaped floater however, a large deviation is observed with *NM2* for the spherical floater. As expected when the waves become more nonlinear, the results using the BEM-based models begin to deviate more from the measured results. This is seen particularly for the numerical model *NM2* in sea state 5. Part of the explanation for the larger deviations in sea states 4 and 5 is likely caused by the larger deviations for the moment around the hinge, as described in Section 7.1 on page 64. From the results, it can also be observed that *NM3*, which uses experimentally determined damping, results in a better description of the sea states 4 and 5 than *NM2*, which uses damping from NEMOH. A possible explanation for this is the assumption of linear wave theory in the BEM, which means that as the waves get higher and steeper the accuracy of the BEM results decrease.

In general, it is found that BEM-based numerical models with a drag contribution calculated with a relative velocity formulation of the Morison equation can be used to describe the motions of various floater geometries in sea states with a significant contribution to the total available wave energy.

Discussion 8

In this chapter, the calculation methods for the forces on the floaters, the numerical models for the motions of the floaters, and the results from the present thesis are discussed.

8.1 Forces on the fixed floater models

As described in the thesis two calculation methods are used to examine the forces on the fixed floater models. Method 1 uses a normal force contribution calculated with the Morison equation and a tangential force contribution calculated from wave-induced pressure. Method 2 uses the boundary element method code NEMOH to determine the forces on the fixed floater models. When using the BEM the part of the floater which is above the SWL is ignored.

The results obtained with the two calculation methods are compared to measured results from model scale experiments performed in the wave flume at Aalborg University. The experiments are performed using regular waves. By comparing the results from the two methods with the measured results it is determined that both methods can be used with reasonable accuracy to determine the wave excitation forces on a cylindrical floater model even when the floater is angled. This is in agreement with expectations because of the Morison equation's prevalent use for the calculation of forces on cylindrical structures.

When the floater geometry is changed to the spherical, conical, and disc-shaped floater models an increase in the deviations is observed for both calculation methods. Method 1 still manages to describe the moment on floater models at an angle of $0\,^\circ$ with good accuracy. However, when the angular position of these floater models is changed it leads to a significant increase in the deviations for Method 1. These deviations likely occur since the geometries for these floater models in combination with the angular position of the floater models are vastly different from the original assumptions for the Morison equation. Method 2 generally provides more accurate results for these floater models when they are placed at an angle because the BEM describes the wave-structure interaction correctly for the geometry below the SWL. Method 2 has larger deviations for sea states 4 and 5. This can be explained by an increase in the wavelength, which potentially violates the assumption in the BEM that the floater is large in comparison to the wavelength. Furthermore, BEM uses linear wave theory which can not accurately describe waves of larger steepness and wave height.

The results for the moment around the hinge are important in the estimation of the motion of the floaters. Therefore, the accuracy of these results is of particular interest. The results for the moment from Method 2 generally deviate less from the measurements than Method 1, however, significant deviations still occur, especially at the largest angles, $\pm 30^\circ$ and $\pm 40^\circ$, and for sea state 5, which has a large wave steepness.

8.2 Motions of the floater models

The motions of the floater models are examined using three numerical models. The first numerical model uses Method 1 to calculate the wave excitation moments. The other two numerical models are based on Method 2 and use the BEM-code NEMOH to calculate the wave excitation moments. The results from the numerical models are compared to results from decay tests and wave excitation tests performed on moving floater models. The experiments are performed using regular waves and without a PTO. This is done to examine the floaters' motion in different sea states and whether the numerical models can accurately describe it. The use of regular waves is limited to the calibration and examination of numerical models since regular waves can not describe a realistic sea environment.

By comparing the results from the numerical models to the measured results from the experiment it is determined that there is a significant difference in the performance of the numerical model which is based on Method 1 and the two numerical models based on Method 2. In most sea states, the Method 1 based numerical model is unable to describe the motions of the floater models with accuracy. However, the Method 2 based numerical models with a drag contribution calculated with a relative velocity formulation of the Morison equation provide an acceptable level of accuracy for various floater geometries. A similar level of accuracy is achieved using both experimental damping coefficients and damping coefficients determined using BEM.

This shows that a BEM-based numerical model can be a valuable tool in the initial design of a WEC. Using the BEM along with a drag contribution it is possible to examine a variety of different floater designs using a relatively coarse resolution and a simplified approach to determine the drag coefficient. In this thesis, BEM calculations are performed at a maximum increment of $10\,^{\circ}$ for the angular position of the floaters and drag coefficients are estimated from literature. Despite the coarse resolution for the angular position and C_D determined based on literature, an acceptable level of accuracy is achieved for sea states 1 to 4, which contribute to approximately half of the total available wave energy. Most of the remaining wave energy contribution occurs for significant wave heights that are similar to the one from sea state 5 or larger. Therefore, it is necessary to examine other methods to accurately describe the wave-structure interaction for these larger wave heights.

8.3 Scale effects

To perform the experiments on the floaters it is necessary to scale both the floater models and the sea states. This scaling is done using the Froude model law, which ensures correct geometric, kinematic, and dynamic similarity. The Froude model law is used since surface waves are gravity-driven. It is also possible to scale using the Reynolds number, which is a ratio between inertia forces and viscous forces. Using Reynolds number to scale ensures that the viscous forces are scaled correctly between the floater model and the full-scale floater. Because the Froude model law is used it is not possible to fulfil the Reynolds model law. This can lead to scale effects due to the effects of viscosity. For the floater of the Exowave WEC, which has a scale ratio of 1:20, the viscous forces on the model scale floater are exaggerated by a factor of 89. [Kamphuis, 2000]

Conclusion 9

This thesis has investigated the forces and motions of the floater of the Exowave WEC. A number of approaches for numerical modelling are applied to describe the wave-structure interaction of the floater. The different approaches are validated by using experimental data as benchmarks for the forces and motions of the floater. This thesis revolves around the following statement:

The aim of this thesis is to investigate the accuracy of different approaches for modelling the wave-structure interaction of the floater of the Exowave WEC.

The wave excitation forces on fixed floaters are examined using two methods. Method 1 is based on the Morison equation and Method 2 is based on the boundary element method. It is determined that Method 1 only manages to calculate the forces on the floaters with an acceptable level of accuracy when the floaters are vertical. Method 1 is unable to accurately determine the forces on inclined floater models other than the cylindrical floater model. Method 2 achieves a good level of accuracy both for vertical and inclined floater models and is able to describe forces on various floater geometries. Method 2, however, struggles to describe wave forces in larger and steeper waves.

The motions of the floater models are examined using three numerical models *NM1*, *NM2*, and *NM3*. The numerical models are all solved using a state-space representation of the equation of motion. *NM1* uses Method 1 to calculate the wave excitation moment. Both *NM2* and *NM3* use Method 2 to calculate the wave excitation moment and take viscous forces into account by including a drag contribution calculated with the Morison equation. The two numerical models differ since *NM2* uses BEM-based damping, and *NM3* uses experimentally determined damping. The results show that *NM1* is not a suitable option for calculating the motions of any of the floater models. *NM2* and *NM3* are both able to describe the motions of the floater models with an acceptable level of accuracy even for waves that can not be described with linear wave theory. Using the approach from the numerical model *NM2* has the advantage that it can provide results of good accuracy for the motions of the floater models using a coarse resolution for the angular positions of the floaters and without the need for experimental data. Furthermore, it is simple to change the floater geometry meaning that this approach can be particularly useful in the initial design of a WECs floater geometry.

Similarly to the examinations of the wave excitation forces it is found that the two numerical models using Method 2 struggle to describe motions in larger and steeper waves. The steepest waves examined in this thesis have a wave steepness of 0.042, for these waves *NM2* and *NM3* are unable to provide accurate results for the motions. Despite these limitations for *NM2* and *NM3* the numerical models are able to describe the motions of the floater models in sea states which contribute approximately half of the total available wave energy.

9.1 Future work

As stated the *NM2* and *NM3* are unable to provide accurate results for steep waves. Because of this, it would be advantageous to examine the limitations more closely and determine a more exact estimate of the limitations of these numerical models. Furthermore, the *NM2* facilitates the possibility of implementing new floater model geometries. *NM2* is solely based on the BEM-code NEMOH and a drag coefficient estimated from literature, which makes it possible to examine different geometries for the purpose of determining a suitable geometry. It should be noted that the results should be validated with an experiment.

A CFD analysis might be insightful in describing the wave-structure interaction with a greater level of accuracy. Furthermore, it could be helpful in describing the wave-structure interaction of floaters in larger and steeper waves. However, CFD is a computationally expensive and is therefore only recommended for analysis once a floater geometry has been settled upon.

This thesis is limited to investigating the forces and motion of the floater models. The following step in the design of a WEC is the determination of the energy production. The power take-off and control subsystem must be examined to estimate the energy production. Furthermore, the forces and motion of the floater are investigated for regular waves. In order to capture a more realistic wave environment, the floater model could be investigated in irregular waves.

A full-scale test with a PTO is planned for the Exowave WEC. The full-scale test can contribute valuable insight into the wave-structure interaction for several parameters. A number of assumptions are applied to determine a representative wave environment in a down-scaled test because of the use of a model law. The scaling can affect the forces in a down-scaled test which is not possible to avoid unless another similar test is conducted with another scale factor. Because of this a full-scale test can provide valuable insight into the scale effects that will impact the Exowave WEC.

Bibliography

Andersen et al., **2014**. Thomas Lykke Andersen, Peter Frigaard and Hans F. Burcharth. *LECTURE NOTES FOR THE COURSE IN WATER WAVE MECHANICS*, 2014.

Aqua-RET, **2008**. Aqua-RET. *WEC animations*, 2008.

Brorsen, **2007**. Micheal Brorsen. *Non-linear Waves*, 2007.

Cash and Karp, **1990**. J.R. Cash and A.H. Karp. *A variable order runge-kutta method for initial-value problems with rapidly varying righthand sides.* ACM Transactions on Mathematical Software, vol. 16, 1990.

Chakrabarti, **2005**. Subrata K. Chakrabarti. *Loads and Responses. Chapter 4 in Handbook of Offshore Engineering*, 2005.

CorPower Ocean, **2022**. CorPower Ocean. *Wave energy – Plugging the wind and solar void.* `https://corpowerocean.com/wave-energy-plugging-the-wind-and-solar-void/`, 2022. Downloaded: 02-06-2024.

DanWEC, **2022**. DanWEC. *Wave buoy data*, 2022.

Dean, **1965**. R.G. Dean. *Stream function representation of nonlinear ocean waves.* Journal of Geophysical Research, 1965.

DNV GL, **2017**. DNV GL. *DNVGL-RP-C205 - Environmental conditions and environmental loads*, 2017.

Exowave, **2024**. Exowave. *Technology - How it works.* `https://exowave.com/technology/`, 2024. Downloaded: 25-01-2024.

Faltinsen, **1990**. O. M. Faltinsen. *Sea loads on ships and offshore structures.* ISBN: 0-521-45870-6, Paperback. Cambridge University Press, 1990.

Freund et al., **2005**. Paul Freund, Anthony Adegbulugbe, Øyvind Christophersen, Hisashi Ishitani, William Moomaw and Jose Moreira. *IPCC Special Report on Carbon dioxide Capture and Storage*, 2005.

Frigaard and Andersen, **2014**. Peter Frigaard and Thomas Lykke Andersen. *Analysis of Waves -Technical documentation for WaveLab 3*, 2014.

Gavin, **2020**. H.P. Gavin. *Numerical Integration in Structural Dynamics.* Department of Civil & Environmental Engineering, Duke University, 2020.

Gerhart et al., **2016**. Philip M. Gerhart, Andrew L. Gerhart and John I. Hochstein. *Munson, Young, and Okiishi's Fundamentals of Fluid Mechanics.* ISBN: 978-1-119-08070-1, Hardback. Wiley, 2016.

Himeno, **1981**. Yoji Himeno. *Prediction of ship roll damping - State of the art*, 1981.

Hughes, **1993**. Steven A. Hughes. *Physical Models and Laboratory Techniques in Coastal Engineering.* ISBN: 981-02-1540-1, Advanced series in Ocean Engineering - Volume 7. World Scientific, 1993.

IEA, **2024**. IEA. *Renewables 2023 - Analysis and forecast to 2028*, 2024.

IPCC, **2023**. IPCC. *CLIMATE CHANGE 2023 Synthesis Report -Summary for Policymakers*, 2023.

IRENA, **2021**. IRENA. *WORLD ENERGY TRANSITIONS OUTLOOK*, 2021.

Iversen et al., **2023**. Sarah K. Iversen, Jacob Andersen, Lars Wigant and Peter Frigaard. *Development of the Exowave Oscillating Wave Surge Converter*, 2023.

Kamphuis, **2000**. J. William Kamphuis. *Introduction to coastal engineering and management*. ISBN: 981-02-3830-4, Advanced series in Ocean Engineering - Volume 16. World Scientific, 2000.

Keulegan and Carpenter, **1958**. G.H. Keulegan and L.H. Carpenter. *Forces on Cylinders and Plates in an Oscillating Fluid*. Journal of Research of the National Bureau of Standards - Vol. 60, No.5, 1958.

Kurnia and Ducrozet, **2022**. Ruddy Kurnia and Guillaume Ducrozet. *NEMOH v3.0 User Manual*, 2022.

Le Mehaute, **1976**. B. Le Mehaute. *An introduction to hydrodynamics and water waves*. ISBN: 978-0387072326, Paperback. Springer-Verlag, 1976.

Lee and Newman, **2005**. C. H. Lee and J. N. Newman. *Computation of wave effects using the panel method*, 2005.

Morison et al., **1950**. J. R. Morison, M. P. O'Brien, J. W. Johnson and S. A. Schaaf. *The force exerted by surface waves on piles*, 1950.

Pecher and Kofoed, **2017**. Arthur Pecher and Jens Peter Kofoed. *Handbook of Ocean Wave Energy*. ISBN: 978-3-319-39888-4, Paperback. SpringerOpen, 2017.

Qualisys, **2020**. Qualisys. *Qualisys Track Manager - User manual*, 2020.

Sarpkaya, **2010**. Turgut Sarpkaya. *Wave Forces on Offshore Structures*. ISBN: 978-0-521-89625-2, Hardback. Cambridge University Press, 2010.

Sarpkaya et al., **1982**. Turgut Sarpkaya, Thomas S. Raines and Dean O. Trytten. *Wave Forces on Inclined Smooth and Rough Circular Cylinders*, 1982.

Schlichting and Gersten, **2017**. Hermann Schlichting and Klaus Gersten. *Boundary-Layer Theory - Ninth Edition*. ISBN 978-3-662-52919-5, Paperback. Springer-Verlag Berlin Heidelberg, 2017.

Stansby, **1992**. Peter K. Stansby. *Forces on a circular cylinder in elliptical orbital flows at low Keulegan-Carpenter numbers*, 1992.

Stokes, **1847**. G. Stokes. *On the Theory of Oscillatory Waves*. Transactions of the Cambridge Philosophical Society VIII, 1847.

The Liquid Grid, **n.d**. The Liquid Grid. *WAVE ENERGY*. `https://theliquidgrid.com/marine-clean-tech-briefs/wave-energy-converters/`, n.d. Downloaded: 03-06-2024.

Wolfson, **2016**. Richard Wolfson. *Essential University Physics - Volume 1 - Third edition.* ISBN: 978-1-292-10265-8, Paperback. Pearson, 2016.

Zhang and Schaffer, **2005**. Haiwen Zhang and Hemming A. Schaffer. *Approximate Stream Function wavemaker theory for highly non-linear waves in wave flumes*, 2005.

Appendix I

MetOcean study A

In this chapter, MetOcean data is analysed in order to determine representative sea states that are used in the report, as the focus is the production states and not the extreme sea states. The sea states are characterised by a significant wave height, a peak period and a water depth.

A.1 MetOcean data

The data used is from a wave buoy at the DanWEC test site at Hanstholm. The wave buoy is placed at the planned site for sea trials of the WEC. The location of the wave buoy is shown in Chapter 1 on page 1 in Figure 1.5.

In Table A.1, the buoy used to measure the data is described.

Wave buoy	Model	Latitude [^{o}N]	Longitude [^{o}E]	Water depth [m]
Wave buoy II	Datawell DRW4/ACM	57.1112	8.5457	14.5

Table A.1. Description of the used wave buoy. [DanWEC, 2022]

The data is from the period July 2016 to October 2022 and is given in intervals of 30 minutes. In Table A.2 a description of the used wave parameters is given.

Parameter	Description
H_{m0}	Estimate of significant wave height. $H_{m0} = 4\sqrt{m0}$
T_z	Estimate of average wave period. $T_z = T_{m02} = \sqrt{\frac{m0}{m2}}$

Table A.2. Description of the data from the wave buoy.

The measured significant wave heights are shown in Figure A.1.

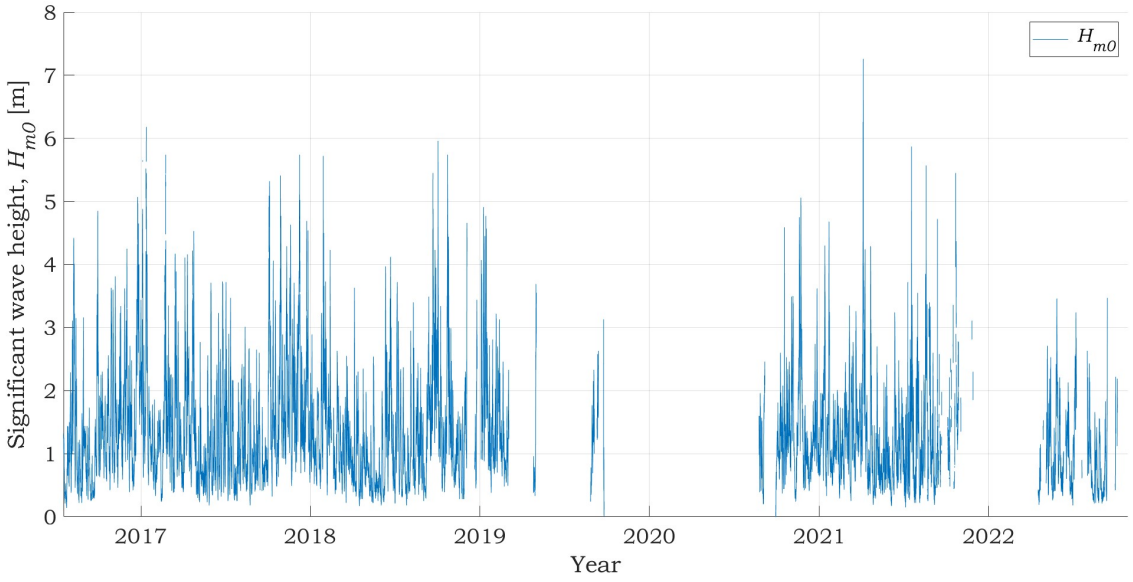

Figure A.1. The measured significant wave heights.

As it can be seen in the figure, the wave buoy had a significant amount of downtime during 2019 and 2020. The missing data is excluded when calculating the representative sea states.

A.2 Representative sea states

The wave conditions at the site are initially described using a scatter diagram (H_{m0}, T_z) showing the percentage of occurrence, P. The scatter diagram is shown in Table A.3. The representative sea states are framed in the scatter diagram.

H_{m0}	T_z [s]												Sum
[m]	1.75	2.25	2.75	3.25	3.75	4.25	4.75	5.25	5.75	6.25	6.75	7.25	[%]
0.25	0.13	1.89	3.50	3.07	2.17	1.17	0.54	0.23	0.15	0.13	0.06	0.01	13.03
0.75		0.32	4.39	8.44	7.23	5.50	2.71	1.21	0.48	0.13	0.07	0.05	30.53
1.25			0.01	2.00	8.73	8.13	3.92	1.61	0.65	0.17	0.04	0.00	25.26
1.75					0.62	6.45	5.11	1.59	0.49	0.15	0.05	0.02	14.49
2.25						0.23	4.18	2.57	0.57	0.16	0.05	0.01	7.77
2.75							0.15	2.76	1.26	0.15	0.03	0.01	4.36
3.25								0.15	1.54	0.49	0.06	0.01	2.25
3.75									0.13	0.75	0.25	0.04	1.17
4.25										0.08	0.39	0.12	0.58
4.75											0.06	0.19	0.25
5.25												0.04	0.04
Sum [%]	0.13	2.22	7.90	13.50	18.75	21.48	16.61	10.13	5.25	2.20	1.07	0.49	99.74

Table A.3. Scatter diagram from data measured by Wave Buoy II from July 2016 to October 2022 in the percentage of occurrence.

In order to have a more concise description of the wave conditions at the test site, different bins in the scatter diagram are grouped to form the sea states. The bins are shown in the scatter diagram and they are chosen to be as few as possible and capture as much of the percentage of occurrence as possible. The election of the sea states is also based on

the wave energy contribution. In order to determine the wave energy contribution, the power in the wave field must be determined. The power in the wave field is determined by Equation (A.1). The power is proportional to the wave period and the wave height squared. The power is determined for each bin in the scatter diagram. The wave power is determine by the energy period, T_e.

$$P_{wave} = \frac{\rho \cdot g^2}{64 \cdot \pi} \cdot H^2 \cdot T_e \tag{A.1}$$

To determine the wave power contribution, the wave power is multiplied by the probability of occurrence. This is shown in Table A.4 where the unit of the wave power contribution is in kW/m of a wave.

H_{m0} [m]	T_z [s] 1.75	2.25	2.75	3.25	3.75	4.25	4.75	5.25	5.75	6.25	6.75	7.25	Sum [kW/m]
0.25	0.00	0.00	0.01	0.01	0.01	0.00	0.00	0.00	0.00	0.00	0.00	0.00	0.03
0.75		0.01	0.08	0.18	0.17	0.15	0.08	0.04	0.02	0.01	0.00	0.00	0.73
1.25			0.00	0.12	0.58	0.61	0.33	0.15	0.07	0.02	0.01	0.00	1.88
1.75				0.00	0.08	0.95	0.84	0.29	0.10	0.03	0.01	0.00	2.32
2.25						0.06	1.14	0.78	0.19	0.06	0.02	0.01	2.25
2.75							0.06	1.25	0.62	0.08	0.02	0.01	2.03
3.25								0.10	1.06	0.37	0.05	0.01	1.58
3.75									0.12	0.75	0.27	0.04	1.18
4.25										0.10	0.54	0.17	0.81
4.75											0.10	0.36	0.46
5.25												0.08	0.08
Sum [kW/m]	0.00	0.01	0.09	0.30	0.84	1.78	2.47	2.60	2.17	1.41	1.02	0.68	13.35

Table A.4. Scatter diagram for wave energy contribution. The energy is shown in kW/m.

The wave energy contribution for each bin is shown in Table A.5. The wave energy contribution is calculated as a percentage of the wave energy contribution in Table A.4.

H_{m0} [m]	T_z [s] 1.75	2.25	2.75	3.25	3.75	4.25	4.75	5.25	5.75	6.25	6.75	7.25	Sum [%]
0.25	0.00	0.02	0.05	0.05	0.04	0.03	0.01	0.01	0.00	0.00	0.00	0.00	0.23
0.75		0.03	0.58	1.31	1.30	1.12	0.62	0.31	0.13	0.04	0.02	0.02	5.47
1.25			0.01	0.86	4.35	4.59	2.48	1.12	0.49	0.14	0.04	0.00	14.09
1.75				0.00	0.61	7.15	6.32	2.18	0.74	0.24	0.10	0.03	17.36
2.25						0.41	8.56	5.81	1.41	0.42	0.15	0.05	16.81
2.75							0.47	9.33	4.64	0.59	0.14	0.05	15.22
3.25								0.73	7.93	2.76	0.36	0.06	11.84
3.75									0.89	5.62	2.02	0.31	8.84
4.25										0.73	4.07	1.29	6.08
4.75											0.73	2.70	3.43
5.25												0.60	0.63
Sum [%]	0.00	0.06	0.63	2.23	6.30	13.30	18.46	19.48	16.24	10.54	7.63	5.10	100

Table A.5. Wave energy contribution as a percentage.

For each sea state, a significant wave height and a wave period are calculated using equation (A.2) and (A.3) respectively.

$$H_{m0_{SS}} = \sqrt{\frac{\sum_{SS,bin=1}^{n} H_{m0_{SS,bin}}^2 \cdot P_{SS,bin}}{\sum_{SS,bin=1}^{n} P_{SS,bin}}} \tag{A.2}$$

$$T_{z_{SS}} = \frac{\sum_{SS,bin=1}^{n} T_{z_{SS,bin}} \cdot P_{SS,bin}}{\sum_{SS,bin=1}^{n} P_{SS,bin}} \tag{A.3}$$

The sea states are shown in Table A.6. The table shows the physical parameters connected with the sea states. The wavelength L is determined by the dispersion relationship. The different types of wave periods are shown for the sea states.

Sea state	H_{m0} [m]	T_z [s]	T_e [s]	T_p [s]	h [m]	L [m]
1	0.63	3.2	3.7	4.1	14.0	26.6
2	1.08	4.4	5.1	5.7	14.0	48.6
3	1.28	3.7	4.2	4.7	14.0	34.4
4	1.94	4.7	5.5	6.1	14.0	54.2
5	2.91	5.5	6.3	7.1	14.0	68.8

Table A.6. Physical parameter of the five sea states.

The wave energy contribution and the percentage of occurrence among other things are shown in Table A.7. The percentage of occurrence is almost 90 % which sea states 1, 2, and 4 have a large contribution to the total occurrence. The percentage of the wave energy contribution illustrated with *Contrib* is at 73%.

Sea state	*Contrib* [%]	Annual hours [hour]	P [%]	P_{wave} [kW/m]	$P \cdot P_{wave}$ [kW/m]
1	3.4	2725	31.1	8.5	1.3
2	8.8	1781	20.3	21.7	2.2
3	5.8	998	11.4	36.7	2.1
4	32.6	1863	21.3	184.1	19.6
5	22.6	502	5.7	225.9	6.5
Sum	73.2	7869	89.8	-	31.6

Table A.7. Sea states including the wave contribution.

Experimental investigation of forces on fixed floaters B

In this chapter the calibration of the waves generated in the flume and the comparison of the force transducer setups are described.

B.1 Setup and equipment

The materials used to conduct the experiment are listed below.

- Flume at Aalborg University in the Department of the Built Environment
- Three wave gauges
- Wave gauge sensor
- Wave gauge cables
- Fixed structure and clamps
- Cylinder
- Bending beam force transducer
- 6-axis force transducer
- Cables to the force transducers
- Floater models
- Weights
- Clamps
- Hinge to connect 6-axis force transducer to the floater model
- Digital protractor
- Data acquisition system
- Analog filter at 8 Hz

The flume is 22.5 m long which includes the wave generator and the absorption and 1.5 m wide. The diameter of the model must not exceed 10 % of the width of the flume to ensure that the boundaries do not influence the waves at the model. The cylindrical floater model does not exceed the size. There is no inclination of the bottom in the flume.

B.2 Scaling the setup

In order to conduct the experiment in the flume, the experiment must be downscaled to match the flume's size. The floaters and the sea states must be scaled to fit the flume. The floater models is shown in Figure B.1. Furthermore, the geometrical scale factor for the scaled floater models is $\lambda_s = 20$.

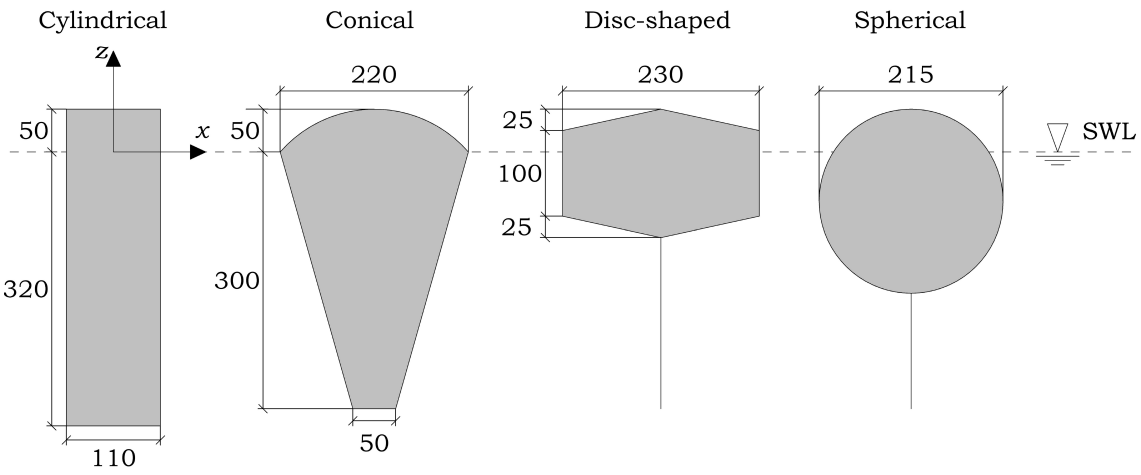

Figure B.1. Floater models with intended SWL. All measurements are in mm.

The sea states are scaled according to the Froude scaling law which is an expression between inertia forces and gravity forces. Therefore, the ratio between the inertia forces and gravity forces is the same for the full-scale floaters as for the down-scaled floater models. The scale ratios used to determine the scaled sea states are shown in Table B.1.

Physical parameter	Unit	Scale ratio
Wave height and length	[m]	λ_s
Wave period	[s]	$\sqrt{\lambda_s}$

Table B.1. Scale factor of the physical parameters. [Hughes, 1993]

The sea states are shown in Table A.6 on page 94 in the MetOcean study. The sea states are scaled according to Table B.1. The sea states of the individual scale factors are shown in Table B.2.

Scale factor	20		
Sea state	H_{m0} [cm]	T_p [s]	d [cm]
1	3.13	0.92	72.0
2	5.38	1.27	72.0
3	6.41	1.05	72.0
4	9.71	1.36	72.0
5	14.54	1.58	72.0

Table B.2. Sea states scaled accordingly to the scale factors.

The scaled setup in the wave flume is shown in Figure B.2.

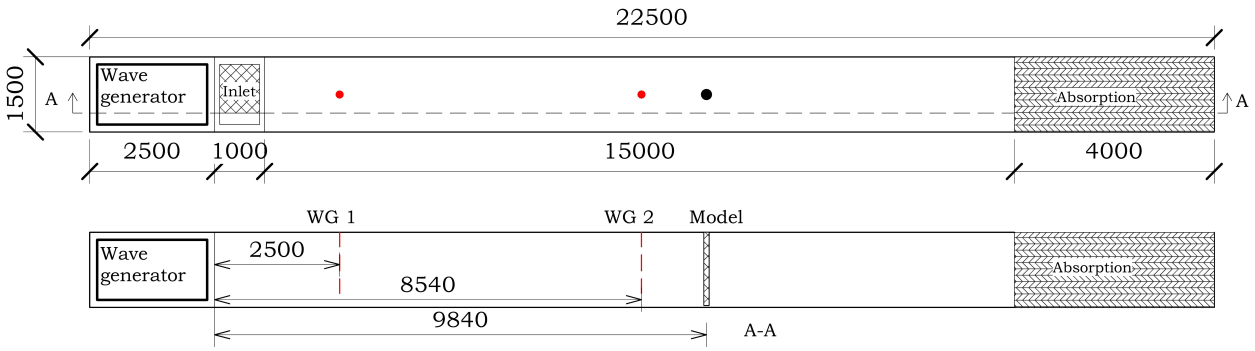

Figure B.2. Flume including the model. All measurements are in mm.

B.3 Calibration of the waves generated in the flume

The wave environment in the flume is examined to ensure that the generated waves are equal to the scaled representative sea states determined in Table B.2. This is ensured by measuring the waves with the wave gauges and correcting the generated waves. Wave gauge 3 is used to match the represented sea state due to it is placed where the model is placed after the calibration is done. Wave gauge 2 and wave gauge 3 are shown in Figure B.3.

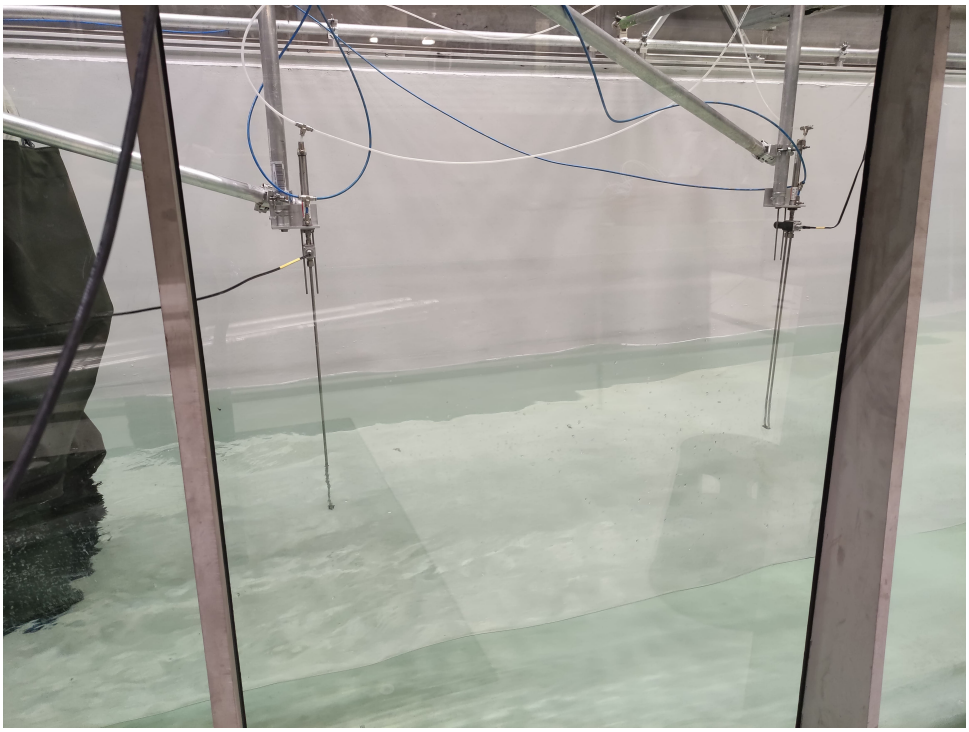

Figure B.3. Wave gauge 2 and wave gauge 3 in the flume.

The waves are calibrated by considering the surface elevation at wave gauge 3. The calibration is performed by generating waves with different heights until the generated wave height is acceptable close enough to the represented wave height for the sea state. The wave period is also checked but the generated period matched the period from the scaled sea state. There is a wait of five minutes between the generated waves to ensure

that the water in the flume is still. The process of calibrating the wave height can be seen in Figure B.4, where the first attempt at generating the correct wave height is shown as well as the final attempt.

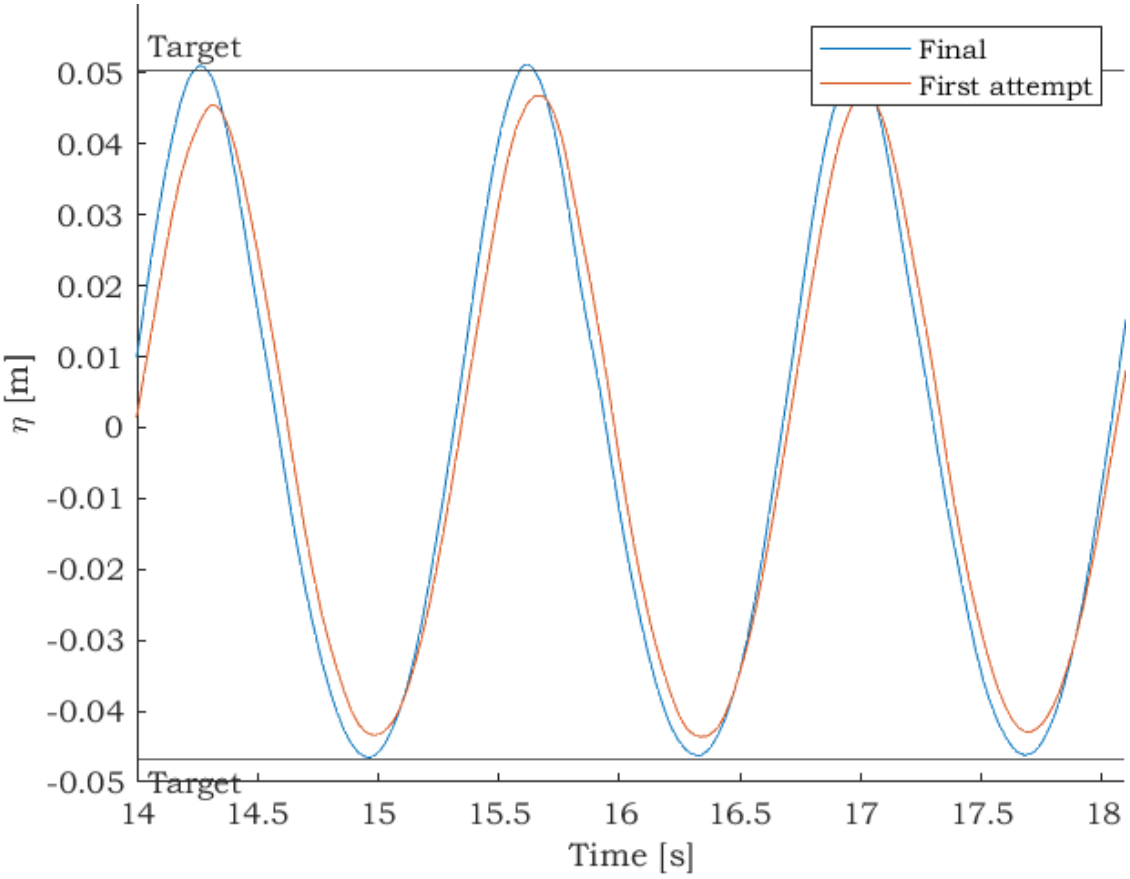

Figure B.4. Comparison of first attempt and final for the correct wave height for sea state 4 with scale 1:20 in the interval for the first 3 fully developed waves.

Table B.3 shows the scaled represented sea states and the calibrated wave heights and wave periods. The depth is the same for the scaled sea states as for the calibrated sea states. The wave heights are determined as an average of the first three fully developed waves at wave gauge 3. In Table B.3 it can be seen that the calibrated wave height matched the scaled sea state.

Sea state scaled 1:20				Calibrated sea state	
Sea state [-]	H_{m0} [cm]	T_p [s]	d	$H_{calibrated}$ [cm]	$T_{calibrated}$ [s]
1	3.13	0.92	72.0	3.06	0.923
2	5.38	1.27	72.0	5.35	1.277
3	6.41	1.05	72.0	6.35	1.050
4	9.71	1.36	72.0	9.71	1.360
5	14.54	1.58	72.0	15.60	1.585

Table B.3. The calibrated sea state for the models scaled 1:20.

B.3.1 Alignment

In order to compare two tests of the same generated wave, it is necessary to be able to align the waves. The alignment is performed by measuring the wave heights from the calibrated sea states and using the surface elevation at wave gauge 1 as a baseline. The next time the same calibrated sea state is carried out, the waves are aligned using wave gauge 1. The assumption is that the same wave must be generated every time for a sea state and the surface elevation must then be the same at wave gauge 1. The wave period can deviate due to a small change in water depth. The raw data is aligned with the calibrated sea state which is shown in Figure B.5. The data shown is the surface elevation measured at wave gauge 1 for the calibrated sea state and a test with the same generated waves.

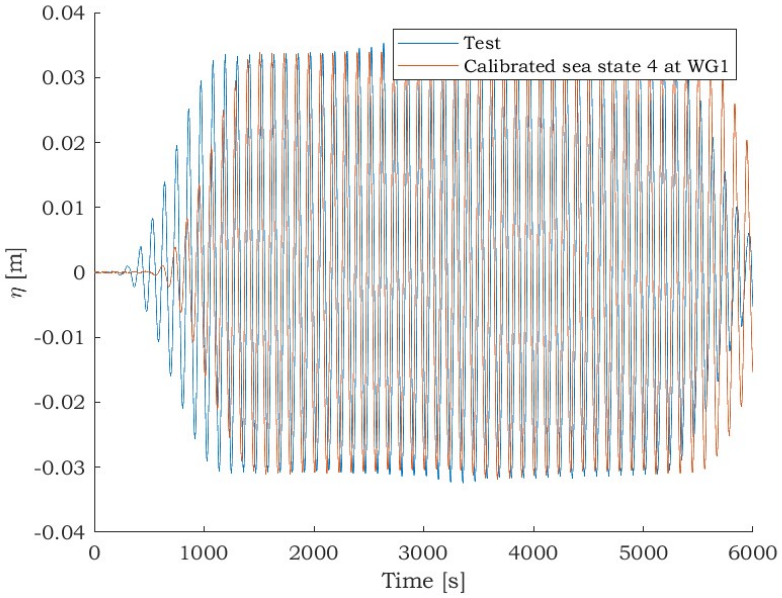

(a) Raw data.

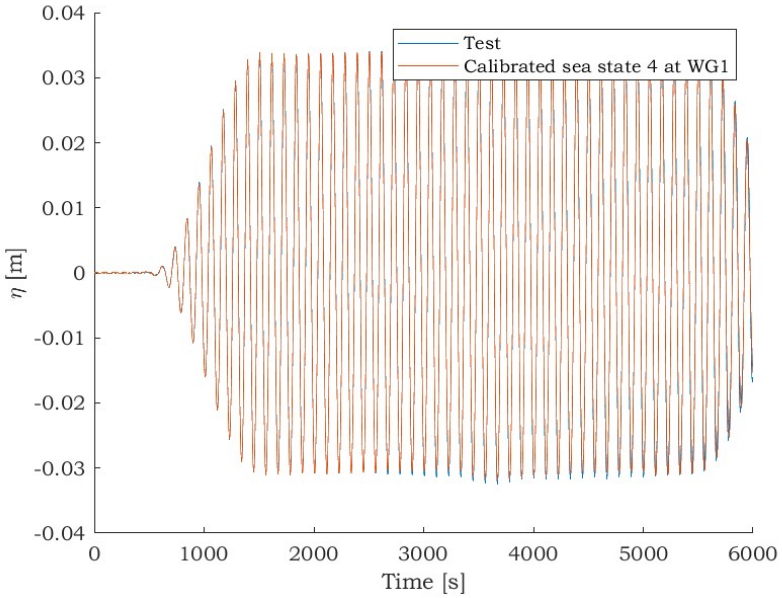

(b) Aligned data.

Figure B.5. Alignment of data to wave gauge 1.

Furthermore, the alignment of the data is also shown in Figure B.6, where the first waves are zoomed in.

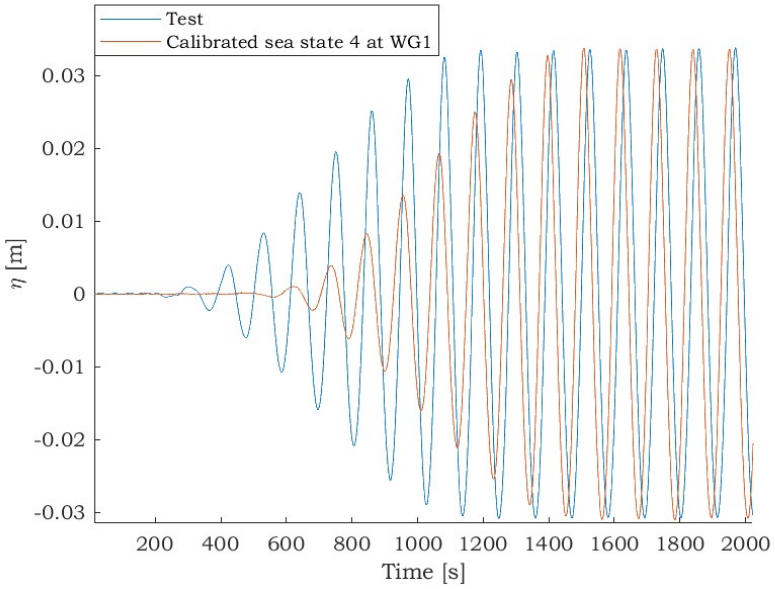

(a) Raw data.

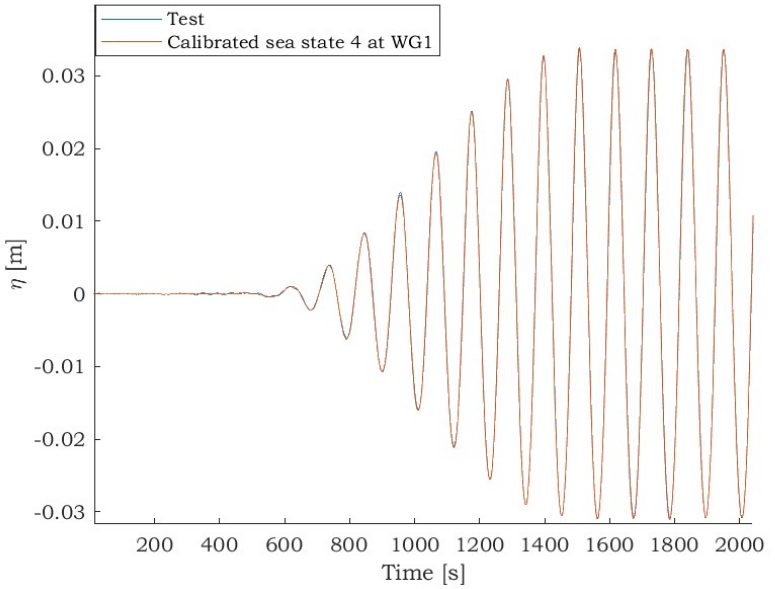

(b) Aligned data.

Figure B.6. Alignment of data to wave gauge 1 zoomed in at the first waves.

B.4 Comparison of force transducer setups

The interest in conducting experiments on inclined floater models necessitates the measurement of both horizontal and vertical wave excitation forces. This makes the commonly used bending beam force transducer impractical since it would be necessary to conduct all experiments twice, first measuring the horizontal force and then the vertical force. Therefore, a different experimental setup with a 6-axis force transducer is considered. The 6-axis force transducer measures forces and moments in three dimensions making it possible to measure all necessary forces in one experiment. Therefore, the purpose of this comparison is to validate the usage of the 6-axis force transducer.

Before the 6-axis force transducer is used in the main experiments on the floater model, it is compared to the bending beam force transducer, and analytical solution which is determined using the Morison equation. This is done using the cylindrical model shown in Figure B.7. This model is used since it complies with the assumptions used in Morison's equation, which are shown in section 2.2 on page 9. The long cylinder prevents overtopping and the cylinder extends almost to the bottom which ensures that the main flow is around the body of the model. The model can be seen in Figure B.7. The model is lifted 2 mm above the bottom of the flume to ensure that the long cylinder model is not supported on both ends. The setups for the model will be estimated to behave as a fixed cantilever beam.

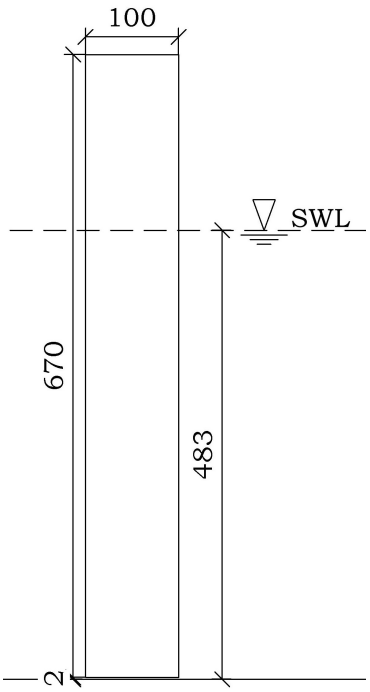

Figure B.7. Long cylinder model with intended SWL. All measurements are in mm.

B.4.1 Setups

Both experimental setups used the aforementioned cylindrical model, which was placed in the same place in the wave flume. The setups are shown in Figure B.8 and B.9.

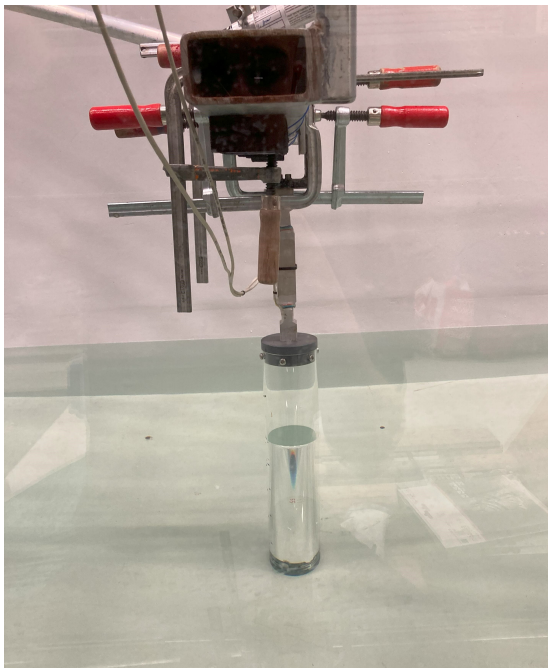

Figure B.8. Setup with the bending beam force transducer.

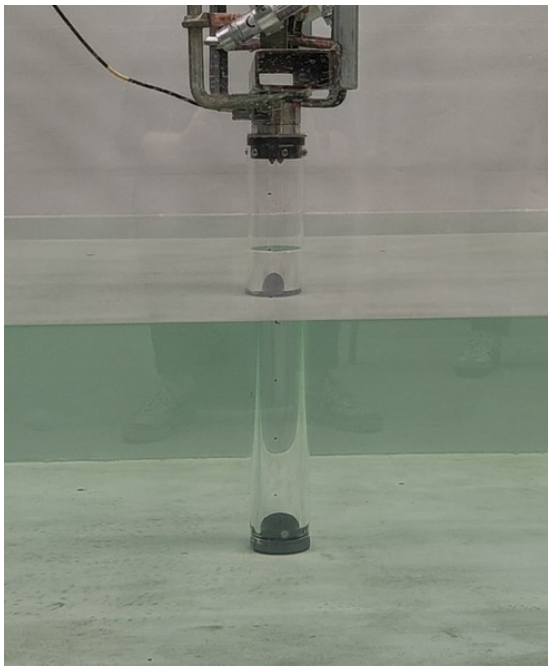

Figure B.9. Setup with the 6-axis force transducer.

In the following further explanation of the two setups is given.

Setup 1 (Bending beam force transducer)

The bending beam force transducer consists of an aluminium beam with two full Wheatstone bridges placed at the slender parts of the beam. The full Wheatstone bridges measure the moments about y, $M1$ at the lower bridge, and $M2$ at the upper bridge. The moment is measured by having strain gauges placed at $M1$ and $M2$. The thickness of the beam at the position of the bridges is 15 mm and the distance between the bridges is 150 mm. The bending beam force transducer is shown in Figure B.10.

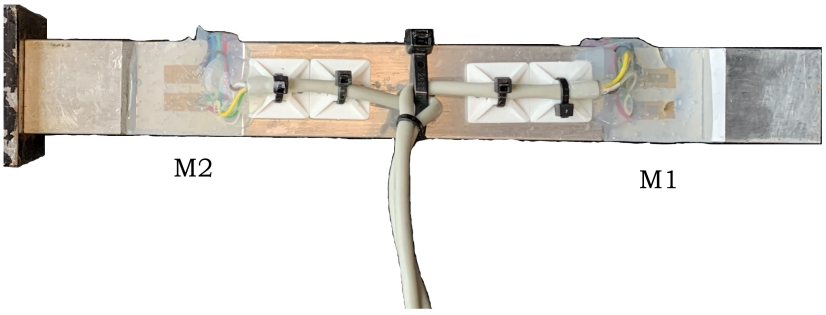

Figure B.10. Bending beam force transducer marked with $M1$ and $M2$.

The moments $M1$ and $M2$ are calculated with a linear calibration function found by calibrating the force transducer using weights and varying the arm. This calibration is performed by knowing the moments at $M1$ and $M2$ and then measuring the moments and

adjusting the range. This calibration is shown in Figure B.11. Afterwards, the resulting horizontal force and its corresponding attack point are calculated from the moments.

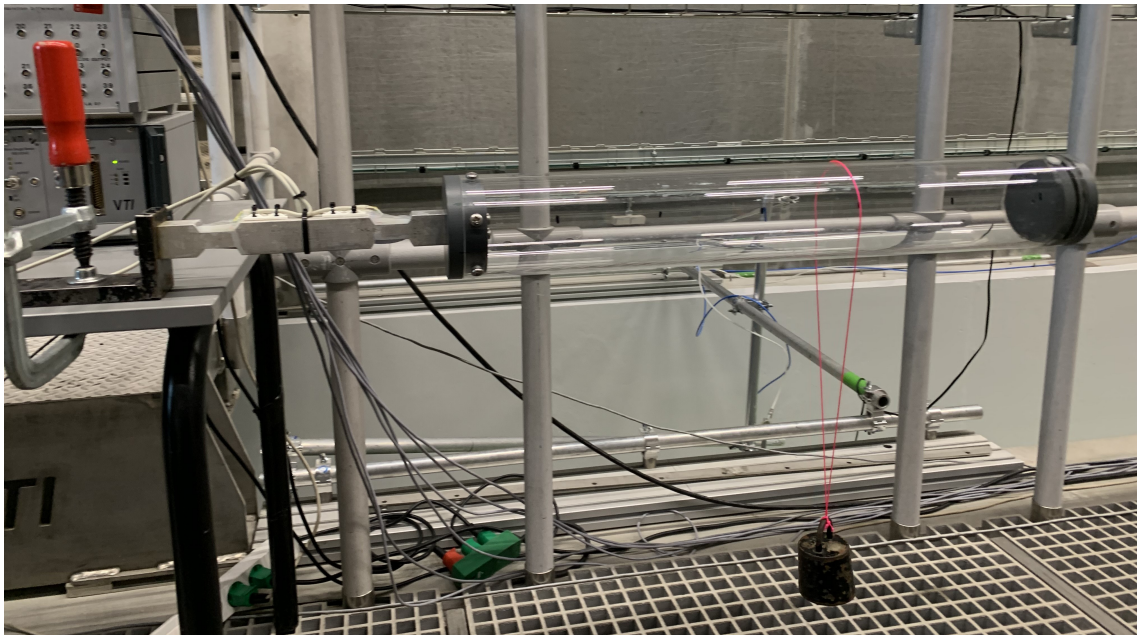

Figure B.11. Calibration of the bending beam force transducer.

Setup 2 (6-axis force transducer)

The 6-axis force transducer is an ATI Industrial Automation Gamma IP68 force transducer which can measure forces and moments in three dimensions. The measurement range is 65 N for F_x, 200 N for F_z, and 5 Nm for the moments. The force transducer is shown in Figure B.12.

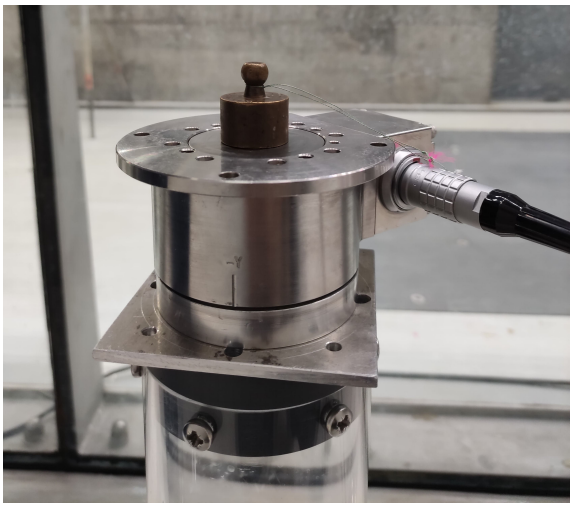

Figure B.12. 6-axis force transducer with 50 g weight placed on top.

A calibration matrix is provided for the 6-axis force transducer. Therefore, a calibration test is not performed. However, to examine the accuracy of the force transducer a similar test with weights and different arms is performed.

Seven weights ranging from 0.1 kg to 1.5 kg are placed at different arms and the forces and moments are measured, of particular interest are the force F_x and the moment M_y. In Figure B.13 and B.14 two examples from this test are shown.

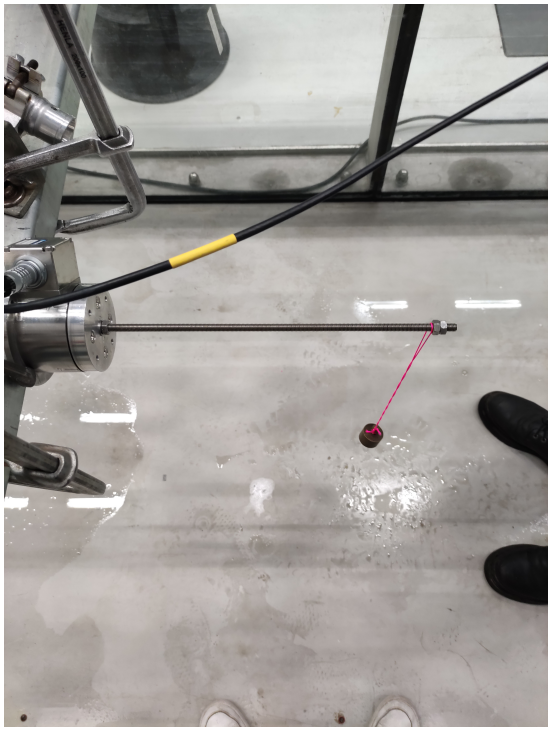

Figure B.13. Test with 100 g weight placed with an arm of 33 cm.

Figure B.14. Test with 200 g weight placed with an arm of 25 cm.

Since both the weight and the arm of the weight are known it is possible to calculate the theoretical values for F_x and M_y. Afterwards, the percent error is calculated. The average percent error for F_x is 1.63 %, after removal of two outliers this is reduced to 1.43 %.

The average percent error for M_y on the other hand is 35.0 %, which is unacceptably high. The error is much larger for the measurements with short arms, which can be caused by larger uncertainty regarding the measurement of the arms. If the measurements for the two shortest arms are removed the average percent error is reduced to 11.4 % which is still too high.

There is a trend that the measurements of M_y are consistently higher than the theoretical values. This could indicate that the measurement point of origin is not placed where it is indicated in the manual. By calculating the arm from the measurements for F_x and M_y it is found that the arm measured by the force transducer is on average 2.65 cm longer than the arm of the weight.

The measurement point of origin for the 6-axis force transducer is thus corrected with 2.65 cm as shown in figure B.15.

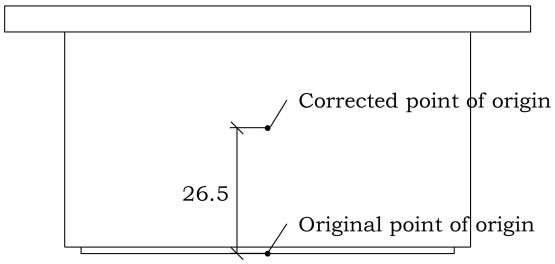

Figure B.15. The manuals and measured point of origin. Measurement in mm.

After this correction, the percent error for the measurements of M_y is reduced to 2.0 %. If the measurements from the two shortest arms are again removed the percent error is reduced to 0.6 %.

Because of this, it is chosen to correct the measurement point of origin for the 6-axis force transducer by moving it 2.65 cm further into the force transducer, as illustrated in Figure B.15. This correction is used in all following data analyses and the experiment on a fixed floater model.

B.4.2 Dynamic amplification

To investigate the influence of dynamic amplification on the setups the modal parameters are determined. This is done by subjecting the model to an impulse load by pulling on a string around the model and then letting go, as illustrated in Figure B.16. This results in a force decay time series, shown in Figure B.17, which is used to determine the modal parameters.

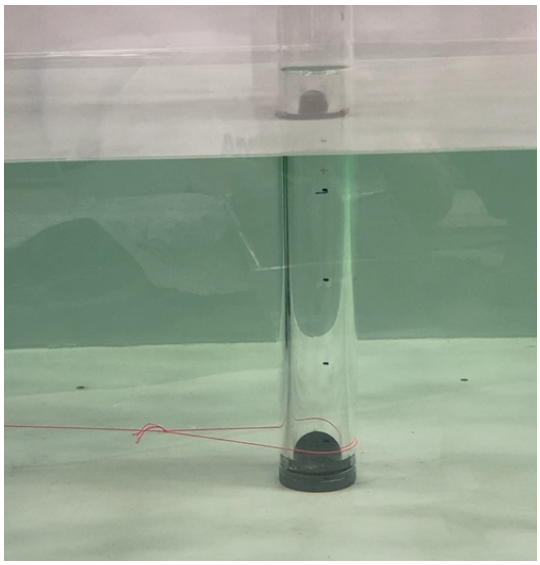

Figure B.16. Method used for subjecting the model to an impulse load.

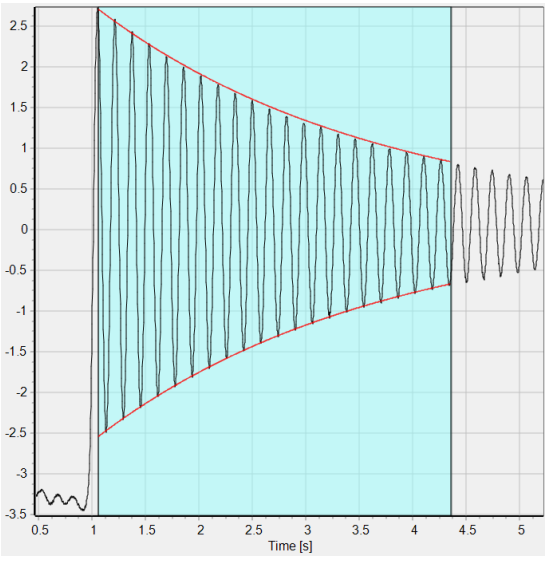

Figure B.17. Force decay time series for setup 1.

The eigenfrequencies of the cylinder are shown in Table B.4. The eigenfrequency is investigated for both the 6-axis force transducer and the bending beam force transducer.

The result shows that the 6-axis force transducer is significantly stiffer than the bending beam force transducer.

Measurement	6 axis force transducer [Hz]	Bending beam force transducer [Hz]
1	9.28	6.26
2	9.27	6.24
3	9.27	6.24
4	9.25	6.25
5	9.24	6.25
Average	9.27	6.25
Standard deviation	0.016	0.006
Variance	$2.84 \cdot 10^{-4}$	$0.39 \cdot 10^{-4}$

Table B.4. Eigenfrequency measurements of the long cylinder.

The modal parameters, undamped eigenfrequency, f_e, and damping ratio, ζ, are calculated with the program WaveLab 3.87 and are shown in Table B.5.

Setup	f_e [Hz]	ζ [-]	$\beta_{c,SS1}$ [%]	$\beta_{c,SS5}$ [%]
1	6.25	0.010	4.90	1.49
2	9.27	0.011	0.95	0.65

Table B.5. Modal parameters for the two setups.

The data is filtered using a dynamic amplification filter to remove the effects of dynamic amplification. A low-pass cut-off frequency of 5 Hz is used. Furthermore, an analogue low-pass filter with a cut-off frequency of 8 Hz was used in the experiments with the 6-axis force transducer.

The effect of filtering the data is assessed by calculating the standard deviation of the difference between the unfiltered data and the filtered data as shown in equation (B.1).

$$\beta_c = \frac{\text{std}(F_{x,UF} - F_{x,F})}{\text{std}(F_{x,F})} \tag{B.1}$$

This is calculated for a single wave in the force-time series for sea state 1 and sea state 5. The results are shown in Table B.5. These sea states are chosen since the effect of filtering is largest for sea state 1 and smallest for sea state 5. The effect of filtering the data is shown in Figure B.18 and B.19 for sea states 1 and 5 respectively.

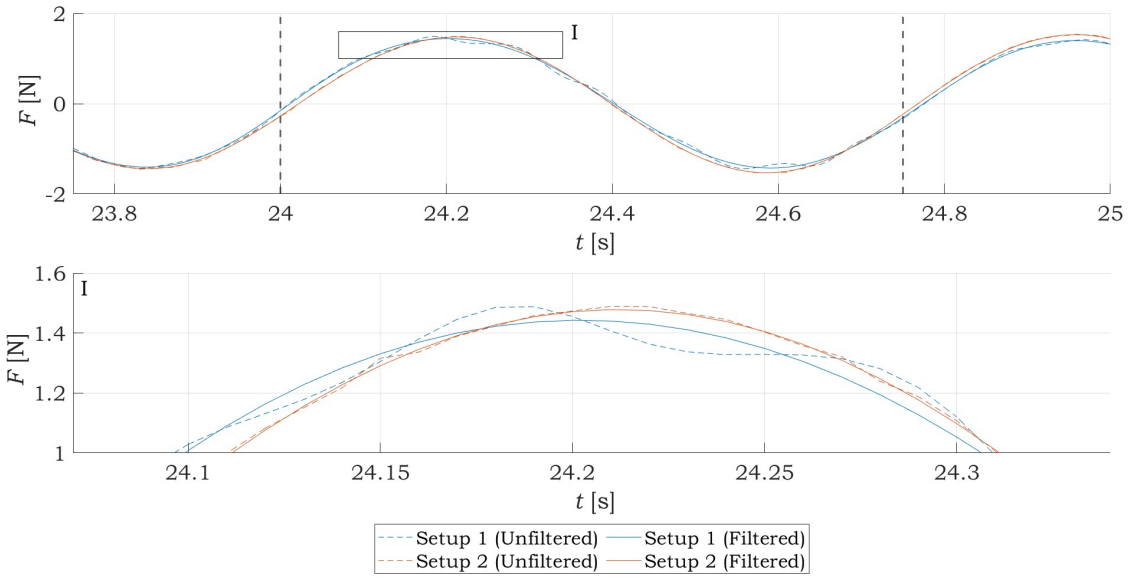

Figure B.18. Effect of filtering on force time series in sea state 1.

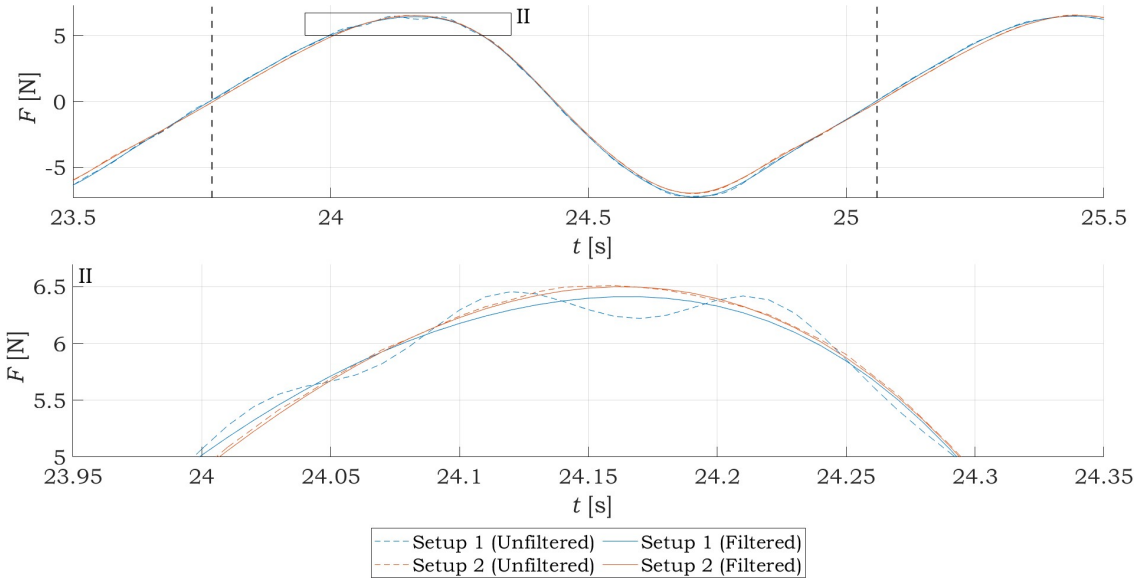

Figure B.19. Effect of filtering on force time series in sea state 5.

As it can be seen in Table B.5 and in the Figures, the effect from filtering, and therefore also dynamic amplification, is largest for setup 1. This is likely because of the lower stiffness of this setup.

B.4.3 Comparison of measurements

To compare the measurements from the two setups, the time series of the force and moment are compared. Firstly a window of the time series is chosen from the surface elevation time series at the model. The chosen window is the first three fully developed waves to minimise the risk of disturbances from reflected waves. The chosen time window is shown in Figure B.20 for sea state 5. In this section sea state 5 is used as an example. The same procedure is performed for the other sea states.

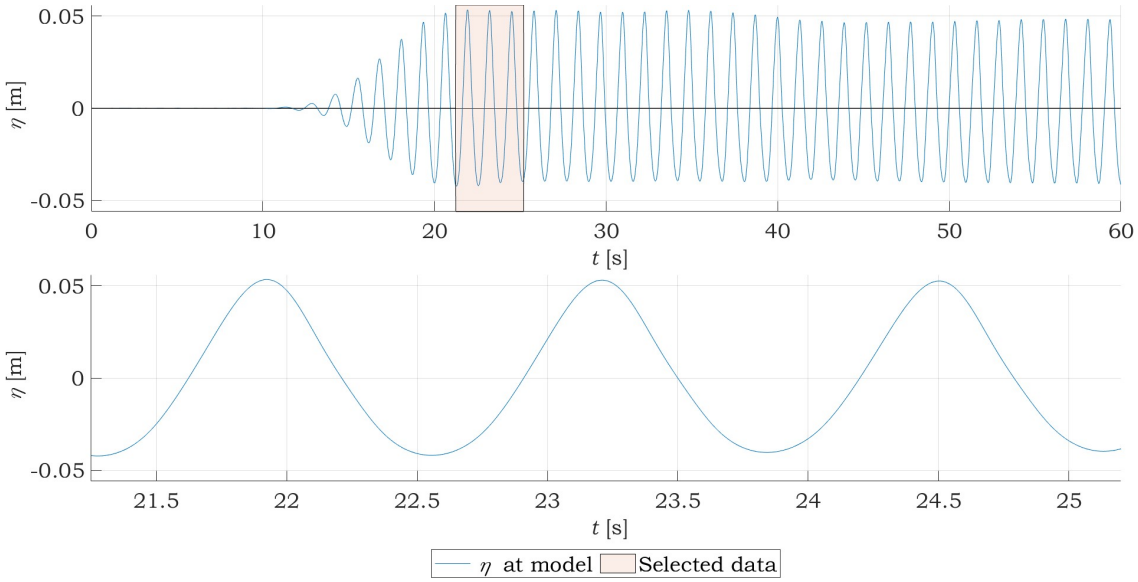

Figure B.20. Selection of time window for sea state 5.

Afterwards, cross-correlation is used to align the force and moment time series with the surface elevation time series measured at the position of the model. The force and moment time series for the two setups are means of the 5 tests that are performed. In Figure B.21, the force and moment time series for the setups are shown along with the surface elevation at the model. Furthermore, a surface elevation calculated with stream function theory (SFT) is shown. This surface elevation is used to calculate the force and moment with the Morison equation. The moments shown in Figure B.21 are at the bottom.

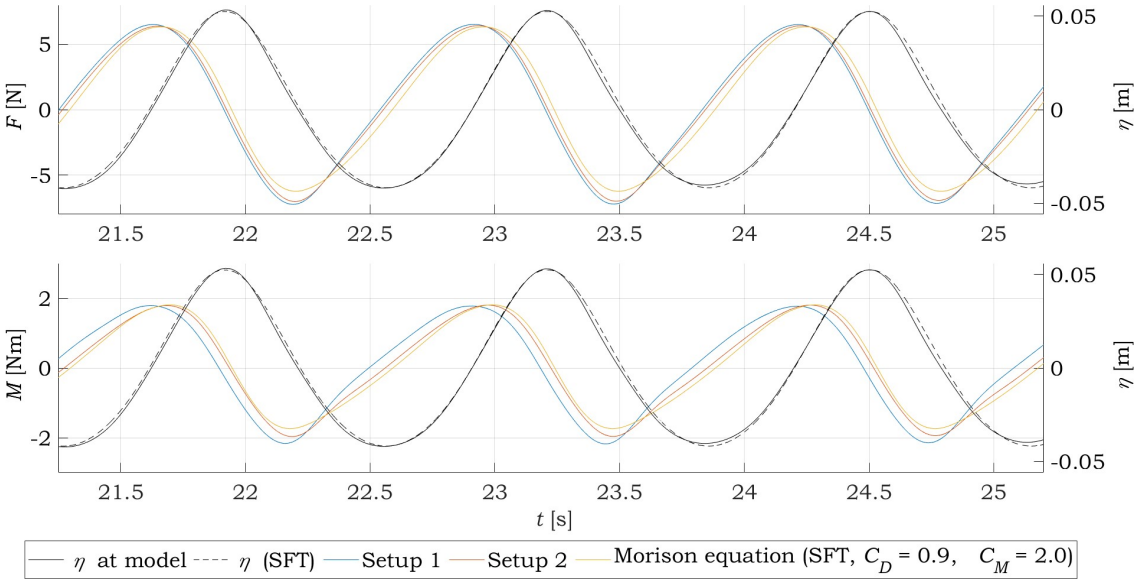

Figure B.21. Force time series and time series for the moment at the bottom shown for sea state 5.

In the Figure, it can be seen that in general there is good agreement between the measurements from setup 1, setup 2 and the results from the Morison equation. However, at the extreme values, there are noticeable differences, particularly for the moment.

These differences in extreme values can also be seen in Figure B.22 where the moment and force are shown.

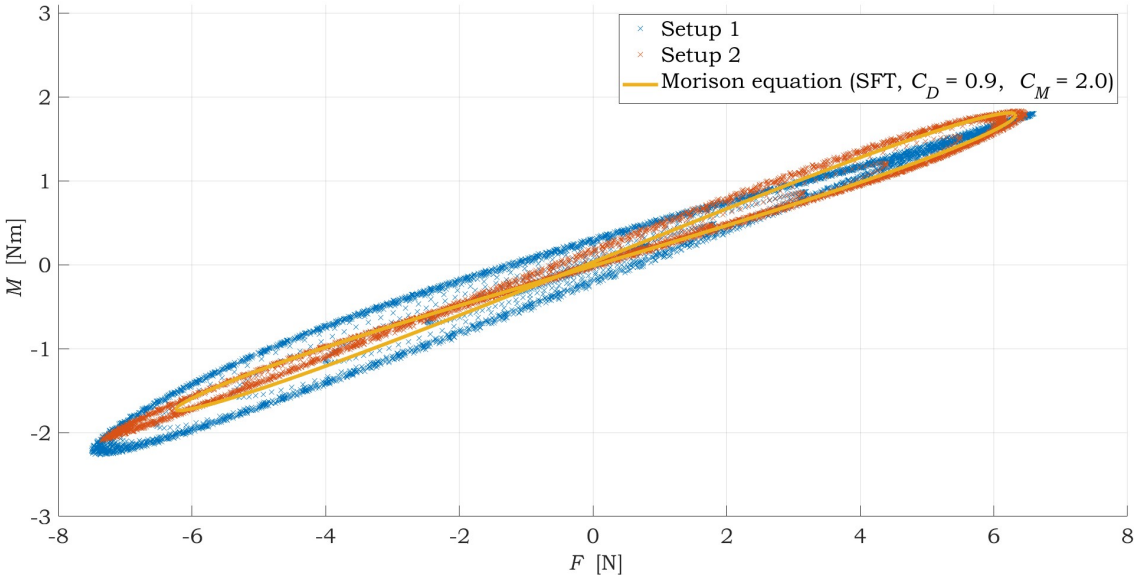

Figure B.22. Moment and force comparison.

It can be seen that the largest differences are at the minimal force and minimal moment where the Morison equation underestimates both the force and the moment.

It is also of interest to calculate the attack point of the force. The attack point is calculated from the bottom. The attack point and force are shown in Figure B.23.

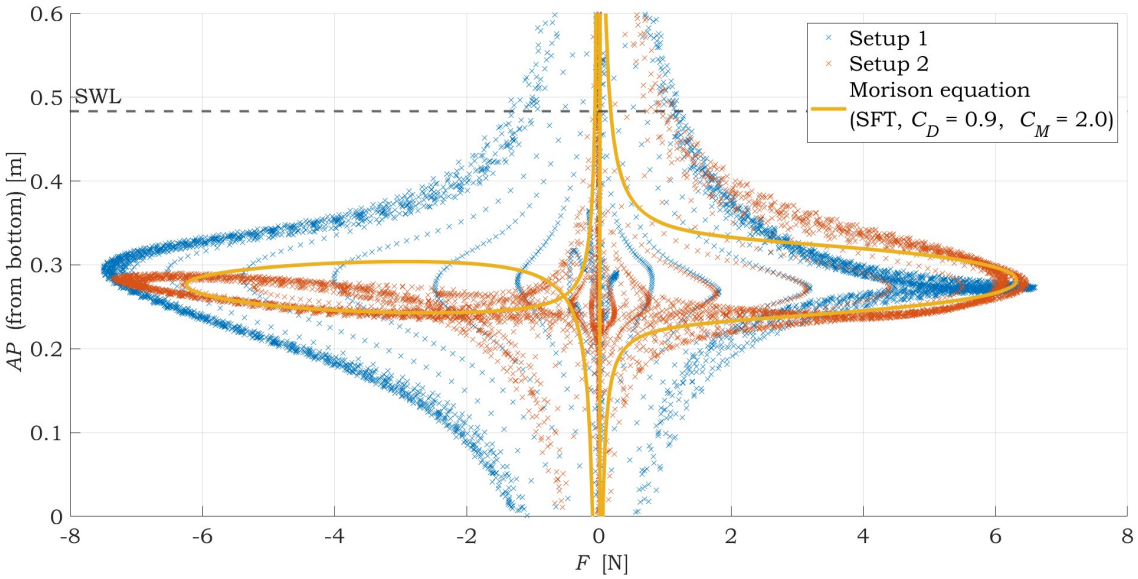

Figure B.23. Attack point and force comparison.

In the Figure, it can be seen that there is good agreement, particularly between setup 1 and the results from the Morison equation when it comes to the position of the attack point. However, setup 2 measures an attack point that is placed lower on the model.

This matches with the calibration of the measurement point of origin of the 6-axis force transducer, which was estimated.

To further compare the results from the two setups and the Morison equation, the maximum force, $F_{x,max}$, is calculated as a mean of the forces from the three first fully developed waves, shown in Figure B.21. In the same way the minimum force, $F_{x,min}$, maximum moment, M_{max}, and minimum moment, M_{min}, is calculated. Furthermore, the attack point for both the largest and smallest values of F_x are determined. This is done for all sea states. The results are shown in Table B.6.

Sea state		$F_{x,max}$ [N]	$F_{x,min}$ [N]	M_{max} [Nm]	M_{min} [Nm]	AP (Pos. F_x) [cm]	AP (Neg. F_x) [cm]
1	Setup 1	1.61	-1.63	0.57	-0.57	35.9	35.6
	Setup 2	1.62	-1.63	0.56	-0.56	34.5	34.0
	Morison eq.	1.58	-1.58	0.56	-0.56	35.2	35.2
2	Setup 1	2.79	-2.92	0.84	-0.90	29.6	31.6
	Setup 2	2.68	-2.84	0.77	-0.82	28.5	29.6
	Morison eq.	2.66	-2.66	0.79	-0.79	29.5	29.5
3	Setup 1	3.37	-3.47	1.12	-1.16	33.0	33.1
	Setup 2	3.29	3.42	1.05	-1.09	32.4	31.8
	Morison eq.	3.20	-3.19	1.05	-1.04	32.6	32.6
4	Setup 1	4.71	-5.04	1.36	-1.55	29.3	30.2
	Setup 2	4.60	-4.90	1.31	-1.41	28.4	29.1
	Morison eq.	4.57	-4.56	1.33	-1.32	28.9	28.8
5	Setup 1	6.51	-7.21	1.78	-2.16	27.3	29.5
	Setup 2	6.40	-6.99	1.80	-1.96	27.8	28.4
	Morison eq.	6.33	-6.24	1.81	-1.74	28.2	27.6

Table B.6. Results from the two setups and the Morison equation.

In the Table, it can be seen that setup 1 consistently measures the largest forces whereas the Morison equation generally results in the smallest forces. For the measured forces from the two setups, it can also be observed that the absolute values of the negative forces are larger than the positive forces. It should also be noted that the measurements from setup 2 consistently result in a lower AP.

The relative deviations, δ, between the results are calculated regarding the minimum absolute value. The relative deviations are shown in Table B.7.

Sea state		$\delta_{F_{x,max}}$ [%]	$\delta_{F_{x,min}}$ [%]	$\delta_{M_{max}}$ [%]	$\delta_{M_{min}}$ [%]	δ_{AP} (Pos. F_x) [%]	δ_{AP} (Neg. F_x) [%]
1	Setup 1	2.34	3.28	2.14	3.05	4.24	4.72
	Setup 2	2.89	3.67	0.00	0.13	0.00	0.00
	Morison eq.	0.00	0.00	0.00	0.00	2.14	3.56
2	Setup 1	4.65	9.66	9.23	14.06	4.01	7.16
	Setup 2	0.55	6.67	0.00	4.74	0.00	0.29
	Morison eq.	0.00	0.00	2.90	0.00	3.66	0.00
3	Setup 1	5.46	8.79	6.83	11.77	2.07	4.24
	Setup 2	2.87	6.98	0.75	4.33	0.00	0.00
	Morison eq.	0.00	0.00	0.00	0.00	0.80	2.67
4	Setup 1	3.01	10.49	3.57	17.30	2.97	4.81
	Setup 2	0.60	7.38	0.00	6.71	0.00	0.98
	Morison eq.	0.00	0.00	1.60	0.00	1.85	0.00
5	Setup 1	2.83	15.46	0.00	24.35	0.00	6.85
	Setup 2	1.16	11.93	1.09	12.51	1.82	2.73
	Morison eq.	0.00	0.00	1.75	0.00	3.31	0.00

Table B.7. Relative deviations between setups and the Morison equation calculated with reference to the minimum absolute value.

From the relative deviations it can be seen that there is generally a good agreement between the results. However, for $F_{x,min}$ and M_{min} there is a significant difference between the measured values, particularly from setup 1, and the results from the Morison equation. This difference seems to increase with increasing wave heights. It is possibly caused by a return current in the wave flume which the Morison equation does not take into account.

B.4.4 Conclusion

After performing an examination to test the agreement between two force transducer setups and analytical results from the Morison equation, it is found that the overall agreement between results from the three methods is good. The best agreement is found when comparing the values measured by the two setups.

By comparing the dynamic amplification of the two setups it is found that setup 1 results in the most dynamic amplification. Therefore, the effect of using a dynamic amplification filter affects the measurements from setup 1 more than setup 2, where little dynamic amplification is experienced.

Based on tests of setup 2 with weights placed with different arms it is determined that the accuracy of setup 2 is satisfactory after a correction of the measurement point of origin is made.

Based on the above and the advantage of being able to measure forces and moments in three directions when using setup 2, it is chosen to use setup 2 to determine the wave forces on the floater, which is done in Chapter 5 on page 27.

B.5 Experiment procedure

When the setup is done, including the wage gauges and the structure that is fixing the 6-axis force transducer, the procedure for each test can go through. The angles that are tested are based on the different shapes. The cylinder is tested in 0°, ±10°, ±20° and ±40° which ensures that the extreme angles are covered.

The floater model, which is represented by a sphere is only tested in 0° since an angle change of the sphere will not change the geometry towards the wave and only slightly change the submerged volume which is assumed will only change the forces slightly and will therefore not be investigated. The disc and the cone are tested in 0°, ±20°, ±30° and ±40°. This is due to the geometry of the floater models being of odd shapes which is more unpredictable and therefore more time is spent getting data for several angles.

The procedure for testing a floater model is first of all setting the floater model at the correct angle. This is done by raising the structure out of the water to set the angle with the least error possible. The angle is measured using a digital protractor. The digital protractor in use can be seen in figure B.24 and B.25. The digital protractor is set to the side of the disc in this example where it is then possible to measure the angle. The angle should be 30° in the example in the figures. The measured angle is the opposite angle, which means that the angle measured is 60°. The accuracy of the angle was within 0.1° according to the digital protractor.

Figure B.24. Setting up a -30° for the disc.

Figure B.25. The final angle of the disc at -30° shown with the digital protrator.

The structure with the floater model is then lowered to the correct height which depends on the angle. An eigenfrequency test is then made on the floater model. The procedure for this is described in the following section. Afterwards, the floater model is ready for impacting waves, which the 6-axis force transducer measures.

B.6 Eigenfrequency

As the eigenfrequencies for the two different force transducers are investigated, the eigenfrequencies for the different floater models are investigated. The system includes a floater model, the 6-axis force transducer, and the structure the force transducer is clamped

onto. The eigenfrequencies for the systems with different floater models are presented in this section. The eigenfrequencies are determined by subjecting the floater model end to an impulse load and measuring the force decay over time. The eigenfrequencies are determined by WaveLab version 3.884. There is performed 5 measurements for each structure in order to have an accurate sample of measurements. The eigenfrequencies for the floater models are determined in the angles the floater models are subjected to, but due to a low difference of the eigenfrequency with the angle, the eigenfrequencies are only shown for 0°. An example of an eigenfrequency test is shown in Figure B.26. The impulse load is subjected by using a string and then releasing it.

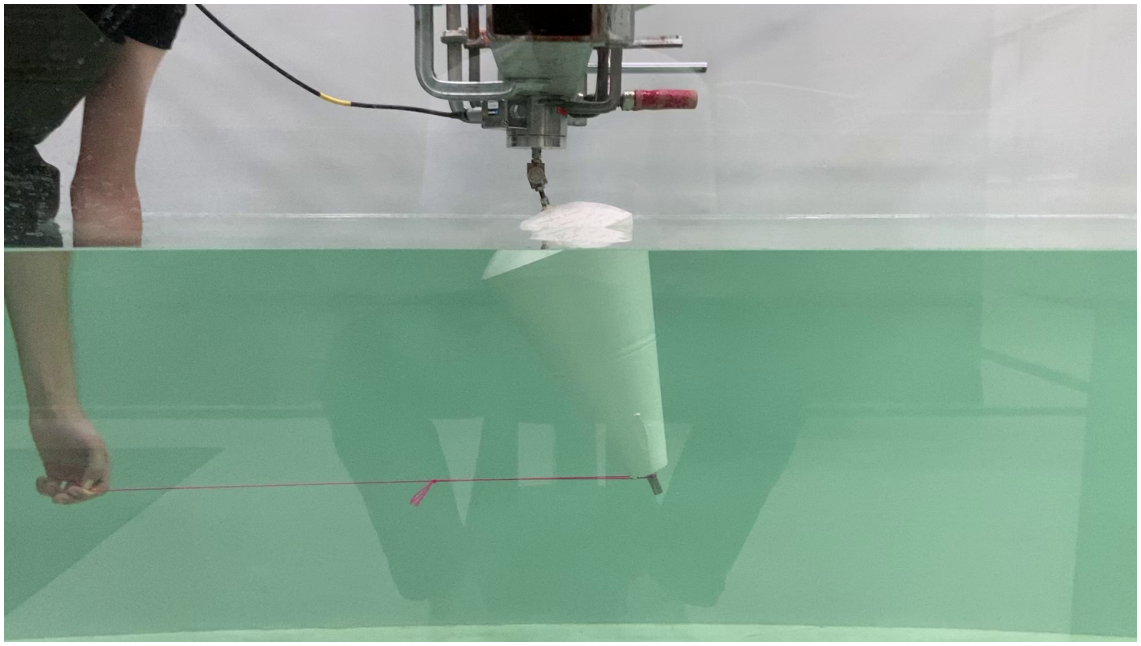

Figure B.26. Eigenfrequency test of the cone in -20°.

The eigenfrequencies for the floater models are shown in Table B.8. The table shows the five measurements, the average, the standard deviation, and the variance. As it can be seen the variance is low which ensures that the eigenfrequency of the system is regular.

Model	Cylindrical [Hz]	Spherical [Hz]	Conical [Hz]	Disc-shaped [Hz]
1	6.10	10.09	6.07	11.67
2	6.10	9.96	6.07	11.21
3	6.10	10.02	6.09	10.97
4	6.10	10.03	6.05	11.66
5	6.10	9.91	6.09	11.64
Average	6.10	10.00	6.07	11.43
Standard deviation	0.002	0.069	0.016	0.322
Variance	$2.30 \cdot 10^{-6}$	$4.75 \cdot 10^{-3}$	$2.69 \cdot 10^{-4}$	0.104

Table B.8. Eigenfrequencies measurements of the floater models at 0°.

B.7 Added mass coefficients

The added mass coefficients calculated by Method 1 with the fitted coefficient for the disc-shaped, conical, and spherical floater models are shown in Figure B.9, B.10, and B.11.

	Angle [°]						
Sea state	-40	-30	-20	0	20	30	40
1	0.20	0.00	0.00	0.49	0.51	0.75	1.44
2	0.41	0.09	0.10	0.53	0.05	0.15	0.62
3	0.03	0.00	0.03	0.49	0.40	0.31	0.70
4	0.17	0.15	0.25	0.48	0.08	0.00	0.00
5	0.00	0.09	0.19	0.32	0.00	0.00	0.00

Table B.9. Added mass coefficients for the disc-shaped floater model.

	Angle [°]				
Sea state	-30	-20	0	20	30
1	0.37	0.39	0.87	1.02	1.30
2	0.77	0.65	0.82	0.69	0.78
3	0.56	0.59	0.80	0.79	0.94
4	0.74	0.68	0.75	0.48	0.50
5	0.54	0.49	0.47	0.17	0.13

Table B.10. Added mass coefficients for the conical floater model.

	Angle [°]
Sea state	0
1	0.89
2	0.78
3	0.80
4	0.65
5	0.36

Table B.11. Added mass coefficients for the spherical floater model.

Motions of floater models C

In this chapter, the additional experiments, calibrations and inputs to numerical models for the motions of the floaters are described.

C.1 Calibration of Qualisys Track Manager

For the QTM to be able to track the markers accurately the cameras have to be calibrated properly. The calibration must be done before doing the first test of the day. The type of calibration method used is an active calibration called the wand calibration method. [Qualisys, 2020]

The calibration used an L-shaped reference structure and a 300 mm carbon wand from the Qualisys carbon fiber wand kit. The L-shaped reference structure is an L-frame with four reflective markers on top positioned in a known accurate position. The 300 mm carbon wand is a wand with two reflective markers positioned with exactly 300.9 mm between them.

Using the L-shaped reference structure generates a coordinate system that QTM can track. The L-shaped reference structure must be aligned with the expected coordinate system of the setup. To make sure the L-shaped reference structure was placed in the same location every time a stand was created to align the L-shaped reference structure with the hinge for the floater model. The stand can be seen in Figure C.1. The stand has a small slit that the L-shaped reference structure fits on to align it the same way each time. The L-shaped reference structure has two small levels that are checked before each calibration to ensure the L-shaped reference structure is level. The base of the stand is aligned with the hinge of the floater model by placing it next to the steel plate of the hinge.

Figure C.1. Stand for placing L-shaped reference structure

The calibration wand shown in Figure C.2 is used to calibrate the volume in which QTM accurately measure the 3D position of the markers, by inputting the exact distance between the two markers in QTM. For an accurate calibration, the wand must be moved in the entire volume expected to be used for measurements. Therefore the wand is moved in the volume of the cylinder's expected motions. The calibration was done for

40 seconds to ensure coverage of the entire volume.

Figure C.2. Qualisys 300 mm Calibration wand

C.2 Activation of other degrees of freedom

During the experiments on moving floaters the rotation should ideally only be in in one direction (1-DoF-system). Therefore it is examined whether other DoF are activated during the experiment.

In Figure C.3 the roll and yaw directions are shown for the cylindrical floater model in sea state 1 as an example.

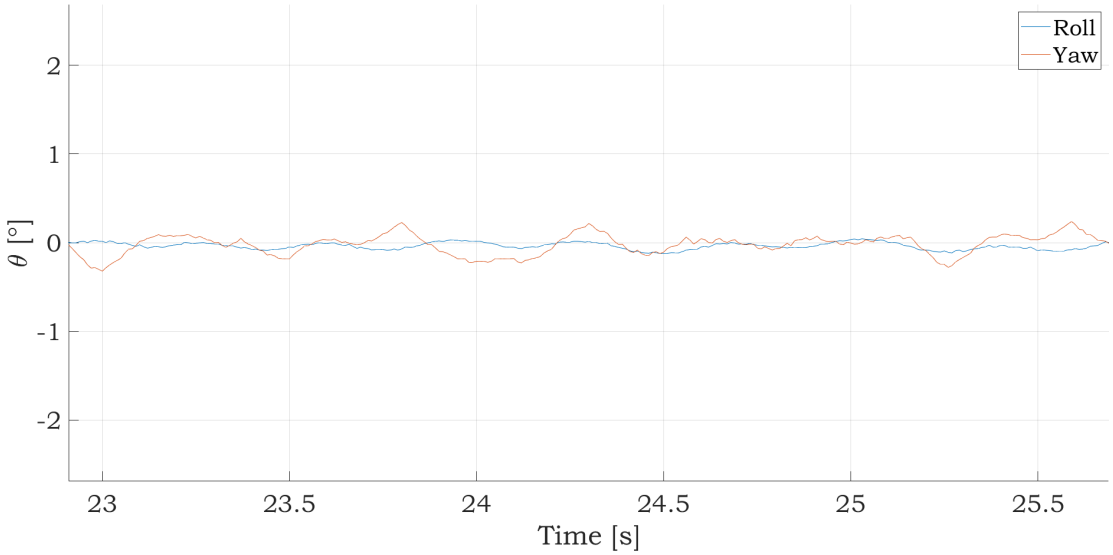

Figure C.3. Plot showing the rotations in the roll and yaw direction for the cylinder in sea state 1 test 1.

As it can be seen in the figure the movements in the other DoF are minimal. This is also examined for the other floater models and sea states and it is concluded that the influence of other DoF is negligible and therefore, it can be considered as a 1-DoF system.

C.3 Experimental determination of mass moment of inertia

In this section the experiment performed to determine the mass moment of inertia of the floaters is described.

The mass moment of inertia describes the resistance of an object against angular acceleration around a rotational axis. Therefore, it is necessary to know the mass moment of inertia to describe the motions of the floaters.

To determine the mass moment of inertia of a floater it is suspended at the end of a piece of string to act like a physical pendulum. To allow for easier measurement of the period of oscillation a long string is used. A picture from the experiment is shown in Figure C.5 and a sketch of the experimental setup is shown in Figure C.4 where CM indicates the center of mass.

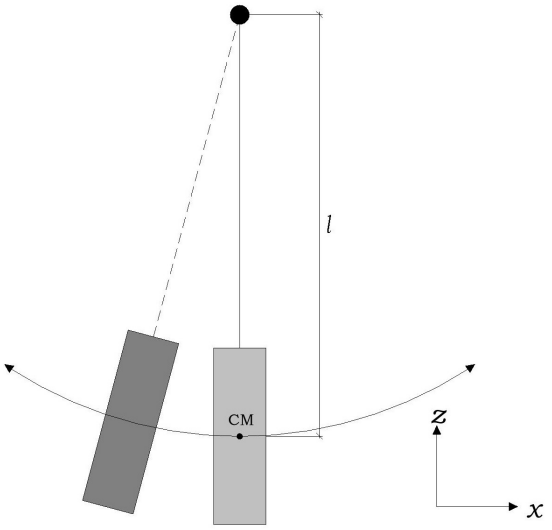

Figure C.4. Sketch of the pendulum experiment.

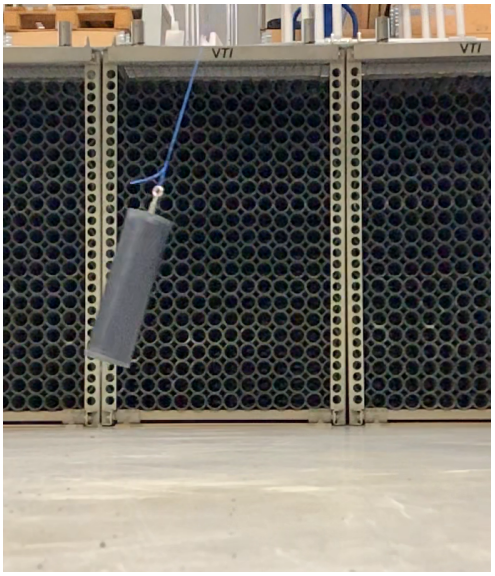

Figure C.5. Picture from the pendulum experiment.

The pendulum is held at an angle and then released to oscillate freely. The oscillation of the pendulum is recorded with a camera filming at 240 frames per second.

After the experiment the recorded videos are analysed frame-by-frame to determine the period of the pendulum. The period is determined as the average of several oscillations.

The theoretical period of a physical pendulum is given by Equation (C.1).

$$T = 2\pi \cdot \sqrt{\frac{I}{m \cdot g \cdot l}} \tag{C.1}$$

Where:

T	Period [s]
I	Mass moment of inertia [$\mathrm{m} \cdot \mathrm{kg}^2$]
m	Mass of floater model [kg]
g	Gravitational acceleration [$\mathrm{m/s}^2$]
l	Distance from centre of mass to point of rotation [m]

Therefore, the mass moment of inertia can be determined by solving for I in Equation (C.2). The mass moment of inertia is given by Equation (C.2).

$$I = \frac{T^2 \cdot m \cdot g \cdot l}{4\pi^2} \tag{C.2}$$

The measured average period can then be used to determine I. However, the mass moment of inertia determined from the experiment is around the point of rotation used in the experiment and not around the hinge, which is the actual point of rotation for the floater. Therefore, the parallel-axis theorem is used to correct the mass moment of inertia and determine the moment of inertia around the hinge. The parallel-axis theorem can be used to find the mass moment of inertia around any axis parallel to the first axis if the distance between the axes, d, is known. The parallel-axis theorem is shown in Equation (C.3). [Wolfson, 2016]

$$I = I_{CM} + m \cdot d^2 \tag{C.3}$$

Where:

I_{CM}	Mass moment of inertia around centre of mass [$\mathrm{m} \cdot \mathrm{kg}^2$]
d	Distance between axes [m]

In Table C.1 the results for the mass moment of inertia around the hinge for the different floater models are shown.

Floater model	I around hinge [$\mathrm{kg} \cdot \mathrm{m}^2$]
Cylindrical	$4.05 \cdot 10^{-1}$
Disc-shaped	$3.35 \cdot 10^{-1}$
Conical	$3.90 \cdot 10^{-1}$
Spherical	$3.34 \cdot 10^{-1}$

Table C.1. Mass moment of inertia around the hinge for the floater models.

C.4 Experimental determination of hydrodynamic damping

In this section the method used to determine the damping coefficients using decay tests is described. Experimental damping coefficients are used in the third numerical model *NM3*.

The hydrodynamic damping coefficient is determined with the method of extinction coefficients as described by Himeno [1981]. The method is described using the cylindrical floater model. Afterwards the results for the other floater models are shown. The damping coefficient is determined using data from the decay tests performed on the floater models.

This is done by fitting a third order polynomial to the measured values of the decrease in amplitude per half cycle, $\Delta\theta_a$. The mean amplitude is given as $\theta_a = \frac{\theta_{n-1}+\theta_n}{2}$ and the decrease in amplitude per half cycle is given as $\Delta\theta_a = \theta_{n-1} - \theta_n$. A half cycle is from trough to peak or vice versa as illustrated in Figure C.6.

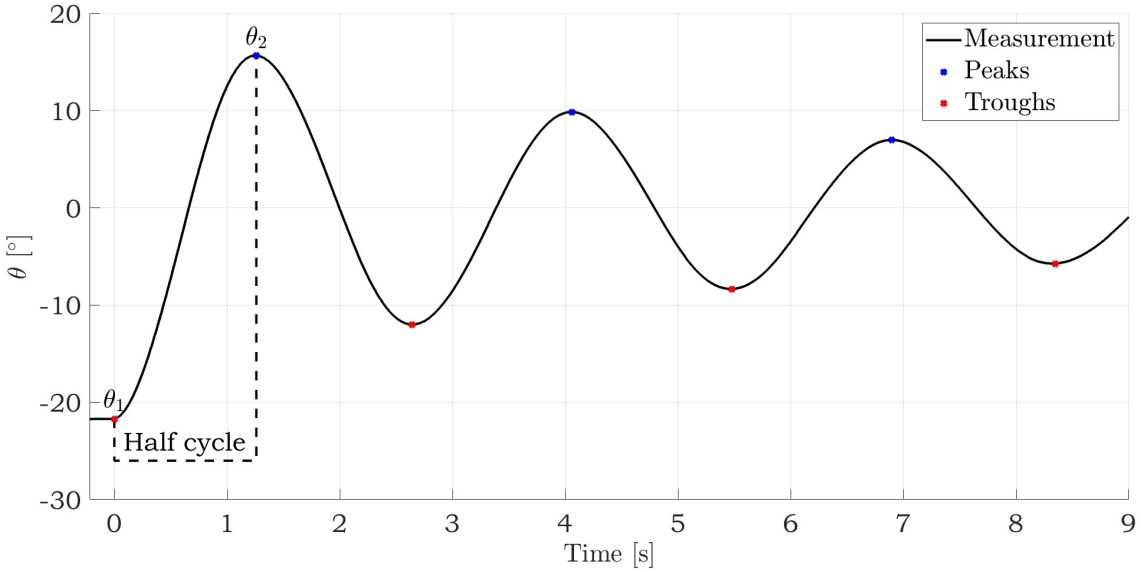

Figure C.6. Decay time series with half cycle shown.

$\Delta\theta_a$ can be expressed as a third order polynomial which depends on the extinction coefficients a, b and c, as shown in Equation (C.4).

$$\Delta\theta_a = a \cdot \theta_a + b \cdot \theta_a^2 + c \cdot \theta_a^3 \tag{C.4}$$

The extinction coefficients are found using a cubic fit which is forced through the origin. This cubic fit is shown along with measured $\Delta\theta_a$ in Figure C.7. The measured values are from five decay tests performed on the floater model.

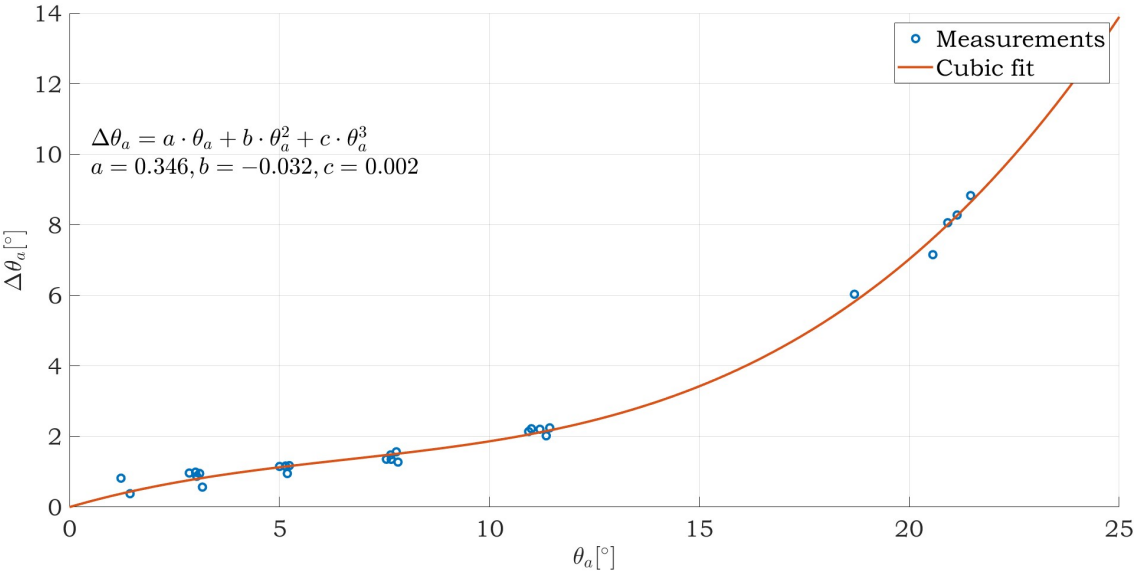

Figure C.7. Cubic fit to determine extinction coefficients and resulting fit for $c_{h,e}$.

After finding the extinction coefficients a linear equivalent damping coefficient, $c_{h,e}$, can be determined from Equation (C.5).

$$\frac{\pi \cdot c_{h,e}}{2\omega_d} = a + b \cdot \theta_a + c \cdot \theta_a^2 \tag{C.5}$$

The linear equivalent damping coefficient is shown in Figure C.8.

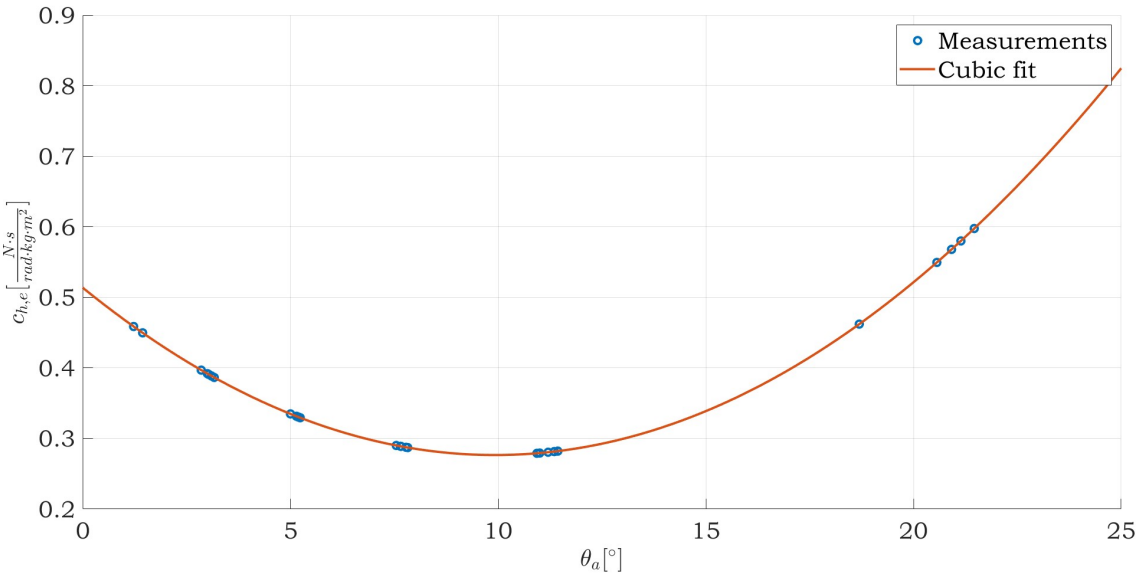

Figure C.8. Cubic fit for linear equivalent damping, $c_{h,e}$, determined from extinction coefficients.

The damping coefficient, c_h, is then determined from $c_{h,e}$ as $c_h = c_{h,e} \cdot (I + m_h)$.

The linear equivalent damping coefficient for the other floater geometries are determined using the same method as described for the cylindrical floater model. The results for the three other floaters are shown in the following sections.

C.4.1 Disc-shaped floater model

In Figure C.9 the cubic fit for the disc-shaped floater model is shown along with measured values of $\Delta\theta_a$

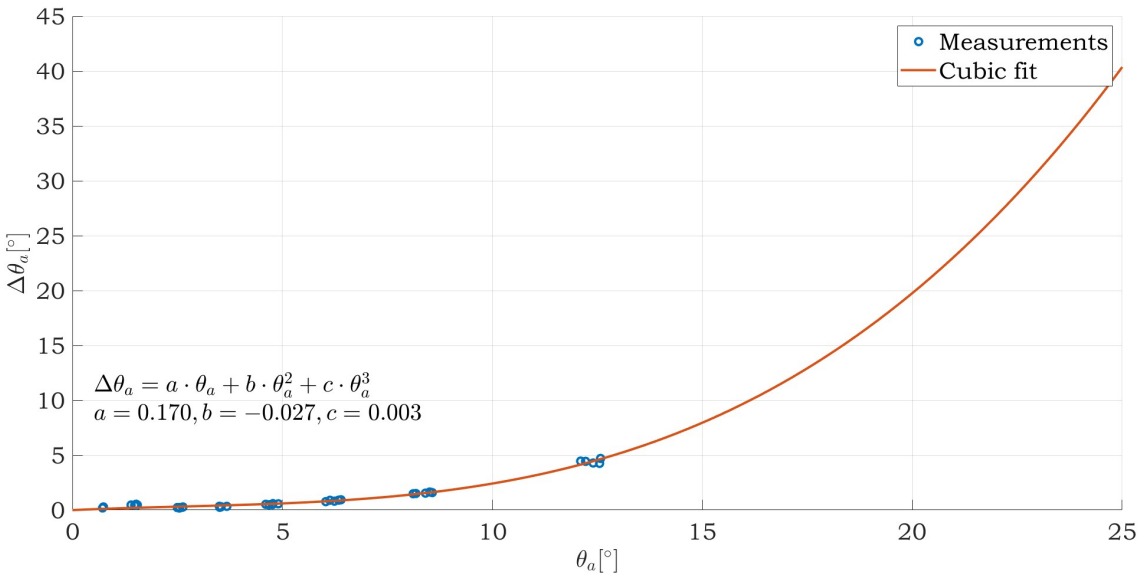

Figure C.9. Cubic fit to determine extinction coefficients and resulting fit for $c_{h,e}$.

The linear equivalent damping coefficient for the disc-shaped floater model is shown in Figure C.10.

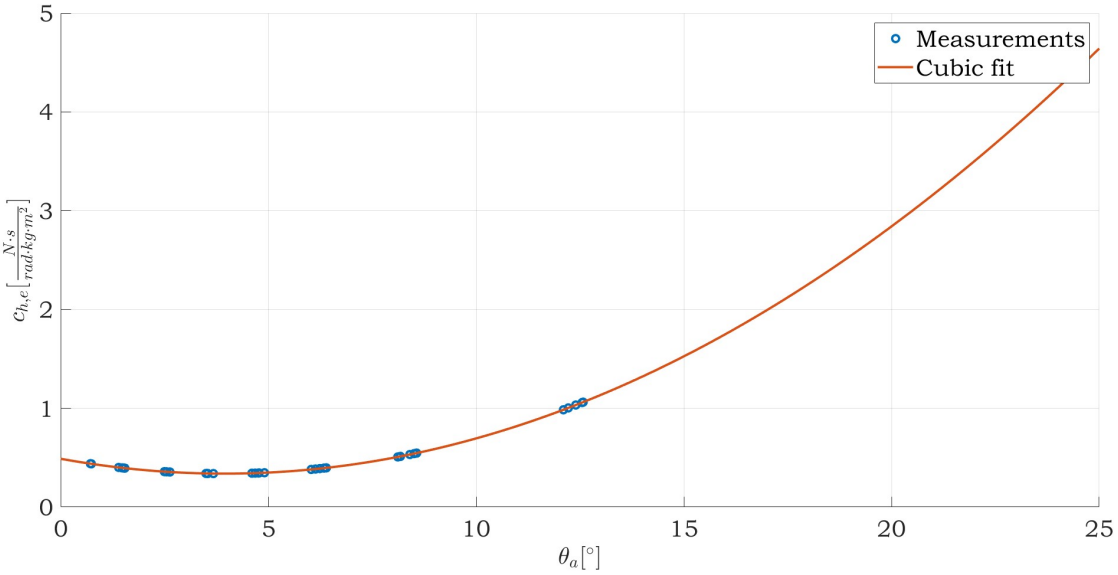

Figure C.10. Cubic fit for linear equivalent damping, $c_{h,e}$, determined from extinction coefficients.

C.4.2 Conical floater model

In Figure C.11 the cubic fit for the conical floater model is shown along with measured values of $\Delta\theta_a$

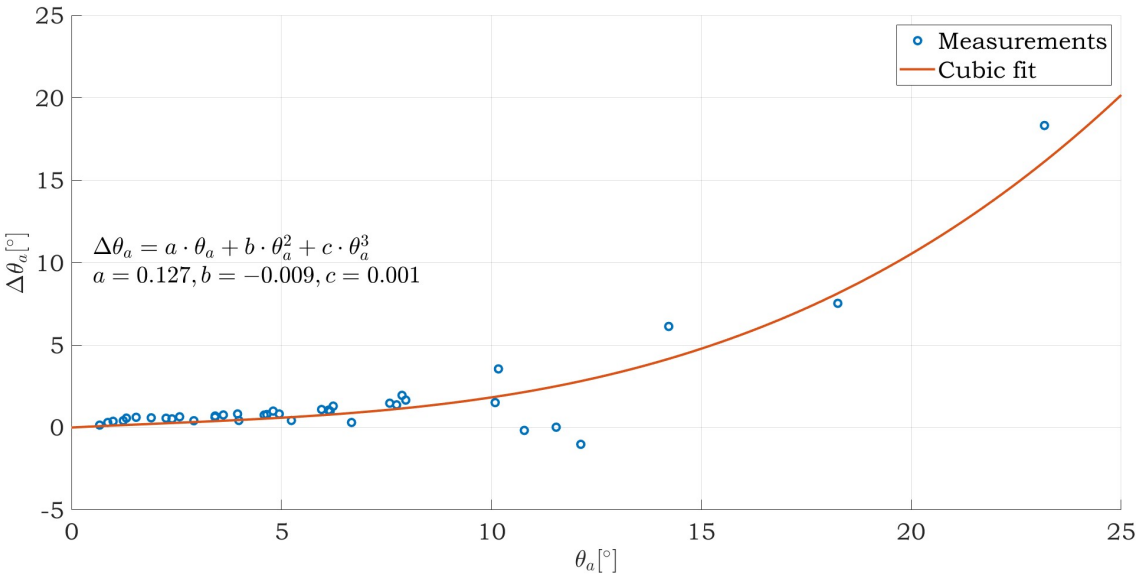

Figure C.11. Cubic fit to determine extinction coefficients and resulting fit for $c_{h,e}$.

The linear equivalent damping coefficient for the conical floater model is shown in Figure C.12.

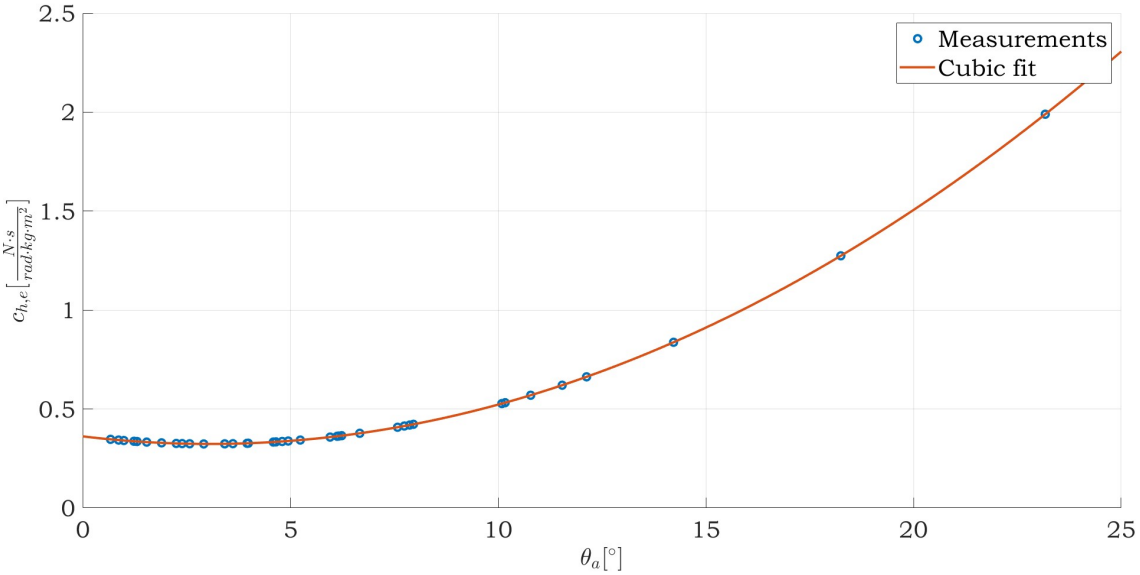

Figure C.12. Cubic fit for linear equivalent damping, $c_{h,e}$, determined from extinction coefficients.

C.4.3 Spherical floater model

In Figure C.13 the cubic fit for the spherical floater model is shown along with measured values of $\Delta\theta_a$

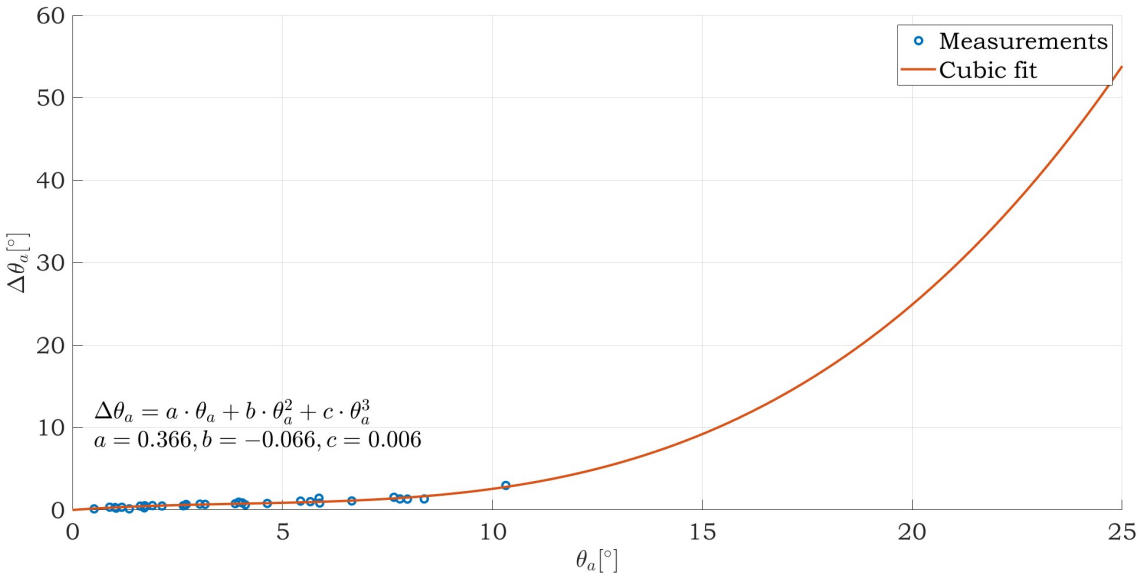

Figure C.13. Cubic fit to determine extinction coefficients and resulting fit for $c_{h,e}$.

The linear equivalent damping coefficient for the spherical floater model is shown in Figure C.14.

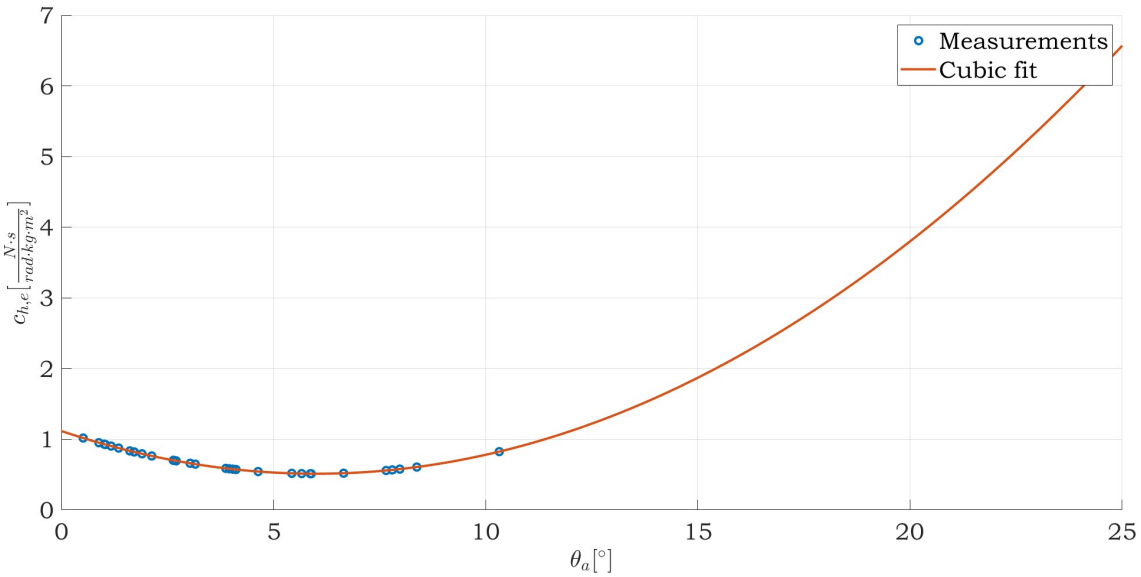

Figure C.14. Cubic fit for linear equivalent damping, $c_{h,e}$, determined from extinction coefficients.

C.5 NEMOH inputs to numerical models

The numerical models *NM2* and *NM3* both use results from the BEM-code NEMOH. These results are presented in the following sections.

C.5.1 Convergence study on cylindrical floater model

As an initial step in the NEMOH calculations, a convergence study is performed on the cylindrical floater model at an angle of $\theta = 0\,°$. This is done in order to determine the number of panels in the mesh that is necessary to achieve a sufficient level of accuracy. The convergency is obtained by investigating for an estimated needed amount of panels and almost twice as many. It is estimated that the needed amount of panels was 743. The following figures show the outputs from NEMOH for both calculations with different amounts of panels. In Figure C.15, a comparison between the added mass coefficients for the two calculations is shown.

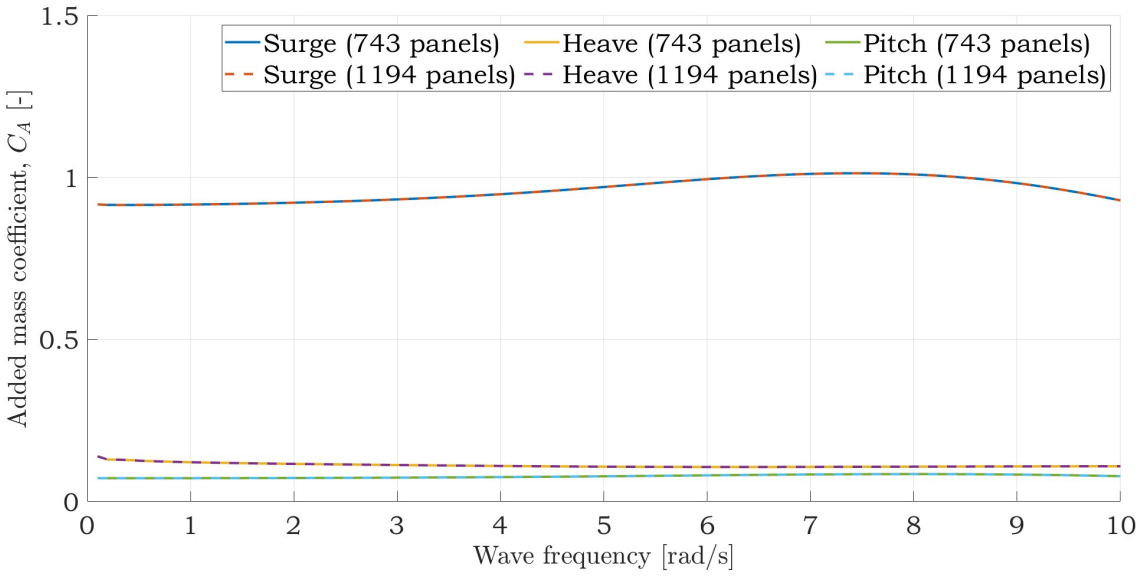

Figure C.15. Convergency study for the added mass coefficient, C_A.

As can be seen, the added mass coefficients are approximately the same for both calculations, which means that convergence is obtained for the added mass coefficient.

The damping coefficients for surge, heave, and pitch are converged as well with 743 panels which is shown in Figure C.16.

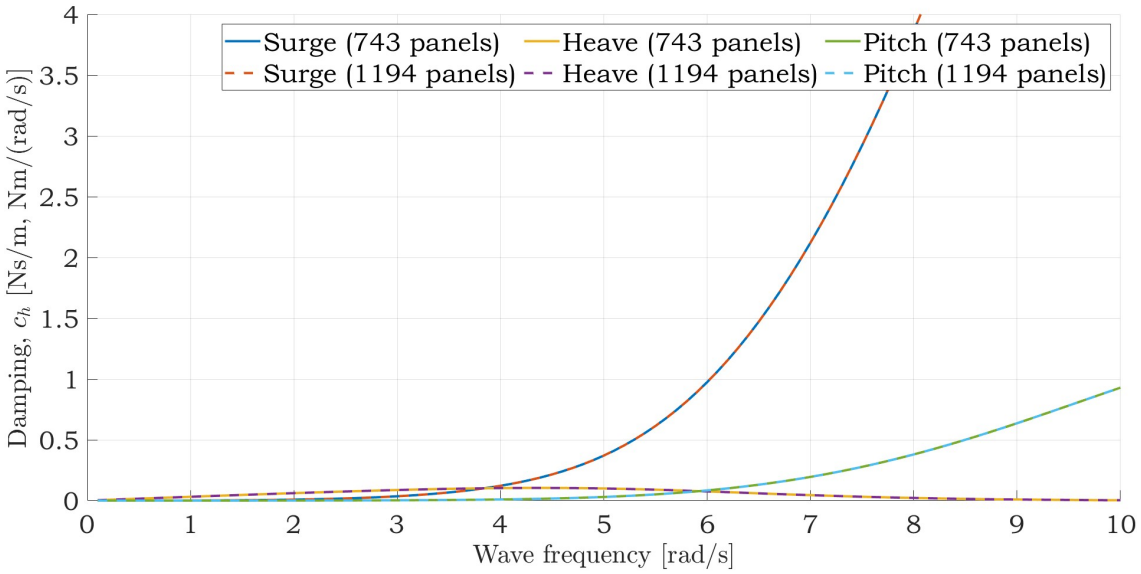

Figure C.16. Convergency study for the damping coefficient, c_h.

As it can be seen in the figure the normalised surge force and corresponding phase are converged. The phase slightly deviates for small wave frequencies and the normalised force slightly deviates for higher wave frequencies, which can be seen in Figure C.17. The deviations are assumed to be negligible.

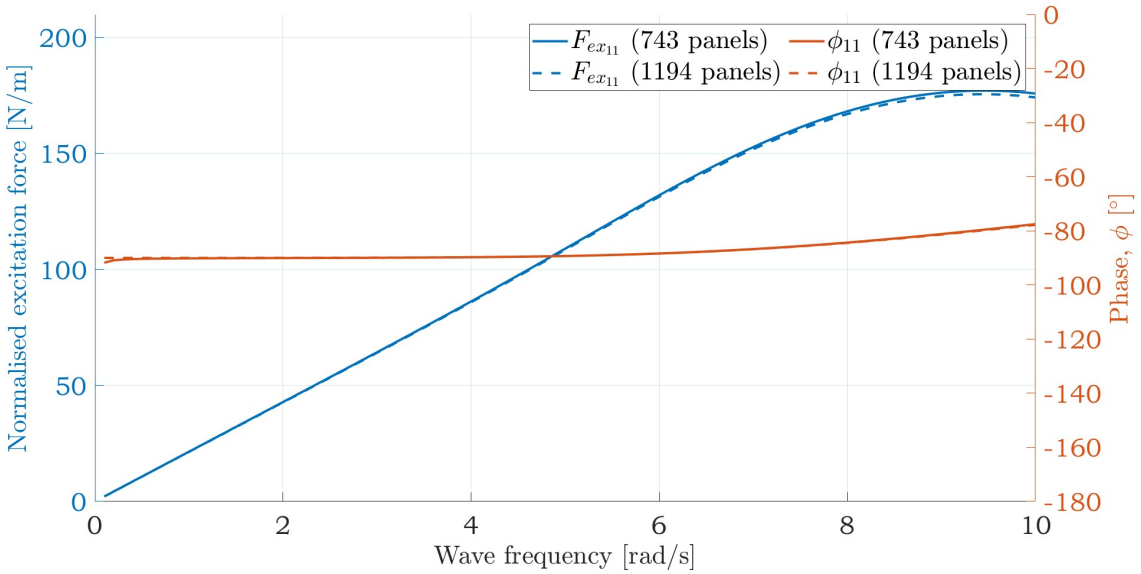

Figure C.17. Convergency study for surge.

The convergency study for the normalised heave and corresponding phase are shown in Figure C.18. As shown the heave deviates for smaller wave frequencies for the two calculations.

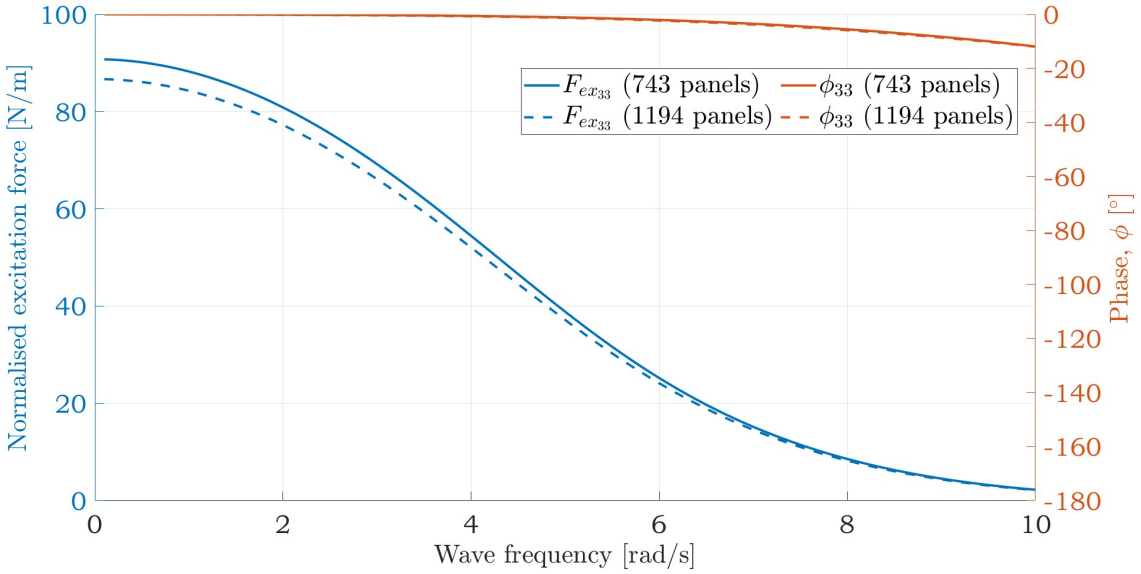

Figure C.18. Convergency study for heave.

The normalised pitch and corresponding phase are converged for the calculation with 743 panels which is shown in Figure C.19.

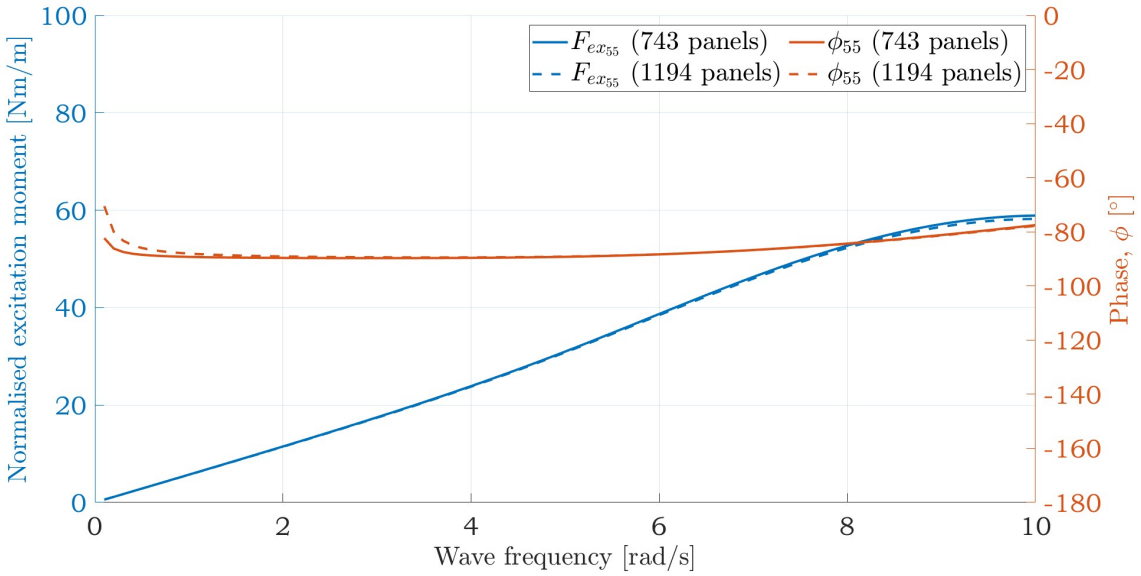

Figure C.19. Convergency study for pitch.

Overall it is determined that 743 panels are enough to achieve convergence for the cylindrical floater model at an angle of 0 °. Therefore, it is ensured that the meshes for the different angles and other floater models have the same or a finer mesh than the one for the cylindrical floater model at 0 °.

C.5.2 Cylindrical floater model

In this section, the NEMOH results for the cylindrical floater model are shown.

In Table C.2 the number of panels used in the meshes for the cylindrical floater is shown.

Angular position θ [°]	-40	-30	-20	-15	-10	-5	0	5	10	15	20	30	40
No. of panels [-]	908	895	836	902	801	856	743	855	801	902	838	896	908

Table C.2. No. of panels in the meshes used for the NEMOH calculations for the cylindrical floater model.

In the following sections the NEMOH results for added mass, damping, and wave excitation moment for the cylindrical floater model are shown.

Added mass

In Figure C.20, the normalised added mass for the cylindrical floater model is shown.

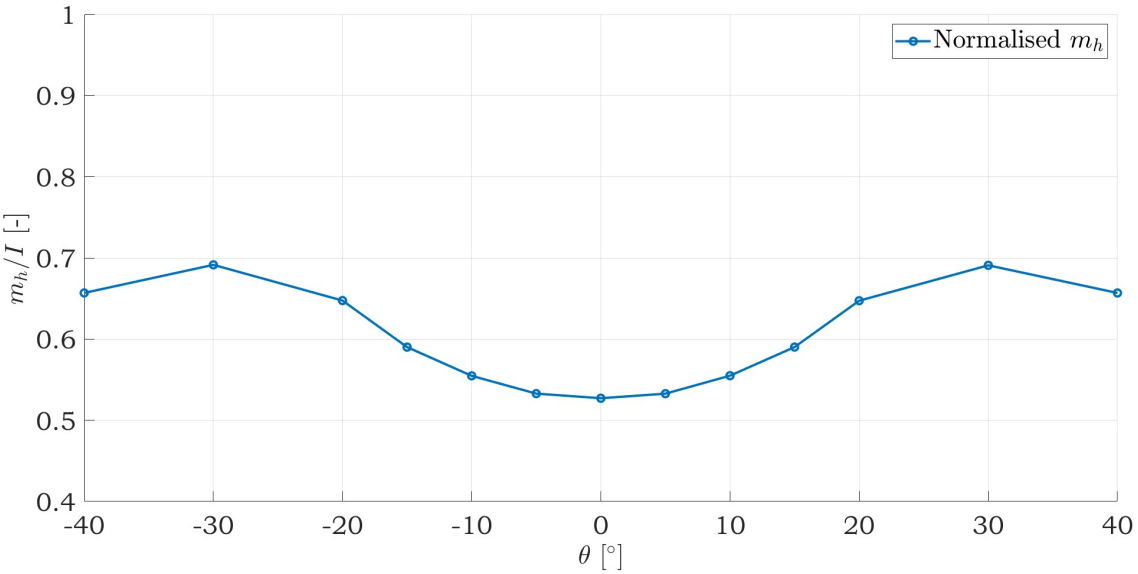

Figure C.20. Normalised added mass at θ from -40° to 40° for the cylindrical floater.

Damping

In Figure C.21 the damping coefficients for the cylindrical floater model for the different angular positions are shown.

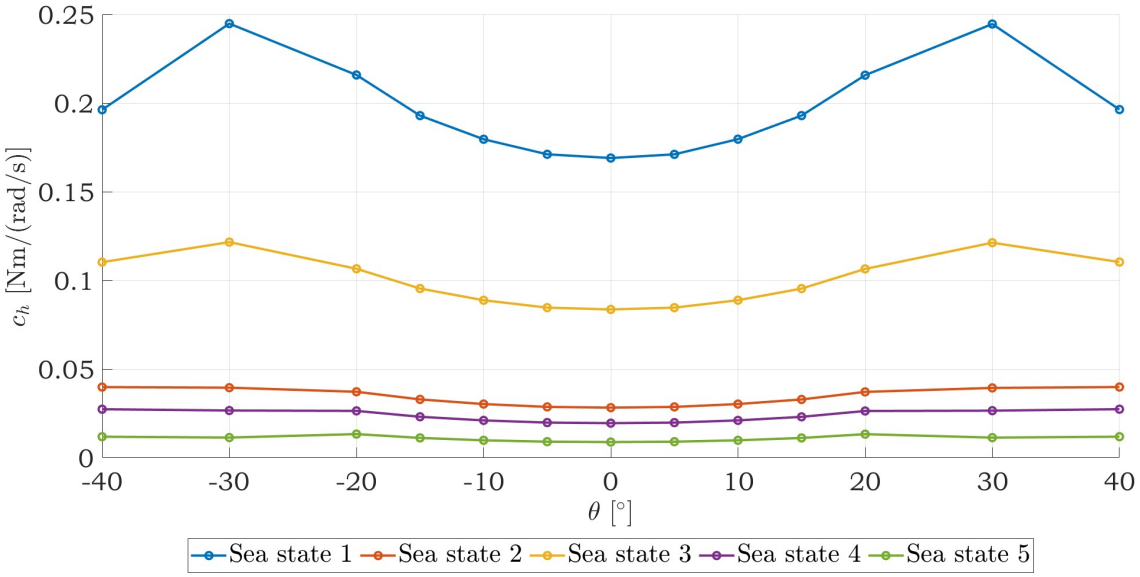

Figure C.21. Damping coefficients at θ from -40° to 40° for the cylindrical floater.

Wave excitation forces

In Figure C.22 the normalised moment is shown for the different angular positions.

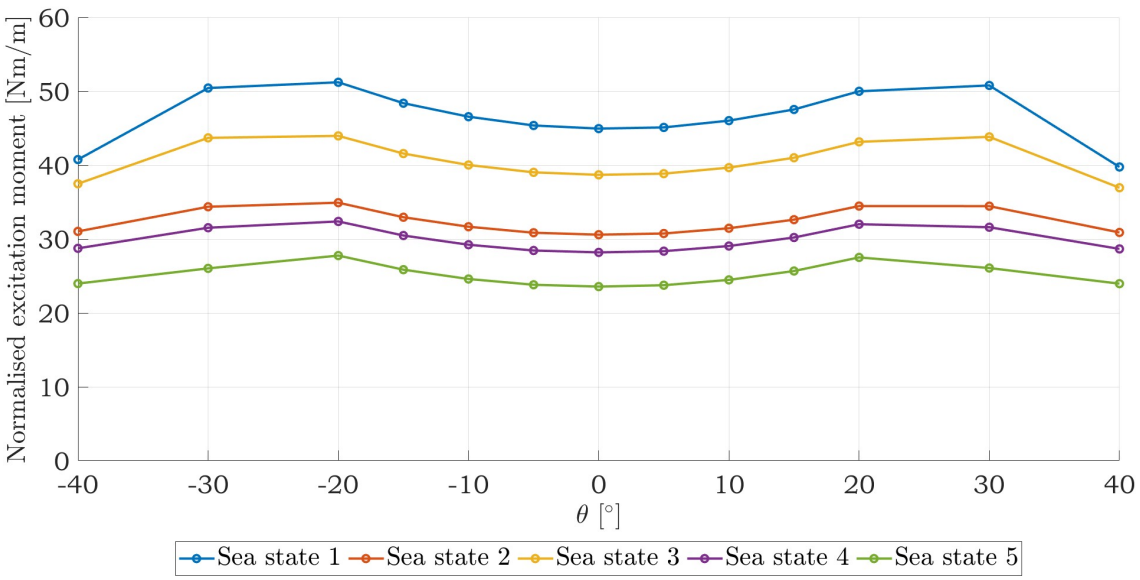

Figure C.22. Normalised wave excitation moment at θ from -40° to 40° for the cylindrical floater.

C.5.3 Disc-shaped floater model

In this section the NEMOH results for the disc-shaped floater model are shown.

In Table C.3 the number of panels used in the meshes for the disc-shaped floater are shown.

Angular position θ [°]	-40	-30	-20	-10	0	10	20	30	40
No. of panels [-]	1564	1495	1181	1016	953	1016	1181	1495	1564

Table C.3. No. of panels in the meshes used for the NEMOH calculations for the disc-shaped floater model.

In the following sections the NEMOH results for added mass, damping and wave excitation moment for the disc-shaped floater model are shown.

Added mass

In Figure C.23 the normalised added mass for the disc-shaped floater model is shown.

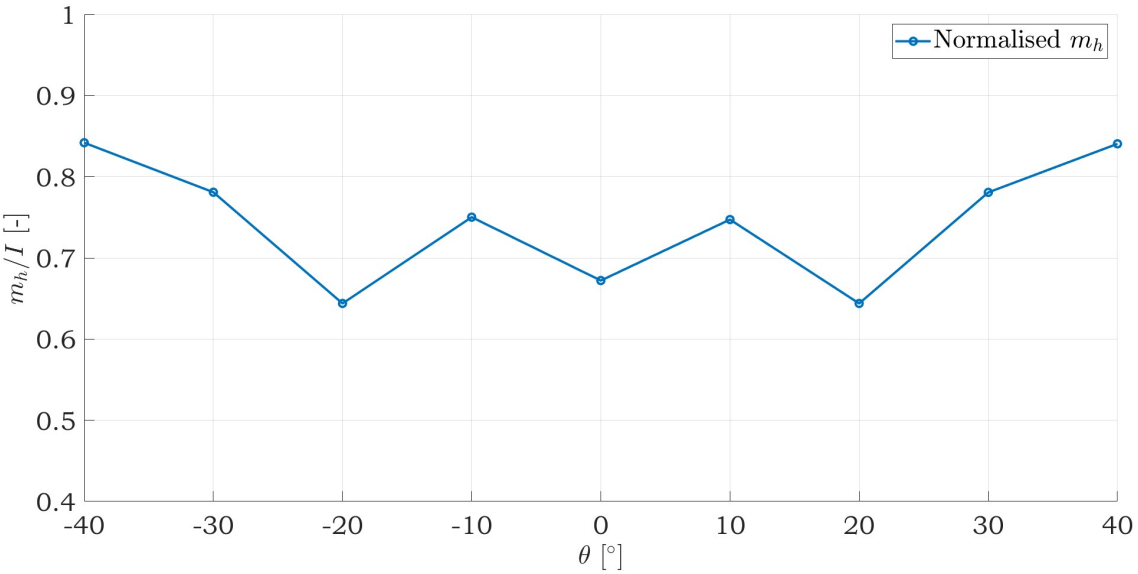

Figure C.23. Normalised added mass at θ from -40° to 40° for the disc-shaped floater.

Damping

In Figure C.24 the damping coefficients for the disc-shaped floater model for the different angular positions are shown.

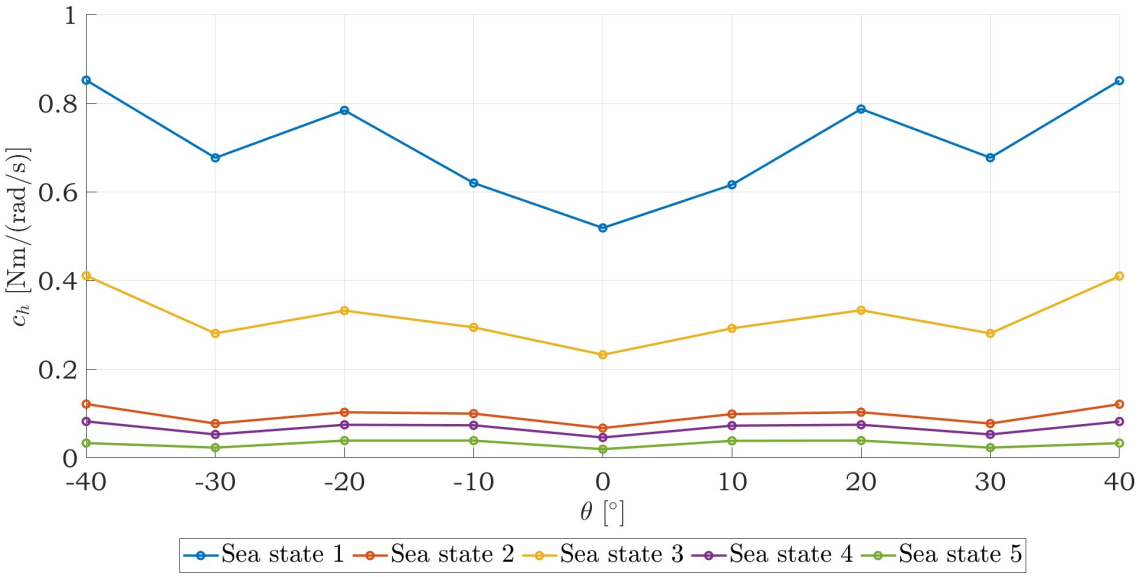

Figure C.24. Damping coefficients at θ from -40° to 40° for the disc-shaped floater model.

Wave excitation forces

In Figure C.25 the normalised moment is shown for the different angular positions.

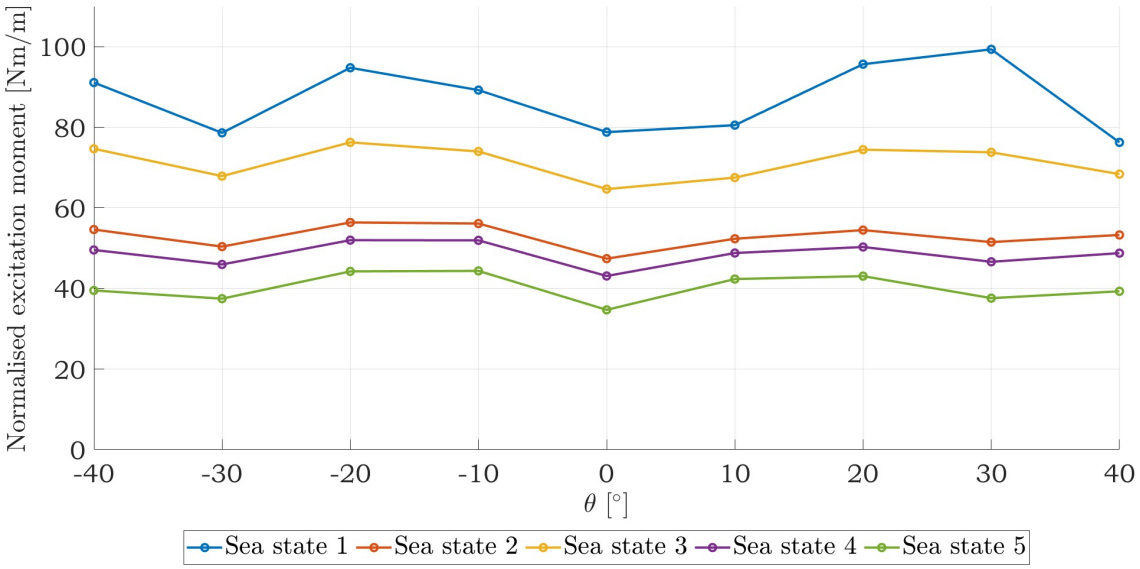

Figure C.25. Normalised wave excitation moment at θ from -40° to 40° for the disc-shaped floater model.

C.5.4 Conical floater model

In this section the NEMOH results for the conical floater model are shown.

In Table C.4 the number of panels used in the meshes for the conical floater are shown.

Angular position θ [°]	-40	-30	-20	-10	0	10	20	30	40
No. of panels [-]	1464	1329	1338	973	855	973	1338	1331	1464

Table C.4. No. of panels in the meshes used for the NEMOH calculations for the conical floater model.

In the following sections the NEMOH results for added mass, damping and wave excitation moment for the conical floater model are shown.

Added mass

In Figure C.26 the normalised added mass for the conical floater model is shown.

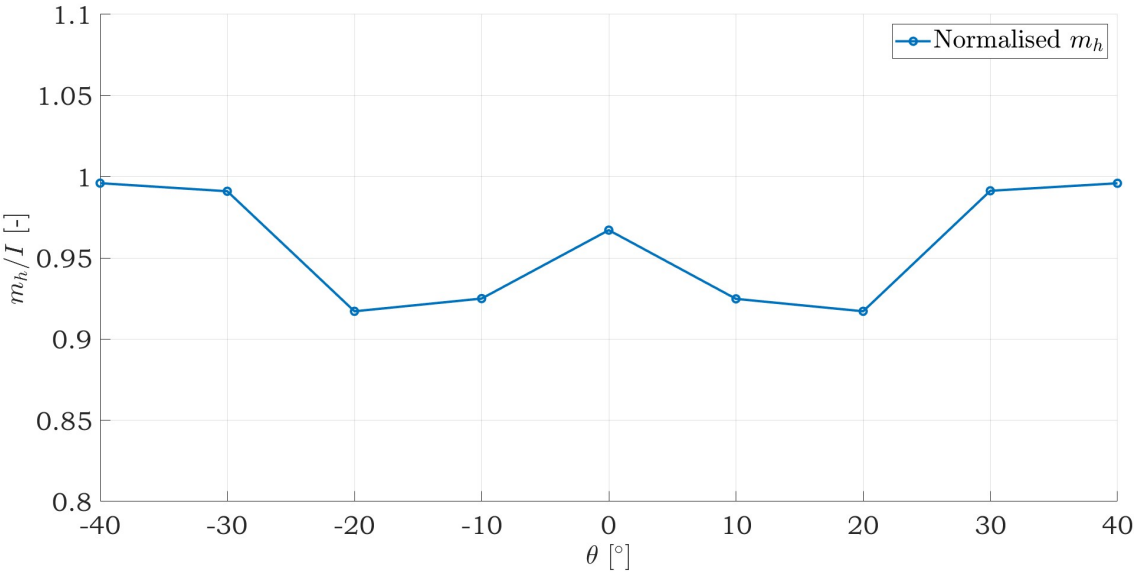

Figure C.26. Normalised added mass at θ from -40° to 40° for the conical floater.

Damping

In Figure C.27 the damping coefficients for the conical floater model for the different angular positions are shown.

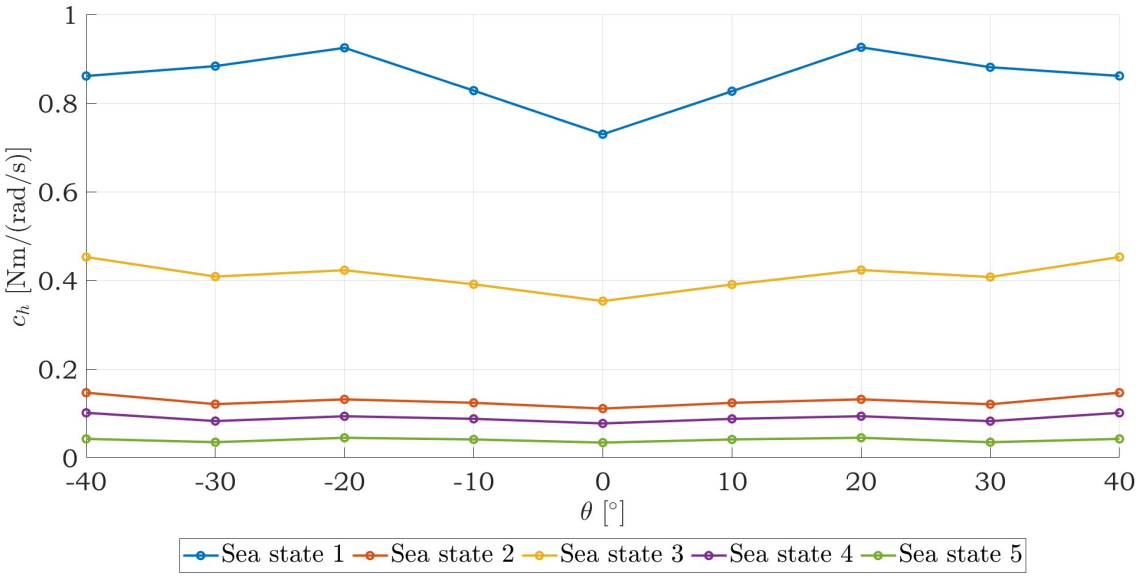

Figure C.27. Damping coefficients at θ from -40° to 40° for the conical floater model.

Wave excitation forces

In Figure C.28 the normalised moment is shown for the different angular positions.

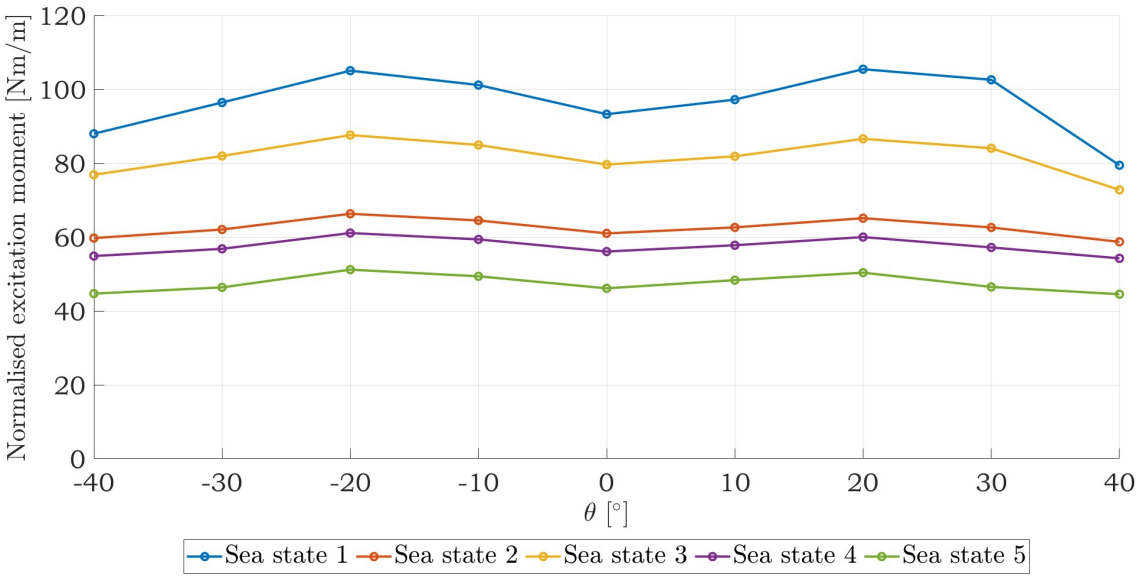

Figure C.28. Normalised wave excitation moment at θ from -40° to 40° for the conical floater model.

C.5.5 Spherical floater model

In this section the NEMOH results for the spherical floater model are shown.

In Table C.5 the number of panels used in the meshes for the spherical floater are shown.

Angular position θ [°]	-20	-10	0	10	20
No. of panels [-]	1550	1395	1218	1392	1546

Table C.5. No. of panels in the meshes used for the NEMOH calculations for the spherical floater model.

In the following sections the NEMOH results for added mass, damping and wave excitation moment for the spherical floater model are shown.

Added mass

In Figure C.29 the normalised added mass for the spherical floater model is shown.

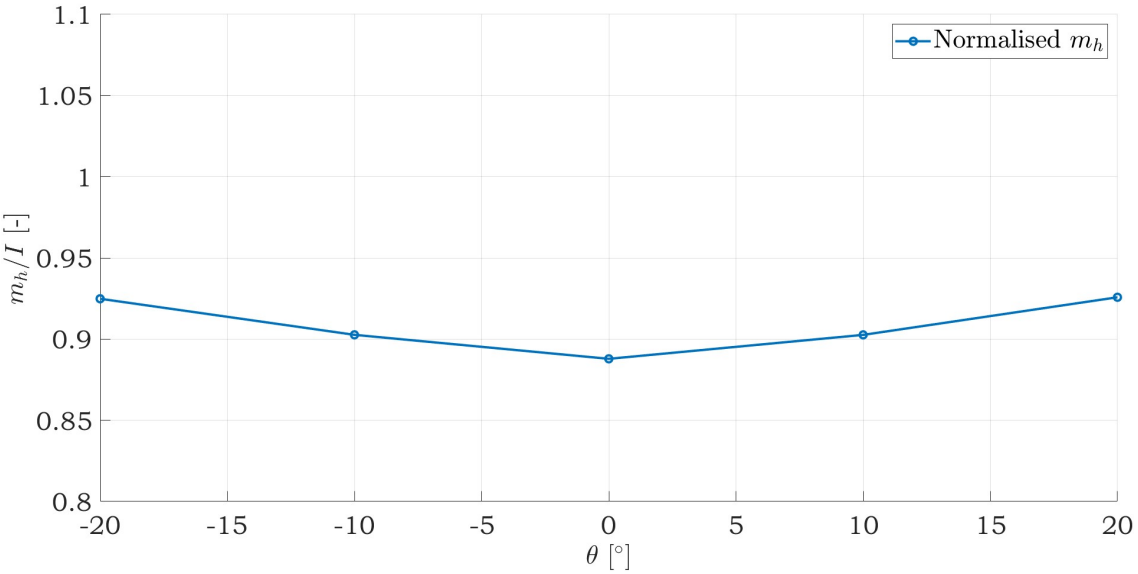

Figure C.29. Normalised added mass at θ from -20° to 20° for the spherical floater.

Damping

In Figure C.30 the damping coefficients for the spherical floater model for the different angular positions are shown.

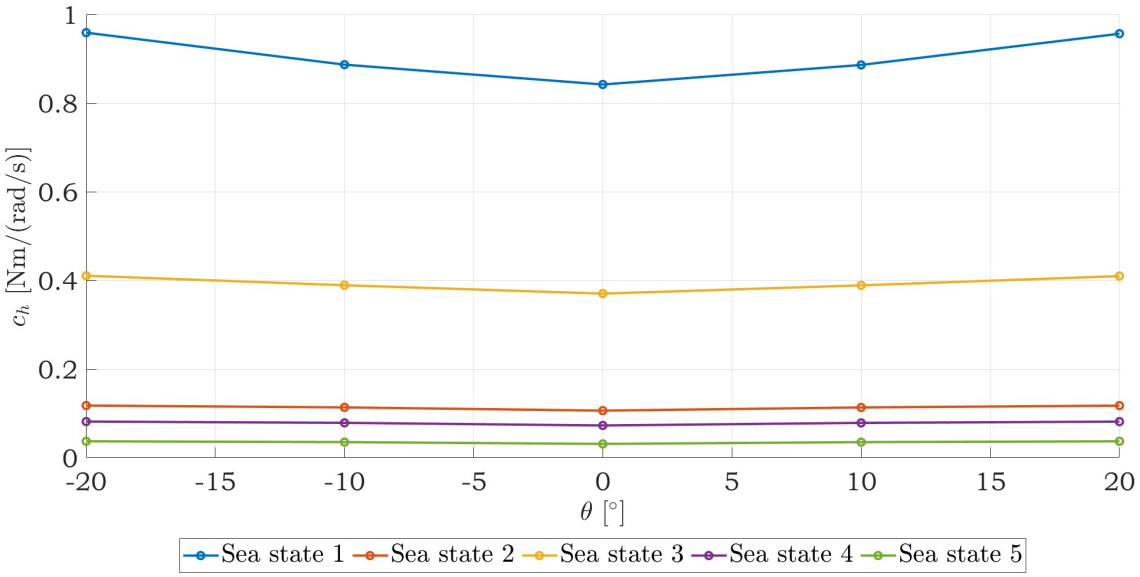

Figure C.30. Damping coefficients at θ from -20° to 20° for the spherical floater model.

Wave excitation forces

In Figure C.31 the normalised moment is shown for the different angular positions.

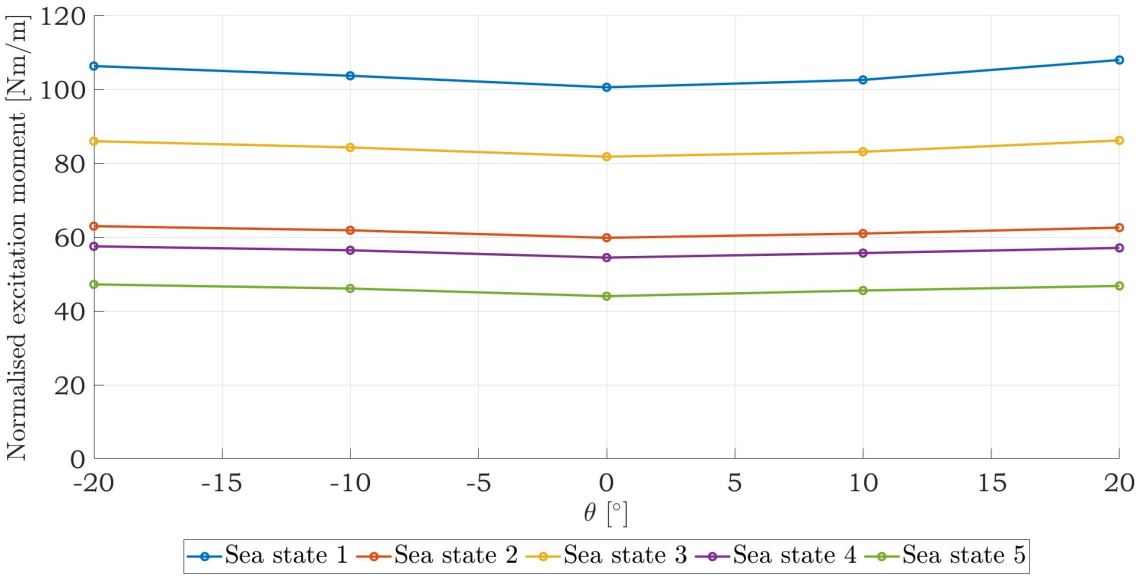

Figure C.31. Normalised wave excitation moment at θ from -20° to 20° for the spherical floater model.

C.6 Results for wave excitation tests

In the following section, the results for the wave excitation tests on all floater models are shown.

C.6.1 Cylindrical floater model

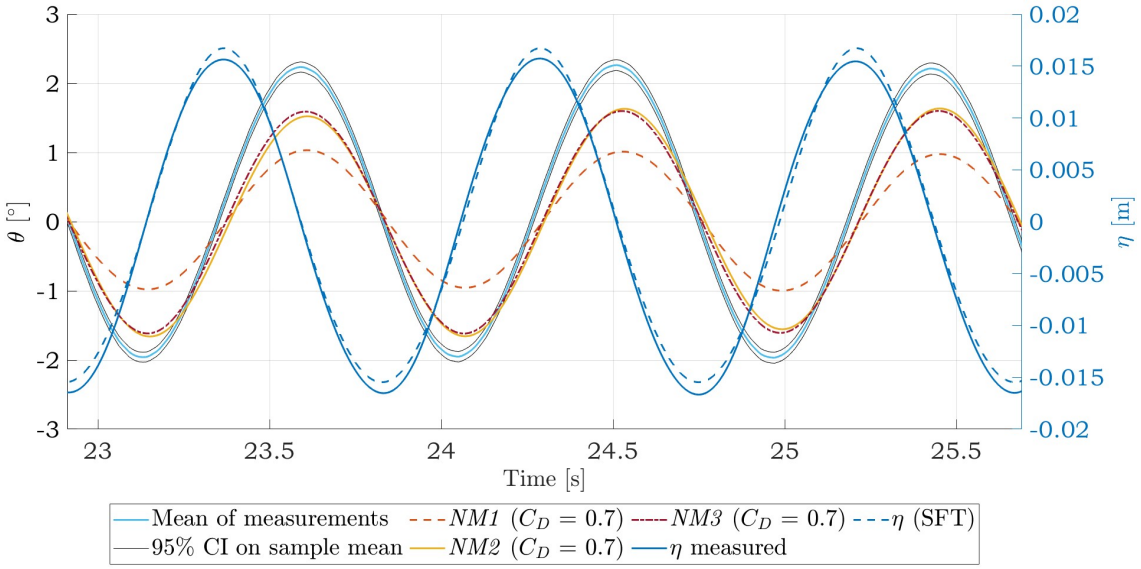

Figure C.32. Comparison of results from numerical models and measured results for sea state 1.

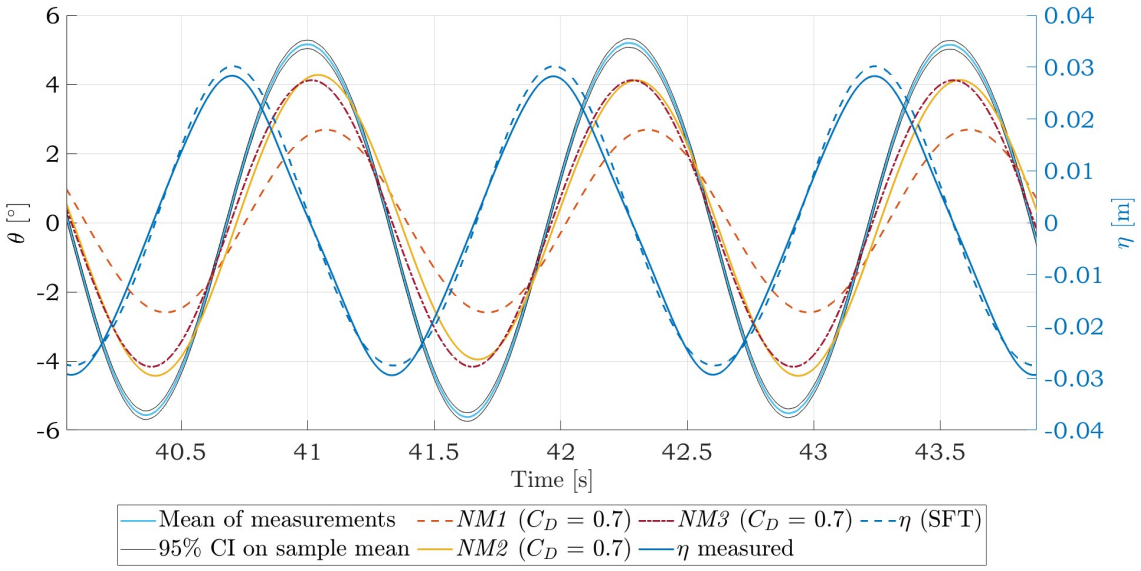

Figure C.33. Comparison of results from numerical models and measured results for sea state 2.

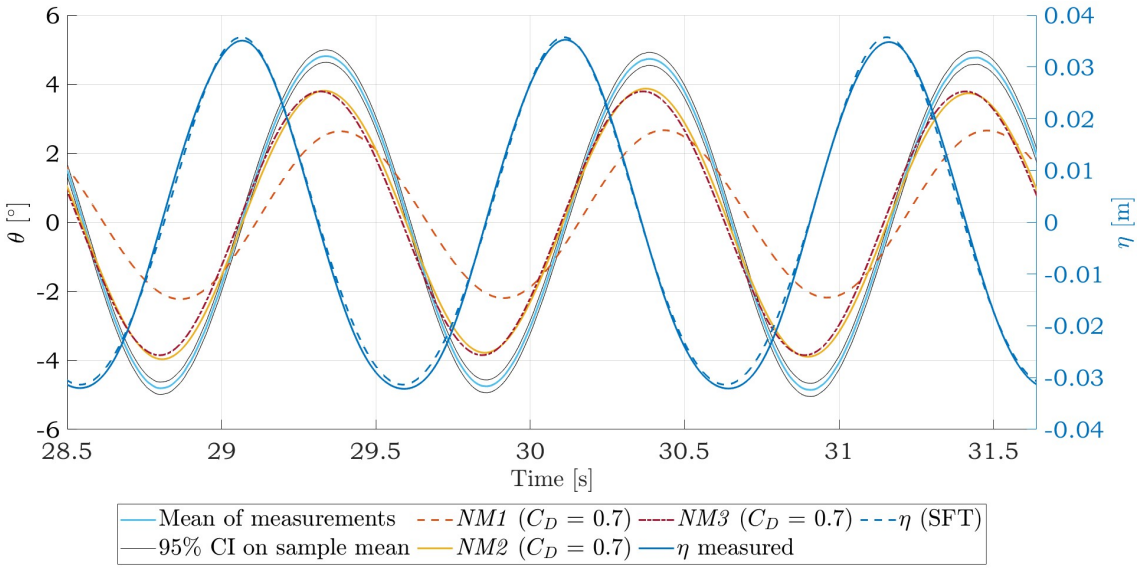

Figure C.34. Comparison of results from numerical models and measured results for sea state 3.

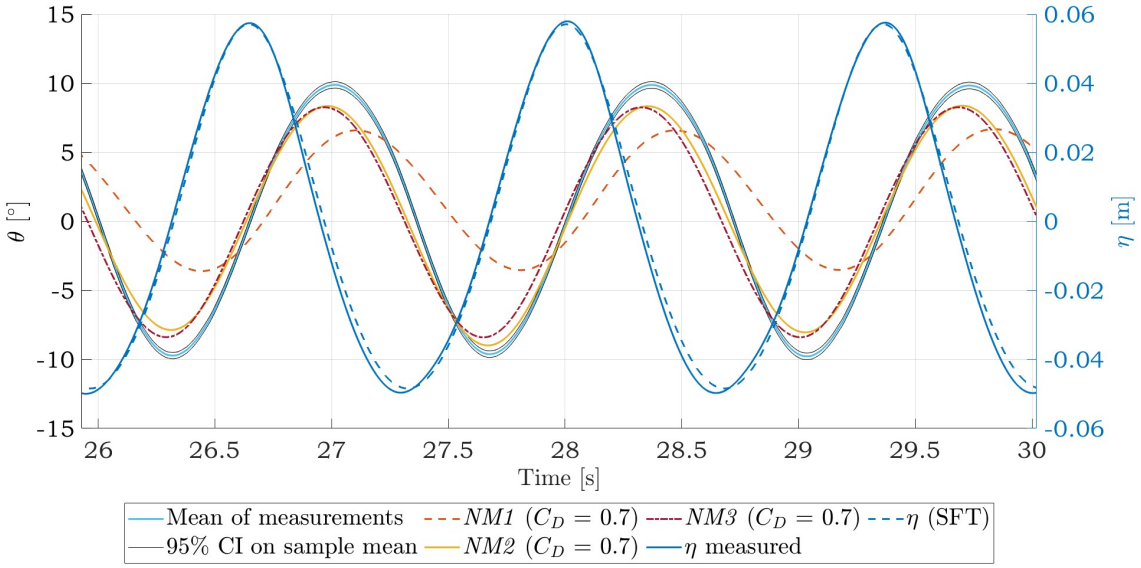

Figure C.35. Comparison of results from numerical models and measured results for sea state 4.

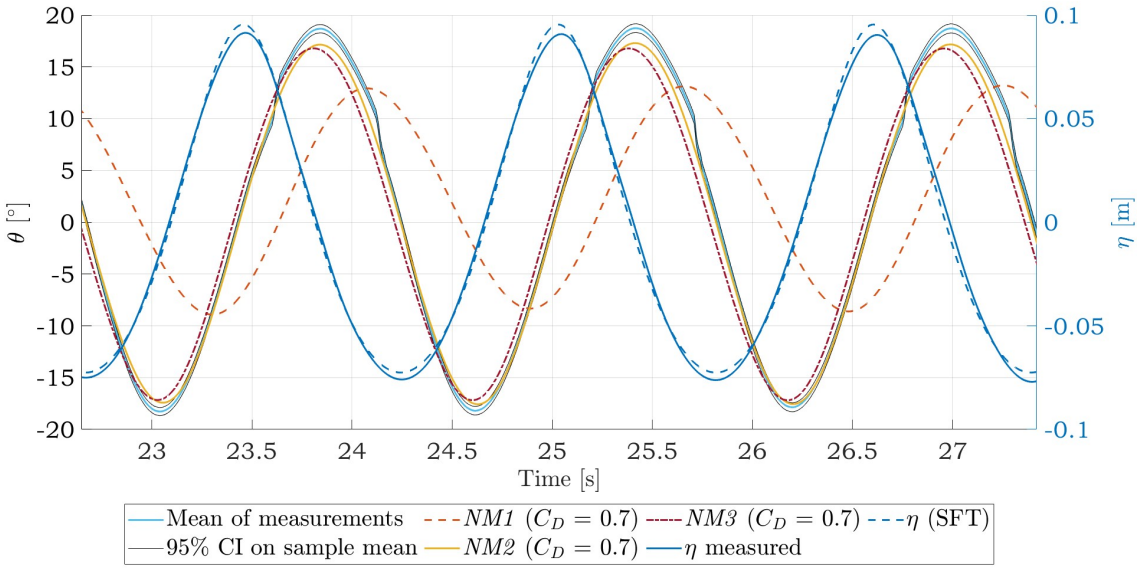

Figure C.36. Comparison of results from numerical models and measured results for sea state 5.

C.6.2 Disc-shaped floater model

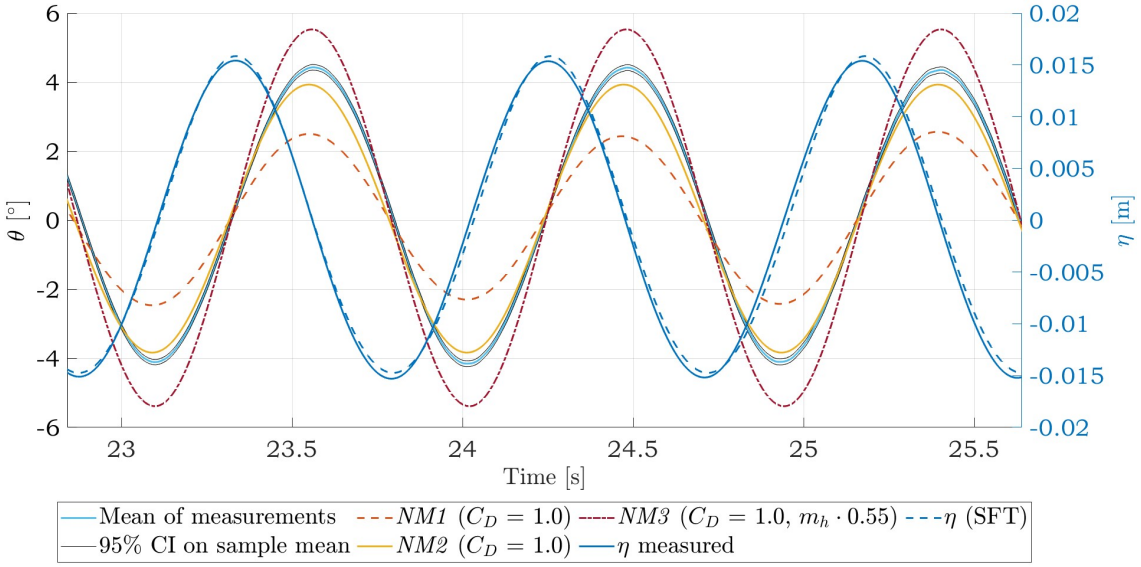

Figure C.37. Comparison of results from numerical models and measured results for the disc-shaped floater in sea state 1.

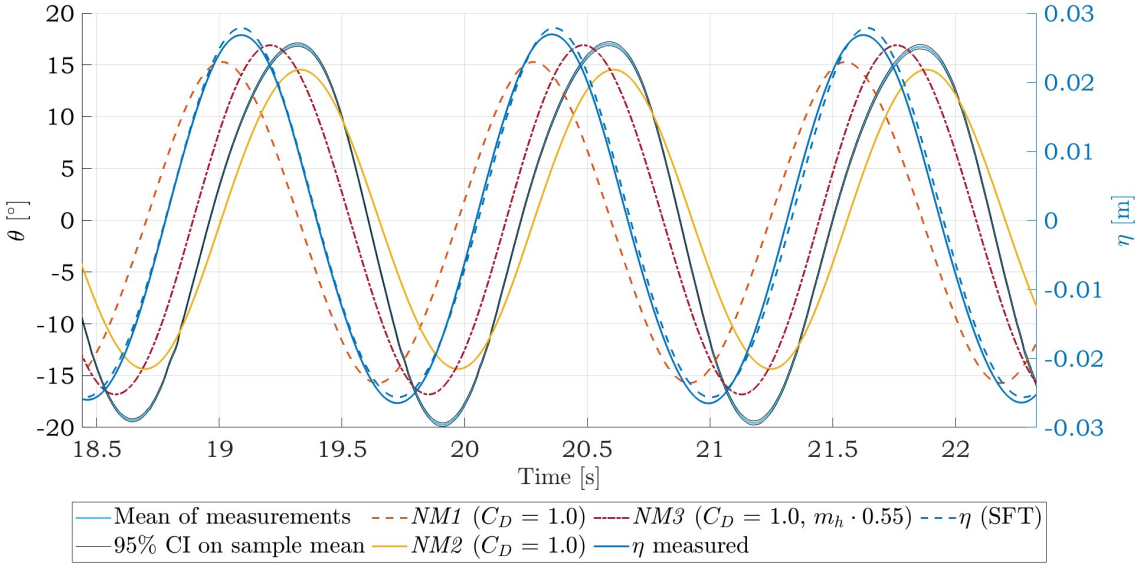

Figure C.38. Comparison of results from numerical models and measured results for the disc-shaped floater in sea state 2.

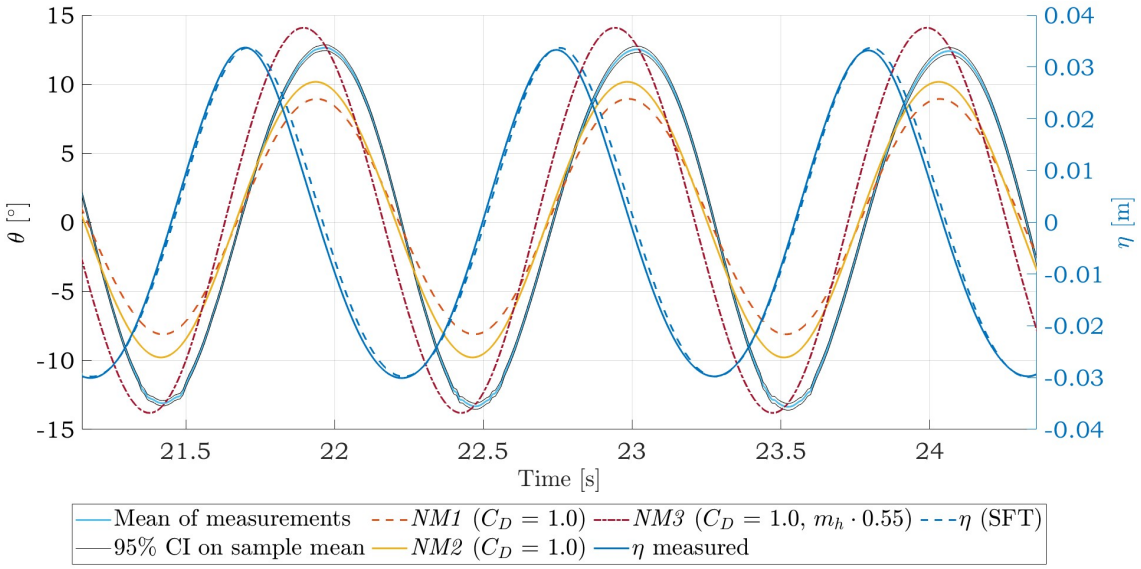

Figure C.39. Comparison of results from numerical models and measured results for the disc-shaped floater in sea state 3.

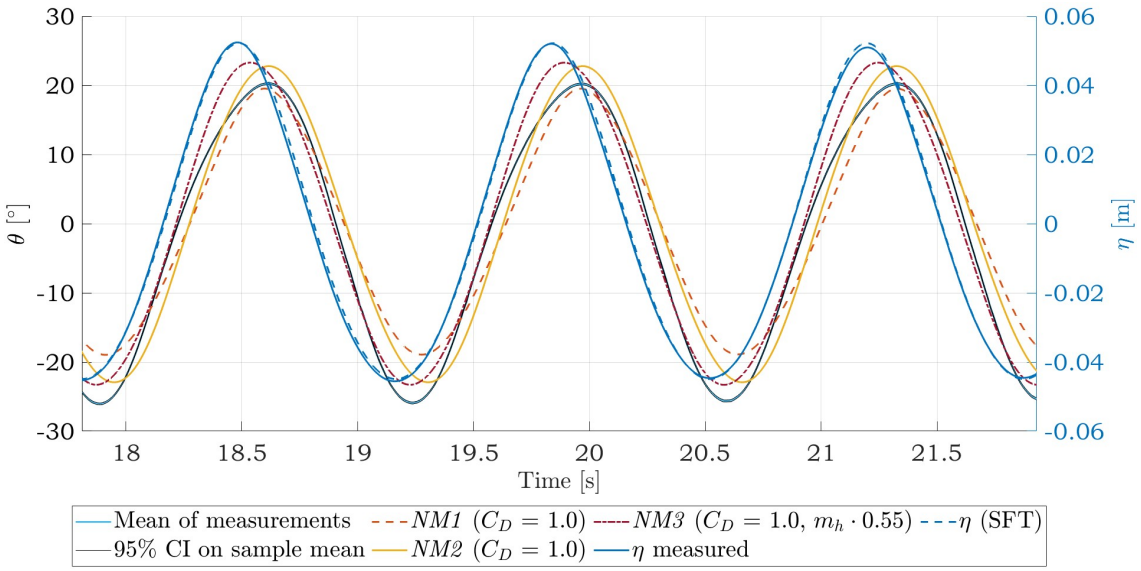

Figure C.40. Comparison of results from numerical models and measured results for the disc-shaped floater in sea state 4.

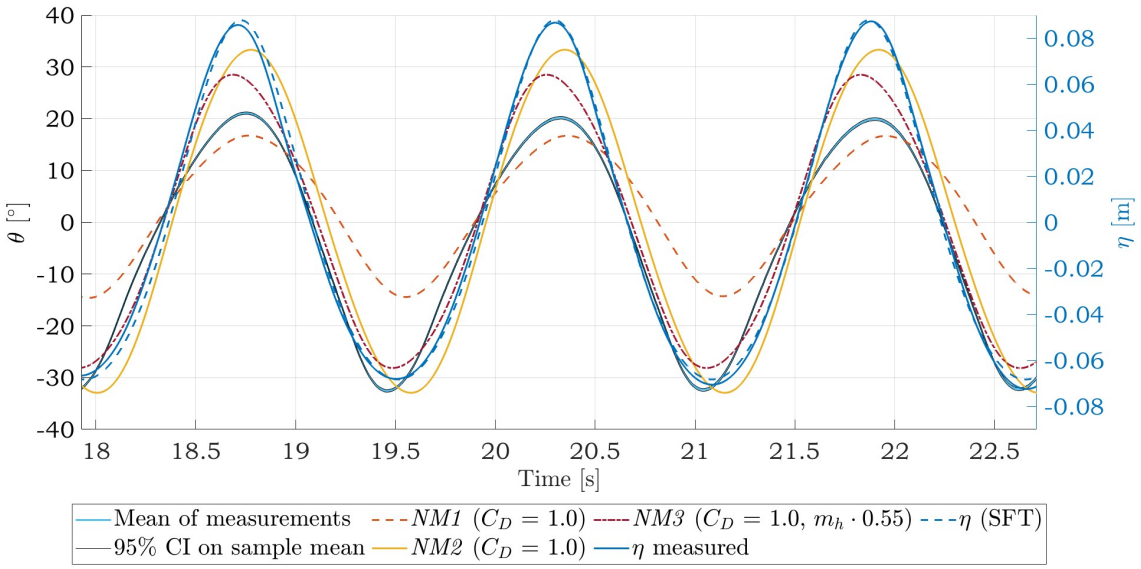

Figure C.41. Comparison of results from numerical models and measured results for the disc-shaped floater in sea state 5.

C.6.3 Conical floater model

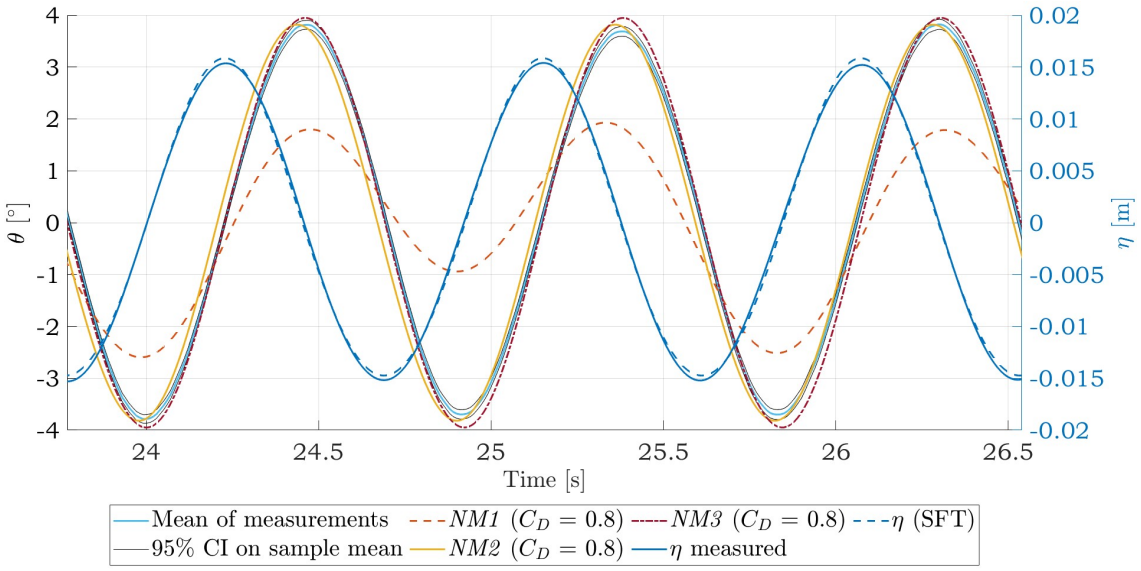

Figure C.42. Comparison of results from numerical models and measured results for the conical floater in sea state 1.

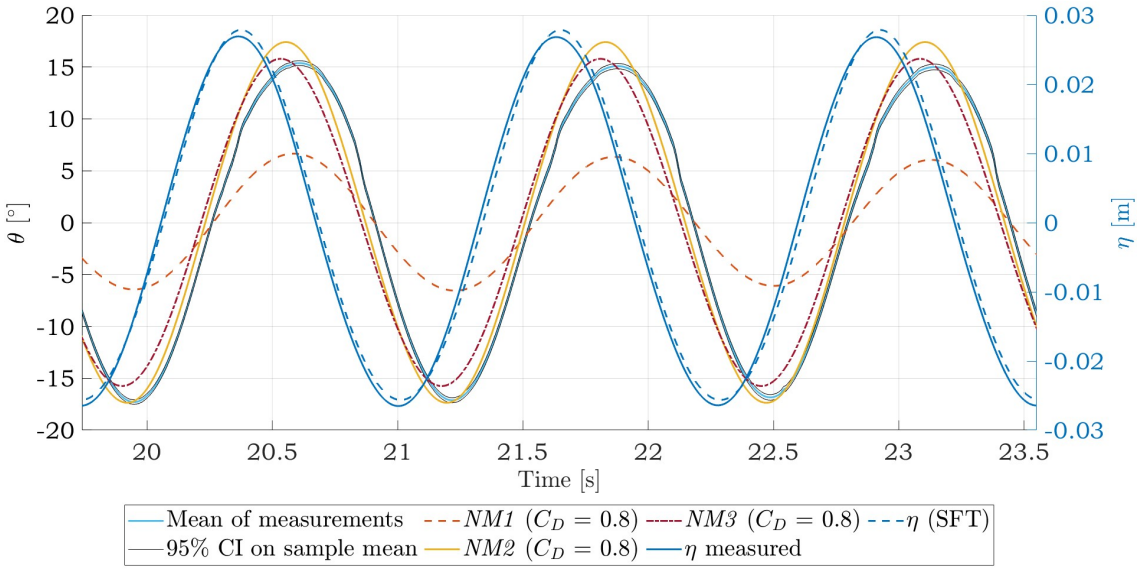

Figure C.43. Comparison of results from numerical models and measured results for the conical floater in sea state 2.

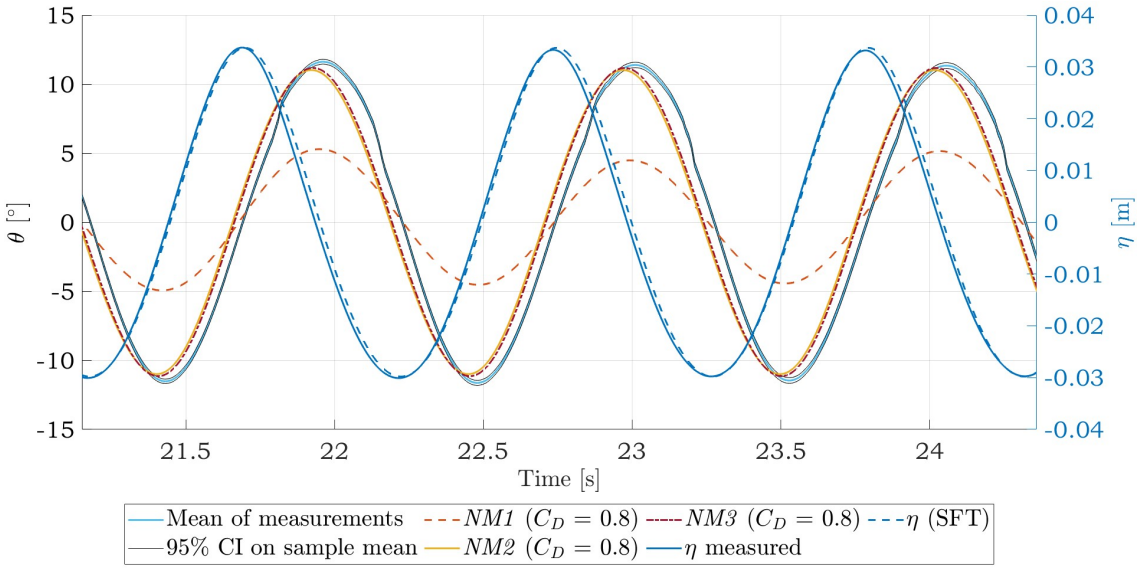

Figure C.44. Comparison of results from numerical models and measured results for the conical floater in sea state 3.

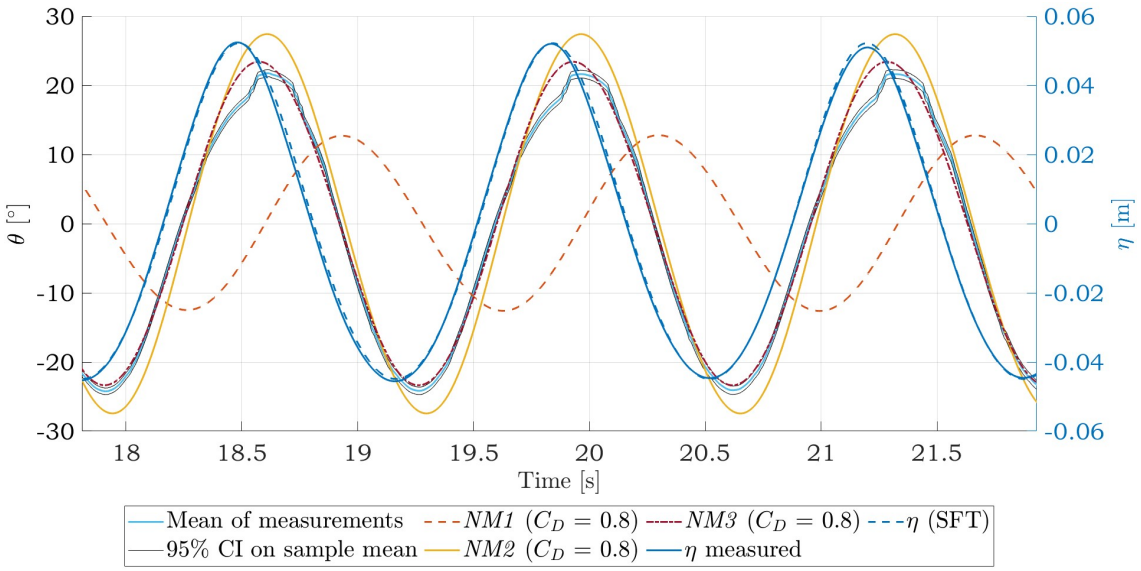

Figure C.45. Comparison of results from numerical models and measured results for the conical floater in sea state 4.

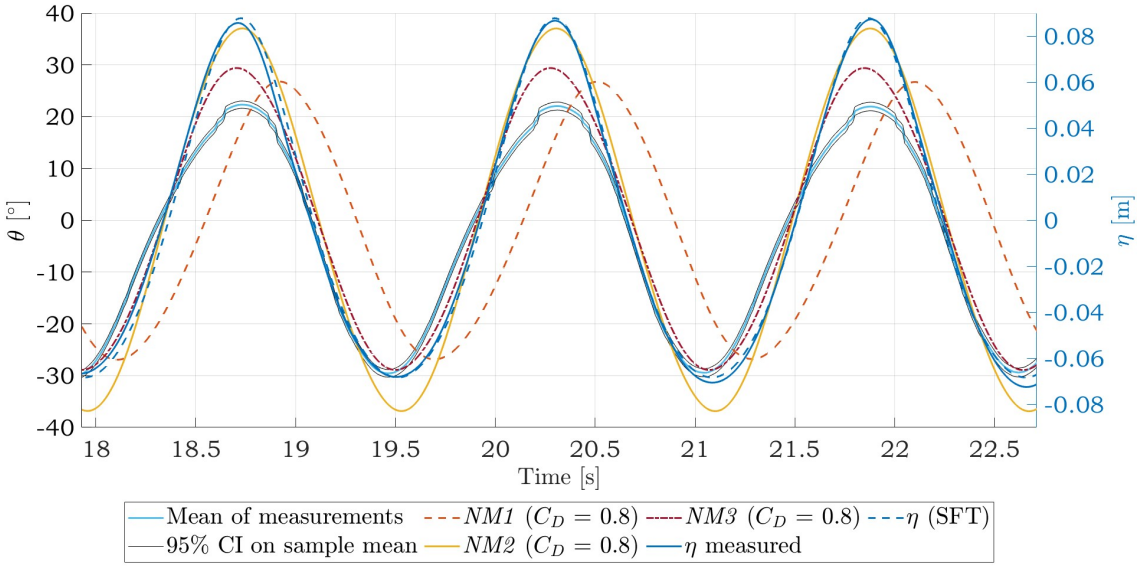

Figure C.46. Comparison of results from numerical models and measured results for the conical floater in sea state 5.

C.6.4 Spherical floater model

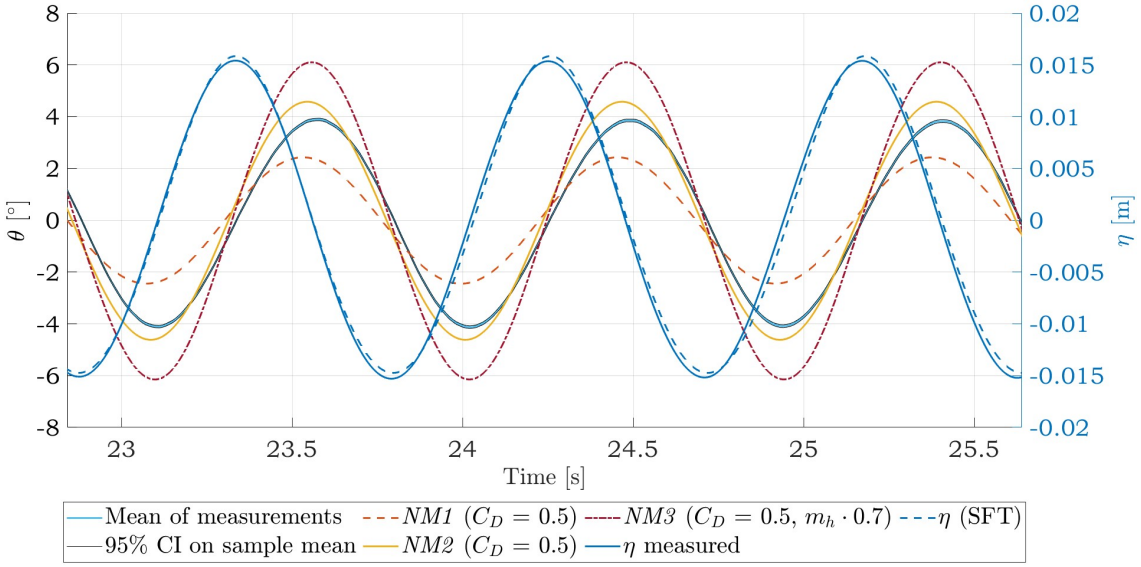

Figure C.47. Comparison of results from numerical models and measured results for the spherical floater in sea state 1.

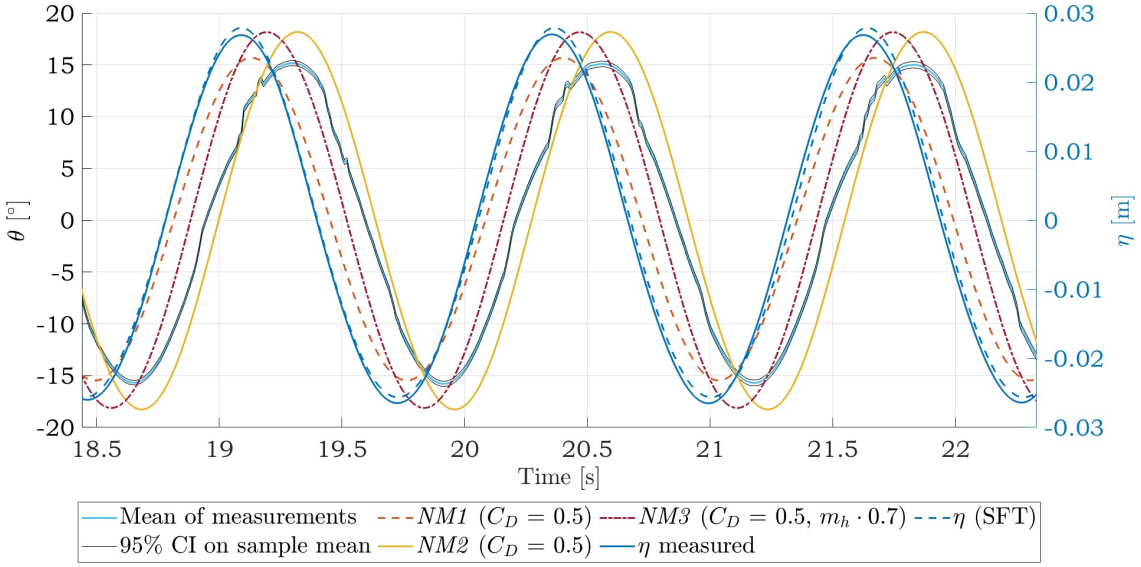

Figure C.48. Comparison of results from numerical models and measured results for the spherical floater in sea state 2.

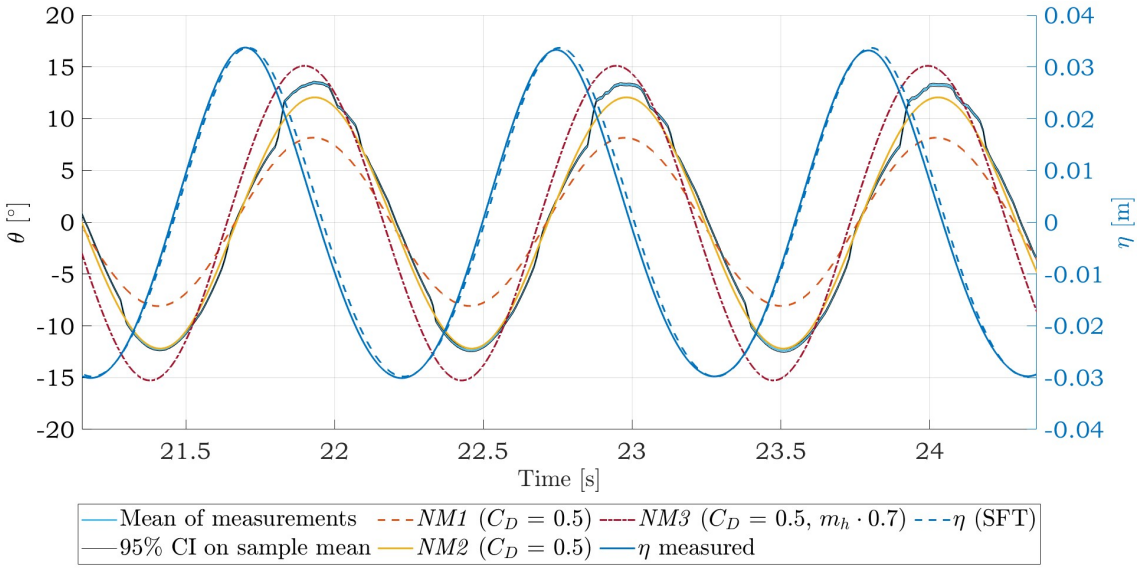

Figure C.49. Comparison of results from numerical models and measured results for the spherical floater in sea state 3.

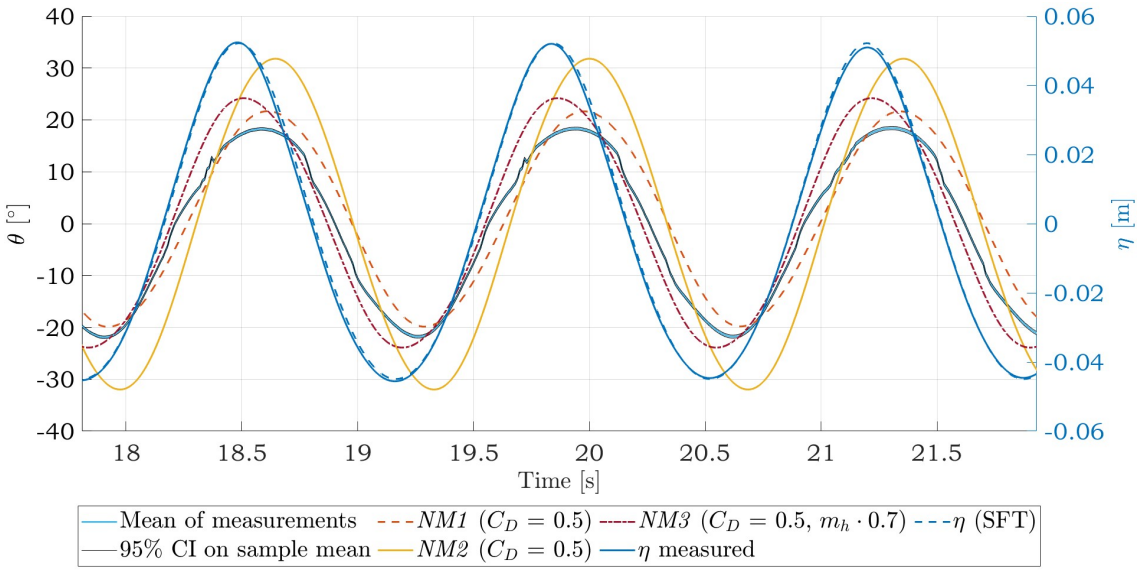

Figure C.50. Comparison of results from numerical models and measured results for the spherical floater in sea state 4.

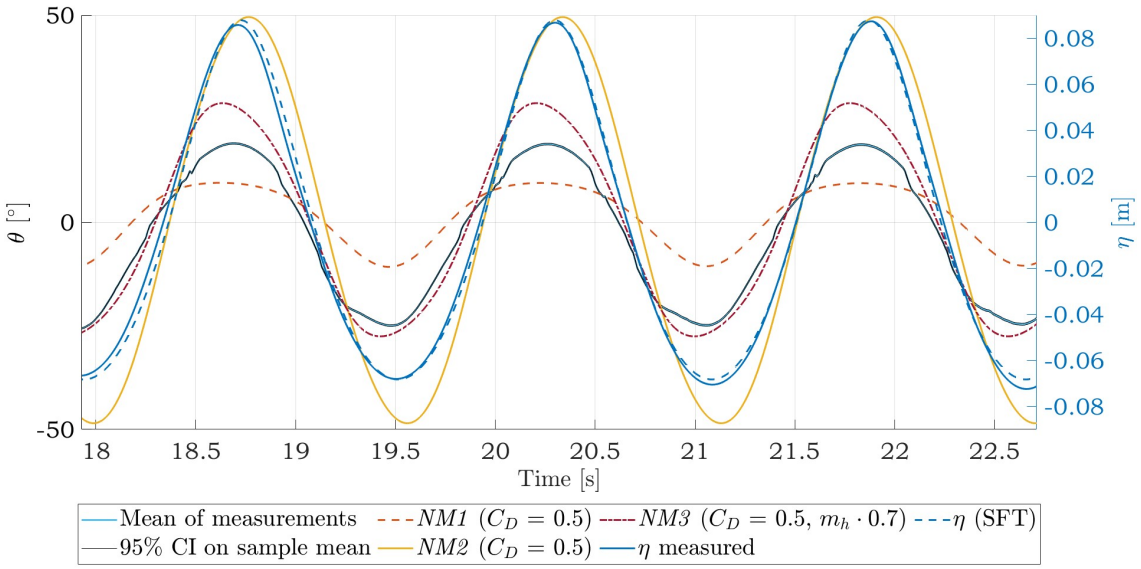

Figure C.51. Comparison of results from numerical models and measured results for the spherical floater in sea state 5.